2014

Islanding detection of distributed generation and classification of voltage sags/swells using machine learning techniques

Mollah R. Alam
University of Wollongong, mra497@uowmail.edu.au

ISLANDING DETECTION OF DISTRIBUTED GENERATION AND CLASSIFICATION OF VOLTAGE SAGS/SWELLS USING MACHINE LEARNING TECHNIQUES

A Thesis Submitted in (Partial) Fulfilment
of the Requirements for the Award of the Degree

DOCTOR OF PHILOSOPHY

from

UNIVERSITY OF WOLLONGONG

by

MOLLAH REZAUL ALAM
School of Electrical Computer and Telecommunications Engineering
Faculty of Engineering and Information Sciences
2014

PUBLICATIONS ARISING FROM THIS THESIS

Journal Articles:

1. M. R. Alam, K. M. Muttaqi, A. Bouzerdoum, "A Multifeature-Based Approach for Islanding Detection of DG in the Subcritical Region of Vector Surge Relays," *IEEE Transactions on Power Delivery*, vol. 29, no. 5, pp. 2349-2358, Oct. 2014.

2. M. R. Alam, K. M. Muttaqi, A. Bouzerdoum, "An Approach for Assessing the Effectiveness of Multiple-Feature-Based SVM Method for Islanding Detection of Distributed Generation," *IEEE Transactions on Industry Applications*, vol. 50, no. 4, pp. 2844-2852, July-Aug. 2014.

3. M. R. Alam, K. M. Muttaqi, A. Bouzerdoum, "A New Approach for Classification and Characterization of Voltage Dips and Swells using 3D Polarization Ellipse Parameters," accepted for publication in *IEEE Transactions on Power Delivery*, DOI (identifier) 10.1109/TPWRD.2014.2361624.

4. M. R. Alam, K. M. Muttaqi, A. Bouzerdoum, "Characterizing Voltage Sags and Swells using Three-phase Voltage Ellipse Parameters," accepted for publication in *IEEE Transactions on Industry Applications*.

Refereed Conference Proceedings:

5. M. R. Alam, K. M. Muttaqi, and A. Bouzerdoum, "A short length window-based method for islanding detection in distributed generation," in *Proc. International Joint Conference on Neural Networks (IJCNN)*, Brisbane, Qld, pp. 1-6, 10-15 June 2012.

6. M. R. Alam, K. M. Muttaqi, A. Bouzerdoum, "An approach for assessing the effectiveness of multiple features based SVM method for islanding detection of distributed generation," in *Proc.2013 IEEE Industry Applications Society Annual Meeting*, Orlando, Florida, 6-11 Oct. 2013.

ACKNOWLEDGEMENT

I would like to gratefully acknowledge the guidance and support provided by my supervisors A/Prof. Kashem M. Muttaqi and Prof. Abdesselam Bouzerdoum in conducting the research works presented in this thesis. In addition, I would like to appreciate the support of the Australian Power Quality and Reliability Centre. Most importantly, the scholarship provided by the SMART infrastructure facility, University of Wollongong, is also acknowledged.

ABSTRACT

This thesis presents innovative approaches for detection, classification and characterization of abnormal events in electricity networks. Due to disturbances and/or faults in electricity networks, the abnormal events are created; one such abnormal event is the formation of power system island containing distributed generating resources and the other is the voltage dips and/or swells. This thesis proposes a Support Vector Machine (SVM) based approach for detection and classification of islanding events in a distribution network embedded with Distributed Generation (DG). Furthermore, two innovative approaches, which include three-phase voltage ellipse method and 3D polarization ellipse technique, are proposed to detect, classify and characterize voltage dips and/or swells in electricity networks.

In order to meet the increasing load demand of future electricity grids, integration of distributed generation (DG) is expected to play an increasingly important role. Prior to the integration of DG into electricity grids, the issue of anti-islanding protection is needed to be considered. Conventional vector surge (VS) and rate-of-change-of-frequency (ROCOF) relays are usually used to detect islanding; however, there is a non-detection zone (NDZ) wherein islanding incidents are undetectable by these conventional relays. For VS and ROCOF relays, NDZ is a function of active and reactive power imbalance, which may exist inside the islanded segment. In this thesis, using the concept of NDZ, the performance of these relays is evaluated for islanding detection. The performance is also assessed using the performance indicators, namely, detection rate (DR) and false alarm (FA). These indicators are also used to establish the limitations of the VS and ROCOF relays for islanding detection, especially when there is a small power imbalance between load and generation inside the islanded segment.

In the context of the problems and the limitations of the conventional relays outlined above, this thesis proposes a multi-feature based technique for islanding detection of synchronous type DG. In the proposed method, features are extracted from five network variables associated with voltage signal. The extracted features are then used as inputs to a support vector machines to classify the event as islanding or non-islanding. The proposed method works effectively for both, outside and inside the NDZ of conventional VS and ROCOF relays. A test network derived from Australian electricity systems is used to generate a large number of islanding and non-islanding events with

different load types. The SVM based method is tested with special emphasis on the most critical islanding cases associated with NDZ of VS and ROCOF relays. Furthermore, all possible combinations of deficit and excess of active and reactive power imbalance, which may exist during the occurrence of an island, are considered in the testing phase. A comparative study between conventional relays (VS and ROCOF) and the proposed SVM based relay (SVMR) is conducted using the performance indicators, i.e., detection rate (DR) and false alarm (FA). Using the concept of detection-time, performance of conventional relays and the SVM based relay is also compared. Experimental results demonstrate that the proposed method can successfully detect islanding events under different network contingencies and conditions including the NDZ, where conventional relays are expected to fail.

Voltage dip is generally considered a power-quality problem of equal importance as long and short interruptions in the supply. At present, it has become very challenging to control the external factors that cause voltage dips. Thus, proper mitigation techniques are desired. However, development of mitigation techniques requires the accurate diagnosis, characterization and classification of voltage dips. Furthermore, classification of voltage dips and swells plays an important role in the assessment of voltage dip ride-through capability and immunity of electrical equipment.

To solve the classification and characterization problems associated with voltage dips and swells in electricity networks, this thesis presents an approach that exploits three-phase voltage ellipse parameters. It employs the instantaneous magnitude of three-phase voltage signals in three axes, which are separated from each other by 120°. Thus, resultant rotating vector, namely, three-phase voltage vector, traces an ellipse. Then, the parameters of the ellipse, which include minor axis, major axis and inclination angle, are used to develop an algorithm for classification and characterization of voltage sags and swells. To this end, the inclination angle is used to classify the types of sags and/or swells, whereas the minor and major axis are used to quantify the severity of sags and swells, respectively. The proposed method is validated using recorded waveforms as well as simulated sags and/or swells arising due to balanced and unbalanced faults at different buses in a practical distribution network of Australia. The feasibility of the proposed approach is demonstrated using extensive simulation for the use as a real-time sag-swell monitoring tool.

The approach, as mentioned above, can be used as a quick screening tool for voltage dips/swells, and it can classify and characterize voltage dips in terms of the severity of dip/swell-phase voltages with less computational effort and time. Moreover, a comprehensive classification approach is devised to classify and characterize voltage dips and swells associated with different dip-types, which may occur in power networks due to propagation of dips through network elements such as power transformers with various winding configurations. This new innovative approach exploits unique signatures and parameters of three phase voltage signals extracted from the polarization ellipse in three-dimensional (3D) co-ordinates. Five ellipse parameters, which include azimuthal angle, elevation, tilt, semi-minor axis and semi-major axis, are used to classify and characterize voltage dips and swells. Seven types of voltage dips, which include a total of 19 groups of dips incorporating different kinds of balanced (three-phase dips) and unbalanced (single-phase or double-phase) dips, are identified and successfully classified using the 3D polarization ellipse parameters. Two types of voltage swells, which include a total of 6 groups, are also classified using the proposed method. The advantage of this method is that it can cope with large angle jumps, and has capability to detect, classify and characterize both voltage dips and swells more accurately. The proposed method is validated using real measurement data, recorded waveforms provided by the IEEE 1159.2 working group, and the data of unbalanced dips associated with phase angle jumps, voltage drops and rotations due to loading effects. Moreover, the proposed detailed approach has been tested for its applicability to assess the voltage sags/swells due to faults/disturbances associated with pre- and post-islanding scenarios, such as, the transitional state of islanding, disconnection of DG or establishment of island with proper control and grid re-synchronization.

All the proposed approaches of this thesis are developed based on multiple features of three-phase voltage signals which can be captured in electricity networks through potential transformers (or PTs). The captured signals can be processed in the high-speed micro-processors and decisions can be made in the decision engine where proposed algorithms are implemented on micro-controllers. Also, cycle by cycle event reports for voltage dips/swells can be published in real-time.

TABLE OF CONTENTS

LIST OF FIGURES

LIST OF TABLES

Chapter 1

INTRODUCTION

1.1 IMPORTANCE OF THE RESEARCH

Normal operation of electric power system ensures the continuous supply of undistorted sinusoidal rated voltage and current at rated frequency to the customer end. However, disturbances and/or faults in electricity networks may create abnormal events. Detection, classification and characterization of these abnormal events are important, as it finds its application for protection and mitigation issues, as well as post-disturbance off-line analysis.

Voltage and current are two important parameters, which are utilized to classify and characterize abnormal events. These parameters (voltage and current) are passed through the instrument transformers, i.e., potential transformer (PT) and current transformer (CT), in order to measure voltage and current respectively. The voltage and current, which come out from the instrument transformers, are regarded as inputs for the abnormal events detection-devices, such as, relays or other intelligent devices. Therefore, reliability of PT and CT is an essential aspect for the detection-devices to detect the abnormalities effectively. According to [1], CT has magnetic saturation issue and it suffers from the error due to non-linearity, especially during fault or abnormal condition. In contrast, PT provides excellent reproduction of primary voltage during both transient and steady-state [1]. Normally, PT does not experience saturation, since power systems are not operated above the voltage limit, and in most cases faults result in a collapse or reduction in voltage, or sometimes voltage may rise but it does not cause saturation [1]. Therefore, classification and characterization of abnormal events utilizing only voltage parameter would certainly provide an accurate insight of the events. Hence, taking voltage and its associated features as input parameters, innovative approaches need to be developed which can detect, classify and characterize abnormal events. To this end, this thesis mainly deals with the detection, classification and characterization of two such abnormal events; first one is the formation of islanding and the second one is the voltage dips and/or swells.

In order to highlight the motivation of the research in details, this Section discusses the issues and the importance of the research related to the detection and classification of islanding and voltage dips/swells. Section 1.1.1 presents the issues related to islanding events and the currently available anti-islanding protection or islanding detection schemes. The importance of new islanding detection method, which will take voltage and its associated features as inputs and will also be able to perform effectively outside as well as inside the non-detection zone of conventional relays, is discussed. Section 1.1.2 discusses the issues related to voltage dips and swells; the presently available voltage dips/swells classification methods and their limitations. The importance of new algorithm for classification and characterization of voltage dips/swells is highlighted as well.

1.1.1 Islanding Detection of Distributed Generation

In order to meet the increasing load demand of future electricity grids, integration of distributed generation (DG) in distribution networks is expected to play an increasingly important role. The penetration of DG is forcing the electricity system planners and operators to develop standards, referred to as Interconnection Guidelines (IG) of distributed resources with electric power system [2, 3]. An essential requirement for IG is the protection of DG *islanding*, also known as the protection of "loss of mains". Islanding is a situation when a portion of electric power system (EPS) is energized solely by one or more Local DG systems while that portion of the EPS is electrically isolated from the rest of the EPS [2]. This electrical isolation may occur due to feeder switching, switchgear operation and/or fault clearing operation, etc. According to IG [2, 3], islanded DG must be disconnected quickly in order to avoid probable hazardous conditions, such as, power quality degradation, damage of utility and customer equipment, etc. The IEEE 1547-2003 standard recommends the disconnection time to be less than 2 seconds. However, recent trend of rapid automatic reclosing can cause serious damage to both the islanded synchronous DGs and to neighbouring utility equipment, if 2 seconds of DG disconnection benchmark is maintained [4]. Therefore, this disconnection benchmark may have to be reduced to allow the disconnection of islanded synchronous DG prior to the completion of first reclosing operation [2, 3,5].

At present, different techniques, such as, active, passive and communication-based techniques are used to implement islanding detection schemes. Commonly used

communication based techniques include “transfer trip” and “power line signalling”. They are reliable but can be costly depending on the availability of communication infrastructure. Active islanding detection techniques are normally applied on the inverter interfaced DG. These techniques involve a special control mechanism in conjunction with the continuous monitoring of the variation of externally generated signals at the DG site. This method provides several advantages as it tends to have fast response with small Non-Detection Zone (NDZ); however, using this method leads to degradation in power quality due to the perturbation imposed on the system. Examples of some active islanding detection techniques, such as, slip-mode frequency shift, active Frequency Drift, Sandia frequency and voltage shift method, have been reported in [6-8]. Passive methods use different system parameters, e.g., voltage, current, frequency, real power, reactive power, etc., and compare the parameter to a pre-specified threshold to decide the occurrence of islanding. Passive methods do not affect the normal operation of the DG system and are easy to implement, but they may not be reliable due to lack in accuracy.

Due to the trade-off between accuracy and cost, conventional relays, which are operated on the principle of passive islanding detection methods, are used for islanding detection. Examples of such conventional relays comprise of Frequency Relay (FR), Vector Surge (VS) relay which is also known as voltage jump relay or vector shift relay, and ROCOF (rate-of-change-of-frequency) relay, etc. VS and ROCOF relays have gained special interest in current industry practice [9-12]. The performance of these relays has a strong correlation with active power imbalance of the islanded system. The performance of VS and ROCOF relays deteriorates, when the power imbalance falls below a certain specified threshold, which gives rise to the limitation of Non-Detection Zone (NDZ) [13]. To overcome this issue, several computational intelligence based passive techniques have been proposed for islanding detection [14, 15]. Fuzzy rule-based classifier, Decision Tree (DT) approach and wavelet based technique have attracted widespread attention [16-18]. However, most of the computational intelligence based passive techniques have utilized voltage and current as input parameters. Since, current will be extracted through CT, and CT has magnetic saturation issue, the performance of these approaches may have some limitations in practical power systems. Besides, performance of all these approaches have not been assessed comprehensively, specially, inside the NDZ of conventional relays, such as, VS and ROCOF relays etc.

Therefore, there is a need for new approach which will take voltage and its associated features as inputs and will be able to detect islanding outside as well as inside the NDZ of conventional relays with confidence.

1.1.2 Classification and Characterization of Voltage Dips and Swells

Over the last few years, the concept of power quality (PQ) has been changed significantly, due to technological progression and customer awareness of better services. A few years ago, the main PQ concerns were the reliability, i.e., the frequency of the discontinuity of electricity supply. At present, the problems related to PQ include voltage dips or sags, fluctuations, temporary interruptions and harmonics [19]. The increased application of non-linear power electronic devices in electric power systems hastens the degradation of PQ, thereby necessitating more attention from electricity sector agents [20].

Voltage dips are generally considered a power-quality problem of equal importance as long and short interruptions in the supply [21, 22]. They are defined as the short-duration reduction in root-mean-square (rms) voltage caused by switching and/or starting of electrical motors, generators and bulk loads, transformer energization and faults or short circuits in the power networks [23]. Even though power utilities and customers are exerting extensive efforts to improve the reliability of power networks, it has been very challenging to control the external factors that cause voltage dips. Thus, proper mitigation techniques are desired. However, development of mitigation techniques requires the accurate diagnosis, characterization and classification of voltage dips. Furthermore, classification of voltage dips and swells plays an important role in the assessment of voltage dip ride-through capability and immunity specifications of electrical equipment.

Voltage dips are usually characterized by the minimum voltage magnitude and total duration [24-27]. According to [28], these standards can be effective for the characterization of single-phase and 3-phase balanced voltage dips; however, these approaches fail to characterize unbalanced voltage dips, including single- and double-phase dips. To resolve this problem, Bollen proposed a seven-type dip classification [22], referred to as ABC classification. Bollen and Zhang also proposed a symmetrical component based technique to classify and characterize voltage dips [23, 29]. In [30], it was reported that the symmetrical component technique has some limitations in

characterizing unbalanced voltage sags originating from large dynamic loads. In [31], a space vector method was presented wherein the ellipse inclination angle was used to classify single-phase and double-phase voltage dips. However, this method is not suitable for classification of voltage dips for the case of large phase angle jump.

The presence of DG in distribution networks is expected to have an impact on the retained voltage during the occurrence of dip. DG can inject reactive power to support the voltage during disturbance; it can also introduce additional phase angle jump which can make the voltage dip classification even more complex. Furthermore, due to pre- and post-islanding scenarios, such as, the transitional state of islanding, disconnection of DG or establishment of island with proper controlling action, grid re-connection, etc., different types of voltage dips and swells may occur which may create the characterization of voltage dips more critical. Therefore, a new algorithm for classifying and characterizing voltage sags and swells is required, which would be unaffected by phase-angle jump and would be suitable for real-time usage as well.

1.2 RESEARCH OBJECTIVES AND METHODOLOGIES

The main goals of this thesis is to develop innovative techniques which will be applicable to solve two crucial issues in electricity network: 1) islanding detection of distributed generation with special emphasis on the critical islanding events associated with non-detection zone of vector surge and ROCOF relays, and 2) detection, classification and characterization of voltage dips and swells, which will be applicable for classification and characterization of voltage dips and swells under different network conditions. The aims of this thesis are achieved through:

- The establishment of theoretical analysis, to examine the performance of conventional vector surge and ROCOF relays for islanding detection, using the concept of non-detection zone.

- The comprehensive investigation of VS and ROCOF relays associated with islanding detection under all possible combinations (deficit and excess) of power imbalance scenarios and at the presence of different types of loads.

- The development of innovative method for detection and classification of islanding events which will take multiple voltage features as input; the proposed method needs to be capable of islanding detection not only outside the NDZ of

VS and/or ROCOF relays but also inside the NDZ associated with the critical events.

- The establishment of theoretical analysis for fault-initiated voltage dips and its validation with simulation study. The investigation of different types of voltage dips, which are originated due to propagation of dips through different network elements. The detailed analysis of DG-impact, which is observed through the depth of voltage-dip and phase-angle jump associated with different types of fault-initiated dips.

- The development of innovative approach for classification and characterization of voltage dips and swells; the developed approach should be applicable for online monitoring of voltage dips/swells as well as offline analysis.

- The development of comprehensive approach for classification and characterization of voltage dips and swells associated with different dip/swell-types. The developed approach should be applicable for classification of voltage dips/swells associated with phase angle jump. It has to be computationally fast in order to make it suitable for real-time dip/swell classification and characterization.

Conventional relays, such as, VS and ROCOF relays, are normally used as anti-islanding protection device. In order to assess the performance of these relays, the concept of detection-time versus active power-imbalance curve is used. To obtain these curves, analytical formulae are developed. These curves are also obtained and verified through repeated dynamic simulations. The concept of critical active power imbalance, required for determining the boundary limit of *non-detection zone* (NDZ) of these relays, is presented using these curves; three types of loads, which include constant impedance, constant current and constant power loads, are considered during the establishment of boundary limit of NDZ. Thus, critical islanding events, associated with NDZ, wherein VS and ROCOF relays fail to detect islanding, are obtained. Moreover, the comprehensive investigations on VS and ROCOF relays are conducted using the performance indicators, namely, detection rate (DR) and false alarm (FA), under four possible combinations of deficit and excess of active and reactive power imbalance scenarios. In summary, the limitations of conventional VS and ROCOF relays are investigated while dealing with the critical islanding events.

To overcome the limitations of conventional relays as stated earlier, an innovative islanding detection technique is proposed. To this end, firstly, the whole problem is identified as a two-class classification problem; the classes are islanding and non-islanding. Then, a binary classifier is applied to classify the events. Support Vector Machine (SVM), which is a binary classifier [32, 33], has been widely used in many applications due to its excellent classification performance [34]. Therefore, to solve the classification problems of islanding and non-islanding events, in the proposed approach, SVM classifier is applied on the extracted features corresponding to different class of events. In this technique, features are extracted from five network variables; they include voltage, frequency, phase angle of voltage, rate of change of frequency, and rate of change of voltage (ROCOV). Then, these multiple voltage features are used as inputs to the SVM to classify the event as islanding or non-islanding. Besides, the feature extraction incorporates a sliding window; and the width of the window is optimally selected considering the Receiver Operating Characteristics (ROC) of the SVM classifier under different window-width. SVM is trained with linear, polynomial and Gaussian RBF kernels; and by tuning the parameters of these kernels, improved classification performance is achieved. In the testing phase, islanding events in the presence of constant impedance, constant current and constant power loads, are investigated. Moreover, combination of deficit and excess of active and reactive power imbalance inside the islanded segment makes the islanding detection even more complex [13]. In this thesis, islanding events, considering all possible combinations of power imbalance scenarios under constant impedance, constant current and constant power loads, are investigated and detected with a high degree of accuracy. The performance of proposed approach, based on reliability and speed of islanding detection, is also evaluated.

Voltage dips, being one of the most common power quality issues, have been investigated through different types of fault-study in electricity networks. Seven types of voltage dips and two types of swells normally exist in power system, due to these different fault-types and their propagation through different network equipment. Classification and characterization of these different types of dips and swells are important to facilitate the development of mitigation techniques. Therefore, in order to solve the classification and characterization problems of voltage dips (or sags) and swells, an innovative approach based on *three-phase voltage ellipse* is proposed. The

proposed approach is effective for the application of sag/swell analysis tool in real-time. In this approach, cycle by cycle classification is carried out to detect the types of sags/swells which include single-phase, phase-to-phase and three-phase. Therefore, classification is conducted based on severely affected dip/swell-phase. To this end, unique signatures, which are composed of major axis, minor axis and inclination angle of ellipse, are extracted from three-phase voltage signals by using three-phase voltage ellipse transformation. The inclination angle is used to classify the types of sags/swells, whereas the minor and major axis are used to quantify the severity of sags/swells. Moreover, a comprehensive classification approach, based on the parameters extracted from 3D polarization ellipse, is devised to classify and characterize voltage dips and swells associated with different dip-types. It should be noted that in this detailed classification approach, a total of seven types of voltage dips (A, B, D, F, E, C and G) [22] which comprise 19 possible groups, and two types of voltage swells (H and I-type) [31] containing 6 possible groups, are considered. The developed method can classify and characterize all possible groups of dips and swells including the dips associated with phase angle jump. In this approach, the parameters extracted through polarization ellipse in 3D co-ordinates, are used to formulate different groups of voltage dips and swells. With the developed formulae, and by following a multi-stage classification algorithm, these seven types of dips, are classified. The main advantages of this method are to analyse voltage dips and/or swell with severely affected dip/swell-phase and its ability to provide complete dip/swell classification using a clear guideline of the decision boundaries developed through the multi-stage classification algorithm. Moreover, the detailed approach has shown its applicability to assess the voltage sags/swells due to faults/disturbances associated with pre- and post-islanding scenarios.

1.3 OUTLINE OF THE THESIS

The contents of the remaining chapters of the thesis are briefly described below:

Chapter 2 is a literature review providing an overview of the definition of islanding, its detection schemes and their issues as reported in literatures. Chapter 2 also provides an overview of a power quality issue, known as voltage dips and swells, their types which arise due to propagation of dips through different network element.

Chapter 3 presents the multi-feature-based SVM based method for islanding detection of DG. The proposed method is tested with the events generated by considering the

practical scenarios of an Australian electricity network. The performance of the method is assessed for critical islanding events associated with low power imbalance in the islanded segment. Feasibility of the proposed method is also presented on the basis of response-time/detection-time.

Chapter 4 describes the performance of vector surge (VS) and ROCOF (rate-of-change-of-frequency) relays for detection of islanding. Comprehensive investigation of NDZ of VS and ROCOF relays are conducted under different network contingencies and conditions. A comparative study of VS and ROCOF relays with the SVM based relay is conducted on the basis of classification performance as well as response-time/detection-time.

Chapter 5 investigates the voltage dips and its associated phase-angle jumps in power network due to four kinds of faults. The presence of synchronous type DG is also included in the voltage dip investigations. Seven types of voltage dips, namely, A, B, D, E, F, E, C and G, which are associated with the four types of faults, are analysed with and without DG.

Chapter 6 describes an algorithm, using three-phase voltage ellipse parameters, for real-time detection, classification and characterization of voltage sags and swells. Validation of the algorithm is conducted using real measurement data and IEEE 1159.2 recorded waveforms. The proposed algorithm has also been demonstrated as a real-time sag/swell monitoring tool.

Chapter 7 describes a comprehensive approach, using polarization ellipse parameters in 3D co-ordinates, to classify and characterize seven types of voltage dips and two types of voltage swells. A multi-stage classification algorithm using the formulae of decision boundaries, are presented. The proposed algorithm is tested and validated with real data, critical sags/swells data associated with phase angle jump and rotation of phase voltages due to loading effects.

Chapter 8 presents a special case study, which includes the investigation of voltage dips and swells associated with pre- and post-islanding scenarios of a distribution network embedded with DG under different network contingencies and conditions. To carry out this investigation, the 3D polarization ellipse technique, as proposed in

Chapter 7, is employed for the classification and characterization of voltage dips and swells.

Chapter 9 summarizes the major outcomes of the work presented in the thesis, and puts forward the recommendations and suggestions for future work arising from this thesis.

Chapter 2

LITERATURE REVIEW

2.1 INTRODUCTION

This chapter gives a brief review of two crucial abnormal events in electricity network. Firstly, islanding of distributed generation and its detection schemes are discussed; in alignment with this, the risk associated with operating an unintentional islanded system and an intensive review of the major techniques available for islanding detection is briefly presented. Secondly, a general introduction to voltage dips or sags, associated with power quality, are presented. The effects of voltage dips, from the customer's as well as supplier's point of view, are discussed. Different types of voltage dips and swells, originated due to propagation of dips through the network element, are presented in brief. The importance of voltage sags/swells classification and a review of the major techniques available for characterization of voltage sags/swells is briefly discussed. Lastly, based on the context of the literatures, a general discussion is summarized highlighting the importance of the work presented in this thesis.

2.2 ISLANDING DETECTION IN DISTRIBUTED GENERATION

A literature review, on islanding and its detection schemes are highlighted in this section. The review of islanding detection schemes, their advantages and limitations as reported in current literature, are discussed in brief.

2.2.1 What is Islanding?

Islanding, also recognized as loss of grid or loss of mains (LOM), takes place when a segment or part of the distribution network becomes isolated (electrically) from the upstream grid side or main supply, yet the isolated segment remains energized by one or more distributed generators (DG) [2]. Island can be developed at various locations with different voltage levels, involving one or more DG and distribution feeders. Typically, islanding takes place due to the opening of a recloser or circuit breaker in response to fault in downstream side. Ideally, the relay used in DG protection should have the

capability of detecting the fault as well as tripping the DG prior to inception of islanding. However, islanding situation can happen due to the failure of DG protection schemes or the manual switching of CB (circuit breaker) [35].

2.2.2 Risk of Islanding

Considering the rapid growth of DG penetration now-a-days, the probability of sustained islanding has increased significantly. As a result, this phenomenon has raised concern over the last few years. As shown in Fig. 2.1, unintentional islanding can occur due to CB tripping for faults or any other disturbances, and this may cause several safety and operational issues [36], for example, power quality may be degraded due to the active and reactive power mismatch between the load and generation inside the island. This mismatch gives rise to a deviation in the frequency and voltage, which can further lead to damaging customers' equipment as well as network equipment. Another issue is the re-closing of circuit breakers in out-of-phase state, which may damage the DG unit when grid-reconnection of island takes place. This damage occurs since the DG is most likely to be out of synchronism with the grid side at the time of reconnection, which may results in large transient currents causing the damage of DG. Finally, line workers are put in risk due to the lack of safety from unintentional islanding, since the island remains electrically active or energized by the DG while they assume it to be electrically inactive or disconnected. Besides, Islanding may keep a particular segment of the utility system unearthed, causing the islanded portion to be potentially unsafe and presenting severe safety and health hazards [37]. Therefore, IEEE Standard 1547-2003 requires the immediate detection of islanding.

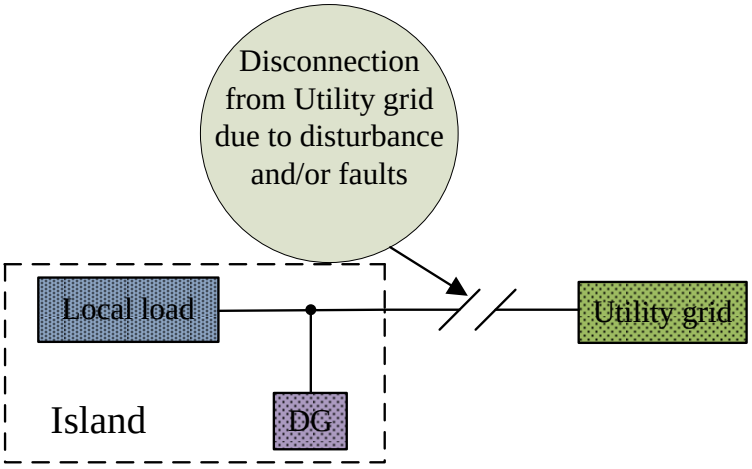

Fig. 2.1. Schematic diagram of a utility network illustrating the concept of DG islanding.

2.2.3 Review of Islanding Detection Schemes

Prior to adopting a loss of mains (LOM) protection schemes, it is important to investigate the characteristics of the DG unit. Generally, two types of DG, which include rotating machine based DG and inverter interfaced DG, are found. Rotating machine based DG can be either induction generator or synchronous generator, whereas inverter interfaced DG can be fed by rotating machine (e.g., induction generator) and non-rotating devices, such as, fuel cells, PV panels, etc. [38]. Among these, the most challenging task is the LOM protection for synchronous type distributed generator. This is due to the availability of limited options for controlling the large generators to facilitate islanding detection [38]. Moreover, synchronous generator deteriorates the situation as it is highly capable of forming and sustaining an island [38]. Considering the importance of LOM protection for synchronous DG, the remainder of this section will focus on the main anti-islanding techniques associated with synchronous DG.

As shown in Fig. 2.2, based on their working principle anti-islanding scheme can be generally classified into two categories, which are local detection methods and communication based methods. Local detection methods are further divided into active and passive methods. The operation procedure and performance of these techniques are described in the following section.

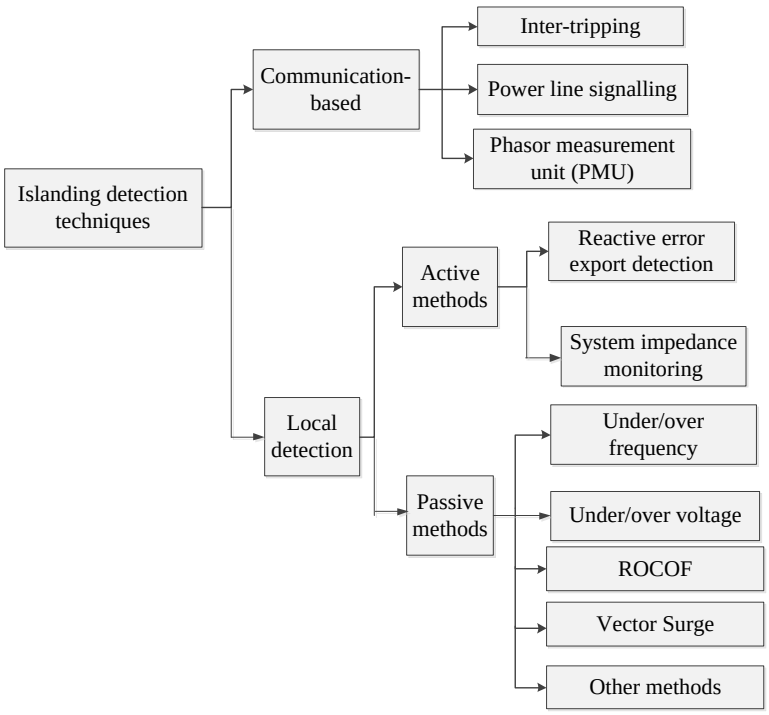

Fig. 2.2. Classification of islanding detection techniques

2.2.3.1 *Communication based Techniques*

Communication based techniques depend on telecommunication system to activate the alert and trip DG units when islanding is detected. Their performances are not dependent on the type of DG involved. They are free from the issues related to non-detection zone and are, therefore, considered as reliable for islanding detection. However, implementation of these techniques incurs a lot of investment, particularly in infrastructure level. Moreover, for small DG units, considering the economic aspects, it becomes less attractive compared to local detection schemes. From the recent development in the communication arena, it is predictable that more reasonably priced means of communication will be available in the near future. This is highly beneficial to the development of anti-islanding techniques. However, if the communication system fails to operate, so does the LOM protection. Therefore, reliability is another important concern that needs to be taken into account. Examples of some communication based techniques are presented below:

- *Inter-tripping Scheme*: This technique exploits communication links among the nodes in the system to guarantee that DG units are disconnected correctly in response to LOM detection [35]. An inter-tripping scheme, also identified as transfer trip [39], operates on the principle of monitoring the status of all the circuit breakers and reclosers that may result in islanding of DG [35, 38]. When utility network is disconnected due to a switching operation, a trip signal is sent to the respective DG units to avoid formation of island. These tripping signals are sent through several possible mediums, such as, leased telephone line, radio wave and hard wire.
- *Power Line Signalling Technique*: This scheme is almost similar to inter-tripping scheme as mentioned before except that it exploits the power line as a medium. Therefore, sometimes it is regarded as a part of the inter-tripping technique [39]. However, this scheme requires only one signal transmitter, unlike those techniques, which require signal transmitters for each and every possible disconnection points in the power network. The transmitter, which is a signal generator, is placed at the secondary side of the substation bus of the utility. It incessantly broadcasts a low-energy signal and the signal is received by the receiver at each DG through the power line. Failure in sensing the signal is considered as islanding condition, and it activates the immediate disconnection of the DG units [38]. This technique can be a very reliable method for anti-

islanding protection. However, the cost associated with the signal generator and its installation may be very high, which make this technique uneconomical, especially when this service is shared by a few DG units. Besides, the issue of interference of the signal with other types of power line communication applications, such as, automatic meter reading, should be taken into account [38].

- *Phasor Measurement Unit (PMU)*: This scheme includes two phasor measurement units (PMU); one unit is installed at utility substation and the other one at the DG site. PMU placed at the utility substation calculates the utility's voltage phase-angle with respect to GPS (Global Positioning System) time-stamp. This information is sent through a certain communication medium to the receiver at DG site. Moreover, the PMU at DG site measures and keeps the voltage phase-angle record at DG site. By using this information from the PMUs at DG site and utility substation, the LOM detection unit then calculates the difference of voltage phase-angle between the DG and utility substation. Then the calculated result is compared with the initial phase-angle difference. If the resulting value surpasses the prespecified threshold setting, a trip signal is activated. In order to avoid the phase error, which may occur due to change of network topology, the initial value of phase-angle difference is updated periodically during steady state [40, 41]. Since this technique compares the relative angular difference between the present state and the initial state, it is not influenced by the phase shift occurred due to transformers connected between two measuring points. In this scheme, 100 km geographical distance between the utility substation's PMU (reference PMU) and the DG's PMU may be found. Therefore, significant communications delay is expected when time-stamped phasor measurements are transmitted in real time. This delay is a function of the communication medium, which can be either shared or dedicated.

2.2.3.2 *Active Methods for Islanding Detection*

Active detection methods introduce disturbances into the system. Based on the system's responses as measured locally, islanding is detected [38]. In comparison to passive methods these methods are more reliable for detection of islanding. The main disadvantage of these methods is the deterioration of the power quality due to the direct interaction. It is also alleged that the reliability of these methods may be compromised

when penetration of multiple DG units are considered these days [42]. Moreover, too much injections of disturbances may drive the power system into instability [43]. Examples of some active techniques are presented below:

- *Reactive Error Export Detection (REED)*: This relay has an interface with the DG's AVR (automatic voltage regulator) to control the DG and generate a certain level of reactive power flow in the inter-tie between the utility grid and the local site. This condition is maintained when the grid is connected. The relay operation is activated when the deviation between the actual and desired reactive power being exported sustains longer than a prespecified time period [35, 44]. This relay is effective in detecting islanding; even when the generator's loading is not changed at all. However, the effective operation time of this relay is very slow, which varies from 2-5 seconds; therefore, this relay finds its suitability as back-up protection along with other "faster" anti-islanding systems. This relay does not work for islanding detection of inverter-based DG system, since inverter based DG normally operates at unity power factor.
- *System Impedance monitoring*: When DG is operated in parallel with the utility grid, the system impedance observed at the DG terminal is governed by the utility and hence, it is very small in comparison to the case when island is formed. This scheme employs this fact and calculates the changes in system impedance for islanding detection [45]. To calculate the system impedance, authors in [46] and [47] proposed a method which superimposes a small high frequency (HF) signal onto the system voltage. This relay operates with very high speed and it is free from nuisance tripping due to the network frequency transients. Moreover, it does not have non-detection zone which arises due to small power imbalance level in the formed island. However, concern arises if there are two or more DGs in the developed island. Besides, the effectiveness of this technique may be deteriorated due to the interference among the disturbances injected by multiple DGs. Cost is also a concern, as this scheme involves a signal generator at each DG end [35].

2.2.3.3 *Passive Methods for Islanding Detection*

Passive methods detect LOM by observing the changes in locally available network parameters [48]. It is based on the assumption that a LOM will result in a measurable deviation of the network parameters, i.e., voltage or frequency [49]. Therefore, the

abnormal operation of DG can be easily detected by monitoring the deviation or variation of one or more of these parameters [35]. The main advantages of these methods are, they do not interact with the system normal operation, and thus do not develop the power quality issues. Furthermore, communication is not needed to build up the whole detection system, thus making them cost-effective options. However, the drawback of these techniques is they suffer from the limitation of non-detection zone. Examples of some passive islanding detection schemes include:

- *Under/Over Frequency Relay*: Under steady state condition, DG maintains relatively constant frequency as it runs in parallel with the upstream utility grid. When islanding occurs, load and generation in the developed island are rarely exactly matched, which results in changes in frequency. Therefore, out of limits of frequency can be used as islanding detection parameter. The threshold setting is required to be out of the range of normal operational limits. In Australia, the recommended settings for under frequency and over frequency relays are 47 Hz and 52 Hz respectively [50]. However, since the frequency does not change instantaneously, this scheme may be rather slow in islanding detection. Furthermore, this method depends on a large power imbalance to drive the frequency out of the prespecified limits. Due to insufficient sensitivity, a large non-detection zone may exist which could increase the probability of island formation [35]. Due to these disadvantages, under/over frequency relays are normally used as backup protection for islanding detection.
- *Under/Over Voltage Relay*: Voltage is another important parameter commonly used for islanding detection [35]. Similar to under/over frequency relays, under/over voltage relays work on the assumption that there is always reactive power imbalance in the formed island. This imbalance leads to a relative change in the voltage level, e.g., excess of reactive power imbalance will drive up the voltage and vice versa. Hence, it can be considered as an indicator of islanding. The change of voltage is relatively faster than the frequency since, there is no mechanical inertia associated with it [35]. The threshold setting for under/over voltage relays should be outside the statutory voltage-limits. The standard settings used in the Australia are +10%/-6% of the nominal voltage [50]. Once the voltage surpasses these limits, the DG is required to be tripped off. However, this method may be affected by many other network disturbances, which can result in nuisance tripping. Moreover, it can be difficult to determine

islanding under the situation where load and generation are closely matched. As a result, island may sustain until the variation of load or generation takes the voltage out of limits.

- *Rate-of-change-of-frequency (ROCOF) Relay*: This is the most commonly employed method to detect the unintentional islanding. It is based on the assumption that there is always an imbalance between the load and generation in the formed island [35, 51]. Soon after islanding, the resulting power imbalance will give rise to a rapid change of frequency which, after neglecting the governor action, can be approximated by the following equation: [35, 52].

$$\frac{df}{dt} = -\left(\frac{P_L - P_G}{2H \times S_{GN}}\right) \times f_r \tag{2.1}$$

whereP_G = Output of DG

P_L = Load in island

S_{GN} = DG rating

H = Inertia constant of generating plant

f_r= Rated frequency

It is worth noting that this approach only considers the frequency change because of islanding, and it does not take into account the effect of fault [35]. The relay is triggered if the corresponding frequency slope (*df/dt*) exceeds the prespecified threshold setting, and vice versa. For ROCOF relays, the typical threshold values used in a 50Hz power system ranges from 0.1 Hz/s to 1 Hz/s [52]. This setting relies on the strength of the network or system, the weaker the system, the higher the setting [35]. ROCOF is usually being considered as a sensitive and reliable method for detecting LOM on a distribution network. However, this relay will fail to detect islanding when the power imbalance in the formed island is small. In addition, ROCOF relays have been reported for several mal-operation, for instance, it fails to discriminate between actual islanding events and other network transients [38, 53], resulting in false operation and nuisance tripping; therefore, the system's integrity is directly jeopardized. Besides, authors in [54] reported that commercially available ROCOF relays, produced by different manufacturers, may respond differently to the same event, even when their settings are same. This phenomenon is most likely due to the different techniques employed by those relays. In general,

ROCOF is considered as a feasible option for islanding detection. However, this relay suffers from the limitation of non-detection zone and cannot provide useful protection when the load-generation imbalance in the formed island is small. Besides, it may cause excessive nuisance tripping due to network transients, i.e. load switching, frequency excursion due to loss of bulk generation and network faults.

- *Vector Surge (VS) Relay*: Vector surge (VS) relays measure the time-duration of an electrical cycle and start a new measurement at each rising zero-crossings of the terminal voltage. The current cycle duration (measured waveform) is compared with the last one (reference cycle). In an islanding situation, the cycle duration is either longer or shorter, depending on if there is deficit or excess of power imbalance in the islanded system, see Fig. 2.3. This variation of the cycle duration results in a proportional variation of the terminal voltage angle $\Delta\delta$, which is the input parameter of VS relays. If the variation of the terminal voltage angle exceeds a prespecified threshold, a trip signal is sent to the CB immediately. Normally, vector surge relays allow this threshold to be adjusted in the range from 2 to 20°. Another important characteristic available in these relays is a block function by minimum terminal voltage. If the terminal voltage drops below an adjustable level threshold V_{min}, the trip signal from the VS relay is blocked. This is to avoid, for instance, the actuation of the VS relay during short circuits or generator start-up conditions.

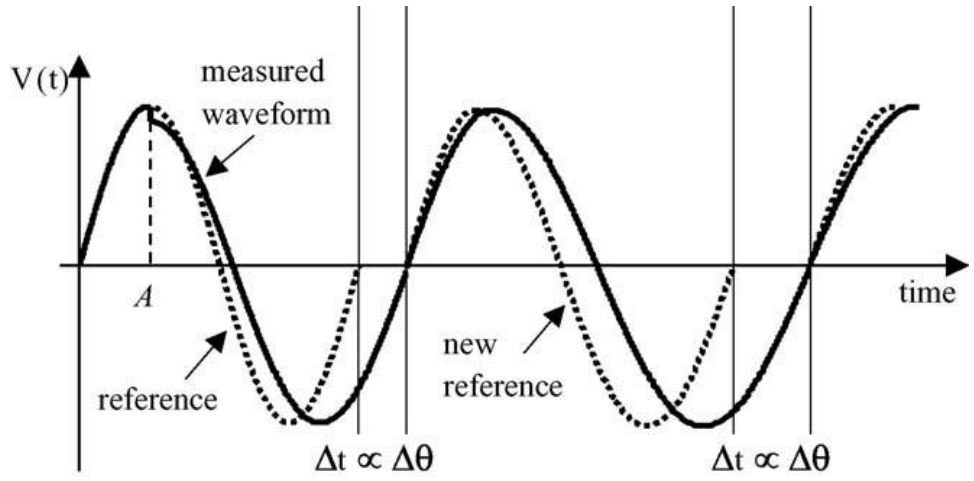

Fig. 2.3. Illustration of the operating principle of vector surge relay [55].

Due to the similarity of this VS relay with other frequency based relays, which are also based on the principle of measuring the cycle duration of the voltage waveform, it can also be categorized as a type of frequency based relay [38, 56]. And hence, it suffers from non-detection zone when the generation-load imbalance in the formed island is very small. Moreover, this relay is susceptible to network fault occurring on adjacent feeder. Other network transients, such as load switching events may also falsely trigger the relay [35]. The mal-operation of this relay has been reported in [54] and [57]. Increasing the threshold setting may help in reducing the false operation, but this will in turn compromise the sensitivity of this relay, making it vulnerable to non-detection zone. Compromise should thus be made between the reliability and sensitivity of the relay.

- *Other Passive techniques:* Passive method using a fuzzy rule-based classifier, Decision Tree (DT) classifier and bi-orthogonal 1.5 wavelet based technique have been discussed in [16-18, 58]. Wavelet based technique in an inverter interfaced DG system [59], and islanding detection technique using voltage unbalance and Total Harmonic Distortion (THD) of current, have been proposed in [60]. In [61], an extension theory based method and in [62], ROCOV (rate-of-change-of-voltage) and ROCOF (rate-of-change-of-frequency) indices-based method have been presented. A new hybrid method is described in [63] and [64]. Detailed co-efficient of wavelet transformed negative sequence voltage and current are used in [65]. Other passive methods, as reported in [66-68], exploited the parameters, such as, ROCPAD (rate of change of phase angle difference), proportional power spectral density of voltage, switching frequency for inverter based DG. In [69], the technique using S-transform based cumulative sum detector (CUSUM) and in [14], data-mining approach is applied and tested for islanding detection. In [70], islanding detection of inverter-based DG was evaluated using seven features and four classifiers: Decision Trees, Radial Basis Functions, SVMs and Probabilistic Neural Networks**.** In [71], the authors carried out a task of islanding detection in the presence of three types of DG units: inverter-interfaced DG, synchronous-type DG, and multiple DG units (synchronous type and/or inverter interfaced DG). In their approach, twenty-one features are first extracted, from which four features are selected as input to a

Random Forest (RF) classifier.

As discussed above, most of the passive islanding detection methods, such as, ROCOF, VS, over/under voltage and over/under frequency relays, etc., suffer from the limitation of non-detection zone (NDZ). NDZ is a function of power imbalance inside the formed island. There are two aspects of power imbalance in an island. One is the active power imbalance and the other is the reactive power imbalance [72]. Any particular power imbalance situation in an island can therefore be presented as a point in the ΔP and ΔQ plane as shown in Fig. 2.4, where Δ denotes power imbalance (a positive value denotes excess or surplus power). There is also a detection time associated with the operating point, which can be illustrated using a third axis shown in Fig. 2.4(a). If one specifies a required detection time, there will be cases whose ΔP and ΔQ values are not sufficient to result in a timely detection of the islanding situation by anti-islanding relays. These cases or points in the ΔQ versus ΔP plane define a non-detection zone. Fig. 2.4(b) is an illustrative plot of such a non-detection zone.

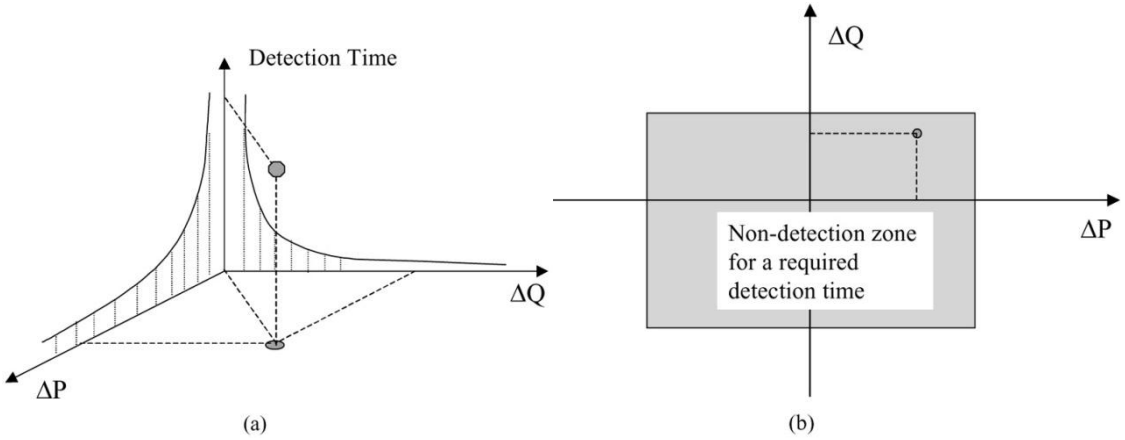

Fig. 2.4.Power imbalance situation in the power mismatch plane and the associated non-detection zone. (a) Detection time for a given power imbalance case, (b) Non-detection zone in the ΔQ versus ΔP plane [72].

2.3 VOLTAGE DIPS AND ITS CHARACTERIZATION

A brief literature review on power quality with special emphasis on voltage dips and swells, their effects, propagation of dips or sags, importance of classification of voltage sags and the available techniques used for characterization of voltage sags and swells are highlighted in this section.

2.3.1 Power Quality and its Significance

The definition of power quality (PQ) is adopted from the book of K. Bhattacharya[73] as mentioned below:

Power Quality is the combination of current quality and voltage quality, involving the interaction between the system and the load. Voltage quality concerns the deviation of the voltage waveform from the ideal sinusoidal voltage of constant magnitude and constant frequency. Current quality is a complementary term and it concerns the deviation of the current waveform from the ideal sinusoidal current of constant magnitude and constant frequency. Voltage quality involves the performance of the power system towards the load, while current quality involves the behaviour of the load towards the power system [73].

In general, the quality of the electrical power involves all stakeholders in the energy field, whether they are system operators, suppliers, producers, or consumers of electricity. It has become a topic of great interest in recent years, mainly for the following reasons:

1) Electrical disturbances have a high cost for industrial sector because they cause downtime, loss of raw materials, a drop in production quality, premature aging of equipment, etc.
2) Now-a-day, power electronics equipment is being widely used because of their flexibility of operation, high efficiency, and high performance. These devices are very sensitive to voltage disturbances and perturbing.
3) Due to the liberalization of the electricity market, power quality has become one of the criteria for choosing an energy supplier over another from the consumers' point of view. The suppliers must provide the energy to the customers with maximum quality.

2.3.2 Voltage Dips or Sags

According to Dugan [74], power quality can be characterized with four categories of electrical disturbances:

- Changes in the voltage amplitude (voltage dips, short interruptions and flicker)
- Fluctuations in frequency around the fundamental frequency,
- Changes in the voltage waveform (harmonics, interharmonics, noise),
- The asymmetry of the three-phase system imbalance.

Thus, voltage dip is one of power quality issues and it is considered as the most important power quality disturbances for industrial customers [75]. According to the existing PQ standards [27, 76-82], voltage sag is defined as a short-duration reduction of voltage magnitude in any or all of the phase-voltages of a single-phase or a polyphase power supply at a point in the electrical system. By definition (according to IEEE Std. 1159), a voltage dip is a voltage drop of 10% to 90% of the nominal value for a period of up to 0.5 cycle to 1 min. The draft Technical Report for Electromagnetic Compatibility regarding voltage dips and short interruption on public electric power systems states that voltage sag is an alternative name for the phenomenon voltage dip [83]. Therefore, both terms dip and sag are used as synonym of each other.

A voltage dip is a multidimensional electromagnetic disturbance, the level of which is mainly determined by the magnitude and duration. Magnitude of a voltage dip is the value of residual voltage during the event. Duration of dip is time for which the root-mean-square (rms) voltage stays below a voltage dip threshold, see Fig. 2.5. As illustrated in Fig. 2.5, voltage dip threshold is set to 0.9 pu. However, different thresholds can be used for different purposes, for example, voltage dip threshold values for monitoring purposes are usually in the range of 85%–95% of the nominal voltage [84], but for contractual purposes, that value can be as low as 70% of the nominal voltage [85].

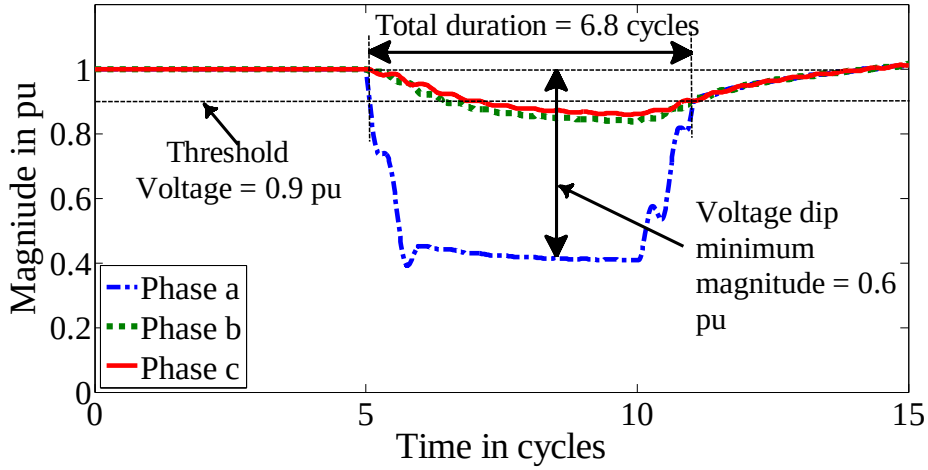

Fig. 2.5.Measurement of voltage dip.

2.3.3 Effects of Voltage Dips

Modern manufacturing methods often involve complex continuous processes utilising many devices acting together. A failure of one single device, in response to a voltage

dip, can stop the entire process. This may be one of the most serious and expensive consequences of voltage dip. Moreover, the effects of voltage dips considering different types of equipment and economic aspect are summarized below:

1) IT and process control equipment uses power electronic converter to convert the AC voltage to regulated DC voltage. If the supply AC voltage drops below a specific limit, due to voltage dip, regulated dc voltage will start to drop and ultimately errors will occur in the digital electronics equipment.
2) Alternating current contactors (and relays) can drop out when the voltage is reduced below about 80% of the nominal for duration of more than one cycle.
3) Harmonic pollution causes extra stress on the networks and makes installations run less efficiently.
4) Electrical equipment (transformers, motors, etc.) may be overheated leading to their lifetime reduction.
5) The existing installations may need to oversize to cope with additional electrical stress which in turn increases the installation and running costs and their associated higher carbon footprint.
6) New sites are refused because the new site would pollute the supply network to a great extent.
7) Power drives can be very sensitive to voltage dips. Such systems generally contain a power converter/inverter, motor, control element and a number of auxiliary components. The effect on the control element can be critical, since it has the function of managing the response of the other elements to the voltage dip. The reduction in the voltage results in a reduction in the power that can be transferred to the motor and hence to the driven equipment. Dips can lead to a loss of control [86]. Moreover, behaviour of certain equipment is influenced by the phase shift and/or point on wave (e.g., [87]) of voltage dips/sags.

Due to the advancement and proliferation of information technology and the widespread use of power electronic devices in recent years, utilities' customers in various industrial fields are suffering economic losses from short interruptions and voltage dips. Losses caused by a voltage dip may only be an annoyance for residential customers (as a shutdown of a personal computer) but in the industrial and commercial sectors the same event may cost millions of dollars [88]. Sometimes, the economic

impact of sags/dips and interruptions is so strong that the total losses caused are expressed in even billions of dollars per year [89, 90].

2.3.4 Cause of Voltage Dips

Voltage dips or sags are predominantly attributable to short circuit affecting the power grid or connected installations, and the start of high power motors. However, the short circuit remains the leading cause of voltage dips and short interruptions. Short circuits may assign one, two or three phases, and can cause additional phase shifts between them. The high power motors (asynchronous typically) can also be the cause of voltage dips. In general, the motor current reaches the start time of 5 to 6 times the rated current and gradually decreases as the machine approaches its rated speed. This overcurrent generates a voltage drop which decreases with the decrease of the current. Voltage dips caused by the starting of high power motors last between few seconds to a few tens of seconds and are characterized by voltage drops on three phases. Moreover, the interconnection of the renewable-resources based distributed generation (DG) system to the existing power system could lead to power quality (PQ) problems, such as voltage sags [91, 92]. Finally, voltage dips can also be caused by transformer saturation or changes in the network structure.

2.3.5 Propagation of Voltage Dips

Voltage dips can be originated at different buses or lines in electricity network due to different reasons as stated in section 2.3.4. Moreover, penetration of distributed generation (DG) could have an impact on voltage-sag propagation and characteristics in distribution networks [93]. However, when voltage dips propagate through different electrical equipment, its magnitude and type are changed at different points as presented below.

2.3.5.1 *Dip propagation through network elements*

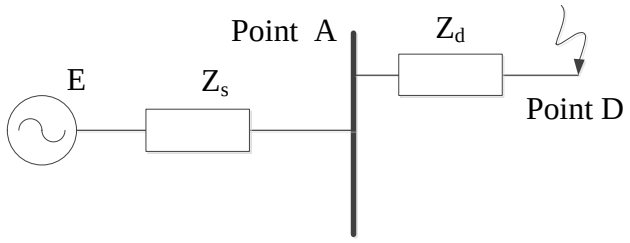

Fig. 2.6. Voltage divider to study the propagation of voltage dips.

Sags propagate through different network elements of the network, and their severity depends on the location of voltage-dip-measurement. The propagation of voltage dips depends on two parameters: the power of short circuit and the distance from the fault location and the measurement location. To better illustrate the propagation of voltage dips, the example of a phase affected by a short circuit at point D is shown in Fig. 2.6.

Due to a short circuit, the voltage at the fault location D is zero. By applying voltage divider rule, the voltage at the measurement point A is

$$V_A = \frac{Z_d}{Z_d + Z_s} E \tag{2.2}$$

If the electric distance between the fault location and the measurement point A is large, the impedance of line Z_d is increased by a significant amount. Accordingly, the amplitude of the voltage V_A gets close to that of the source E, i.e., the voltage dips measured at point A is mitigated. From Fig. 2.6 and Equation (2.2) it is obvious that voltage dips are reduced when they are propagating upstream in the network. However, voltage dips propagate downstream without significant change in dip-magnitude. Indeed, if we take the example of Fig. 2.6, assuming that the short circuit is occurred before the measurement point A, the voltage at the measuring point is zero; therefore, the potential downstream point D is also zero.

2.3.5.2 *Dip propagation through transformers*

The type of voltage dips can be changed by the transformers located within the network. For example, the voltage dip at left of Fig. 2.7 is characterized by a drop of voltage on one phase only. As it passes through the transformer Dy11, it turns into a drop of voltage on two phases, namely a and b.

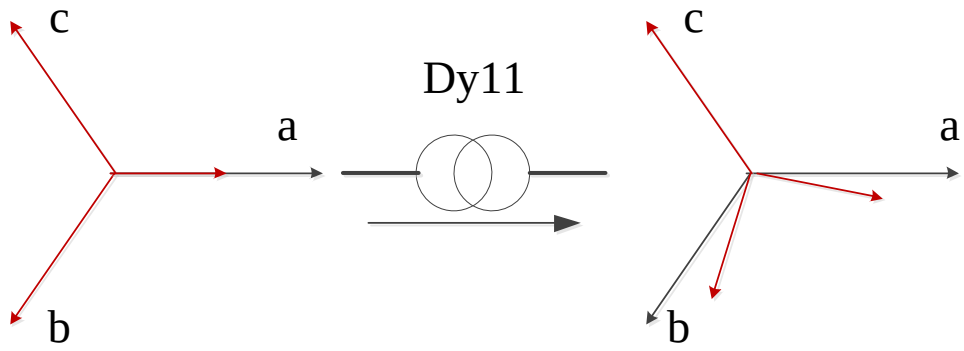

Fig. 2.7. Change of type of voltage dips through a transformer Dy11.

Indeed, a voltage dip can be characterized by different signatures on the primary side and secondary side of a transformer based on its type and connection. Depending on the changes introduced in the signatures of voltage dips, there are three families of transformers [94].

❖ *Transformer through which the signature of the voltage dip is not changed*

Voltage on the secondary side could be equal to the voltage of the primary side; transformer of $Y_N y_n$ kind belongs to the group. The ratio of the voltages on the primary side (v_{ABC}) to the secondary side (v_{abc}) can be represented as follows:

$$v_{abc} = kTv_{ABC} \tag{2.3}$$

where k is the ratio and T is the transformation matrix. The transformation matrix for this type of transformer is the identity matrix, i.e.

$$T_1 = \begin{bmatrix} 1 & 0 & 0 \\ 0 & 1 & 0 \\ 0 & 0 & 1 \end{bmatrix} \tag{2.4}$$

❖ *Transformer through which the sequence component is removed*

Voltages on the secondary side are obtained by removing the zero-sequence voltages of primary side. The transformers residing in this family are Dd, Dz, $Y_N Y$, YY_N. Their transformation matrix is defined by:

$$T_2 = \frac{1}{3}\begin{bmatrix} 2 & -1 & -1 \\ -1 & 2 & -1 \\ -1 & -1 & 2 \end{bmatrix} \tag{2.5}$$

❖ *Transformer through which the phase voltages are changed*

The voltages on the secondary side are proportional to the difference of two voltages on primary side. The transformers residing in this family are Dy, Yz, Yd. Their transformation matrix is defined by:

$$T_3 = \frac{j}{\sqrt{3}}\begin{bmatrix} 0 & 1 & -1 \\ -1 & 0 & 1 \\ 1 & -1 & 0 \end{bmatrix} \tag{2.6}$$

Similarly, connecting the loads determines the type of voltage sags that they suffer. Loads connected in delta or star with floating neutral change the type of voltage dips.

2.3.6 Parameters determining the types of voltage dips and swells

Sags and swells signatures usually depend on several parameters: fault location, fault type, system grounding and connection point of monitors[31]. The influence of these parameters on the voltage sags and swells signatures is explained below.

1) Fault Type: Four major types of faults are found in electricity networks, which include single line-to-ground, double line-to-ground, phase-to-phase and balanced three-phase. Among these faults, single line-to-ground faults are the most common. They are characterized by a drop in one of the phases; the other two phases remain unchanged or increase as a function of system grounding. Double line-to-ground faults initiate major drops in two phases with or without phase-angle shift as a function of system grounding. The voltage in the non-faulted phase remains unchanged or increases. Double phase-to-phase faults are characterized with drops and phase angle shifts of two of the phases. The non-faulted phase remains unchanged. Balanced three-phase faults are the most severe fault type. They are characterized by equal drops on the three phase voltages without phase angle shift.

2) System Grounding: The system grounding influences the magnitudes of the non-faulted phases [95]. In high-impedance grounded or ungrounded systems, non-faulted phases at the fault location experience voltage rise. In grounded system or low impedance grounded systems, the non-faulted phase is not affected.

3) Fault Location: Transformers usually remove the zero-sequence voltage [94]and in this way they change the signature of the PQ disturbance. Therefore, voltage dips propagate down to the network changing their phasors' relation as a function of the transformer type. Swells caused by faults do not propagate; they are measured only at the same voltage level, where the fault occurs.

4) Connection of Monitors: Monitors can be connected either between phase and neutral (star connection) or between phases (delta connection) [96, 97]. Phase-to-phase connection of monitors is usually used in systems with delta connecting loads since they measure PQ disturbances as experienced by the loads. However, concerning systems with either star or delta connecting loads, phase-to-neutral measurements are recommended. Star connection of monitors provides more information about the system, for example the fault number and location. Another reason to choose star connection is that phase to phase voltages can be deduced from phase to neutral voltages, while the contrary is not possible.

2.3.7 Different types of voltage dips and swells

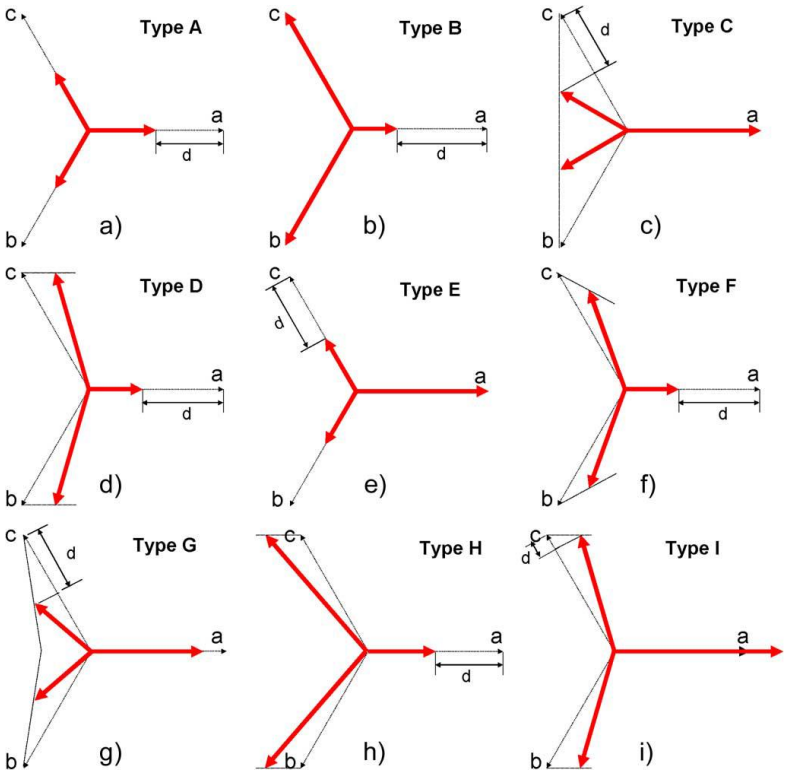

Fig. 2.8. Voltage dips and swells signatures [31].

According to the classification of voltage dips universally recognized [22], there are 7 main types of voltage dips denoted by the letters A to G shown in Fig. 2.8, where *d* is the amplitude of the largest drop in phase-voltage, also called the depth of the voltage dip. For voltage dips of type C, G and I, dip-depth *d* does not correspond exactly to the depth of the voltage dip due to additional phase shifts of voltages. However, for insignificant amount of voltage drops, *d* can be considered identical to the depth of voltage dip.

Sags A, B, C and E are measured voltage level where the fault occurs. They propagate downstream network by modifying their signature depending on the type of transformers, giving rise to other types of voltage dips that can be categorized as C, D, F and G. Fig. 2.9 and Table 2-I show the transformation of voltage dips A, B, C and E, as they propagate downstream network, via the Dy (delta-wye) transformers. Sag type A, due to 3-phase faults, has the voltage drops of same depth on all three phases without additional phase shifts. This type of voltage dip propagates downstream network without changing its signature. Sag Type B owes its origin to single-phase faults. They are characterized by a voltage drop on one of the phases; the phases are not affected by

the phase-shift. This type of voltage dip propagates downstream network by changing its signature. For example, passing through a transformer-type Dy it becomes two-phase voltage-type C. Sag Type C is produced either by phase-to-phase faults or by the propagation of voltage dips of type B or D via transformers. They are characterized by voltage drops with additional phase shifts of two phases; the third phase is not changed. Propagating downstream in the network, these dips are transformed into type D. Sags type D owes their origin to the spread of voltage sag type C via transformers. They are characterized by a drop on a main phase and a relatively low additional voltage drops and phase shifts for the other two phases. While propagating downstream network, these dips are transformed into type C. Sag type E originates from the faults between two phases and earth, and has voltage drops without phase-shift. They spread downstream network by generating voltage dips type F. Sag type F originates from the spread of dip-type E via transformers. They are characterized by a voltage drop on one of the phases and phase difference between the other two phases is changed with small amount of voltage-drop. Their propagation through a transformer gives rise to dip-type G. Sag type G has voltage drops with additional phase shifts on two phases and a low voltage drop for the third phase. This type of dip comes from the double transformation of a voltage sag type E.

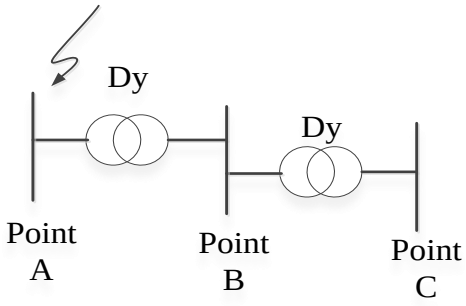

Fig. 2.9. Transformation of the types of voltage dips

TABLE 2-I
PROPAGATION OF VOLTAGE DIPS

Voltage level	Point A	Point B	Point C
Types of voltage dips	A	A	A
	B	C	D
	C	D	C
	E	F	G
	-	H/I	-

Sags with swells due to faults in ungrounded systems are not represented in the classification of [22] because they do not spread, and they are not experienced by delta connected loads. However, these dips are considered in our study because they can identify and locate some faults. Sags with swells are denoted by the letters H and I, and their signatures are also shown in Fig. 2.8 where their depth is given by *d*. Sag type H exhibits voltage drop on one phase and overvoltage on the other two phases. Sag type I is characterized by voltage drops on two phases and a voltage of the third phase. Type H is caused by single line-to-ground fault and type I is caused by double line-to-ground fault.

Sags type B, D and F are often called single phase dip because they are characterized by a voltage drop on one of the phases. Sags Type C, E and G are characterized by voltage drop on the two phases and they are called double-phase dips. The voltage sag type A is called three-phase dip. Sags type H and I are characterized by both voltage drops and swells; they are also called voltage dips with swells.

2.3.8 Importance of voltage dips/swells classification and the existing methodologies to classify voltage dips/swells

Several methods have been reported to classify Power Quality (PQ) events on power systems, but insufficient effort has been given on classifying voltage sags based on measurements. Only limited number of algorithms, as found in the literature, are well known to characterize voltage sags using direct measurements data, without considering the internal circuit behind the phenomenon [22]. The importance in voltage sag characterization was first addressed to obtain statistics and then applied in equipment testing and stochastic prediction [30]. Lately, advances in PQ monitoring and the development of expert systems [98] have required new algorithms and mathematical approaches to identity and classify disturbances in power systems to enhance mitigation techniques and to improve new control schemes.

Significant efforts have been directed toward the complete characterization of voltage sags. Most of the existing standards and methods characterize voltage dips or voltage sags [99], through minimum magnitude and total duration [21, 26-28, 76, 77, 81, 82, 100]. This voltage sag characterization approach, only suitable for single-phase or balanced 3-phase voltage sags, which gives conservative characterization [28]. The other notable consequences of this approach are discussed in [29, 30], and [28]. Moreover, several methods have been proposed to characterize the types of voltage sags

from recorded waveforms. In [101], the potential gradient of positive- and negative-sequence components of voltages is used for characterization; however it possesses a limitation of identifying the single-phase voltage sag only. The SP (six-phase) algorithm [30], [102] is a computationally simple algorithm, but gives erroneous characterization with large negative phase-angle jump and for reasonable drops in voltage [30]. Recently, Bollen and Zhang proposed a symmetrical component based technique to classify and characterize voltage dips [23, 29]. In [30], it was reported that the symmetrical component technique has some limitations in characterizing unbalanced voltage sags originating from large dynamic loads. In [31], a space vector method was presented wherein the ellipse inclination angle was used to classify single-phase and double-phase voltage dips. However, this method is not suitable for classification of voltage dips for the case of large phase angle jump.

2.4 LITERATURE DISCUSSION AND SUMMARY

In the previous two sections, i.e., Sections 2.2 and 2.3, a literature review has been presented regarding two crucial abnormal events: islanding of distributed generation and voltage sags/swells. The conclusions on the literature survey can be summarized as follows:

Islanding of Distributed Generation and its Detection Schemes:

- Due to disturbance or fault, a segment of distribution network energized with DG may be disconnected from the upstream grid side or main supply, which gives rise to the situation of islanding.
- The risk associated with unintentional islanding operation is severe, therefore, several islanding detection techniques have been proposed in current literatures.
- A review of the common islanding detection techniques, which include, active, passive and remote islanding detection methods, is conducted in Section 2.2.3.
- Each of the islanding detection techniques has their distinctive benefits and drawbacks. For example, remote methods are effective but expensive; active methods are reliable but they suffer from PQ disturbance; and passive methods are cost-effective but they suffer from the limitation of non-detection zone (NDZ).
- In recent literatures, with the introduction of intelligent based approaches in islanding detection methods, the performance of passive islanding detection

method has been critically evaluated and compared with the performance of the new intelligent based approaches. However, the performance of passive islanding detection methods has not been critically evaluated inside the NDZ of conventional relays, such as, vector surge, ROCOF relays. Therefore, there is a need for the development of new intelligent basedrelays for detection of islanding which can perform effectively inside as well as outside the NDZ of conventional relays.

Voltage Sags/Swells and its Classification and Characterization Methodologies:

- Voltage dips are one of the most important power quality disturbances for industrial, commercial as well as household appliances.
- Voltage dips are caused by faults and other large increases in currents, which could be triggered by transformer energization, motor starting, disconnection of distributed generation (DG), etc., both inside the industrial plants and outside of them.
- Propagation of voltage dips through different network elements result in seven types of voltage dips. Besides, two types of voltage swells are also found in power systems.
- Classification and characterization of voltage dips and swells are important to enhance mitigation techniques and improve new control schemes.
- Significant efforts have been given to conduct complete characterization of voltage sags, which is evident from the study of current literatures. The literature surveyreveals that there is a need for new algorithm for classifying and characterizing voltage sags and swells, which would be unaffected by phase-angle jump and suitable for real-time applications.

Chapter 3

ISLANDING DETECTION OF DISTRIBUTED GENERATION USING MULTIPLE-FEATURE-BASED SUPPORT VECTOR MACHINES

3.1 INTRODUCTION

In this Chapter, a multiple-feature-based support vector machine (SVM) approach is proposed for islanding detection of DG. The proposed method uses multiple-features extracted from different network variables, such as, voltage, frequency and rotor angle, which show distinguishable variation during the formation of islanding. The extracted features are then used as inputs to a support vector machine (SVM) to classify the event as islanding or non-islanding. The method has the potential to overcome the limitations of conventional protection schemes. To demonstrate the performance of SVM based approach, a set of features is generated from numerous set of off-line dynamic events simulated under different network contingencies, operating conditions and power imbalance levels. Features associated with different islanding and non-islanding events are used to train the SVM. The trained SVM is tested on a practical distribution network of Australia containing multiple DG units.Variation of detection time as a function of power imbalance scenarios is also assessed in the testing phase. Furthermore, the performance of the proposed approach is evaluated in terms of reliability and speed of islanding detection.

The remainder of the Chapter is organized as follows. Section 3.2 presents a brief overview of the theory of SVM, which is relevant to the classification of two classes. Section 3.3 describes the multiple-feature-based SVM method. The experimental evaluation of the proposed method is highlighted in Section 3.4. Considering the reliability and response-time or detection-time as performance indicators, assessment of the SVM based method is conducted in Section 3.5. Discussions followed by Conclusion are presented in Sections 3.6 and 3.7.

3.2 BRIEF OVERVIEW OF THE THEORY OF SVM

For a two-class classification problem, a real valued *d*-dimensional input or feature vector $(\boldsymbol{x}_n \in \Re^d)$can be labeled as $y_n = \{-1,+1\}$, which indicates the class of $\boldsymbol{x_n}$. The SVM separates the two classes by establishing a decision boundary hyperplane defined by its normal vector $\boldsymbol{w}$ and a scalar bias *b*,

$$g(\boldsymbol{x}) = \boldsymbol{w}^T \boldsymbol{x} + b \tag{3.1}$$

The function $\mathrm{sgn}(\boldsymbol{w}^{\mathrm{T}} \boldsymbol{x} + b)$ can be used as a decision function to obtain an output y_n = -1 or +1, indicating the class of the input feature vector $\boldsymbol{x_n}$. If the two classes are linearly separable, i.e., no input sample $\boldsymbol{x_n}$ satisfies $\boldsymbol{w}^T \boldsymbol{x_n} + b = 0$, then

$$\boldsymbol{w}^T \boldsymbol{x_n} + b \begin{cases} > 0, & \text{for } y_n = +1 \\ < 0, & \text{for } y_n = -1 \end{cases} \tag{3.2}$$

To control separability, instead of (3.2), the following inequalities are considered:

$$\boldsymbol{w}^T \boldsymbol{x}_n + b \begin{cases} \geq 1 & \text{for } y_n = +1 \\ \leq -1 & \text{for } y_n = -1 \end{cases} \tag{3.3}$$

Here, 1 and –1 on the right-hand sides of the inequalities can be a constant *a* (> 0) and $-a$, respectively. But by dividing both sides of the inequalities by *a*, (3.3) is obtained [103]. The expression in (3.3) is equivalent to

$$y_n \left(\boldsymbol{w}^T \boldsymbol{x}_n + b \right) \geq 1 \quad \text{for } n = 1, 2, ..., N \tag{3.4}$$

The Euclidean distance between the hyperplane and the training data nearest to the hyperplane is called *margin*. The objective of SVM is to find the optimal separating hyperplane which maximizes the margin and thus, to maximize the generalization ability of the classifier. This optimal separating hyperplane is obtained by considering the maximum Euclidean distance to the closest training samples known as Support Vectors (SVs).

The Euclidean distance from a training data $\boldsymbol{x}$ to the separating hyperplane is given by $|g(\boldsymbol{x})| / \|\boldsymbol{w}\|$. Therefore, all the training data must satisfy

$$\frac{y_n g(\boldsymbol{x}_n)}{\|\boldsymbol{w}\|} \geq \eta \qquad \text{for } n = 1, 2, ..., N \tag{3.5}$$

whereη is the margin. If ($\boldsymbol{w}$, *b*) is a solution, ($a\boldsymbol{w}$, *ab*) is also a solution, where *a* is a positive scalar. Thus, the following constraint can be imposed [103]

$$\eta\|\boldsymbol{w}\| = 1 \tag{3.6}$$

From (3.5) and (3.6), it is evident that the optimal separating hyperplane can be achieved by obtaining $\boldsymbol{w}$ with the minimum Euclidean norm that satisfies (3.4). Therefore, the optimal separating hyperplane can be achieved from the following convex optimization problem

$$\underset{w}{\text{minimize}} \quad \frac{1}{2}\|\boldsymbol{w}\|^2 \tag{3.7}$$

$$\text{subject to } y_n\left(\boldsymbol{w}^T \boldsymbol{x}_n + b\right) \geq 1 \qquad \text{for } n = 1, 2, ..., N \tag{3.8}$$

In (3.7), the square of the Euclidean norm $\|\boldsymbol{w}\|$ is used to make the optimization problem quadratic programming (QP) [103].

Soft-margin support vector machine is applied to deal with linearly non-separable training sets. To this end, the amount of training errors is measured by introducing a slack variable $\boldsymbol{\xi}$. For example, the decision boundary hyperplane for linearly separable and non-separable training sets of two classes of data are shown in Figs. 3.1(a) and 3.1(b), respectively. As shown in Fig. 3.1 (b), the decision boundary hyperplane with non-separable training sets necessitates the introduction of slack variable ξ_n to measure the amount of training error for one misclassified training sample. Therefore, to deal with linearly non-separable training sets, QP expressions of (3.7) and (3.8) are reformulated as follows:

$$\underset{w,\xi}{\text{minimize}} \quad \frac{1}{2}\|\boldsymbol{w}\|^2 + C\sum_{n=1}^{N}\xi_n \tag{3.9}$$

$$\begin{aligned} \text{subject to} \quad & y_n\left(\boldsymbol{w}^T \boldsymbol{x}_n + b\right) \geq 1 - \xi_{\boldsymbol{n}} \quad \text{for } n = 1, 2, ...N \\ & \xi_n \geq 0 \qquad\qquad\qquad\qquad \text{for } n = 1, 2, ...N \end{aligned} \tag{3.10}$$

where ξ_n is a slack variable and the parameter C in (3.9) is a regularization parameter, which determines the trade-off between the maximization of the margin and the minimization of classification errors.

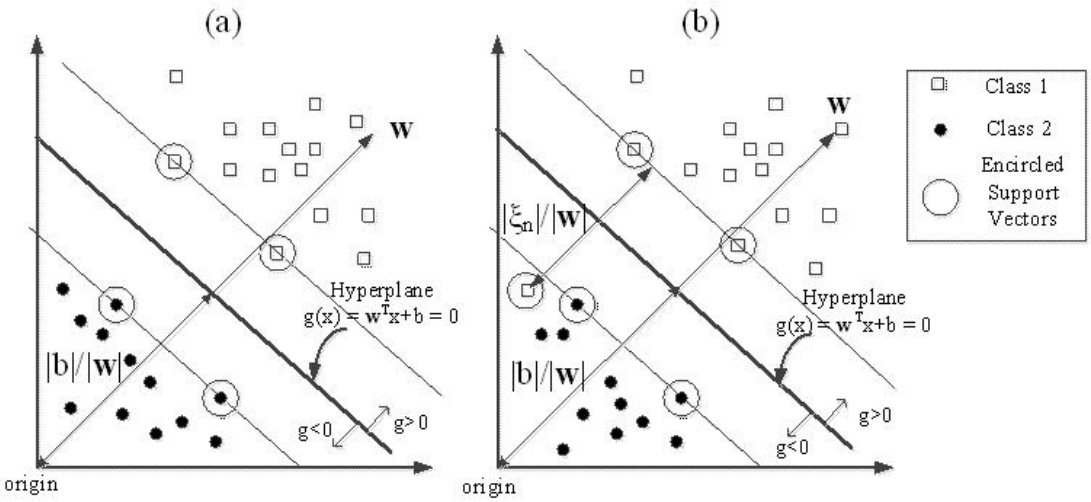

Fig. 3.1. Linear separating hyperplane for data belongs to: (a) separable training sets, and (b) non-separable training sets.

To solve the constrained QP problem presented in (3.9) and (3.10), Lagrange multipliers $\beta_n \geq 0$ and $\gamma_n \geq 0$ are introduced. Hence, the Lagrange functional given as [103]:

$$\boldsymbol{Q}(\boldsymbol{w},b,\xi,\boldsymbol{\beta},\boldsymbol{\gamma}) = \frac{1}{2}\|\boldsymbol{w}\|^2 + C\sum_{\boldsymbol{n}=1}^{N}\xi_{\boldsymbol{n}} - \sum_{\boldsymbol{n}=1}^{N}\beta_{\boldsymbol{n}}\left\{y_{\boldsymbol{n}}\left(\boldsymbol{w}^T\boldsymbol{x}_{\boldsymbol{n}}+b\right)-1+\xi_{\boldsymbol{n}}\right\} - \sum_{\boldsymbol{n}=1}^{N}\xi_{\boldsymbol{n}}\gamma_{\boldsymbol{n}} \quad (3.11)$$

For the optimal solution, the following Karush–Kuhn–Tucker (KKT) conditions must be satisfied

$$\frac{\partial Q(\boldsymbol{w},b,\boldsymbol{\xi},\boldsymbol{\beta},\boldsymbol{\gamma})}{\partial \boldsymbol{w}} = \boldsymbol{w} - \sum_{\boldsymbol{n}=1}^{N}\beta_n y_n \boldsymbol{x}_n = \boldsymbol{0} \quad (3.12)$$

$$\frac{\partial Q(\boldsymbol{w},b,\boldsymbol{\xi},\boldsymbol{\beta},\boldsymbol{\gamma})}{\partial b} = -\sum_{\boldsymbol{n}=1}^{N}\beta_n y_n = 0 \quad (3.13)$$

$$\frac{\partial Q(\boldsymbol{w},b,\boldsymbol{\xi},\boldsymbol{\beta},\boldsymbol{\gamma})}{\partial \xi_n} = C - \beta_n - \gamma_n = 0 \quad (3.14)$$

$$\beta_n\left[y_n\left(\boldsymbol{w}^T\boldsymbol{x}_n+b\right)-1+\boldsymbol{\xi}_n\right] = 0 \quad \text{for } n=1,2,....N \quad (3.15)$$

$$\gamma_n\xi_n = 0,\ \beta_n \geq 0,\ \gamma_n \geq 0,\ \xi_n \geq 0 \qquad \text{for } n=1,2,....N \quad (3.16)$$

Solving (3.12) to (3.14) and substituting for $\boldsymbol{w}$ and γ_n in (3.11), we obtain the so-called Wolfe dual problem:

$$\underset{\boldsymbol{\beta}}{\text{maximize}} \quad \left\{\sum_{n=1}^{N}\boldsymbol{\beta}_n - \frac{1}{2}\sum_{n=1}^{N}\sum_{m=1}^{N}\boldsymbol{\beta}_n\boldsymbol{\beta}_m y_n y_m \boldsymbol{x}_n^T\boldsymbol{x}_m\right\} \quad (3.17)$$

$$\text{subject to } \sum_{n=1}^{N}\beta_n y_n = 0 \text{ and } C \geq \beta_n \geq 0 \quad \text{for } n=1,2,....N \quad (3.18)$$

The solution of the dual problem of (3.17) and (3.18) yields the Lagrange multipliers β_n $(n=1,2,....N)$. From (3.12), the solution for$\boldsymbol{w}$ has the form:

$$\boldsymbol{w}=\sum_{n=1}^{N}\beta_n y_n \boldsymbol{x}_n \tag{3.19}$$

Clearly, the form of $\boldsymbol{w}$ is determined only the training data corresponding to a non-zero Lagrange multipliers β_n, for which the constraints in (3.10) are exactly met; these training samples are referred to as *support vectors* (SVs). The bias *b* is determined from Equation (3.15) using any support vector. The final decision boundary *g(**x**)* can be expressed as

$$g(\boldsymbol{x})=\sum_{\beta_n>0}\beta_n y_n \boldsymbol{x}_n^T \boldsymbol{x}+b \tag{3.20}$$

where$\boldsymbol{x}$ is the input test vector. As indicated earlier, the decision function can be taken as $sgn\big(g(\boldsymbol{x})\big)$, with a tuning parameter *C*.

A trick of kernel function is incorporated with SVM to deal with the problem of nonlinearly separable classes. Suppose the input feature vectors $\boldsymbol{x_n}$ are mapped to a high-dimensional feature space as follows

$$\boldsymbol{z_n}=\Phi(\boldsymbol{x_n}) \tag{3.21}$$

The solution now involves the feature vectors z_n instead of x_n. A kernel function is defined as a function which computes the inner product of feature space mappings of original data points. Using a kernel function the inner product becomes $\langle \Phi(\boldsymbol{x_n}) , \Phi(\boldsymbol{x_m}) \rangle = K(\boldsymbol{x_n}, \boldsymbol{x_m})$. Therefore, replacing the inner product $\boldsymbol{x_n^T x}$ in (3.20) with the kernel function $K(\boldsymbol{x}_n, \boldsymbol{x})$ yields the decision function

$$g(\boldsymbol{x})=\sum_{SVs\ or\ \beta_n>0}\beta_n y_n K(\boldsymbol{x}_n, \boldsymbol{x})+b \tag{3.22}$$

The values of the kernel are evaluated over all training samples, in order to solve the optimization problem in (3.9)-(3.10). Some popular choices of kernel functions for SVMs include

- Radial basis function (RBF) kernel:

$$K(x,y)=\exp\left\{-\frac{|x-y|^2}{2\sigma^2}\right\}$$

- Polynomial kernel of degree *p*:

$$K(x, y) = (x^T y + 1)^p$$

wherekernel parameters *p* (degree of polynomial) and σ are just like regularization parameter *C* and these are input parameters to the SVM training process and are tuned to obtain the desired classification performance.

3.3 ISLANDING DETECTION OF DISTRIBUTED GENERATION USING MULTIPLE-FEATURE-BASED SVM

The proposed SVM (support vector machine) based methodology is narrated in the following three sub-sections. Section 3.3.1 presents the behaviour of network variables under islanding situation. Section 3.3.2 describes the process of feature extraction from credible islanding and non-islanding events. Section 3.3.3 narrates the proposed SVM based method, which include the training and testing procedure of SVM using multiple features extracted from islanding and non-islanding events.

3.3.1 Characterization of Network Variable under Islanding Situation

The behaviour of network variables can be observed by simulating a test network of Fig. 3.2, which illustrates the single line diagram of a simple distribution network energized with a synchronous generator (SG) based DG. Simulation yields the vector diagram of Fig. 3.3, which shows the voltage behaviour at DG connection point; it is drawn based on the values obtained by simulating the islanding scenarios generated by opening the circuit breaker (CB) in the system shown in Fig. 3.2. During islanding period, the system is composed by the synchronous generator and load only. At this instant, the synchronous machine begins to feed a larger (or smaller) load because the current provided by (or injected into) the utility side is abruptly interrupted. Thus, the generator begins to decelerate (or accelerate) its rotor speed to reduce the power mismatch. Therefore, the terminal voltage and angle with respect to a reference are affected; which are illustrated in one pre-islanding (solid line) and two post-islanding scenarios (dashed and dash-dotted lines) of Fig. 3.3. The dashed and dash-dotted lines represent the behaviour of voltage at the connection point of DG during 6^{th} and 7^{th} cycle after the onset of islanding. In islanded mode, change of voltage behaviour in each cycle is observed, which is influenced by the dynamics of synchronous generator.

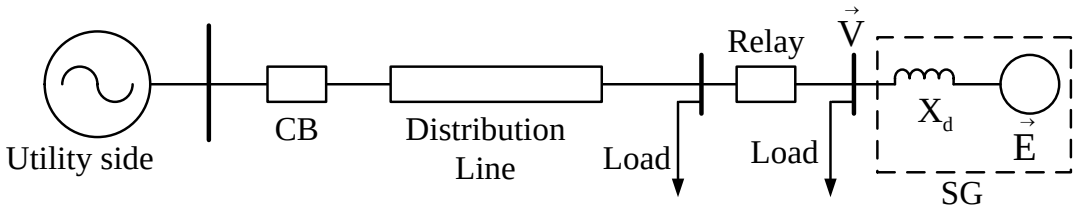

Fig. 3.2.A simple radial distribution network embedded with synchronous generator (SG) based DG.

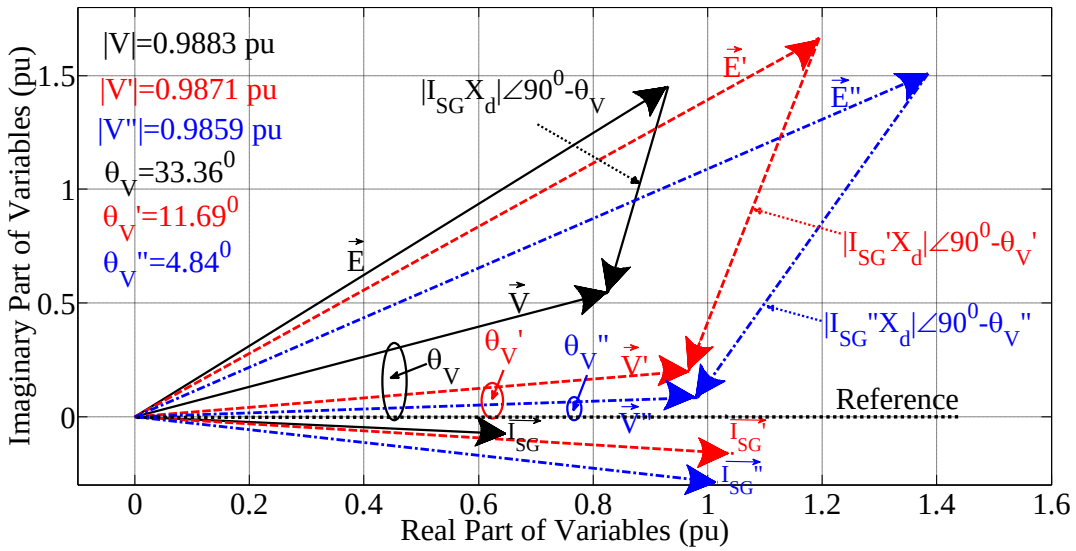

Fig. 3.3.Phasor diagram representing the voltage behaviour at DG connection point of the system shown in Fig. 3.2 during pre- and post-islanding condition.

From Fig. 3.3, it is noticeable that islanding provokes the variations of voltage magnitude and phase angle. Moreover, a change in frequency is also observed from the change of period of voltage cycle. Therefore, in the proposed method, five variables are used for feature extraction: frequency (*f*), rate of change of frequency $\left(\rho_f = df/dt\right)$, rotor angle ($\delta$), voltage (*V*) in pu, and rate of change of voltage $\left(\rho_v = dV/dt\right)$. In this sub-section, in order to show the behaviour of five variables under islanding condition, mathematical formulations are carried out followed by the simulation results. The dynamic behaviour of the synchronous generator can be determined by using the machine swing equation as presented below [104]:

$$\frac{2H}{\omega_0}\frac{d^2\delta}{dt^2} = \Delta P \tag{3.23}$$

where H is the generator inertia constant, ω_0 is the synchronous speed, and δ is the rotor angle with respect to synchronously rotating reference frame. Assuming the network is

operating at steady-state prior to islanding ($d\delta/dt$ = 0), integrating (3.23) yields

$$\delta(t) = \delta_0 + \frac{\omega_0 \Delta P t^2}{4H} \tag{3.24}$$

whereδ_0 is the rotor angle at steady state prior to islanding. The rotor angle δ is measured with respect to synchronously rotating reference frame and it varies with time during the transient period of islanding. The variation of the rotor angle during the transient is given by

$$\frac{d\delta}{dt} = \frac{\Delta P \omega_0 t}{2H} \tag{3.25}$$

The rotor speed ω_r can be represented as

$$\omega_r = \omega_0 + \frac{d\delta}{dt} \tag{3.26}$$

From (3.25) and (3.26), the rotor frequency can be expressed as

$$f_r = f_0 + \frac{\Delta P f_0 t}{2H} \tag{3.27}$$

Therefore, the rate-of-change-of-frequency is

$$\frac{df_r}{dt} = \frac{\Delta P f_0}{2H} \tag{3.28}$$

According to [105], islanding condition with reactive power imbalance is analogous to an incident when a pure reactive load is applied to the generator operating under no-load condition for which the voltage behaviour can be presented as

$$V_t = X_e.V.\left[\frac{1}{|Z|} + \left(\frac{1}{|Z'|} - \frac{1}{|Z|}\right)e^{-\frac{t}{\tau_0}} + \left(\frac{1}{|Z''|} - \frac{1}{|Z'|}\right)e^{-\frac{t}{\tau_1}}\right] \tag{3.29}$$

whereX_e is the reactive load, V_t is the generator terminal voltage in pu. In (3.29), direct axis transient and subtransient time-constant have been presented as τ_0 and τ_1 respectively. And direct axis synchronous, transient, subtransient reactances have been presented as ($|Z|$), ($|Z'|$), and ($|Z''|$) respectively. Time domain analysis for 1 second duration is carried out where islanding occurs at 0.5 second. For this event, the terminal voltage, V_t can be rewritten in the following form

$$V_t = \begin{cases} V & 0<t\leq 0.5 \\ X_e.V.\left[\frac{1}{|Z|}+\left(\frac{1}{|Z'|}-\frac{1}{|Z|}\right)e^{-\frac{(t-0.5)}{\tau_0}}+\left(\frac{1}{|Z''|}-\frac{1}{|Z'|}\right)e^{-\frac{(t-0.5)}{\tau_1}}\right] & 0.5<t\leq 1 \end{cases} \quad (3.30)$$

From (3.30), rate-of-change-of-voltage (*dV/dt*) can be obtained as below

$$\frac{dV_t}{dt} = \begin{cases} 0 & 0 < t \leq 0.5 \\ X_e.V.\left[-\frac{1}{\tau_0}\left(\frac{1}{|Z'|}-\frac{1}{|Z|}\right)e^{-\frac{(t-0.5)}{\tau_0}}-\frac{1}{\tau_1}\left(\frac{1}{|Z''|}-\frac{1}{|Z'|}\right)e^{-\frac{(t-0.5)}{\tau_1}}\right] & 0.5 < t \leq 1 \end{cases} \quad (3.31)$$

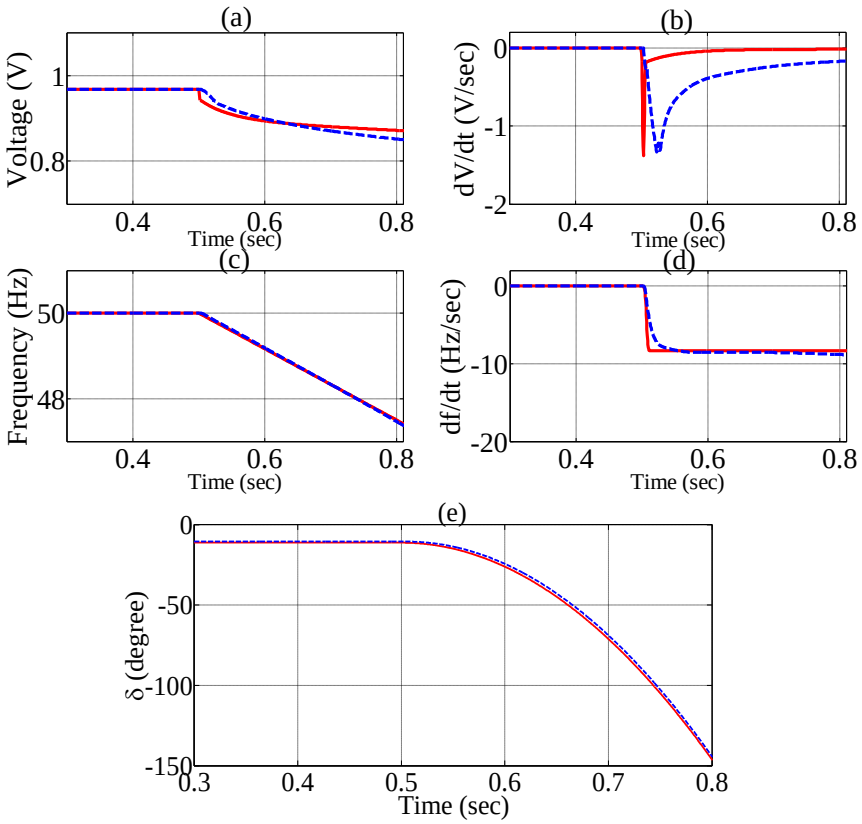

Fig. 3.4. Behaviour of five network variables: (a) *V*, (b) *dV/dt*, (c) *f*, (d) *df/dt*, and (e) δ under islanding condition (event inception at 0.5 second) using theoretical formula (solid line) and simulation (dash line).

Formulation of five variables, which include δ, *f*, *df/dt*, *V* and *dV/dt*, are presented in equations (3.24), (3.27), (3.28), (3.30) and (3.31), respectively. Response characteristic of these five variables is carried out by simulating the network of Fig. 3.2 in MATLAB SIMULINK. Under islanding situation, behaviour of five variables (using network simulation and theoretical formula) is presented in Fig. 3.4, considering a deficit of active power imbalance of 50% between load and generation within islanded network. It should be noted that a simplified model of synchronous generator (SG) is used for

theoretical formula, whereas in simulation, a detailed model of SG (6^{th}-order 3-phase model in *d-q* rotor reference) equipped with an automatic voltage regulator is applied. Hence, a slight difference is found in Fig. 3.4 for theoretical formula and simulation.

3.3.2 Extraction of Features

In the proposed method, five variables are used for feature extraction: normalized frequency *f*, rate of change of frequency ρ_f = *df/dt*, normalized rotor angle δ, normalized voltage *V*, and rate of change of voltage ρ_v = *dV/dt*. These variables are extracted from the terminal voltage of the DG. The frequency variable, *f*, is obtained by taking the time-inverse of the duration of two consecutive rising zero-crossing points of voltage signal. ROCOV (ρ_v) and ROCOF (ρ_f) are extracted from the change of voltage and frequency within small time interval Δt (where Δt can be typically 5×10^{-4} s). Rotor angle δ cannot be obtained from terminal voltage of DG in a straightforward manner. However, to obtain one such variable which is analogous to the characteristic of rotor angle δ and could be available from terminal voltage of DG, phase angle of voltage (θ) is used. The process of extraction of phase angle (θ) of *V* is described below.

In order to obtain the phase angle (θ) from the terminal voltage *v(t)*, the synchronously rotating reference frame is represented by a reference signal *s(t)* with 50 Hz frequency. Assuming a detection time of 200 ms and the power system frequency of 50 Hz, *s(t)* of 10 cycles is shown in Fig. 3.5 (a), and *v(t)* of 10 cycles duration is processed to obtain the phase angle deviation from reference signal *s(t)* as shown in Fig. 3.5 (b). As indicated in Fig. 3.5 (b), four points – two zero-crossing points, one positive half-cycle peak and another negative half-cycle peak points, are determined in each cycle. This procedure is followed to obtain *m+1* number of points during the duration of 10 cycles of *v(t)* signal; the points are denoted as $t_0, t_1, t_2, \ldots t_m$. Then $\theta(m)$, as shown in Fig. 3.5 (c), is obtained by using the following expression

$$\theta(m)=\left[m\times\frac{T}{4}-(t_m-t_0)\right]\times\frac{360}{T}\ \ for\ \ m=0,1,2,.. \qquad (3.32)$$

where $\theta(m)$ = phase angle of *v(t)* in degrees with respect to *s(t)*, and *T* = time period of *s(t)*. Thus, phase angle of voltage (θ) is obtained from (3.32) and then, normalized θ is used and denoted as δ, which is usedas one of the variables for classification of islanding and non-islanding events.

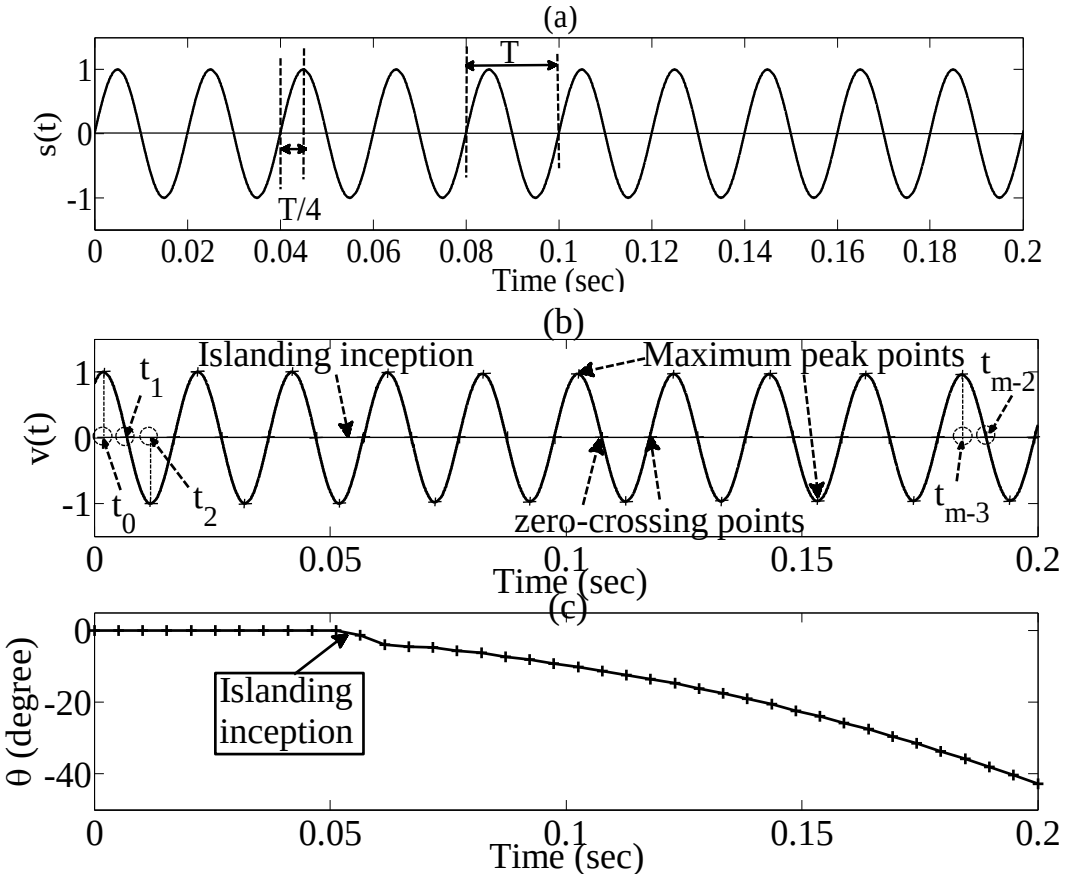

Fig. 3.5. Extraction of phase angle (θ): (a) Reference signal *s(t)*, (b) Terminal voltage *v(t)*, and (c) Phase angle of *v(t)* with respect to *s(t)*.

Five features are extracted from the five variables as mentioned above, by taking Standard Deviation (SD) inside a sliding data-window having a width of ΔT. For instance, feature from a signal *s′(t),* which could be any of the five network variables, are extracted by taking SD inside the ΔT width of a sliding data-window, as shown in Fig. 3.6. Following the same procedure, five features are extracted from five network variables, which are obtained during islanding situation with active power imbalance (ΔP) of 50% in the islanded segment (see Fig. 3.7). As illustrated in Fig. 3.7, all five variables show significant variations from normal condition since ΔP is comparatively high, i.e., ΔP = 50%. But for ΔP< 10%, these variables do not show major variations and they look almost similar of those corresponding variables obtained under non-islanding situations such as capacitor switching, load switching etc., as presented in [106].

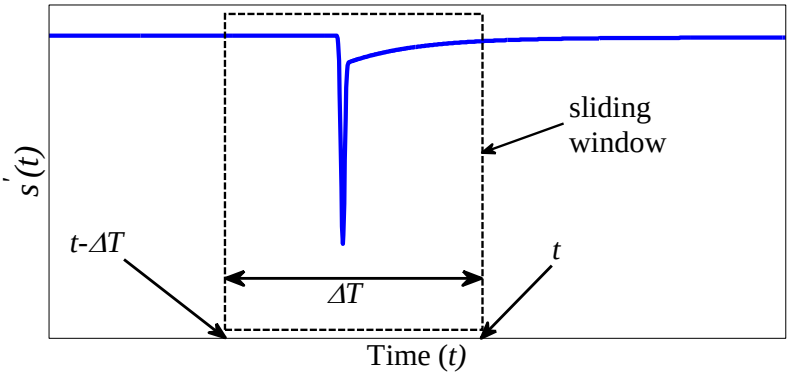

Fig. 3.6. Illustration of feature extraction from a general signal *s′(t),* using a sliding data-window.

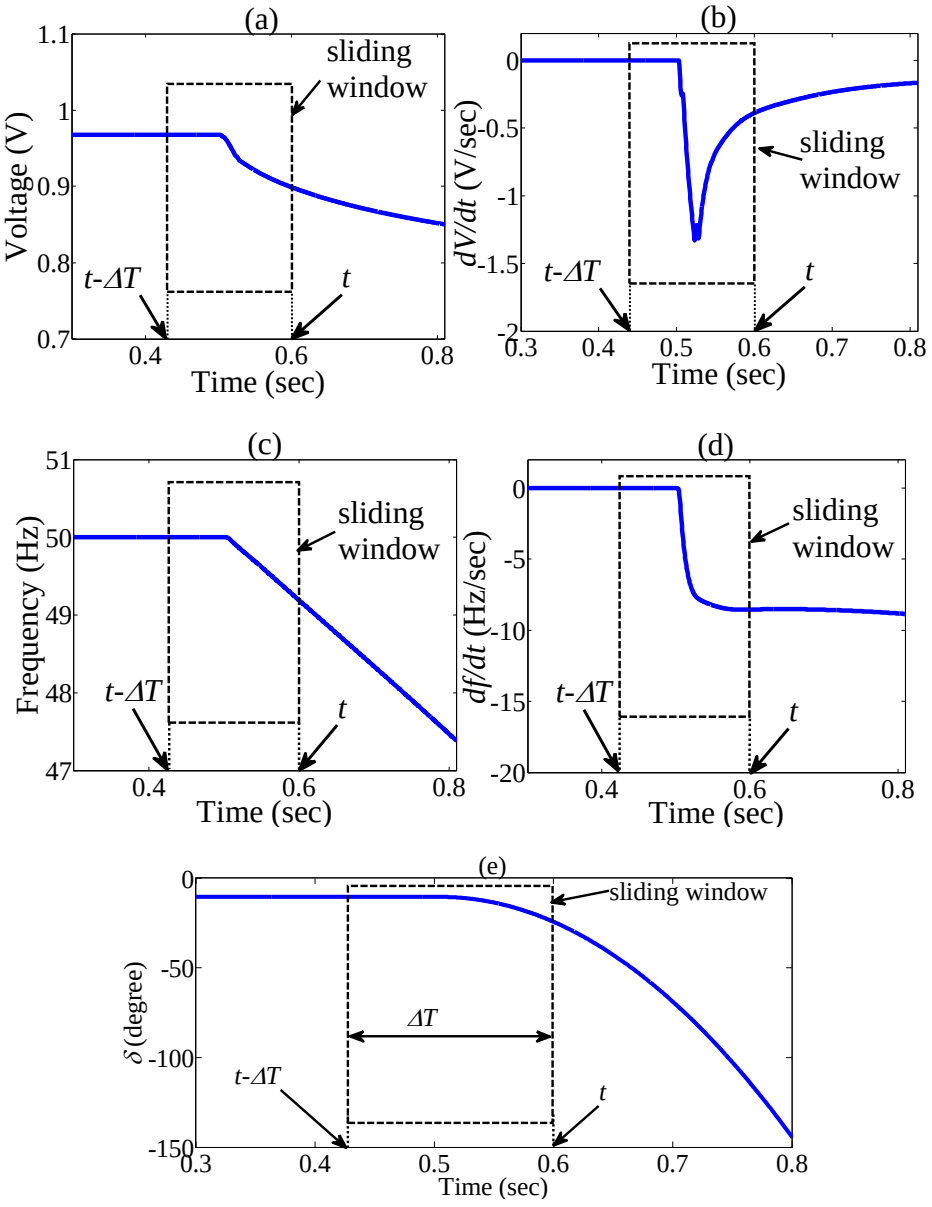

Fig. 3.7. Illustration of feature extraction from five network variables: (a) *V*, (b) dV/dt, (c) *f*, (d) df/dt, (e) *δ;* using a sliding data-window of *ΔT* width.

Mathematically, the expressions of the five features are given by

$$\sigma_v = std\{v(\tau)\,;\, \tau \in [t-\Delta T,\, t]\} \tag{3.33}$$

$$\sigma_f = std\{f(\tau)\,;\, \tau \in [t-\Delta T,\, t]\} \tag{3.34}$$

$$\sigma_\delta = std\{\delta(\tau)\,;\, \tau \in [t-\Delta T,\, t]\} \tag{3.35}$$

$$\sigma_{\rho_v} = std\left\{\frac{dv(\tau)}{dt}\,;\, \tau \in [t-\Delta T,\, t]\right\} \tag{3.36}$$

$$\sigma_{\rho_f} = std\left\{\frac{df(\tau)}{dt}\,;\, \tau \in [t-\Delta T,\, t]\right\} \tag{3.37}$$

where σ_v ,σ_f ,σ_δ ,$\sigma_{\rho v}$ and $\sigma_{\rho f}$ represent the features extracted from the network variables: voltage (*V*), frequency (*f*), rotor-angle (δ), rate-of-change-of-voltage (ρ_v) and rate-of-change-of-frequency (ρ_f), respectively. Therefore, the feature vector can be presented as

$$\boldsymbol{x} = [\sigma_v \;\; \sigma_f \;\; \sigma_\delta \;\; \sigma_{\rho_v} \;\; \sigma_{\rho_f}]^T \tag{3.38}$$

where $[.]^T$ denotes the transpose operator.

3.3.3 SVM based Method for Islanding Detection

The proposed method can be described in three stages. The first stage involves the training of Support Vector Machine (SVM) with different features obtained under several islanding and non-islanding situations. In the second stage, the trained SVM is applied to test the performance of the proposed approach under different network contingencies and conditions. Third stage describes the flowchart of the proposed algorithm, which is applied for the detection of islanding.

- Training of SVM

  In accordance with the definition of supervised learning process, training of SVM is conducted off-line and it can be summarized as follows.

1) A large number, i.e., *n* number of islanding and non-islanding events, which may exist in the power system, are generated in a test network through repeated dynamic simulation.

2) For each event, the feature vector ***x,*** containing five features, are obtained by following the Equations (3.33)-(3.38), considering a typical window width of ΔT. It is worth noting that in this experiment, the location of islanding inception is known *a priori* (ground-truth);therefore, any feature vector extracted from a window which contains the islanding inception anywhere is labelled as an islanding event.

3) For n number of training events, the feature vectors are kept in a feature matrix as mentioned below

$$\boldsymbol{F}(n) = \begin{bmatrix} \boldsymbol{x}_1 & \boldsymbol{x}_2 & \boldsymbol{x}_3 & \ldots\ldots & \boldsymbol{x}_n \end{bmatrix}^T = \begin{bmatrix} \sigma_v(1) & \sigma_f(1) & \sigma_\delta(1) & \sigma_{pv}(1) & \sigma_{pf}(1) \\ \sigma_v(2) & \sigma_f(2) & \sigma_\delta(2) & \sigma_{pv}(2) & \sigma_{pf}(2) \\ \sigma_v(3) & \sigma_f(3) & \sigma_\delta(3) & \sigma_{pv}(3) & \sigma_{pf}(3) \\ \ldots\ldots & \ldots\ldots & \ldots\ldots & \ldots\ldots & \ldots\ldots \\ \sigma_v(n) & \sigma_f(n) & \sigma_\delta(n) & \sigma_{pv}(n) & \sigma_{pf}(n) \end{bmatrix} \quad (3.39)$$

4) Each training data$\boldsymbol{x}_n$ corresponds to five features describing a particular signature which belongs to one of two classes i.e. $y_n = -1$ for islanding or $y_n = +1$ for non-islanding.

5) Applying supervised learning algorithm, k-fold cross-validation is conducted using the training data. Firstly, the data are divided into k subsets. Then, k-1 subsets are used for training, and the remaining subset is used for testing. Using soft-margin SVM classification technique and employing linear, polynomial and Gaussian RBF kernels, performance of the classifier is computed. The whole process is repeated k times and the average classification performance is calculated.

6) Tuning the regularization parameter C, kernel-parameters σ for the RBF kernel and the degree p for the polynomial kernel, k-fold cross-validation are conducted several times. Thus, the optimal values of C, σ and p are selected by observation.

7) Using the optimal value of C, and the kernel-parameters corresponding to Gaussian RBF, linear, and polynomial kernels, training of SVM is accomplished.

- Performance Evaluation of Proposed Approach using trained SVM

Training of SVM yields the decision function based on a number of support vectors (SVs). Thus, by obtaining decision rule $sgn(g(\boldsymbol{x}))$ from decision function (3.22), the input test data $\boldsymbol{x}$ is classified as islanding or non-islanding event.

In this approach, the binary classification problems, which include islanding class and non-islanding class, are encountered. Typically, DR (Detection Rate) and FA (False Alarm) are used to show the performance of classifiers while dealing with classification problems and it can be presented as below [107].

$$DR = TP/(TP + FN) \text{ and } FA = FP/(FP + TN)$$

where TP = True Positive, TN = True Negative, FP = False Positive and FN = False Negative. In this study, "Positive" implies that an event has been classified as "islanding" whereas "Negative" indicates the classified event as "non-islanding". Therefore, TP indicates the successful classification of islanding events, and FP implies that non-islanding events have been classified as islanding or in other words, FP indicates the misclassification of non-islanding events. Similarly, TN indicates the successful classification of non-islanding events and FN specifies the misclassification of islanding events. Thus, performance of the proposed approach is assessed using the DR related to islanding detection and FA related to nuisance tripping. In short, DR indicates the ratio of successfully detected islanding events to the total number of islanding events whereas FA indicates the ratio of misclassification of non-islanding events to the total number of non-islanding events. In other words, DR indicates the accuracy of the proposed approach in islanding detection whereas FA specifies the rate of nuisance tripping of DG during non-islanding conditions.

- Detection of Islanding using trained SVM

The flow chart presented in Fig. 3.8 shows the algorithm and steps of applying the trained SVM to detect islanding. Five dimensional features $(\boldsymbol{x}_n)$ are obtained from the available voltage signal at DG connection point. These features are tested with the trained SVM. Thus, the classification result which leads to either islanding $(y_n = -1)$ or non-islanding $(y_n = +1)$ is obtained. If islanding is detected, a trip signal is sent to disconnect the DG.

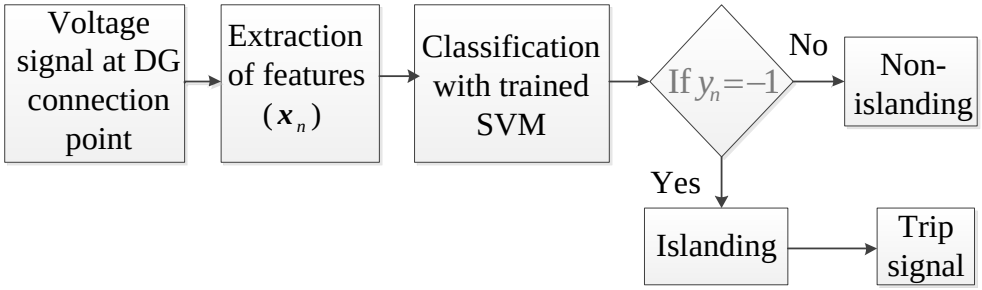

Fig. 3.8.Flow chart for detection of islanding.

3.4 TEST RESULTS

The proposed method has been tested on a practical network in New South Wales, Australia. Results will be presented in the following subsections.

3.4.1 Test System

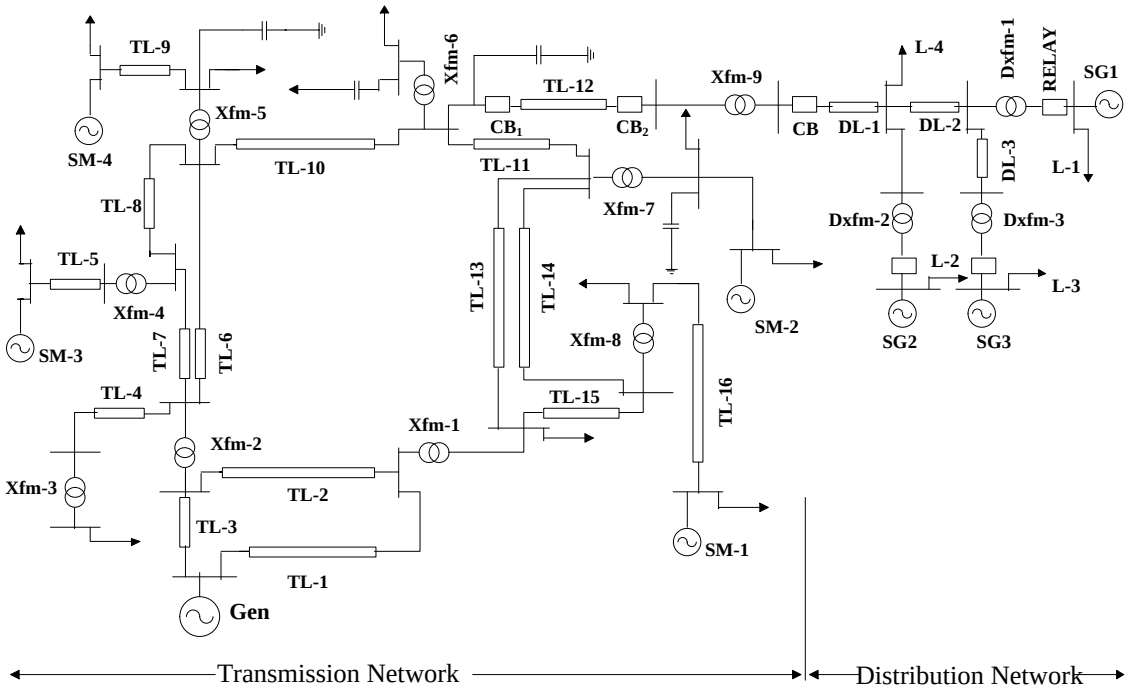

Fig. 3.9.Single line diagram of a test distribution network under study.

Repeated dynamic simulation is carried out using the test network of Fig. 3.9 to extract the features corresponding to different islanding and non-islanding conditions. The simulation is conducted using MATLAB/SIMPOWER software with 2 KHz sampling rate. The test network comprises a radial distribution network which is connected with the transmission network of Moree substation, New South Wales

(NSW), Australia. Data of transmission network side, such as, transmission lines, transformers, etc., are collected from TransGrid, a Transmission utility of NSW, Australia. Distribution network side comprises three 6-MW synchronous generators (SGs) operating as DG. They are connected to the network through 33/0.69 kV transformers. The transformers adjacent to SG1, SG2 and SG3 are used for locating the relays of circuit breakers. These relays monitor the voltage signals in real-time. Data of transformers, transmission lines, distribution lines and DGs are presented in **Appendix A.1**. It should be noted that the simulation study involves the sampling rate of 2 KHz, therefore, the relays at circuit breaker's end would receive the voltage at 2 KHz sampling rate (i.e. 40 samples/cycle for 50 Hz system); this sampling rate is realistic in power system, since for phasor measurement unit (PMU), which is a reliable device for measuring the voltage in electricity grids, can process 10 to 256 samples in each cycle for 50 Hz system [108].

3.4.2 Generation of Events

The events for which a part of the network energized by DG is isolated from the grid system are considered as islanding conditions. These conditions are generated by artificially created instantaneous faults at some nodes in the transmission or distribution feeder that result in DG islanding. Normal events that may exist in practical power systems due to capacitor switching, loss of lines, load addition, load disconnection, etc., for which DG energized network is not isolated, are considered as non-islanding conditions. Typically, in the test network, the situations that could be present during islanding and non-islanding conditions are as follows [15, 109]:

- Tripping of main circuit breaker (CB) resulting to an islanded system with DG at the presence of different range of active and reactive power imbalance in the islanded section.
- Opening of any breakers between main grid and DG.
- Events that could trip breakers (CB_1 or CB_2) in transmission network (see Fig. 3.9), and eventually island the DG under study.
- Load disconnection from the distribution network.
- Switching of capacitor bank in the network.
- Loss of line in the distribution system, apart from the line connected to the target DG.

- Occurrence of three phase fault in a distribution line, apart from the line connected to the target DG.

Several islanding and non-islanding events are generated by conducting repeated dynamic simulation on the test network of Fig. 3.9. Total 1 second time domain simulation is carried out for each event, and an observation period of ΔT cycle is considered for extracting the features. As presented in [15], several features are extracted by taking the average value of 8 cycles of different network variables such as voltage, frequency etc. Similarly, in this study, standard deviation of 10 cycles (i.e. 0.2 sec duration for fundamental frequency of 50 Hz) of each of the five network variables, which include voltage, frequency, rate-of-change-of-frequency, rate-of-change-of-voltage, and rotor angle, have been considered to extract the features required for classification of events.In other word, a typical window width of ΔT = 10 cycles of observation period has been considered to extract the features. A list of generated islanding and non-islanding events are presented in Table 3-I.

Variation of active and reactive power is considered to generate a large set of islanding events. As presented in [72], active and/or reactive power imbalance in the islanded segment, acts as a significant factor in the detection of islanding, especially when vector surge or frequency relays are applied. Moreover, four possible combinations of power imbalance scenarios may exist during the period of islanding [72]. They are:

1) Scenario (*a*): Deficit of ΔP (active power imbalance) and deficit of ΔQ (reactive power imbalance),
2) Scenario (*b*): Excess of ΔP and excess of ΔQ,
3) Scenario (*c*): Excess of ΔP and deficit of ΔQ, and
4) Scenario (*d*): Deficit of ΔP and excess of ΔQ.

Therefore, in this study, all these scenarios are taken into account while generating the islanding events. Variation of active and reactive power imbalance is accomplished by changing the load and generation profiles. In this study, deficit and excess of active and reactive power imbalances are taken into account and the process of generating these scenarios are described below.

- *Variation of active power imbalance*: The deficit of active power imbalance is simulated by keeping the active loads at their nominal values and gradually varying the active power output from 0 to 1 pu. The excess of active power imbalance is simulated by keeping the active power generation at their nominal values i.e. 1 pu, and gradually varying the active power loads from 1 to 0 pu.
- *Variation of reactive power imbalance*: To generate the situation of deficit of reactive power imbalance, the AVR (Automatic Voltage regulator) set point is varied from 0.95 to 1 pu and the reactive components of the loads are kept at their rated values. This guarantees that there are cases of deficit of reactive power in the islanded system. Similarly, excess of reactive power imbalance is generated by varying the AVR set point from 1.01 to 1.05 pu. For each AVR set point, simulation is carried out as suggested in [72].

TABLE 3-I

SAMPLE LIST OF THE EVENTS UNDER ISLANDING AND NON-ISLANDING CONDITIONS

Event name	Event description	Monitoring end	No. of Events
Islanding	Tripping of CB at the presence of the followings: 1) Three types of load: constant impedance (const. *Z*), constant current (const. *I*) and constant power (const. *P*) [72]. 2) All 4 possible combinations of power imbalance scenarios, i.e., deficit and excess of active power imbalance from 0% to 99.9% and reactive power imbalance from 0% to 50% in the islanded network [72].	DG-1/SG1	434
		DG-2/SG2	434
		DG-3/SG3	434
Non-islanding	At the presence of three types of load (constant impedance, constant current and constant power), several non-islanding events are generated by considering the following actions [109]: 1) Switching of capacitor, inductive load and non-linear load at different time within 10 cycles of observation period. 2) Balanced three phase fault with fault clearing time from 0.05 sec to 0.1 sec within the observation period. 3) Disconnection of other DGs apart from the monitoring one.	DG-1/SG1	240
		DG-2/SG2	240
		DG-3/SG3	240

3.4.3 Pattern of Features under Islanding and Non-islanding conditions

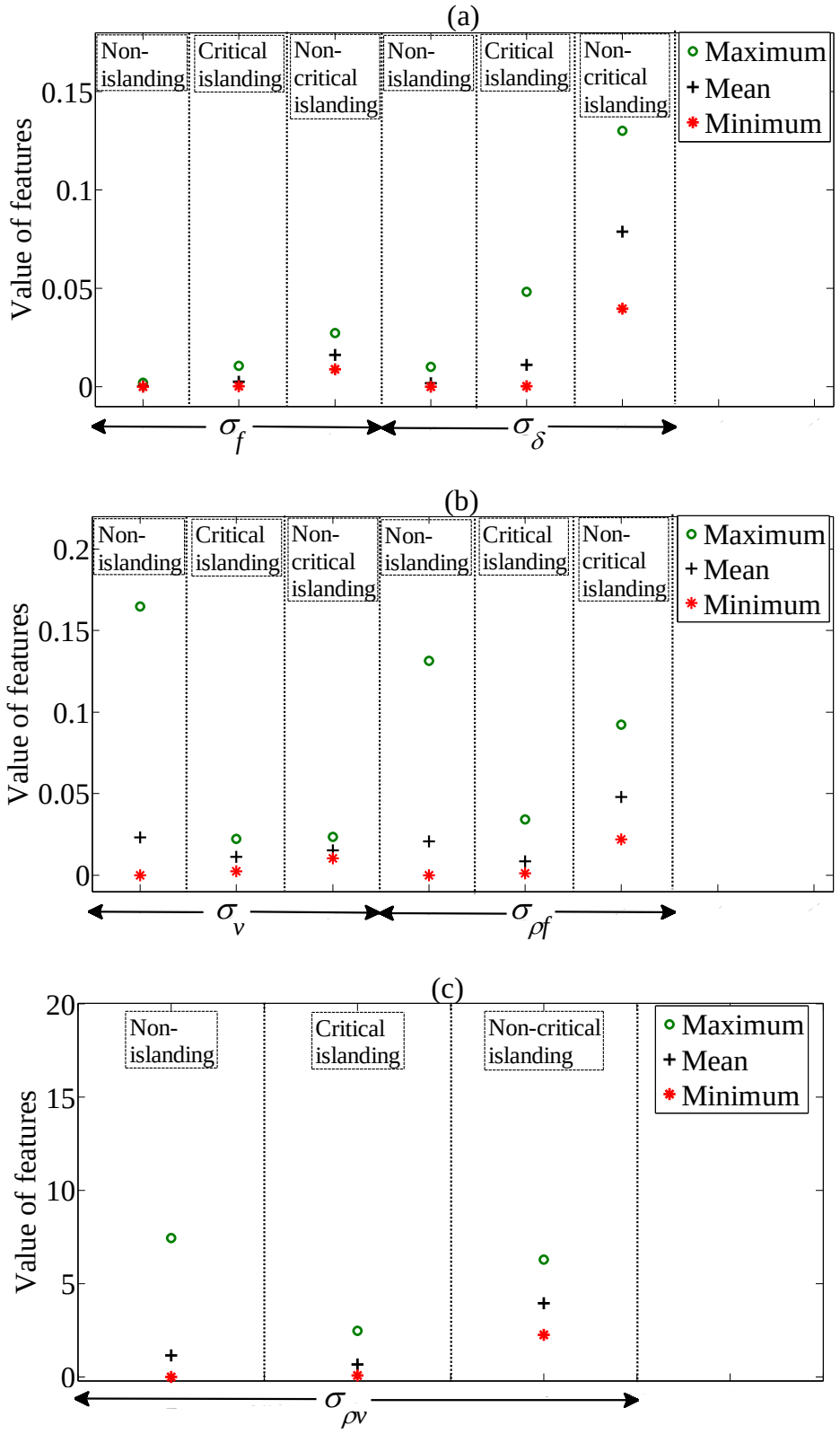

Fig. 3.10. Variation of features under critical islanding, non-critical islanding and non-islanding cases represented by minimum, maximum and average value of features: (a) σ_f, σ_δ (b) σ_v, $\sigma_{\rho f}$ (c) $\sigma_{\rho v}$.

As presented in Table 3-I, a total of 2,022 events (including 1,302 islanding and 720 non-islanding) are generated and 5 features for each events are extracted. These features correspond to the events: islanding and non-islanding, and therefore, prior to performing the classification task, pattern of features are explored in this sub-section.

In [104],theeffectiveness ofthe conventional Vector Surge (VS) relay, was investigated, and the *non-detection zone* (NDZ) associated with power imbalance factor of the islanded network was discussed. According to [104], for a particular relay setting of 10° and detection time (200 ms), a minimum of 43.86% active power imbalance is needed for a VS relay to detect islanding in the test network energized with Synchronous Generator (Inertia constant H = 1.5). Hence, in order to highlight the problematic islanding cases of low power imbalance, islanding events with power imbalance of less than 43.86% are considered as critical islanding cases whereas power imbalance of greater than 43.86% are considered as non-critical islanding cases. In Fig. 3.10, minimum, maximum and mean value of features under critical islanding (a total of 900 events), non-critical islanding (a total of 402 events) and non-islanding cases (a total of 720 events) are shown separately.

From Fig. 3.10 (a), it is observed that considering two features σ_f and σ_δ, minimum value of non-critical islanding events is higher than the maximum value of non-islanding events. Therefore, using these two features σ_f and σ_δ, non-critical islanding cases can be separated from non-islanding cases quite easily. But, the minimum value of critical islanding features falls inside the range of the value of non-islanding features as shown in Figs. 3.10 (a)-(c). Thus, classification becomes challenging for the critical islanding events and non-islanding events. Hence, it is evident that classification will give poor results if only one or two features are taken into account. Therefore, in the proposed method, multiple features have been used to classify the islanding and non-islanding events.

3.4.4 Classification Results of multiple-feature-based SVM Method

As stated earlier, by simulating the test network of Fig. 3.9, a total of 2,022 events are generated. This includes 1,302 islanding and 720 non-islanding events. The number of training and test events (including islanding and non-islanding) are presented in Table 3-II. From Table 3-II it is observed that three types of load has been given equal importance (i.e., evenly distributed) while generating these events. Table 3-II also

reveals that training stage possess less number of data than testing stage. It gives the opportunity of comprehensive scrutiny of the proposed trained SVM tool with as many testing data as can be present during different network contingencies and conditions. Moreover, it should be noted that the training data was a different subset from the test data; however, both sets are taken from the same system modelled in SimPower SIMULINK.

TABLE 3-II

GENERATED ISLANDING AND NON-ISLANDING EVENTS AT THE PRESENCE OF DIFFERENT TYPES OF LOAD

Type of load	Islanding				Non-islanding	
	Deficit and excess		No. of events		No. of events	
	ΔP (%)	ΔQ (%)	Training	Test	Training	Test
Const. *P*	0-100	0-50	80	354	80	160
Const. *I*	0-100	0-50	80	354	80	160
Const. *Z*	0-100	0-50	80	354	80	160
Total			240	1062	240	480

SVM is trained using the procedure presented in section 3.3.3. During the training process, *k*-fold (with $k = 5$) cross-validation results in optimal regularization parameter $C = 225$. Using the trained SVM, a total of 1,542 test events (consisting of 1,062 islanding and 480 non-islanding) are tested to investigate the performance of the method. The classification-performance of the SVM based method is presented below.

3.4.4.1 *Overall Performance of Proposed Method*

Trained SVM produces a limited number of SVs (Support Vectors) for different kernel functions; and with these SVs, an optimal hyperplane is achieved. Using this optimal hyperplane, test data are classified. Overall, the performance of the proposed method using linear kernel SVM is shown in Table 3-III considering three types of load separately and collectively. DR (Detection Rate) and FA (False Alarm) are used as two key performance indicators. The performance of the proposed method using Gaussian RBF kernel and polynomial kernel SVM is also investigated and test results are presented in Table 3-IV . From Table 3-IV it is evident that if parameters of the kernel are properly tuned, the decision boundary can be established with small number of SVs.

TABLE 3-III

ISLANDING DETECTION USING AN SVM CLASSIFIER WITH LINEAR KERNEL

Type of load	DR (Detection Rate)	FA (False Alarm)
Constant *P*	99.72%	0.63%
Constant *I*	100%	2.5%
Constant *Z*	100%	2.5%
Constant *Z*, *P* and *I*	99.91%	1.88%

TABLE 3-IV

ISLANDING DETECTION USING SVM CLASSIFIER WITH DIFFERENT KERNELS

Kernel	Parameter value	SVs	DR	FA
Gaussian RBF	$\sigma = 1$	42	97.3%	0.4%
Polynomial	$p = 2$	18	98.3%	0.2%

3.4.4.2 *Performance under most Critical Islanding Cases*

In order to scrutinize the performance under the most critical islanding cases, the proposed method is further tested with islanding events associated with power imbalance (ΔP) ranging from 0.5% to 10%. To accomplish this task, all four scenarios of power imbalance presented in section 3.4.2 are taken into account. At first, critical islanding events corresponding to scenario (*a*), i.e., deficit of active and reactive power imbalance scenarios, are tested. A total of 945 islanding events, considering deficit of ΔP ranging from 0.5% to 10% in conjunction with deficit of ΔQ from 0% to 50%, are generated. These test data were a new set and not a subset of the training data.Then DR is obtained using linear, polynomial and Gaussian RBF kernel for each ΔP level. Total 480 non-islanding test events as mentioned in Table 3-II are also classified to detect FA under each ΔP level of classification. The results are presented in Table 3-V and the corresponding performance curve is shown in Fig. 3.11. From Table 3-V and Fig. 3.11, it is observed that under most critical islanding cases, the three kernels show almost similar performance if a trade-off between detection rate and false alarm rate is considered. However, throughout the experimental results and considering less than 1% false alarm into account, optimistic performance is achieved for polynomial kernel which has successfully classified the islanding events with ΔP of 2% or higher; whereas linear or Gaussian RBF kernel needs the power imbalance of 3% or higher to achieve

100% accuracy in classifying the islanding events. Considering the pessimistic performance (with Gaussian RBF or linear kernel) of the proposed method it is revealed that detection rate falls below 100% when islanding events associated with ΔP < 3% are encountered. However, for ΔP ≥ 3%, multi-feature based approach shows satisfactory results even for the pessimistic performance scenarios.

TABLE 3-V

PERFORMANCE OF SVM CLASSIFIER USING DIFFERENT KERNELS UNDER MOST CRITICAL ISLANDING CASES ASSOCIATED WITH DEFICIT OF ΔP AND ΔQ

ΔP (%)	No. of islanding events	Gaussian RBF kernel		Polynomial kernel		Linear kernel	
		DR (%)	FA (%)	DR (%)	FA (%)	DR (%)	FA (%)
0.5	135	89.6	0.00	92.6	0.83	82.2	0.42
1	135	92.6	0.00	96.3	0.83	92.6	0.42
2	135	98.3	0.00	100	0.83	99.3	0.42
3	135	100	0.00	100	0.83	100	0.42
5	135	100	0.00	100	0.83	100	0.42
7	135	100	0.00	100	0.83	100	0.42
10	135	100	0.00	100	0.83	100	0.42

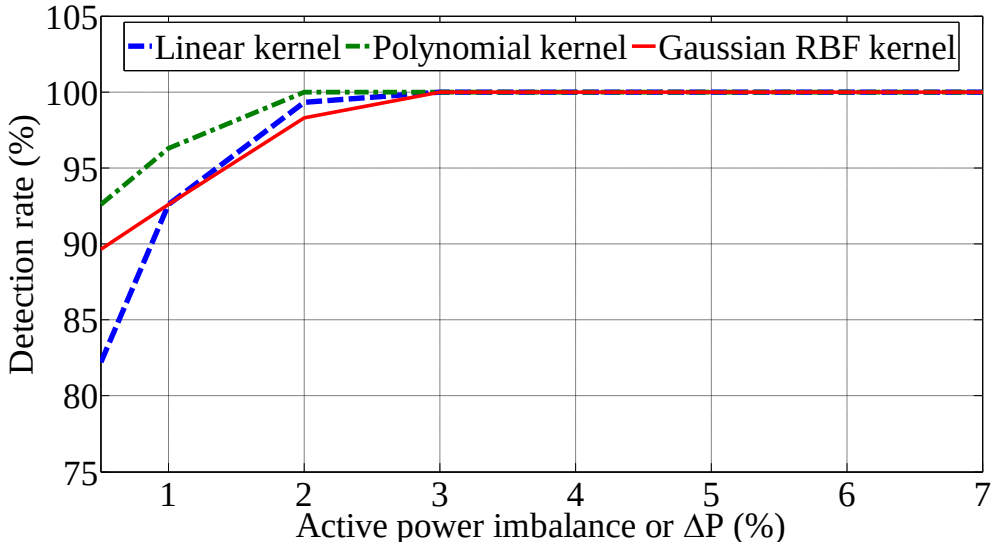

Fig. 3.11. Performance curve of multi-feature based SVM method with linear, polynomial and Gaussian RBF kernel under most critical islanding cases.

To investigate the classification performance of the proposed method, the other three combinations, scenarios (*b*), (*c*) and (*d*) as presented in section 3.4.2, are also taken into account. Thus, a total of 1,440 islanding events are generated considering ΔP from 0.5% to 7% in conjunction with ΔQ from 0% to 50% at the presence of three types of loads (constant *Z*, constant *I* and constant *P*). SVM with polynomial kernel of order 3 ($p = 3$) is applied to test the performance. Test results for scenario (*b*), (*c*) and (*d*) are shown in Table 3-VI. From the classification results presented in Table 3-VI, it is observed that under two scenarios: (*d*) deficit of ΔP and excess of ΔQ, and (*b*) excess of ΔP and excess of ΔQ, 100% accuracy with 0.83% false alarm is obtained for all the test cases; whereas the scenario (*c*) represented by the combination of excess of ΔP and deficit of ΔQ yields 100% accuracy for $\Delta P \geq 5\%$.

TABLE 3-VI

PERFORMANCE OF SVM CLASSIFIER UNDER MOST CRITICAL ISLANDING CASES INCLUDING THREE COMBINATIONS OF DEFICIT AND EXCESS OF ΔP AND ΔQ

ΔP (%)	No. of islanding events	Scenario (*c*): Excess ΔP and Deficit ΔQ (0%-50%)		Scenario (*d*): Deficit ΔP and Excess ΔQ (0%-50%)		Scenario (*b*): Excess ΔP and Excess ΔQ (0%-50%)	
		DR (%)	FA (%)	DR (%)	FA (%)	DR (%)	FA (%)
0.5	60	91.7	0.83	100	0.83	100	0.83
1	60	91.7	0.83	100	0.83	100	0.83
2	60	91.7	0.83	100	0.83	100	0.83
3	60	91.7	0.83	100	0.83	100	0.83
4	60	91.7	0.83	100	0.83	100	0.83
5	60	100	0.83	100	0.83	100	0.83
6	60	100	0.83	100	0.83	100	0.83
7	60	100	0.83	100	0.83	100	0.83

3.4.4.3 *Performance of SVM based Method with Training and test Data extracted from different Monitoring ends*

To investigate the performance of the multiple-feature-based SVM method under different monitoring ends, SVM is trained with the features obtained from the voltage signal available from one monitoring end (located at a point close to SG1of Fig. 3.9) and it is tested with the features extracted at other monitoring ends located at other places, such as the locations close to SG2 and SG3. Thus, 434 islanding and 240 non-islanding events (see Table 3-I) are used for training purpose and the remaining events (868 islanding and 480 non-islanding events) are used for test purpose. The test results are presented in Table 3-VII.

TABLE 3-VII

PERFORMANCE OF SVM BASED ISLANDING DETECTION (TRAINING AND TEST AT DIFFERENT MONITORING ENDS)

Kernel	Parameter value	No. of SVs	DR (%)	FA (%)
Linear	C = 225	24	99.54	0
Polynomial	p = 2	16	99.09	0.31
	p = 3	7	99.64	6.69

From the test results of Table 3-VII, it can be concluded that both linear and polynomial kernels show almost similar performance when training and testing are carried out at different monitoring ends. However, from the simulation results, it is revealed that SVM classifier using linear kernel shows 99.54% detection rate (DR) with 0% false alarm (FA), whereas polynomial kernel (with p = 2) shows DR of 99.09% at the cost of 0.31% false alarm.

3.4.4.4 *Performance of Proposed Method under Change in Network Topology*

To test the proposed method under slight change in network topology, several test cases are generated separately by eliminating one branch (DL-3), two branches (DL-3 and the branch connected through Dxfm-2) and shifting the open (or disconnection) point (near the bus bar in between DL-1 and DL-2, and near the bus bar in between DL-2 and DL-3) in the test network of Fig. 3.9. Thus a total of 640 test islanding events are generated and these test events are classified using the trained SVM. It should be noted that the trained SVM, which was developed using the training data of Table 3-II, is used to test these new set of 640 islanding data. In other word, retraining was not conducted to test the proposed method under the change of network topology. Considering the data generated under the change in network topology as mentioned earlier, the test results of SVM based method using linear and polynomial kernels are illustrated in Table 3-VIII. In this study, a total of 480 non-islanding test events as mentioned in Table 3-II are classified to detect FA. From the test results of Table 3-VIII it is evident that higher order polynomial kernel (p = 3) shows better performance than lower order polynomial kernel (p = 2) in terms of detection rate (DR). However, polynomial kernel of order 3 shows higher false alarm (FA) than lower order (p = 2) polynomial kernel. On the other hand, linear kernel shows 99.79% DR at the cost of only 0.15% false alarm.

TABLE 3-VIII

PERFORMANCE OF SVM BASED ISLANDING DETECTION UNDER MINOR CHANGE IN NETWORK TOPOLOGY

Kernel	Parameter value	DR (%)	FA (%)
Linear	C = 225	97.1	0.15
Polynomial	p = 2	82.1	0
	p = 3	97.86	4.4

3.4.4.5 *Flexibility and Adaptability of Proposed SVM based Method*

The proposed SVM based method is flexible to adapt changes in configuration. In the proposed approach, the decision boundary of the SVM based classification technique is established throughout the simulation results of a test network with multiple DGs. The main criteria that define the decision boundary are based on the number of training cases covering as many different non-islanding and islanding events as possible including the different network contingencies and power imbalance levels. Therefore, if significant changes are made in the network or in the circuit topology, decision boundary needs to be re-established by new simulations and with new training sets. However, throughout the simulation results, overall performance of the proposed method shows satisfactory results even under most critical islanding cases of low power imbalance. To scrutinize this method, training and testing are carried out at different monitoring ends and under minor change of network topology. With properly tuned kernel parameters, test results give detection rate of 98% and above, with less than 2% false alarm and thereby show the acceptability of this method. But, to avoid the probable false operation of the proposed method under significant change in network topology, it is suggested to conduct the training of SVM at each monitoring end separately using as many different islanding and non-islanding cases as possible so that the SVM based method can adapt the new environment or change in configuration.

3.4.5 Comparative Analysis between SVM based Method and an Intelligent Approach for Islanding Detection

As a comparative study with the method given in [14], the SVM based method has been tested by simulating the test network of [14]. A total of 54 events have been generated under the same operating conditions and network contingencies as presented in [14]. Thus, five features of the proposed method corresponding to 54 events (27 islanding and 27 non-islanding) are generated. Event-wise plot of features

corresponding to 54 events are shown in Fig. 3.12 and scatter plots of the features are shown in Fig. 3.13. It should be noted that features of the proposed method were different from the features of [9] and the 27 islanding events represented those islanding cases where $\Delta P \geq 5\%$, as reported in [14]. Visual analysis of the proposed features indicates that islanding features can be easily distinguished from the non-islanding features (as shown in Figs. 3.12 and 3.13).As a result, multi-feature based SVM method shows 100% accuracy with 0% false alarm for all test cases. In summary, test results indicate that the proposed technique can detect all islanding events in the test cases, unlike, the method presented in [14], which fails to detect 3 islanding cases at the presence of 5% power imbalance as reported by the authors. However, the proposed approach is aimed at critical islanding events, which are associated with low ΔP (specifically for $\Delta P < 5\%$) in conjunction with all possible combinations (deficit and excess) of active and reactive power imbalance. For those cases, the two classes are not linearly separable, as shown in Fig. 3.14. Using the proposed approach, those critical islanding events can be easily classified as demonstrated in Tables 3-V and 3-VI of section 3.4.4.

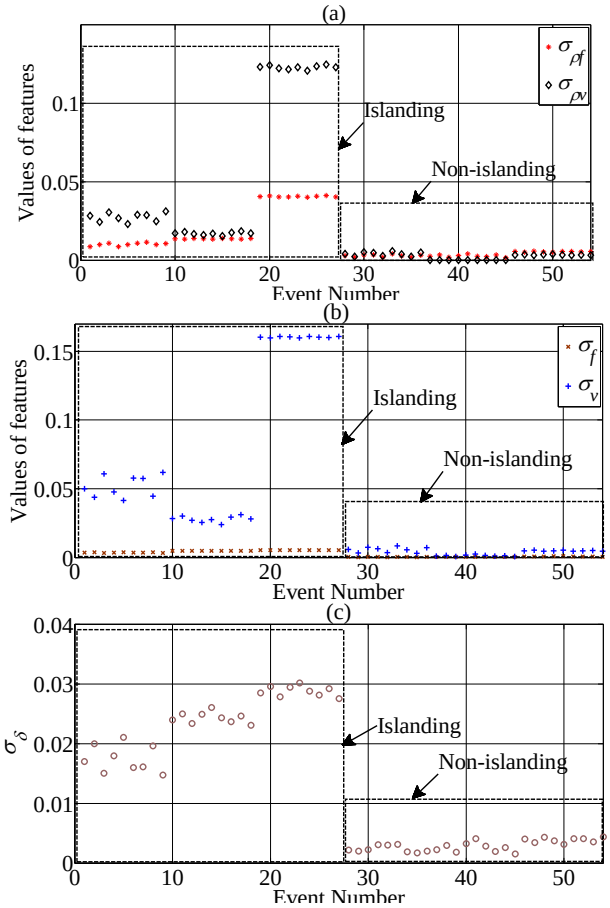

Fig. 3.12. Event-wise plot of features for 27 islanding and 27 non-islanding events of [14].

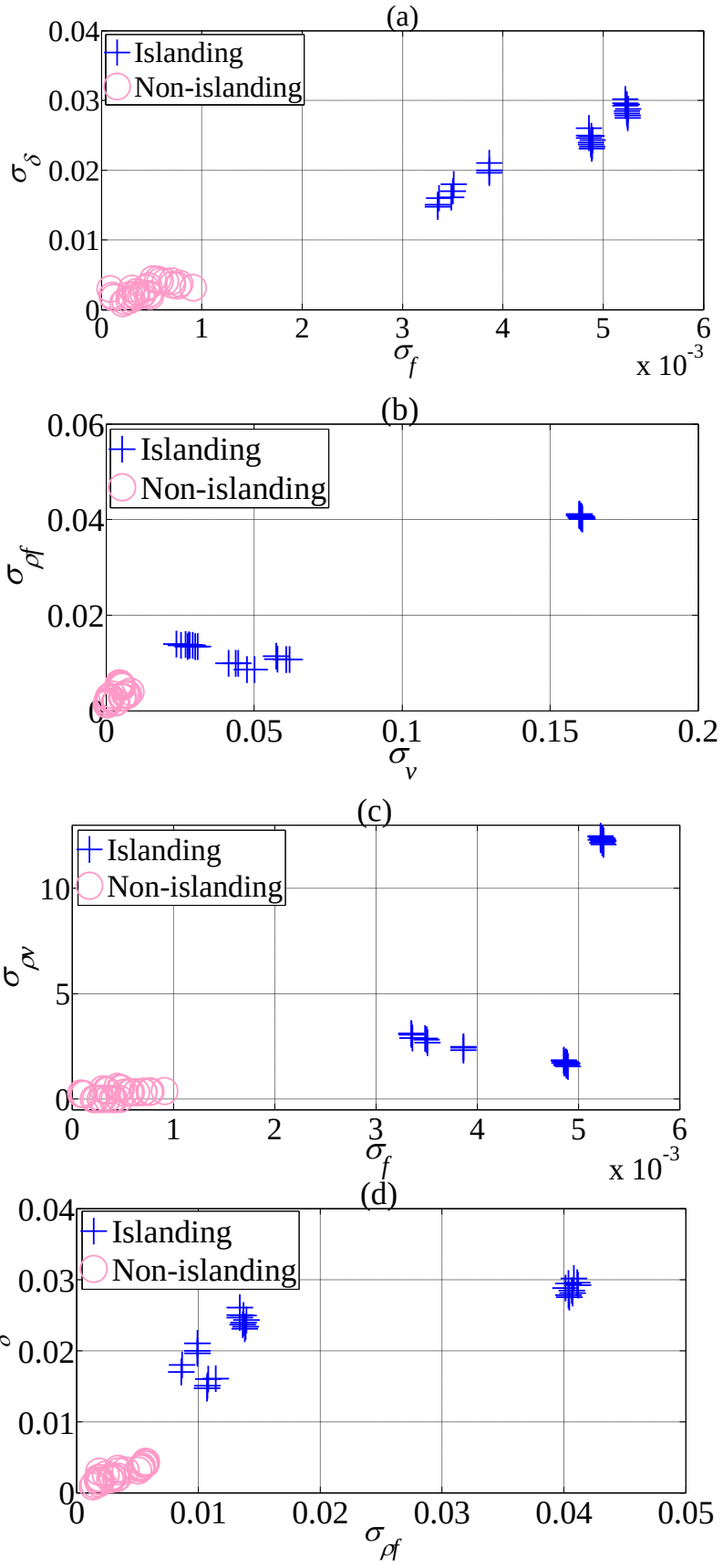

Fig. 3.13. Scatter plots of features for 54 events of [14]: (a) σ_δ versus σ_f, (b) $\sigma_{\rho f}$ versus σ_v, (c) $\sigma_{\rho v}$ versus σ_f, (d) σ_δ versus $\sigma_{\rho f}$.

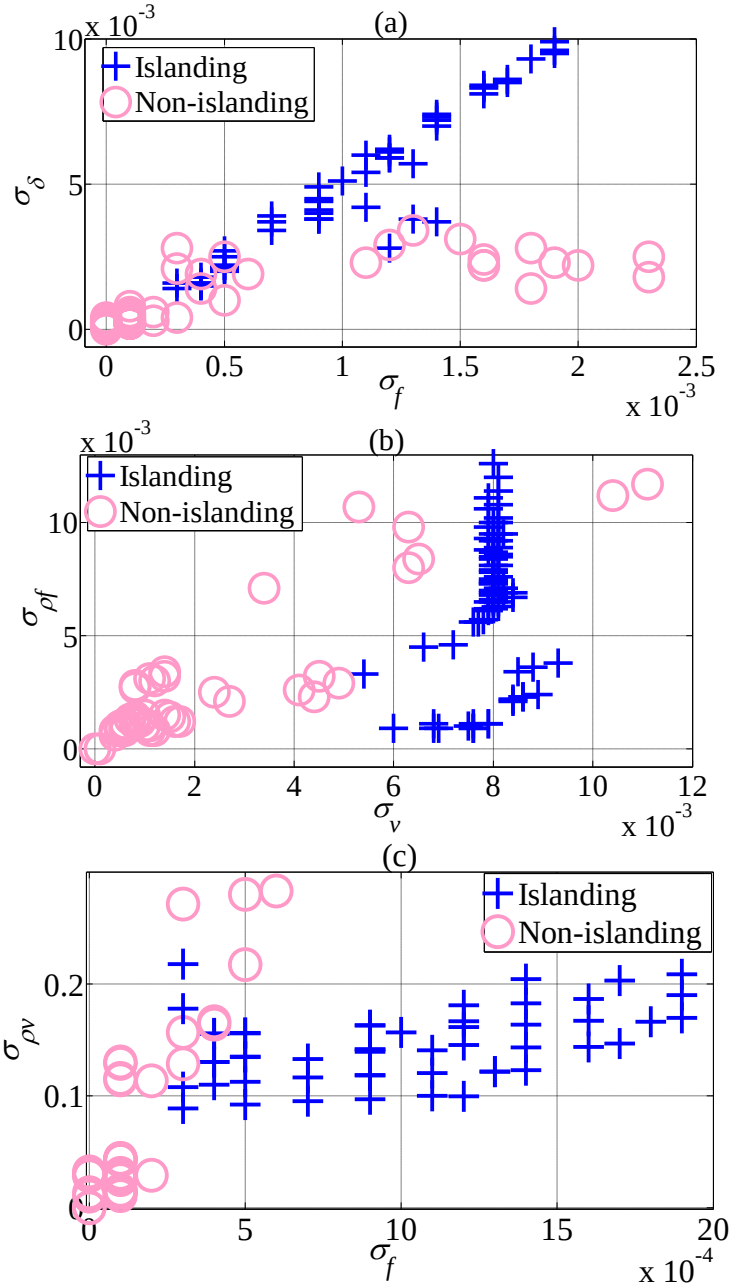

Fig. 3.14. Scatter plots of features for non-islanding and islanding events with ΔP < 5%: (a) σ_{δ} versus σ_f, (b) $\sigma_{\rho f}$ versus σ_v,(c) $\sigma_{\rho v}$ versus σ_f.

3.5 ASSESSING THE EFFECTIVENESS OF SVM BASED METHOD ON THE BASIS OF RESPONSE-TIME FOR ISLANDING DETECTION

In section 3.4, performance of the SVM based method is assessed considering the classification results obtained through the detection rate and false alarm for a significant amount of islanding and non-islanding events. All these performance analysis demonstrate the reliability of the proposed method in terms of accuracy of islanding detection with a minor risk of nuisance tripping (false alarm). However, islanding

detection tool has to be implemented in real-time application. Therefore, speed and response-time or detection-time of the SVM based algorithm embedded relay or SVMR (SVM based Relay) needs to be investigated. It should be noted that in this context, speed implies the processing speed of SVMR and it is expected to be fast, given the fact that the features extracted in real-time are passed through the trained SVM containing a small number of support vectors. And, response-time or detection-time of relay is defined as the time-delay, which starts soon after the onset of islanding and finishes as soon as islanding is detected. Therefore, detection-time of SVMR at the presence of all possible combinations of power imbalance scenarios is explored in this sub-section. To this end, the trained SVM, developed in section 3.4.4 using the training data of Table 3-II, will be used to assess the performance of SVMR. However, a total of 2,319 test events, which comprises of 1,848 islanding and 471 non-islanding events, are generated separately (see Table 3-IX) by simulating the test network of Fig. 3.9 to investigate the performance of SVMR on the basis of response-time for islanding detection.

TABLE 3-IX

GENERATED ISLANDING AND NON-ISLANDING EVENTS FOR THE ASSESSMENT OF SVMR ON THE BASIS OF RESPONSE-TIME

Scenarios	Islanding events	Non-islanding events
Scenario (*a*): Deficit ΔP and Deficit ΔQ	462	471
Scenario (*b*): Excess ΔP and Excess ΔQ	462	
Scenario (*c*): Excess ΔP and Deficit ΔQ	462	
Scenario (*d*): Deficit ΔP and Excess ΔQ	462	
Total	1848	471

The remaining part of this Section is structured as follows. Firstly, width of the data-window, which is used during feature extraction process, is optimally selected considering the Receiver Operating Characteristics (ROC) of the SVM classifier under different window-width. Then, a decision-rule is proposed considering the detection-time and reliability of islanding detection. Lastly, flowchart of the proposed SVMR and its performance is presented on the basis of detection-time. It should be noted that response-time and detection-time are same and will be used interchangeably in this Section.

3.5.1 Optimal selection of the width of Data-window for SVM based method

In section 3.4, a typical value of data-window-width ΔT was selected as 10 cycles for extracting the feature-vector required for classification of islanding and non-islanding events. Moreover, for the test data, the location of onset of islanding was a ground-truth;therefore, any feature-vector extracted from a data-window which contains the islanding inception anywhere was labelled as an islanding event. As a result, detection-time after the inception of islanding was not reflected in the classification results. However, if detection-time is considered, then width of data-window ΔT will play a vital role. If small ΔT is selected, the detection-time will be small which implies the fast response; but it increases the risk of false alarm along with poor detection rate. Large ΔT, on the contrary, increases the detection-time. Therefore, the performance of SVM classifier is assessed from the classification results of numerous events of Table 3-IX, by using the five features extracted through a data-window of ΔT width, as presented in section 3.3.2. The width of the data-window is optimally selected by conducting the SVM based classification, using the features extracted from the situations having window-width (ΔT) of one-cycle, five-cycle, eight-cycle and ten-cycle. For each situation, the threshold value of SVM classifier is varied gradually to obtain the Detection Rate (DR) and False Alarm (FA). Thus, the Receiver Operating Characteristics (ROC) curve, as shown in Fig. 3.15, is obtained.

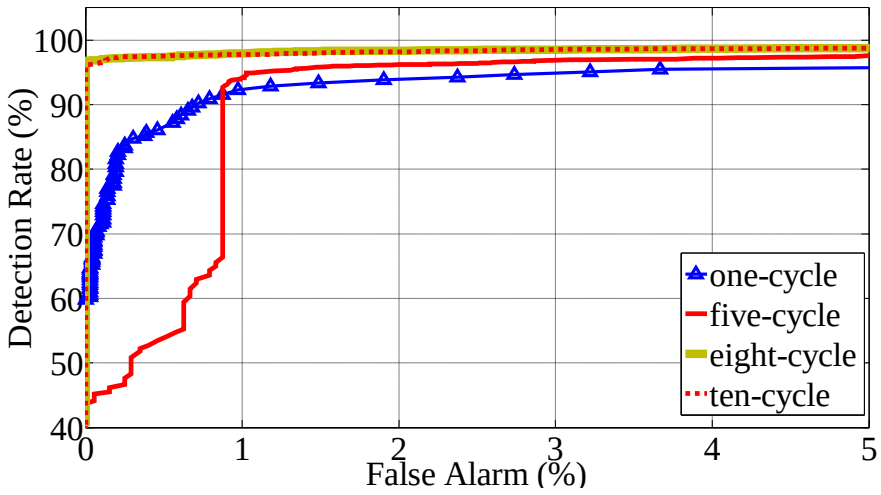

Fig. 3.15.ROC curve of the proposed approach for one-cycle, five-cycle, eight-cycle and ten-cycle data-window length.

As indicated in the ROC curve of Fig. 3.15, it is worth noting that the classifier's performance using eight-cycle and ten-cycle data-window are almost similar; and their

performances are comparatively better than the five-cycle and one-cycle data-window for FA $\leq$ 5%. However, considering the speed and performance, eight-cycle data-window has been selected as optimal data-window to investigate the performance of the proposed method on the basis of islanding detection-time.

3.5.2 Development of a Decision-rule for SVMR on the basis of Reliability and Response-time of islanding detection

In order to assess the performance of SVMR on the basis of reliability and response-time, features are needed to be extracted in real-time. Moreover, in practical situation, the inception-time of islanding is not known in advance. Therefore, to investigate the performance of the proposed SVMR on the basis of reliability and detection-time, sliding data-window of eight-cycle width is moved by a typical step-size of one cycle, and the features are extracted inside each window block or sample to classify the event as islanding or non-islanding. To accomplish this task, at first, features of the generated islanding and non-islanding events are considered with known event inception-time (ground-truth). Then eight-cycle data-window, which starts from 15 cycles prior to event inception, are moved by one cycle step-size until 20 cycles posterior of event inception-time is reached. Thus, 28 samples are obtained for each event including islanding and non-islanding. These samples are classified using the trained SVM and decisions are made based on the majority voting of the classification results of consecutive samples, for example, 3, 5, 7 or 9 samples. Moreover, the decision-rule based on the classification results of 1 sample, which does not require majority voting, is considered. Higher number of samples, e.g., 11 or higher, may also be investigated for the decision making process; however, it would require higher detection-time and, eventually makes it less practical option. It should be noted that odd number of samples are considered for the decision-rule, since it simplifies the decision making process; for example, 9 samples decision-rule requires at least 5 samples to be classified as islanding for the detection of an actual islanding event. Again, note that majority voting of 9 samples consider the previous consecutive 9 samples in descending order; and it implies that in time-domain, the rightmost end of eight-cycle data-window of 9^{th} sample specifies the instant of "event classification time" or detection-time (see Fig. 3.16). Decision-rule of 3, 5 and 7 samples follow the same technique as used for 9 samples' decision-rule.

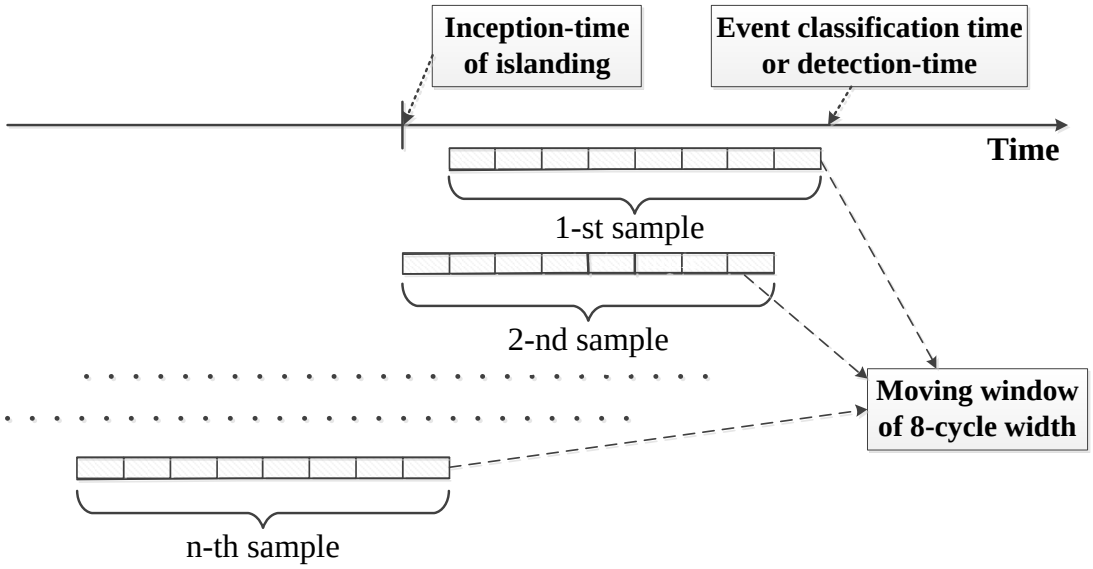

Fig. 3.16. Data-stream for illustrating the rule of majority voting applied in SVMR (SVM based Relay).

Fig. 3.17 illustrates the DR and FA of the proposed approach, using sliding data-window of eight-cycle width and applying the decision-rule based on the majority voting of the classification results of 9 samples, 7 samples, 5 samples, 3 samples and one sample. In Figs. 3.17(a) and (b), the *x*-axis is the "event classification time" or detection-time, which starts soon after the inception of islanding and non-islanding events, respectively. From Fig. 3.17(a) it is evident that one sample decision-rule can yield almost 100% DR within 100 ms of islanding inception. But, this decision-rule imposes the risk of 1% FA after 100 ms of event (non-islanding) inception; and it can reach to a maximum of 7% FA after 250 ms (see Fig. 3.17(b)). The decision-rule, obtained from the majority voting of 7 consecutive samples, gives the performance level in between 9 samples and 5 samples. Similarly, the decision-rule of 3 consecutive samples yields the performance level in between 5 samples and one sample, see Fig. 3.17 for illustration. In summary, if 200 ms is taken as an allowable detection-time, then keeping a trade-off between response-time/detection-time and the reliability as demonstrated by the classification results (i.e., DR and FA), decision-rule of 9 samples yield comparatively better performance than the decision-rule of 7, 5, 3 samples and one sample, see Figs. 3.17(a)-(b). Therefore, 9 samples decision-rule is selected and applied for the application of SVMR.

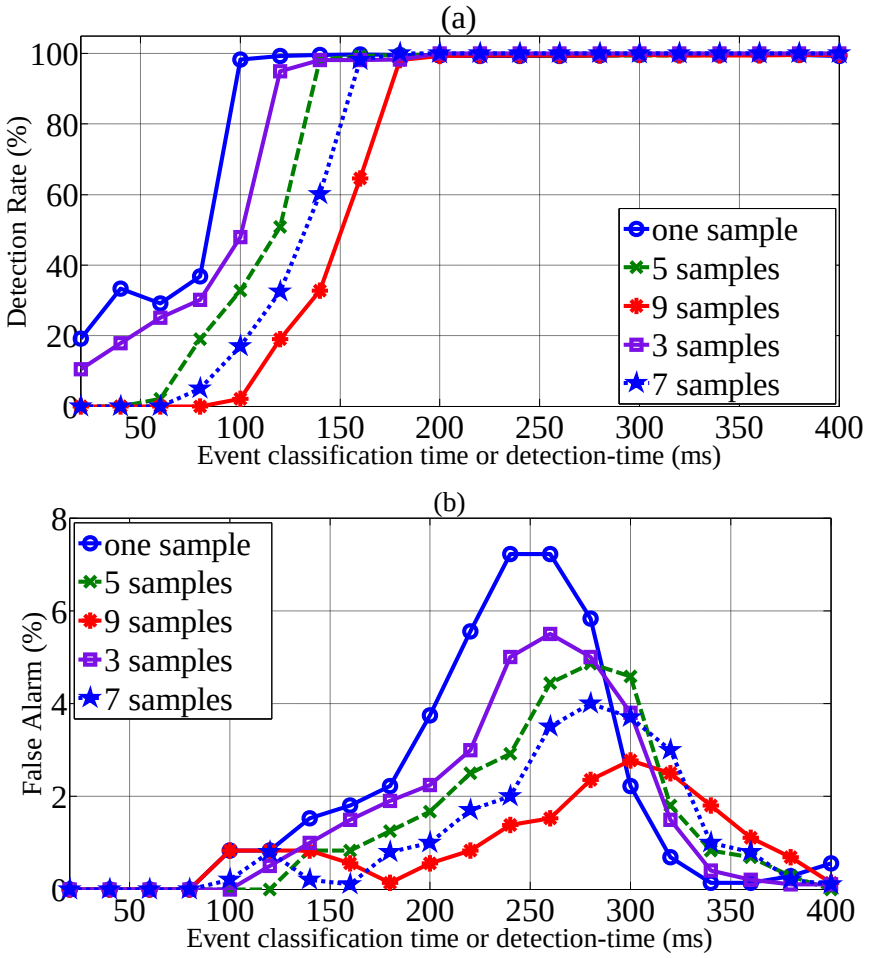

Fig. 3.17. Performance of the proposed SVM based approach, indicated by (a) Detection Rate and (b) False Alarm, using decision-rule of 9 samples, 7 samples, 5 samples, 3 samples and one sample.

3.5.3 Operational flowchart for the application of SVMR and its Performance Evaluation on the basis of detection-time

The operational steps, involved for islanding detection using SVMR, are shown in the flowchart of Fig. 3.18. It is to be noted that decision-rule, using 9 samples of majority voting, is applied in this flowchart. The whole process is summarized below.

1) Voltage (V), frequency (f) and rotor angle (δ) are extracted in real-time at the target DG location.
2) 5 features, which include standard deviation of V, f, δ, dV/dt and df/dt, are extracted in real-time considering 8 cycles of data-window.
3) Feature vector $\boldsymbol{X}(i)$ is formed as below:

$$\boldsymbol{X(i)}=\{\sigma_v,\sigma_f,\sigma_\delta,\sigma_{\rho v},\sigma_{\rho f}\}$$

where i represents the observation instant in terms of cycle of voltage signal.

4) $\boldsymbol{X}(i)$ is classified with trained SVM and result is obtained as $Y(i)=-1$ for islanding or $Y(i)=+1$ for non-islanding.

5) If $Y(i)=-1$, then decision of islanding is made for the *i*-th sample and a counter is set to count the number of islanding sample; if $Y(i)=+1$ then counter value is set to zero.

6) If 9 samples of decisions are not available, i.e., $i < 9$, then increasing i by 1, i.e., $i=i+1$, steps 1) to 5) are repeated 9 times until the decisions (islanding or non-islanding) of 9 samples are available.

7) When decisions of 9 samples are available, then the decision-rule using majority voting of previous consecutive 9 samples are applied. Therefore, event will be detected as islanding, if at least 5 out of 9 samples detect the event as islanding. And, a trip signal is sent to disconnect the DG. Otherwise, non-islanding event is detected and steps 1) to 7) are repeated from the next cycle by increasing i by 1 i.e. $i=i+1$.

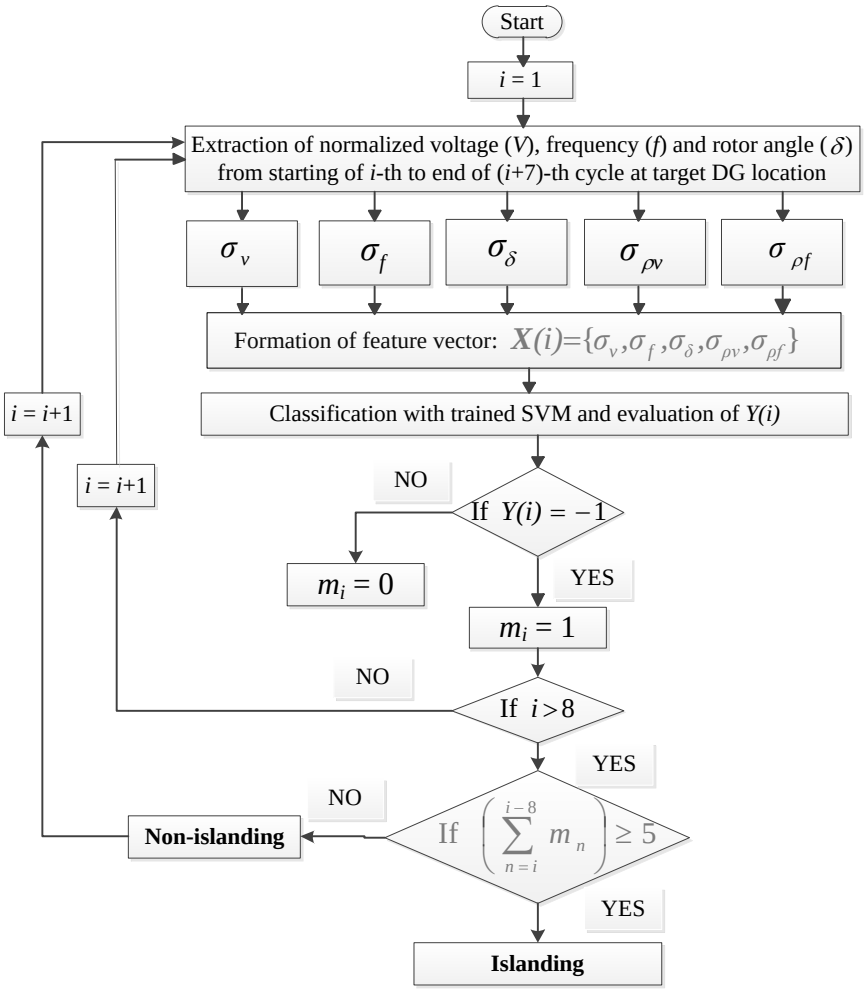

Fig. 3.18.Operational flowchart for islanding detection using SVMR.

Performance of proposed algorithm based SVMR is evaluated by considering the response-time of islanding detection. To this end, Fig. 3.19 illustrate the islanding detection-time of SVMR, during all possible combinations of power imbalance scenarios, which include deficit and excess of active power imbalance (ΔP) and reactive power imbalance (ΔQ) inside the islanded network. In Fig. 3.19, *y*-axis refers to "detection time" which is considered to be started soon after the onset of islanding. Islanding events, which are used for comparative analysis, are generated by keeping ΔP = 0.5%, 1%, 1.5%, ……, 99.9% (deficit or excess) in combination with ΔQ = 10%, 20%, …, 50% (deficit or excess) inside the islanded segment, by varying the load-generation profile and AVR setting of exciter model of synchronous generator as stated in section 3.4.2. Thus, the islanding events corresponding to four possible combinations of power imbalance scenarios are obtained. Then "detection time" for each event is determined using the SVMR. It should be noted that decision-rule of SVMR has employed 9 samples majority voting due to its reliability, as demonstrated in section 3.5.2. From Fig. 3.19 it is revealed that islanding detection time of SVMR falls within the range of 120 ms to 300 ms, which is much lower than the IEEE 1547-2003 recommended standard tripping times of 2 seconds.

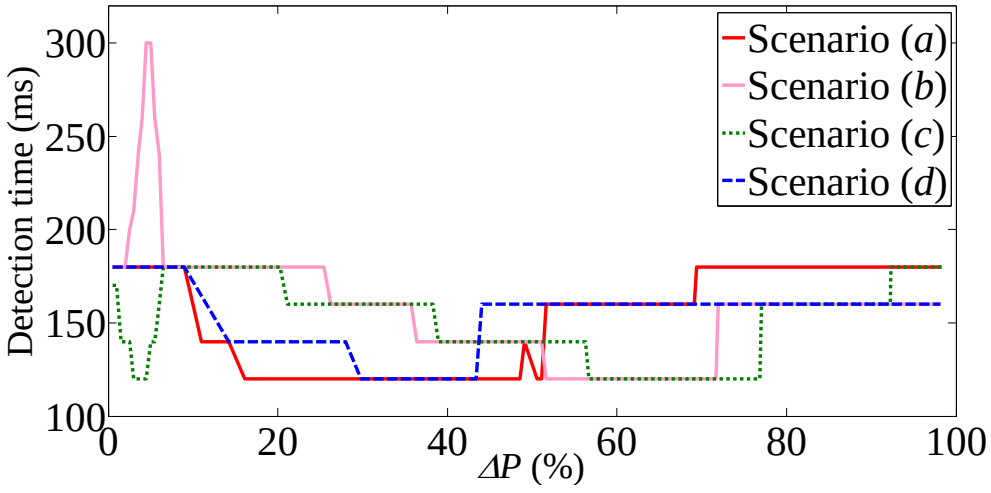

Fig. 3.19. Detection time of the proposed SVM based relay (SVMR) under four possible combinations of power imbalance: scenario (*a*) - deficit of ΔP and ΔQ, scenario (*b*) - excess of ΔP and ΔQ, scenario (*c*) - excess of ΔP and deficit of ΔQ, and scenario (*d*) - deficit of ΔP and excess of ΔQ.

3.6 DISCUSSIONS

Proposed multi-feature based SVM method can be applied in real networks provided that the SVM is trained with most expected circuit configurations and covering all

forms of power imbalance level for islanding events along with all possible types of non-islanding events which may occur in the system. Moreover, the speed of response of the algorithm embedded relay is expected to be fast, given the fact that the features extracted in real-time are passed through the trained SVM containing a small number of support vectors. Since the features of the proposed approach depend only on the terminal voltage parameters (amplitude, frequency, phase angle, etc.), retraining is not needed for this algorithm embedded relay, if minor changes occur in the system, e.g., if a new line or DG is installed, or a normally open point is shifted. To confirm this assertion, the trained SVM, which was kept unchanged, was tested with several test cases (A total of 640 islanding events) generated separately by eliminating one branch, two branches and shifting the open point in the test network of Fig. 3.9. The test results are presented in Table 3-VIII, which indicates that the performance deteriorates by only 1% in DR in comparison to the results shown in Tables 3-III and 3-IV. Numerically, in the proposed approach, active power imbalance of 0% to 100% and reactive power imbalance of 0% to 50% in the islanded system, were considered by varying the load and generation profiles (applying the procedure presented in [72]). For islanding cases, variations of active and reactive power imbalance, play a vital role in the variation of system parameters, such as, voltage, frequency, phase angle, etc. In the proposed approach, all possible combinations of active and reactive power imbalances were taken into account. Therefore, the trained SVM classifier is expected to be independent of network topology. Nevertheless, minor changes in the network can decrease the accuracy slightly (1% is obtained in the above test). But, this slight degradation of accuracy may be avoided, if larger volume of training data is considered. Therefore, retraining is not required if minor changes occur in the system provided that SVM is trained with larger volume of data covering all possible combinations of islanding and non-islanding events. However, for safe operation of the network with the distributed generation, if significant changes in network topology take place, for example, addition or disconnection of large DG unit and addition or disconnection of line that plays a significant role in the operation of the network, then the system must be remodelled to generate the training data and the SVM has to be retrained accordingly.

3.7 SUMMARY

This chapter presents a SVM based method for islanding detection of synchronous type DG units. The proposed approach employs multiple features which are extracted

from five network variables, and then, these features are fed to a support vector machine (SVM) classifier to classify the event as islanding or non-islanding. Several islanding and non-islanding events have been generated by simulating the practical scenarios in a test network of Australia. Supervised SVM classifier with linear, polynomial and Gaussian RBF kernels are used to train the selected features of these numerous islanding and non-islanding events. With the training data, grid search is carried out to fine-tune the kernel parameters (i.e. p and σ). Using the tuned parameters of trained SVM, islanding cases are tested and detected.Applicability of the proposed method is also tested on the basis of reliability and detection-time. To this end, an optimally selected sliding data-window is used; the optimal selection is conducted by analysing the Receiver Operating Characteristics (ROC) curve of the SVM classifier using different window-width. In summary, the contributions of this chapter can be summarized as follows:

- Islanding events at the presence of constant *Z*, constant *I* and constant *P* load along with all possible combinations of deficit and excess of active and reactive power imbalance, are detected by the proposed SVM based method with a high degree of accuracy, and the rate of false alarm is limited.

- Proposed method is scrutinized by testing several critical islanding events associated with low active power imbalance (for both, deficit and excess) in combinations with deficit and excess of reactive power imbalance.

- For the example test system, the proposed technique has successfully detected the islanding events for active power imbalance of 5% and above.

- The performance of SVM based relay (SVMR), which can be developed from the proposed algorithm, is evaluated as an effective tool. The evaluation index includes the reliability, which comprises the detection rate (DR), false alarm (FA), and the speed represented by the detection-time of islanding.

Chapter 4

COMPARATIVE STUDY BETWEEN CONVENTIONAL AND SVM BASED RELAYS FOR ISLANDING DETECTION

4.1 INTRODUCTION

Due to the rapid increase in the penetration of distributed generation (DG) in the distribution networks, the correct operation of islanding or detection of loss-of mains (LOM) is an important requirement. Conventional relays, such as, Vector Surge (VS) and ROCOF (rate-of-change-of-frequency) relays are usually used to detect islanding; however, there is a Non-Detection Zone (NDZ) wherein islanding incidents are undetectable by these relays.

Now-a-days, utilities have raised their voice over the issue related to the false operation or malfunctioning of VS and ROCOF relays, which is commonly employed as LOM detection method. Normally, setting of VS and ROCOF relays is established by the generators' manufacturers and the utility guidelines for interconnecting distributed generation units. Typically, this relay-setting is kept within the range of 0.1 to 1.2 Hz/s for ROCOF and 2° to 20° for VS relays [104, 110]. Tuning these relay-setting at very small value, e.g., close to 0.1 Hz/s for ROCOF or 2° for VS relay, allows them to operate during small frequency variations in the power system, which may violate the IEEE guidelines [2] by creating nuisance tripping during normal events of the power system. To avoid this violation and nuisance tripping, these relays can be set at larger value; but this may cause a failure of islanding detection within the pre-specified time for an islanded network with small power imbalance. As a result, Non-detection Zone (NDZ), wherein VS and ROCOF relays fail to detect islanding, becomes larger. In short, the NDZ of VS and ROCOF relays and the incidents of nuisance tripping, associated with islanding detection, are a function of relay-setting.

This Chapter presents the performance of VS and ROCOF relays in islanding detection; the concept of NDZ is used for this performance study. An analytical formula is developed for determining the NDZ of VS and ROCOF relays. Extensive simulation is conducted to verify the formula, as well as to investigate the boundary limit of NDZ under different types of voltage-dependent loads and considering all possible combinations of power imbalance scenarios. Moreover, performance of VS and ROCOF relays is compared with the proposed SVM based approach using the performance indicators, namely, detection rate (DR) and false alarm (FA). Using the concept of detection-time, performance of VS and ROCOF relays is also compared with the SVM based relay (SVMR). A test network derived from Australian electricity systems is simulated to generate a large number of credible islanding and non-islanding events. In the testing phase, all possible combinations of deficit and excess of active and reactive power imbalance scenarios, which may exist during the period of islanding, are considered.

The remaining part of the Chapter is organised as follows. In Section 4.2, the basic operating principle of VS relay is discussed; an analytical formula is presented for determining the boundary limit of NDZ of VS relay for islanding detection. Moreover, extensive simulation is conducted to investigate the boundary limit of NDZ under different types of voltage-dependent loads, which include constant impedance, constant current and constant power loads; during these investigations all possible combinations of deficit and excess of active and reactive power imbalance scenarios are considered as well. In Section 4.3, the boundary limit of NDZ for ROCOF relay is investigated under different network conditions. In Section 4.4, a credible number of islanding and non-islanding events, generated by simulating a test network of Australia, are tested to investigate the performance of VS and ROCOF relays with variable relay-setting and detection time. The comparative analysis of VS and ROCOF relays with SVM based approach is carried out in Section 4.5. Section 4.6 concludes the Chapter.

4.2 BOUNDARY LIMIT OF NON-DETECTION ZONE OF VECTOR SURGE RELAY

This Section investigates the boundary limit of non-detection zone (NDZ) of vector surge (VS) relay applied in islanding detection. To do so, performance curve of the relay is analysed using the concept of NDZ. Section 4.2.1 describes the basic operating principle of VS relay followed by the derivation of an analytical formula of NDZ in

Section 4.2.2. Detailed simulation is conducted in Section 4.2.3 to verify the formula as well as to investigate the boundary limit of NDZ considering the impacts of load dynamics and reactive power imbalance. During this simulation study, all possible combinations of active and reactive power imbalance scenarios (deficit and excess), are taken into account. Considering all aforementioned conditions, the pessimistic boundary limit of NDZ for VS relay is achieved.

4.2.1 Operating principle of VS Relay

Commercial vector surge relay measures the time-duration of an electrical cycle and starts a new measurement at each rising zero-crossing points of the terminal voltage. The current cycle duration of the measured waveform is compared with the previous one (reference cycle). In an islanding condition, the cycle duration is found to be either longer or shorter, depending on if there is a deficit or excess of power in the islanded subsystem, see Fig. 4.1. This change of the cycle duration yields a proportional change of the terminal voltage angle $\Delta\delta$, which is fed to the vector surge relay as input parameter. If $\Delta\delta$ exceeds a pre-determined threshold angle α, a trip signal is sent to the circuit breaker immediately. Normally, vector surge relay permits this threshold value to be tuned in the range from 2° to 20° [104]. VS relay also uses a block function by minimum terminal voltage V_{min}. If terminal voltage falls down to V_{min}, the trip signal from the vector surge relay is blocked. This is performed to avoid, for example, the activation of the VS relay during short-circuit or generator start-up conditions.

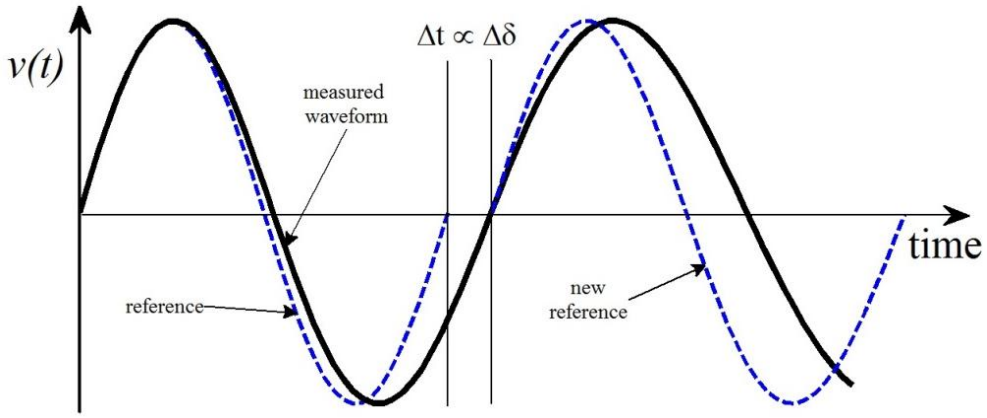

Fig. 4.1.Illustration of cycle by cycle measurement of terminal voltage for the operation of vector surge relay.

4.2.2 Analytical Formula for determining the Non-detection Zone of VS Relay

For VS relays, the critical power imbalance is the active power imbalance for which the relay can marginally detect islanding; for any smaller value, it is unable to perform within a permissible timeframe. The zone below the critical power imbalance is referred to as the Non-Detection Zone [72]. Critical active power imbalance (ΔP_{vs_crit}) acts as a separation boundary between detection and non-detection zone of VS relays. This separation boundary also indicates the boundary limit of NDZ. Therefore, the formulation of the boundary limit of NDZ is carried out by using the concept of critical active power imbalance.

Figure 4.2 illustrates a network with a synchronous generator (SG) type DG operating in a grid-connected mode. During islanding, the load is fed from the DG source only. Therefore, the boundary of the NDZ of the VS relay can be determined by analysing the operation of the SG. The dynamic behaviour of the synchronous generator can be characterized using the machine swing equation [104]:

$$\frac{2H}{\omega_0}\frac{d^2\delta}{dt^2} = P_m - P_l = -P_S = \Delta P \tag{4.1}$$

where H is the generator inertia constant, ω_0 is the synchronous speed, and δ is the rotor angle with respect to the synchronously rotating reference frame. Since δ varies with time during the transient period of islanding, the rotor speed ω_r can be presented as:

$$\omega_r = \omega_0 + \frac{d\delta}{dt} \tag{4.2}$$

Assuming t_0 is the onset of islanding, at $t = t_0$, $\omega_r = \omega_0$ and hence $d\delta/dt = 0$. Taking this initial condition into consideration and integrating equation (4.1) twice, yields the rotor angle δ at time t:

$$\delta(t) = \delta_0 + \frac{\omega_0 \Delta P}{4H}\left(t - t_0\right)^2 \tag{4.3}$$

where δ_0 is the rotor angle at steady state prior to islanding.

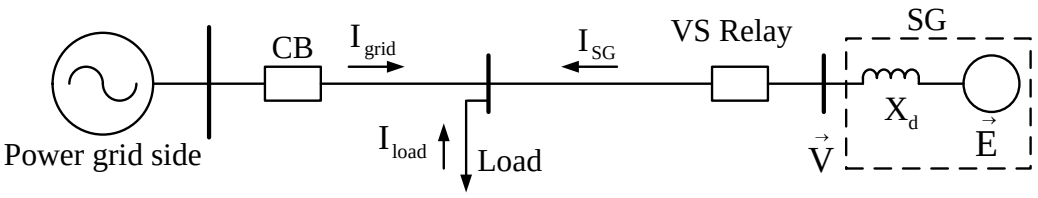

Fig. 4.2.A synchronous type DG operating in a grid-connected mode.

For VS relay, the difference of δ within each cycle interval is measured and compared with VS relay setting α. The VS relay is triggered when the difference between rotor angles ($\Delta\delta$) within any of the cycle intervals crosses the relay setting α. Figure 4.3 illustrates an islanding situation where the variation of the terminal voltage $v(t)$ is shown in Fig. 4.3(a), and the rotor angle $\delta(t)$ is presented in Fig. 4.3(b). A moving window of fixed width ΔT seconds in duration is proposed to calculate the change in rotor angle.

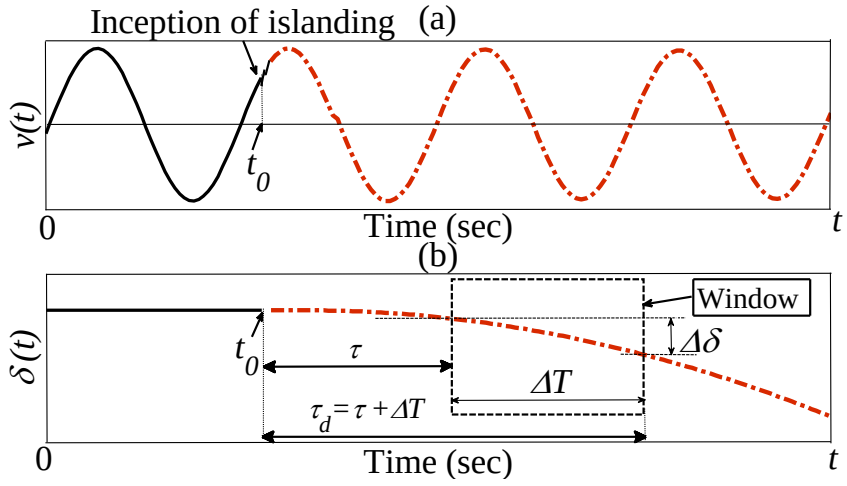

Fig. 4.3. Pre-islanding (solid line) and post-islanding (dash-dot line): (a) terminal voltage $v(t)$ at SG (Synchronous Generator) end (b) rotor angle $\delta(t)$ with moving window to detect rotor angle change.

Let $\Delta\delta(t)$ denote the rotor angle change between t and $(t+\Delta T)$. Using (4.3), the rotor angle change is obtained as:

$$\Delta\delta(t+\Delta T)=\delta(t+\Delta T)-\delta(t)=\frac{\omega_0\Delta P}{4H}\left(2\tau\Delta T+\Delta T^2\right) \tag{4.4}$$

where $\tau = t - t_0$. An islanding event is detected if $\Delta\delta(t)$ exceeds the relay setting α, which gives

$$\frac{\omega_0\Delta P}{4H}\left(2\tau\Delta T+\Delta T^2\right)\le\alpha \tag{4.5}$$

where ΔP is negative considering load is higher than generation during islanding, and

$\alpha$is negative due to proposed moving window based method of detecting $\Delta\delta$ with negative ΔP. Using the expression of total detection time τ_d ($\tau_d = \tau + \Delta T$), expression (4.5) can be re-written as:

$$\frac{\omega_0 \Delta P}{4H}\left(2\tau_d \Delta T - \Delta T^2\right) \leq \alpha \tag{4.6}$$

Taking the equality constraint of (4.6) and setting ΔT = 0.02 sec (i.e. one cycle in 50 Hz system), Fig. 4.4 (i.e. τ_d versus ΔP) is obtained for a specific relay setting. For an allowable detection time (τ_d), the critical power ΔP_{vs_crit}, which separates detection and non-detection zone, is indicated by the vertical dotted line.

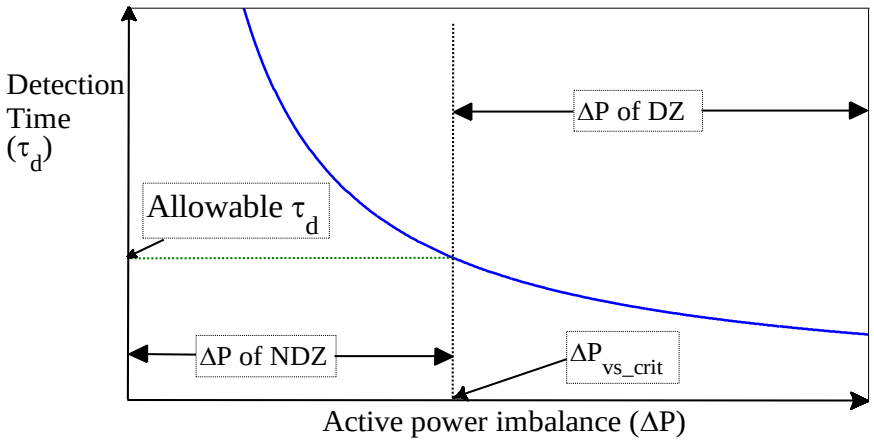

Fig. 4.4.Islanding detection time of VS relay as a function of ΔP; and ΔP_{vs_crit} or boundary limit of NDZ separating detection zone (DZ) and NDZ.

To find the minimum absolute value of ΔP, i.e. critical active power imbalance (ΔP_{vs_crit}) of VS relay, a window width (ΔT) of 0.02 second is considered, as it is the period of fundamental frequency of 50 Hz voltage signal. So, by putting ΔT = 0.02 sec and τ_d = 0.2 sec in (4.6), ΔP of VS relay can be obtained with specific relay setting α. Thus, as an example, for absolute value of α = 10° and H = 1.5, the minimum absolute value of ΔP, i.e. ΔP_{vs_crit} of VS relay can be obtained as 0.4386 pu which indicates the boundary limit of NDZ.

Constant power load model is assumed for developing the expression given in (4.6). To extend it in a general form, the load dynamics and power imbalance factor are taken into consideration as reported in [104]; thus, the generalized expression of critical active power imbalance for constant power (constant P), constant impedance (constant Z), or constant current (constant I) load can be obtained from the following:

$$\Delta P = \Delta P_0^{1/PF} \tag{4.7}$$

where ΔP_0 is the initial power imbalance value at the instant of islanding, ΔP denotes the final active power imbalance for constant *Z*, constant *I* or constant *P* load; and *PF* is a factor which is in the range of $1.2 \geq PF \geq 0.8$ considering average power imbalance variation of ± 20%. Empirical value of *PF* is selected as 1, 0.8 and 0.9 for constant *P*, constant *Z* and constant *I* load respectively when there is a deficit of electric power [104]. Thus, by replacing ΔP given in (4.6) with $\Delta P_0^{1/PF}$ given in (4.7), the absolute critical active power imbalance for constant *P*, constant *I* and constant *Z* load can be obtained as 0.4386 pu, 0.4763 pu and 0.5172 pu respectively. Hence, boundary limit of NDZ for the VS relay corresponds to the boundary when active power imbalance within the islanded network falls down to 43.86%, 47.63% and 51.72% for constant *P*, constant *I* and constant *Z* load respectively.

4.2.3 Simulation study to investigate the pessimistic boundary limit of NDZ of VS relay

Four possible combinations of power imbalance scenarios, as presented in Section 3.4.2 of Chapter 3, may exist during the period of islanding [13]. For each scenario, pessimistic boundary limit of NDZ is defined in terms of maximum numerical value of critical active power imbalance for a typical detection time. Firstly, in Section 4.2.3.1, scenario (*a*), i.e., deficit of ΔP (active power imbalance) and deficit of ΔQ (reactive power imbalance), is considered while investigating the pessimistic boundary limit of NDZ. To this end, performance of VS relays under different load-types and different range of reactive power imbalance are explored. Then, scenario (*b*) – excess of ΔP and excess of ΔQ, scenario (*c*) – excess of ΔP and deficit of ΔQ, and scenario (*d*) –deficit of ΔP and excess of ΔQ, are investigated in Section 4.2.3.2.

4.2.3.1 *Influence of Load Types and Reactive Power Imbalance on NDZ*

The analytical expression (4.7) reveals that load-types have significant impact on the boundary limit of NDZ for VS relay. In this sub-section, a time-domain simulation is carried out to investigate the impact of load-types and reactive power imbalance (ΔQ) on NDZ. Scenario (*a*) is considered during this simulation study.

Fig. 4.5 shows the single diagram of the test system used for the simulation study. In Fig. 4.5, 132 kV, 50 Hz, sub-transmission system with short-circuit level of 1500 MVA feeds a 33 kV distribution system through a 132/33 kV transformer. Three phase model of all network components are used. Two pi-section distribution lines have been

modelled with each 10 km long. Synchronous generator (SG) based DG is embedded with automatic voltage regulator (AVR) and it is used for this study. Islanding condition has been simulated by opening the circuit breaker (CB) at 1.5 sec. The simulation procedures for the variation of active and reactive power imbalance are adopted from [72]. Thus, repeated dynamic simulation is conducted with different ranges of active and reactive power imbalance for different load-types, which include constant impedance, constant current and constant power loads. Then the detection time for specific relay setting (i.e. α = 10°) is obtained. The power imbalance corresponding to the detection time of 200 ms [13] is considered as critical active power imbalance; for VS relay, it is denoted as ΔP_{vs_crit}.

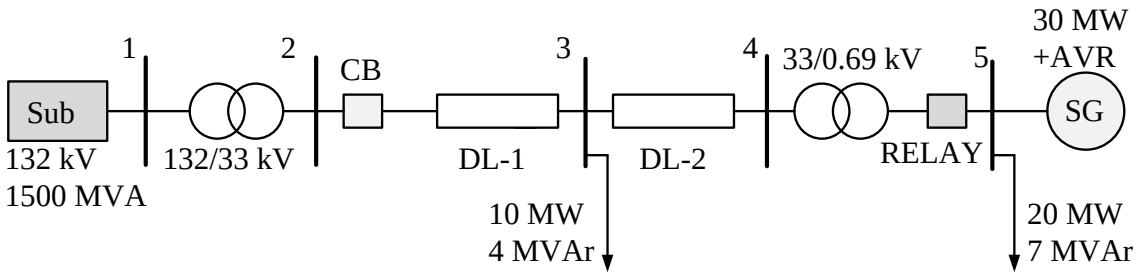

Fig. 4.5.A five-bus network with synchronous type DG and conventional relay.

From the simulation results, it is observed that ΔQ has negligible impact on the boundary limit of NDZ for constant P load; ΔP_{vs_crit} is obtained as 45.8% for different ranges of ΔQ. But the influence of ΔQ on boundary limit of NDZ is quite evident for constant Z and constant I load, as shown in Fig. 4.6. From Fig. 4.6, it can be observed that the pessimistic boundary limit of NDZ is obtained by keeping the reactive power imbalance at its maximum. In this study, a reactive power imbalance of 50% has been considered as the maximum reactive power imbalance, since during electric system islanding the system voltage may collapse whenever the reactive power imbalance exceeds 50% [111]. Thus, for VS relay (α = 10° and detection time = 200 ms), the boundary limit of pessimistic NDZ is indicated by the active power imbalance level of 66%, 58% and 45.8% for constant Z, constant I and constant P load respectively, see Fig. 4.6.

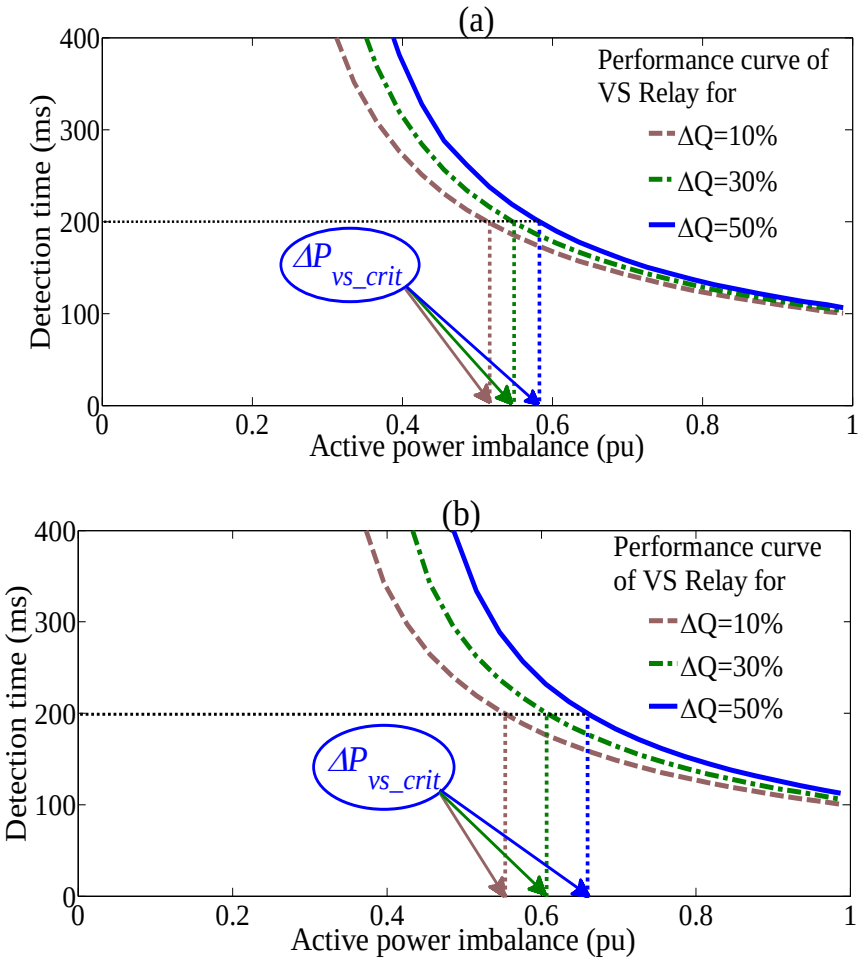

Fig. 4.6. Impact of ΔQ on ΔP_{vs_crit} or boundary limit of NDZ of VS relay (relay-setting = 10°) for (a) constant current and (b) constant impedance load.

4.2.3.2 *Influence of active and reactive power imbalance scenarios on NDZ*

In Section 4.2.3.1, scenario (*a*), i.e., the scenario consisting of a deficit of active and reactive power imbalance in the islanded system, is considered for investigating the boundary-limit of NDZ. It concludes that the pessimistic boundary-limit of NDZ is obtained for constant *Z* load. Therefore, in this sub-section, the remaining three scenarios, i.e., scenarios (*b*), (*c*) and (*d*), are investigated at the presence of constant *Z* load to obtain the pessimistic boundary-limit of NDZ.

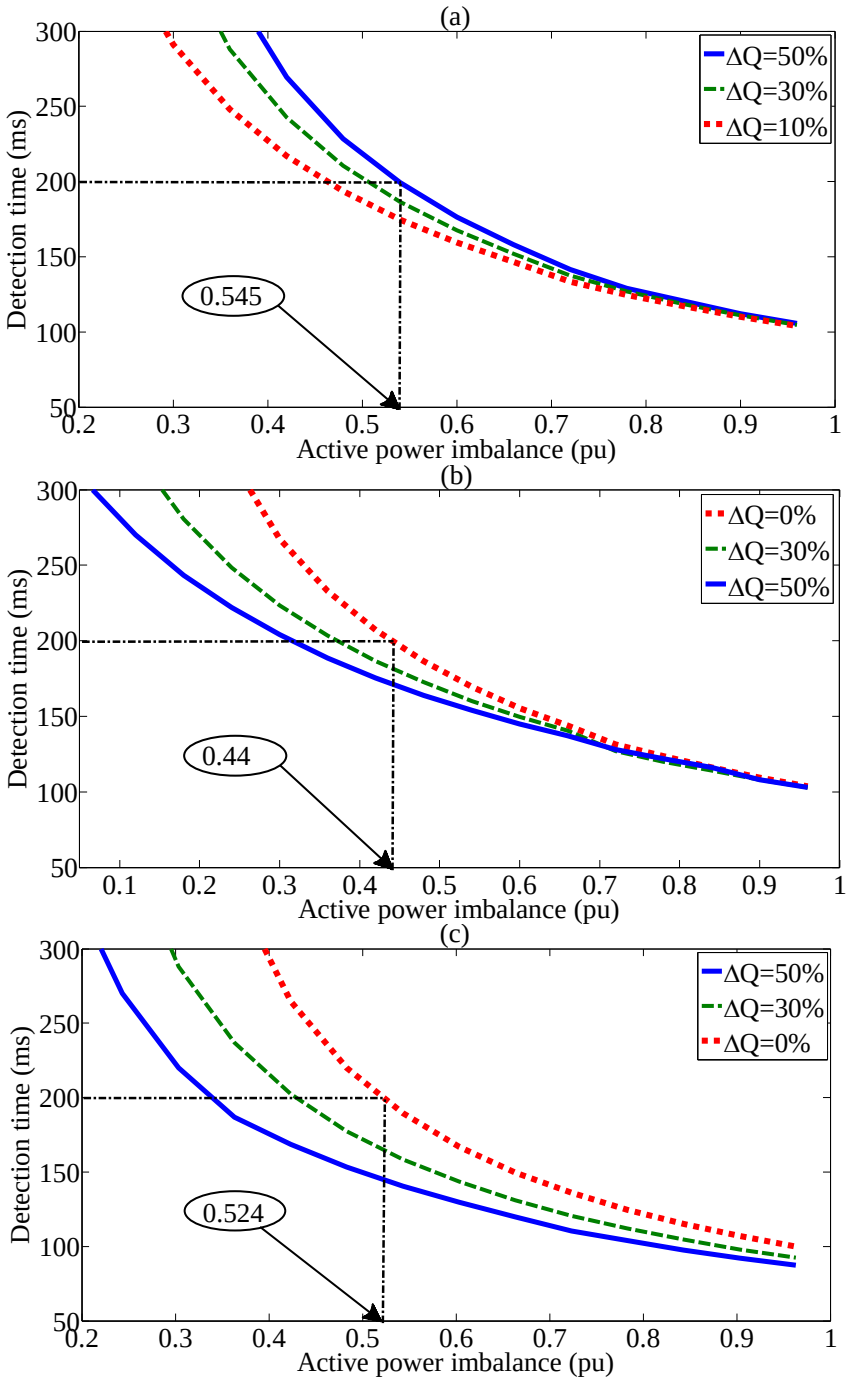

Fig. 4.7. Illustration of pessimistic boundary limit of NDZ of VS relay (relay-setting= 10°) under power imbalance conditions: (a) excess of ΔP and excess of ΔQ, (b) excess of ΔP and deficit of ΔQ, and (c) deficit of ΔP and excess of ΔQ.

Varying ΔP (deficit or excess) and ΔQ (deficit or excess) on the test system of Fig. 4.5, detection times for scenarios *(b)-(d)* are obtained. Thus, the test results for scenarios (*b*), (*c*), and (*d*), are acquired and they are illustrated in Figs. 4.7 (a), (b), and (c), respectively. Fig. 4.7 (a) shows that for scenario (*b*), pessimistic boundary limit of NDZ or maximum numerical value of ΔP_{vs_crit} is achieved when ΔQ *i*s kept at its maximum

value, i.e., ΔQ = 50%. However, for scenarios (*c*) and (*d*), the pessimistic boundary limit of NDZ is obtained at ΔQ = 0%, as shown in Figs. 4.6 (b)-(c). In summary, the pessimistic boundary-limit of NDZ of VS relay under four possible power imbalance scenarios are presented in Table 4-I.

TABLE 4-I

PESSIMISTIC BOUNDARY LIMIT OF NDZ OF VS RELAY UNDER FOUR POWER IMBALANCE SCENARIOS (RELAY-SETTING = 10° AND DETECTION TIME = 0.2 SECONDS)

Power imbalance scenarios	ΔQ (%)	ΔP_{vs_crit} (%)
(*a*): Deficit ΔP and deficit ΔQ	50	66
(*b*): Excess ΔP and excess ΔQ	50	54.5
(*c*): Excess ΔP and deficit ΔQ	0	44
(*d*): Deficit ΔP and excess ΔQ	0	52.4

4.3 BOUNDARY LIMIT OF NON-DETECTION ZONE OF ROCOF RELAY

In this Section, boundary limit of non-detection zone (NDZ) for ROCOF relay is investigated. To this end, the performance-curves specifying the NDZ, is analysed which in turn evaluates the performance of the relay for islanding detection. Section 4.3.1 describes the basic operating principle of ROCOF relay; using the concept of NDZ, an analytical formula is developed in Section 4.3.2. Extensive simulation is conducted in Section 4.3.3 to verify the formula as well as to investigate the behaviour of ROCOF under different types of voltage-dependent loads, which include constant impedance, constant current and constant power loads. During this performance study, all possible combinations of active and reactive power imbalance scenarios (deficit and excess), are taken into account. Considering all aforementioned conditions, the pessimistic boundary limit of NDZ for ROCOF relays is achieved.

4.3.1 Operating principle of ROCOF Relay

A simplified diagram of a distribution network is illustrated in Fig. 4.8 to describe the operating principle of ROCOF relay. A synchronous generator (SG) based DG, embedded with ROCOF relay, is allowed to operate while connected with upstream side. Disconnection of DG (By opening the circuit breaker of Fig. 4.8) from the upstream grid side, due to faults or any other disturbances, results in islanding.

Consequently, SG becomes the only source to feed the loads in the formed island. Therefore, a power imbalance between load and generation occurs due to the presence of the power mismatch, which was provided by the grid to the DG or injected into the grid from the DG, prior to the formation of islanding. This power imbalance causes the system frequency to vary dynamically, and this change of frequency is proportional to the power imbalance inside the islanded segment. This implies that the islanding events with low power imbalance may not be detected within a pre-specified time if change of frequency is considered. Therefore, to accelerate the detection process, rate of change of frequency is selected as a decisive threshold for ROCOF relays.

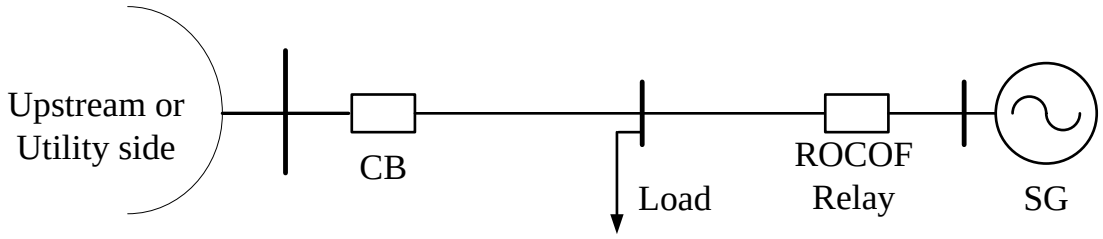

Fig. 4.8. A simplified diagram of a network with synchronous type DG and ROCOF relay.

For ROCOF relays, rate-of-change-of-frequency is calculated within a measuring window, typically 2 cycles to 40 cycles of width [110]. The obtained "rate-of-change-of-frequency" signal is then passed through a low-pass filter $1/(T_a s+1)$, see Fig. 4.9, to eliminate the high-frequency transients. The filtered "rate-of-change-of-frequency" signal is compared with a pre-specified relay-setting λ; if it exceeds λ, a trip signal is sent. Typically, λ lies in the range of 0.1 to 1.2 Hz/s. To avoid the relay tripping during generator start-up, the generator's terminal voltage is also monitored and if it falls below a specified level V_{min}, then the ROCOF relay is not allowed to operate (see Fig. 4.9).

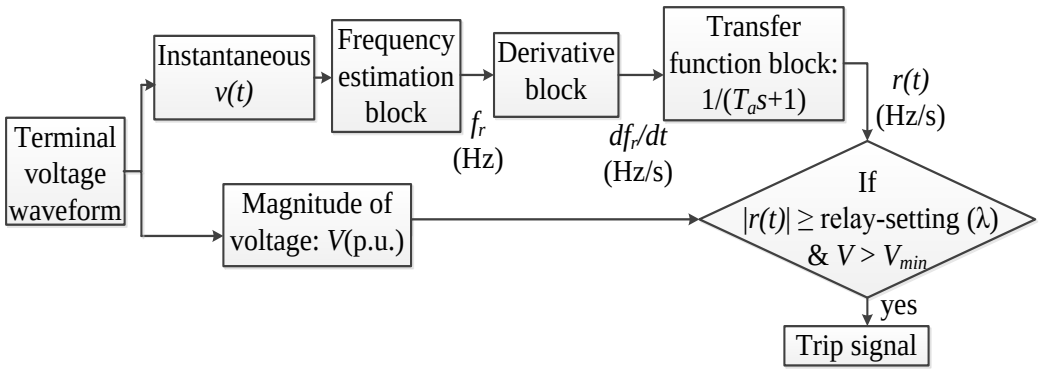

Fig. 4.9. A simplified schematic diagram illustrating the operation-algorithm of ROCOF relays.

4.3.2 Non-detection Zone of ROCOF Relay

Non-detection Zone (NDZ) of ROCOF relays can be defined by using the concept of critical power imbalance, which is considered to be the minimum active power imbalance required in a formed island so that ROCOF relay can detect islanding within a pre-specified time and relay-setting [13]. The separation between detection and non-detection zone is marked by the critical active power imbalance, as shown in Fig. 4.10. In order to develop the analytical expression of critical power imbalance of ROCOF relay, the machine swing equation (4.1) and the rotor speed ω_r, as shown in (4.2), is taken into account. From (4.2), the frequency f_r at time t is obtained as

$$f_r = f_0 + \frac{f_0 \Delta P}{2H}(t - t_0) \tag{4.8}$$

where$f_0$andf_r represents the frequency in Hz. Differentiating (4.8) with respect to t, the rate-of-change-of-frequency is given by

$$\frac{df_r}{dt} = \frac{f_0 \Delta P}{2H} \tag{4.9}$$

The obtained rate-of-change-of-frequency, as given in (4.9), is passed through the first-order transfer function block, see Fig. 4.9. Moreover, in (4.9) the parameters f_0 and$H$ are constant terms; ΔP is also constant for constant power load model. Thus, in the Laplace domain the output of transfer function block can be presented as

$$R(s) = \frac{f_0 \Delta P}{2Hs(T_a s + 1)} \tag{4.10}$$

Applying inverse Laplace transform in (4.10) yields the response in the time-domain

$$r(t) = \frac{f_0 \Delta P}{2H}\left(1 - e^{-t/T_a}\right) \tag{4.11}$$

Considering the time delay of Δt, which occurs due to the measuring window applied in calculating the rate-of-change-of-frequency, the allowable detection time τ_d becomes

$$\tau_d = t + \Delta t \tag{4.12}$$

Thus, from (4.11) and (4.12), *r(t)* can be expressed as

$$r(t) = \frac{f_0 \Delta P}{2H}\left(1 - e^{-(\tau_d - \Delta t)/T_a}\right) \tag{4.13}$$

Now, the output signal *r(t)* is monitored by the ROCOF relay; if *r(t)* exceeds the pre-

specified relay-setting λ, then the relay triggers. Thus, the condition for triggering the relay can be presented as

$$\frac{f_0 \Delta P}{2H}\left(1-e^{-(\tau_d-\Delta t)/T_a}\right) \geq \lambda \tag{4.14}$$

The terms ΔP and λ can be both positive or negative depending on the excess and deficit of active power imbalance in the formed island. Moreover, the relay setting λ should be less than the steady-state value, $\frac{f_0 \Delta P}{2H}$, as obtained from (4.11). Therefore, considering the equality constraint in (4.14) with the condition: $\lambda < \frac{f_0 \Delta P}{2H}$, τ_d as a function of ΔP becomes

$$\tau_d = \Delta t - T_a ln\left(1-\frac{2H\lambda}{f_0 \Delta P}\right) \tag{4.15}$$

Equation (4.15) defines the performance curve of ROCOF relay, which is illustrated in Fig. 4.10. For an allowable detection time τ_d and relay-setting λ, the critical power imbalance ΔP_c, which defines the non-detection zone, is marked in Fig. 4.10.

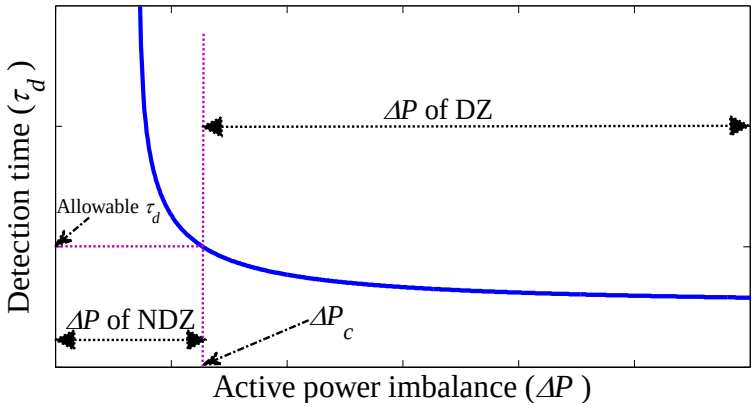

Fig. 4.10.Performance curve of ROCOF relays represented by detection time (τ_d) versus active power imbalance *(ΔP)*; and critical power imbalance ΔP_c separating detection zone (DZ) and NDZ.

Numerically, for τ_d = 0.2 s and λ = 1.2 Hz/s, the value of ΔP_c for ROCOF relay can be obtained from (4.15). Thus, as an example, selecting the parameters as Δt = 0.1 s, T_a = 0.12 s, H = 1.5, and f_0 = 50 Hz, ΔP_c yields 12.7%, which indicates the boundary limit of NDZ of ROCOF for a relay-setting of 1.2 Hz/s and detection time of 0.2 s.

Expression (4.15) is derived by considering constant *P* (constant power) load model, and hence it is valid for constant *P* load only. As reported in [110], the load dynamics influence the boundary of NDZ for ROCOF relays, and the impact is represented by the

following expression

$$\Delta P_F = e^{k.ln\,(\Delta P_0)} \tag{4.16}$$

where ΔP_0 represents the ΔP_c for constant *P* load, ΔP_F indicates the ΔP_c for constant *P* or constant current (constant *I*) or constant impedance (constant *Z*) load; *k* is a function of relay-setting λ. For constant *P* load *k* = 1, whereas for constant *Z* and constant *I* load, *k* is obtained empirically through repeated dynamic simulations [110].

4.3.3 Simulation study to investigate the boundary limit of NDZ of ROCOF Relay

As stated in Section 4.2, four possible combinations of power imbalance scenarios may exist under islanding condition. Firstly, in Section 4.3.3.1, scenario (*a*), i.e., deficit of ΔP (active power imbalance) and deficit of ΔQ (reactive power imbalance), is considered while investigating the boundary limit of NDZ, which is obtained through the performance curves of ROCOF relays under different load-types and reactive power imbalance. Then, scenarios (*b*), (*c*) and (*d*) are investigated in Section 4.3.3.2.

4.3.3.1 *Influence of Load Types and Reactive Power Imbalance on NDZ*

As shown in (4.16), for different load-types, the boundary limit of NDZ or ΔP_c can be obtained through non-linear relationship, which is dependent on the empirical analysis. Therefore, a time-domain simulation is carried out to investigate the influence of constant *P*, constant *Z*, and constant *I* load on the boundary-limit of NDZ. A simple 5 bus network, shown in Fig. 4.5, is used for this simulation study, wherein the network parameters and other relevant data are adopted from [13]. The ROCOF relay is implemented using the algorithm illustrated in Fig. 4.9. However, to incorporate the effect of measuring window, the estimated frequency is passed through the operation of "derivative block" using the following expression

$$\frac{df_r}{dt} = \frac{1}{N}\sum_{m=1}^{N}\frac{\Delta f_m}{\Delta t_m} \tag{4.17}$$

where*m* specifies the number of cycles, Δf_m is the change of frequency within *m*-th cycle, and Δt_m is the duration of *m*-th cycle in seconds. The value of *N* typically lies within 2 to 40 cycles; in this study, *N* is selected as 5 cycles [110, 112].

Repeated dynamic simulations are conducted on the system presented in Fig. 4.5, employing different ranges of active power imbalance and different load-types, which

include constant *P*, constant *Z* and constant *I*. Then, considering a specific relay-setting (i.e. λ = 1.2 Hz/s), the detection time is obtained. The minimum power imbalance, which is required for the ROCOF relay to detect islanding within 200 ms [13], is regarded as critical active power imbalance ΔP_c. Fig. 4.11 shows that for a specific relay-setting and detection time, the pessimistic boundary-limit of NDZ or ΔP_c is obtained for constant *Z* load (i.e. ΔP_c = 19.9%), whereas the optimistic NDZ is obtained for constant *P* load (i.e. ΔP_c = 11.8%).

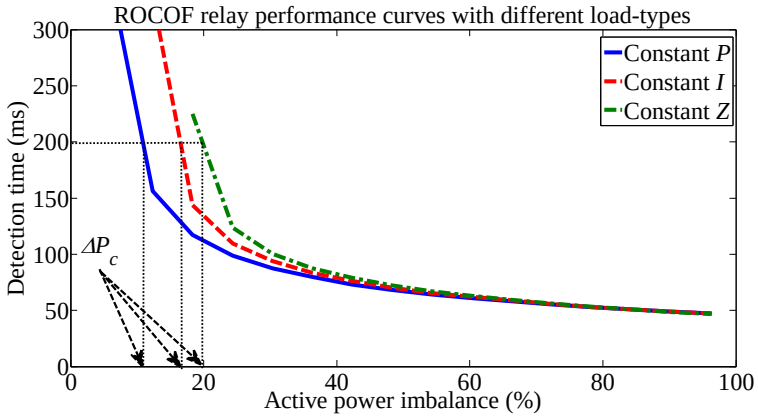

Fig. 4.11. Performance curves of ROCOF relays under three types of load (relay-setting: λ= 1.2 Hz/s).

Since the pessimistic boundary-limit of NDZ is acquired for constant *Z* load, further investigation on the boundary-limit of NDZ, is conducted by analysing the impact of reactive power imbalance (ΔQ) at the presence of constant *Z* load. To this end, repeated dynamic simulation is carried out with different ranges of active and reactive power imbalance when the loads are of constant *Z* type. Keeping 0%, 10% and 30% of ΔQ, the performance curves are illustrated in Fig. 4.12, which shows that ΔQ has significant impact on the boundary-limit of NDZ or ΔP_c for constant *Z* load.

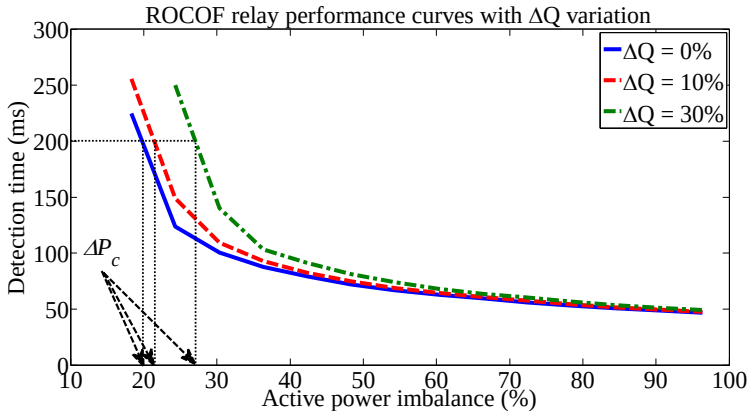

Fig. 4.12. Performance curves of ROCOF relays with the variation of ΔQ and at the presence of constant impedance load (relay-setting: λ= 1.2 Hz/s).

4.3.3.2 *Impact of active and reactive power imbalance Scenarios on NDZ*

Among the four possible power imbalance scenarios, scenario (*a*) was explored in section 4.3.3.1, while investigating the performance of ROCOF relays. Therefore, in this sub-section all four scenarios are investigated to obtain the pessimistic boundary-limit of NDZ for each scenario. In this performance analysis, the maximumvalue of ΔQ is selected as 50% since exceeding this value may collapse the voltage level of the system [111].

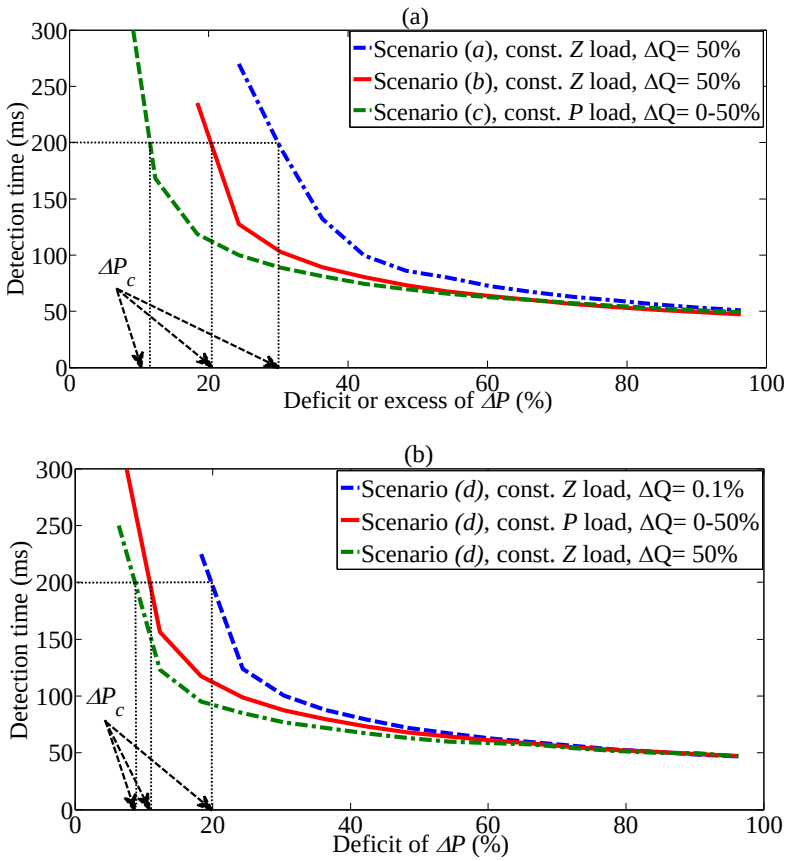

Fig. 4.13. Performance curves of ROCOF relays (relay-setting: λ= 1.2 Hz/s) under (a) scenario (*a*): deficit of ΔP and ΔQ, scenario (*b*): excess of ΔP and ΔQ, scenario (*c*): excess of ΔP and deficit of ΔQ; (b) scenario (*d*): deficit of ΔP and excess of ΔQ.

Fig. 4.13 illustrates the performance curves of ROCOF relays under four possible power imbalance scenarios, considering the pessimistic boundary-limit of NDZ. To obtain the pessimistic limit of NDZ, each scenario is investigated with constant *P*, constant *I* and constant *Z* load for 0% $<\Delta Q \leq$ 50% and 0% $<\Delta P <$ 100%. Then, the maximum numerical value of ΔP_c is considered as the pessimistic limit of NDZ of ROCOF relay. For scenarios (*a*) and (*b*), the pessimistic limit of NDZ is obtained for constant *Z* load with ΔQ of50%,whereas investigation of scenario (*c*) reveals that the pessimistic limit of NDZ is found for constant *P* load with ΔQ ranges from 0% to

50%,see Fig. 4.13 (a). By analysing the performance curves of scenario (*d*), it is evident that when ΔQ gets close to50%, a constant *P* load yields the pessimistic limit of NDZ. Moreover, for constant *P* load, the performance curve does not show significant variation when ΔQ changes from 0% to 50%. However, varying ΔQ towards0% yields the numerically maximum ΔP_c for constant *Z* load, as depicted in Fig. 4.13(b). Table 4-II summarizes the pessimistic boundary-limit of NDZ, i.e., ΔP_c, of ROCOF relay under all four scenarios.

TABLE 4-II

PESSIMISTIC BOUNDARY LIMIT OF NDZ OF ROCOF RELAY UNDER POWER IMBALANCE SCENARIOS (RELAY-SETTING = 1.2 HZ/S AND DETECTION TIME = 0.2S)

Power imbalance scenarios	Load-type	ΔQ (%)	ΔP_c (%)
(*a*): Deficit ΔP and deficit ΔQ	Constant *Z*	50	29.5
(*b*): Excess ΔP and excess ΔQ	Constant *Z*	50	20.5
(*c*): Excess ΔP and deficit ΔQ	Constant *P*	0-50	12
(*d*): Deficit ΔP and excess ΔQ	Constant *Z*	0-0.1	19.9

In summary, considering all possible power imbalance scenarios and using a specific relay-setting of λ = 1.2 Hz/s and a detection time τ_d = 200 ms, the variation of ΔP_c is observed for all three types of load; the maximum numerical value of ΔP_c is obtained as 29.5% for scenario (*a*) i.e. deficit of ΔP and ΔQ. Besides, for scenarios *(b)*, *(c)* and *(d)*, ΔP_c is obtained as 20.5%, 12% and 19.9%, respectively.

The investigations on NDZ of VS and ROCOF relays, as presented in Sections 4.2 and 4.3, have provided the insight into the performance of these conventional relays for a particular relay-setting (α = 10° for VS and λ = 1.2 Hz/s for ROCOF relay) and detection-time (200 ms). In continuation with this study, the following Section investigates the performance of VS and ROCOF relays under variable relay-setting and detection-time.

4.4 CASE STUDY FOR INVESTIGATING THE PERFORMANCE OF VS AND ROCOF RELAYS

A case study is conducted to investigate the performance of VS and ROCOF relays for different relay-setting and detection-time. To do so, a total of 6,000 events, which include 4,800 islanding and 1200 non-islanding, are generated from the test network of Fig. 3.9 (presented in Chapter 3). It is worth noting that all four possible combinations,

i.e., deficit and excess of ΔP (0%-100%) and ΔQ (0%-50%), are considered while generating the islanding events. Table 4-III shows the number of islanding and non-islanding events used for the investigation. As shown in Table 4-III, three types of loads are given equal importance while generating the islanding and non-islanding events. Besides, even distribution of ΔP is maintained in the generated islanding events under each type of load. For example, for scenario (*a*) and constant *Z* type-load, total 400 events have been generated by keeping ΔP of 1%, 2%,…,100%, where 4 events are generated for ΔP = 1%, another 4 events are generated for ΔP = 2%, and so on. In the remaining part of this Section, performance of vector surge and ROCOF relays is investigated; in Section 4.4.1 and 4.4.2, performance of VS relay is investigated, whereas performance of ROCOF relay is assessed in Section 4.4.3 using a wide range of relay-setting and detection-time.

TABLE 4-III

ISLANDING AND NON-ISLANDING EVENTS USED FOR THE PERFORMANCE ANALYSIS OF VS, ROCOF AND SVM-BASED APPROACH

Power imbalance scenarios	Islanding events				Non-islanding events
	Load-type			Total	
	Const. *Z*	Const. *I*	Const. *P*		
(*a*): Deficit ΔP and deficit ΔQ	400	400	400	1200	1200
(*b*): Excess ΔP and excess ΔQ	400	400	400	1200	
(*c*): Excess ΔP and deficit ΔQ	400	400	400	1200	
(*d*): Deficit ΔP and excess ΔQ	400	400	400	1200	

4.4.1 Performance of VS relay under variable relay-setting

In this sub-section, using the concept of critical active power imbalance (ΔP_{vs_crit}), VS relay is evaluated as a function of relay-setting (α). To do so, a curve, which represents ΔP_{vs_crit} as a function α, can be obtained from the equality constraint of (4.6), assuming the parameters *H*, τ_d and ΔT are constant. The curve is illustrated in Fig. 4.14 for *H* = 1.5 s, τ_d =200 ms and ΔT =20 ms. The curve reveals the minimum amount of active power imbalance or ΔP_{vs_crit} required for a VS relay to detect islanding at different relay-setting (α), when DG is synchronous generator (inertia constant *H = 1.5 s*) type and allowable islanding detection time (τ_d) is 200 ms.

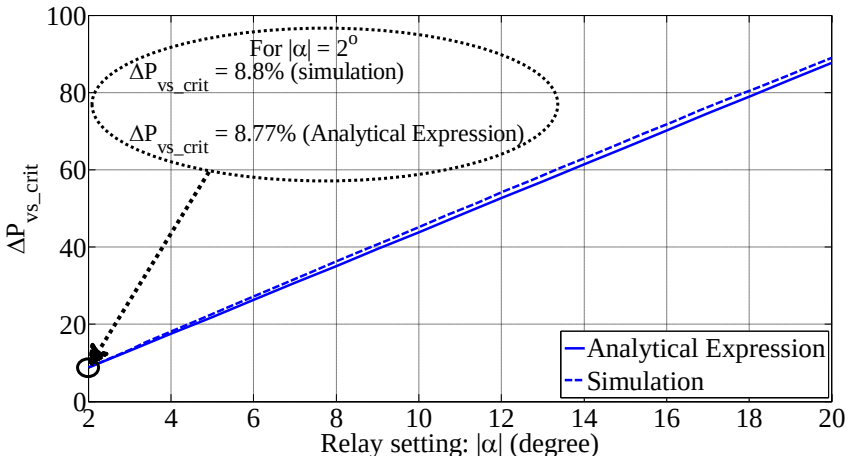

Fig. 4.14. Critical active power imbalance (ΔP_{vs_crit})associated with islanding detection of synchronous generator using VS relay with variable relay-setting $|\alpha|$.

According to [104], normally VS relay allows the setting of α in the range from 2° to 20°. Moreover, using the absolute value of α smaller than 2° may create nuisance tripping and as a result, performance of VS relay may degrade severely. Therefore, in Fig. 4.14, the curve of VS relay corresponding to different value of ΔP_{vs_crit} is plotted as a function of absolute value of α considering $|\alpha| \geq 2°$ and using (4.6) with equality constraint. The curve obtained from analytical expression given by (4.6) is also validated by the simulated data of Table 4-III and results are plotted in Fig. 4.14. From Fig. 4.14, it can be concluded that VS relay fails when power imbalance is less than 8.8% considering the minimum relay setting of $|\alpha| = 2°$.

4.4.2 Performance of VS relay as a function of relay-setting and detection-time

As stated earlier, normal operating range of VS relay lies within 2° to 20°. Hence, by tuning the relay-setting from 2° to 20°, performance of VS relay is investigated using the data of Table 4-III and considering a typical detection time ranging from 110 to 200 ms. In this context, false alarm (FA) and detection rate (DR) are selected as the two key performance indicators. Firstly, FA corresponding to 1200 non-islanding events, see Table 4-III, are calculated by varying the relay-setting from 2° to 20° for a specific detection time (τ_d) , e.g., 110 ms. Then, τ_d is changed to 120 ms and FA is calculated for the aforementioned range of relay-setting. Thus, Fig. 4.15 is obtained using variable relay-setting and detection time, and it highlights the FA of VS relay. Similarly, DR for all four power imbalance scenarios is determined. For each power imbalance scenarios, a total of 1200 islanding events are considered separately. The test results are illustrated

in Figs. 4.16(a)-(d).

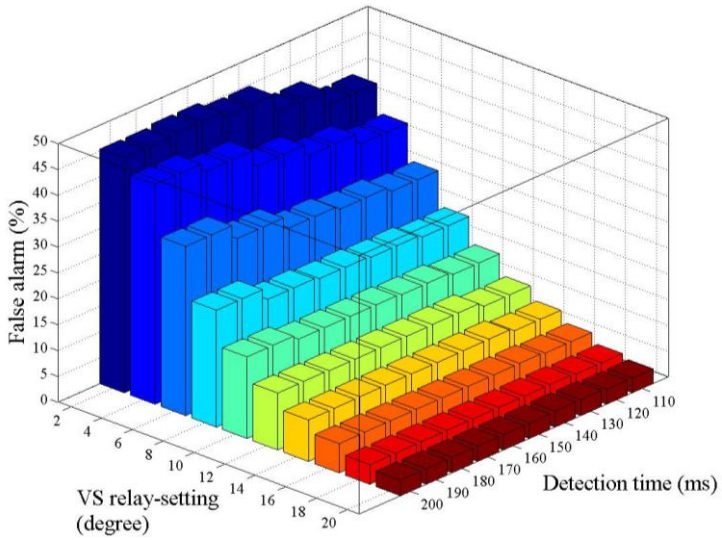

Fig. 4.15. False alarm of VS relay with variable relay-setting and detection time (τ_d).

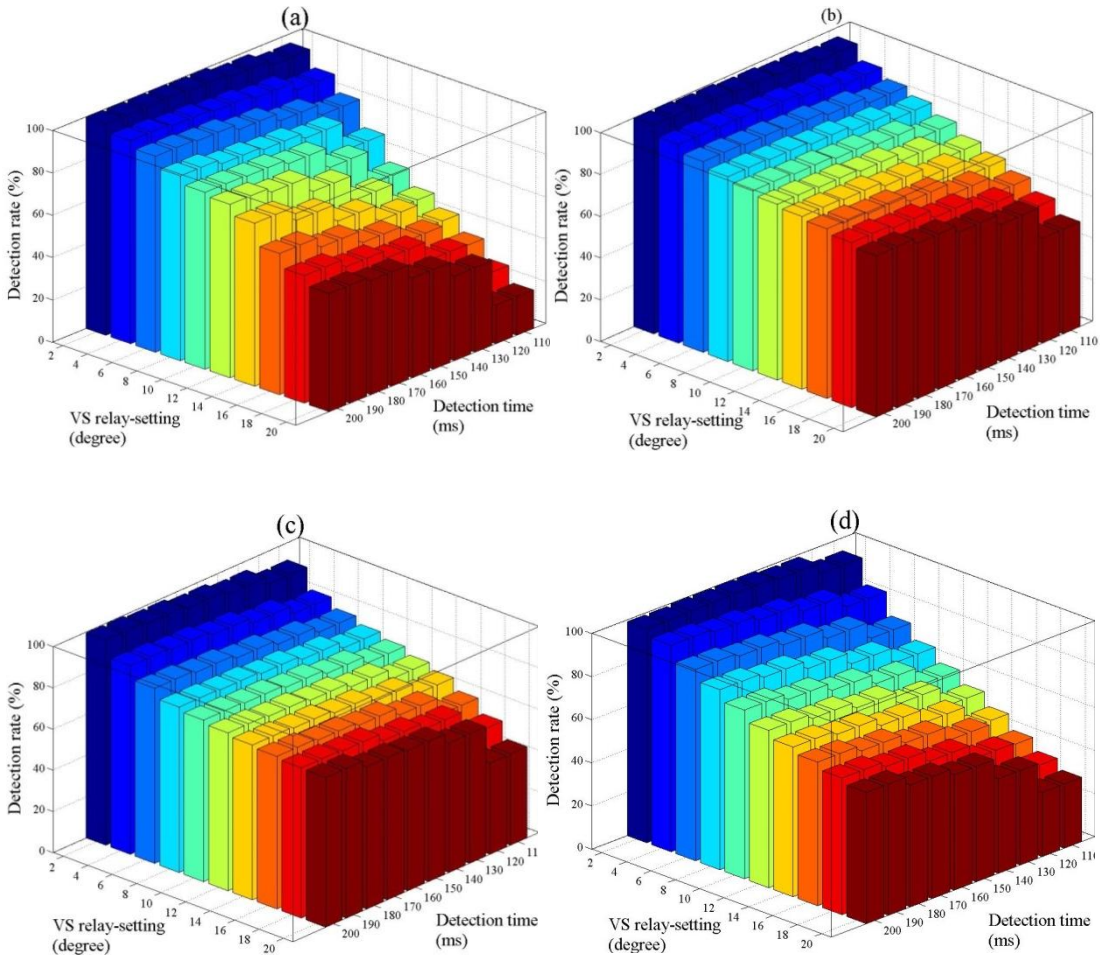

Fig. 4.16. Detection rate (DR) of VS relay as a function of relay-setting and detection time (τ_d), under four possible power imbalance scenarios: (a) deficit of ΔP and deficit of ΔQ, (b) excess of ΔP and excess of ΔQ, (c) excess of ΔP and deficit of ΔQ, and (d) deficit of ΔP and excess of ΔQ.

Fig. 4.15 shows that keeping a very small value of relay-setting, i.e., close to 2°, yields a very high percentage of FA. For example, if the relay is set below 10°, the risk of FA reaches 20% or more (see Fig. 4.15). Figs. 4.16(a)-(d) illustrate the opposite picture of Fig. 4.15 in terms of relay-setting. As shown in Figs. 4.16(a)-(d), for a relay-setting of 10° or less, DR of 80% or more can be achieved. Moreover, Figs. 4.15 and 4.16(a)-(d) reveals that, for small relay-setting and small detection time, performance is improved in terms of FA (i.e. less FA) whereas poor performance is achieved if DR is considered. Therefore, in order to keep a trade-off between DR and FA, settings of VS relay are adjusted as per utility and standard requirement.

4.4.3 Performance of ROCOF relay as a function of relay-setting and detection-time

Normally ROCOF relay is operated by keeping the relay-setting from 0.1 Hz/s to 1.2 Hz/s. Therefore, by tuning the relay-setting from 0.1 Hz/s to 1.2 Hz/s, performance of ROCOF relay is investigated using the data of Table 4-III and considering a typical detection time ranging from 100 to 200 ms. Following the similar strategy as used for VS relay, firstly, FA corresponding to 1200 non-islanding events are calculated by varying the relay-setting from 0.1 Hz/s to 1.2 Hz/s for a specific detection time (τ_d) , e.g., 100 ms. Then, τ_d is changed to 101 ms and FA is calculated for the aforementioned range of relay-setting. Thus, Fig. 4.17 is obtained using variable relay-setting and detection time, and it highlights the FA of ROCOF relay. Similarly, DR for all four power imbalance scenarios is determined. For each power imbalance scenarios, a total of 1200 islanding events are considered separately. The test results are illustrated in Figs. 4.18(a)-(d).

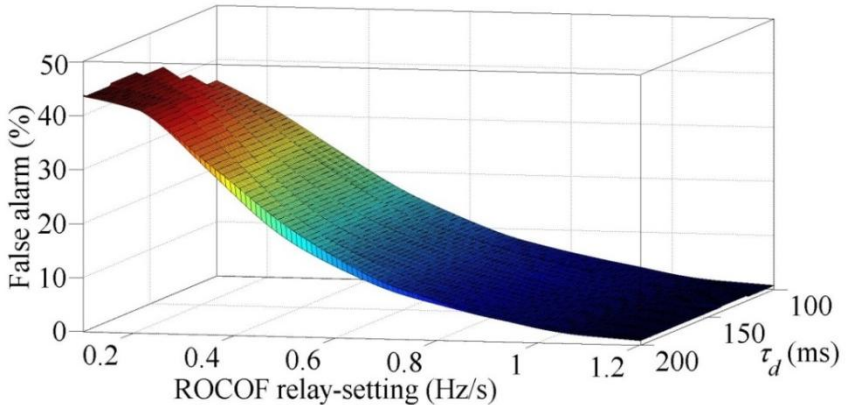

Fig. 4.17. False alarm of ROCOF relay with variable relay-setting and detection time (τ_d).

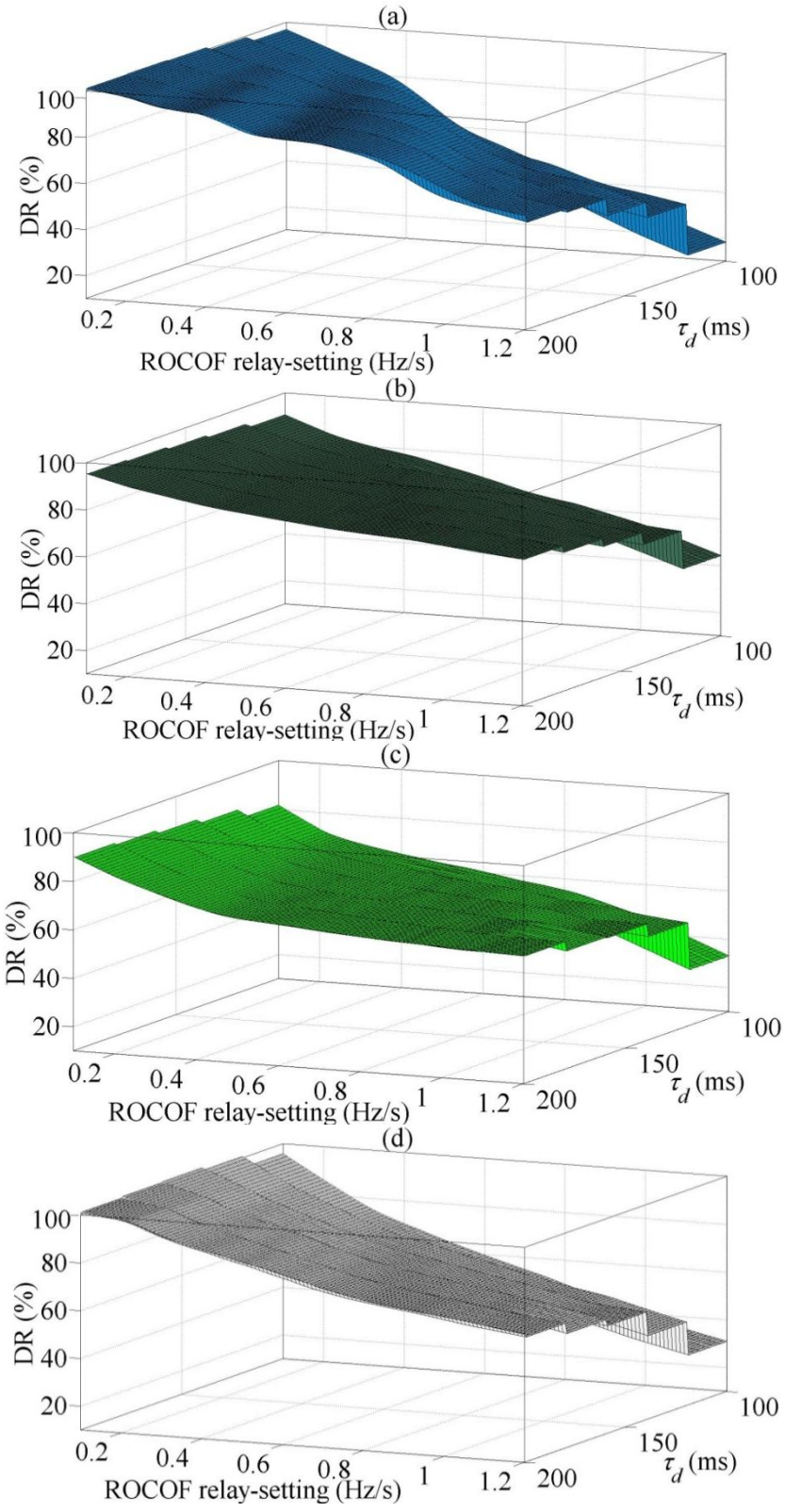

Fig. 4.18. Detection rate (DR) of ROCOF relay as a function of relay-setting and detection time (τ_d), under four possible power imbalance scenarios: (a) deficit of ΔP and deficit of ΔQ, (b) excess of ΔP and excess of ΔQ, (c) excess of ΔP and deficit of ΔQ, and (d) deficit of ΔP and excess of ΔQ.

As expected, Fig. 4.17 shows that keeping a very small value of relay-setting, i.e., close to 0.1 Hz/s, yields a very high percentage of FA. For example, if the relay is set below 0.5 Hz/s, the risk of FA reaches 20% or more (see Fig. 4.17). Figs. 4.18(a)-(d) illustrate the opposite picture of Fig. 4.17 in terms of relay-setting. As shown in Figs. 4.18(a)-(d), for a relay-setting of 0.5 Hz/s or less, DR of 70% or more can be achieved. Moreover, Figs. 4.17 and 4.18(a)-(d) reveal that, for small relay-setting and small detection time, performance is improved in terms of FA (i.e. less FA) whereas poor performance is achieved if DR is considered. Therefore, in order to keep a trade-off between DR and FA, settings of ROCOF relay are adjusted as per utility and standard requirement. Moreover, visual inspection of Figs. 4.18(a) and 5.18(d) reveals that scenarios (*a*) and (*d*) follow almost similar trend of DR with the variation of relay-setting.

4.5 COMPARATIVE ANALYSIS OF VECTOR SURGE AND ROCOF RELAYS WITH SVM BASED APPROACH

TABLE 4-IV

ISLANDING DETECTION USING AN SVM CLASSIFIER WITH LINEAR KERNEL

Type of load	Detection rate	False alarm
Constant *P*	98.64%	0.63%
Constant *I*	100%	2.5%
Constant *Z*	100%	2.5%

In Chapter 3, performance of SVM-based approach for islanding detection of DG is elaborately presented. However, in order to conduct the comparative analysis of VS and ROCOF relays with SVM-based approach, the events of Table 4-III are tested using the trained SVM. It is to be noted that trained SVM, as developed in Chapter 3, were kept unchanged, i.e., no re-training was conducted to test the events of Table 4-III. The test results are illustrated in Table 4-IV, which indicate the successful classification of the islanding events with limited rate of false alarm (less than 3%). In Section 4.5.1, comparative analysis between VS and SVM relay is conducted; then, comparative study between ROCOF and SVM relay is carried out in Section 4.5.2 on the basis of ROC (Receiver Operating Characteristic) curves and detection-time of islanding.

4.5.1 Comparative Study between VS relay and SVM based Method

In this sub-section, VS relay and SVM based method is compared using two criteria of performance evaluation. First criteria is based on the ROC curves which is obtained by applying the VS and SVM based methods in islanding detection; second criteria is based on the performance of VS and SVM relays, by assessing the detection-time of islanding using both methods. The comparative study between SVM and VS relays using these two performance criteria are presented in Sections 4.5.1.1 and 4.5.1.2, respectively.

4.5.1.1 Comparative Performance Analysis between VS relay and SVM Method using ROC curves

In order to conduct the comparative analysis between VS and SVM-based approach, detection time of 200 ms is considered for both methods. In 50 Hz system, 10 cycle corresponds to 200 ms; therefore, feature extraction of SVM-based approach is performed by using a sliding time window of ΔT = 10 cycle duration, see Section 3.3. Thus, using the common platform, i.e., same data of Table 4-III and equal detection time of 200 ms, performance of VS and SVM-based approach is compared. The Receiver Operating Characteristic (ROC) curves, as shown in Fig. 4.19, are used for this comparative analysis. To this end, ROC curves corresponding to four possible combinations of power imbalance scenarios are taken into account. Tuning the threshold setting of both methods, FA and DR are obtained which gives rise to the ROC curves. For instance, VS relay-setting is varied from 2° to 20°, and at each relay-setting, FA and DR are considered for plotting the ROC curves of VS relay. In the similar approach, decision boundary of trained SVM is tuned by changing the bias value *b* and the ROC curves are acquired thereby. As illustrated in Fig. 4.19, SVM-based approach produces significantly better performance than VS relay for scenarios (*a*), (*b*), (*c*) and (*d*), which include all possible combinations of deficit and excess of active and reactive power imbalance scenarios soon after the inception of islanding. However, VS relay can produce almost same DR of SVM method if FA of 40% or more, i.e., a risk of high percentage of nuisance tripping, is allowed in the system, see Figs. 4.19(a)-(d).

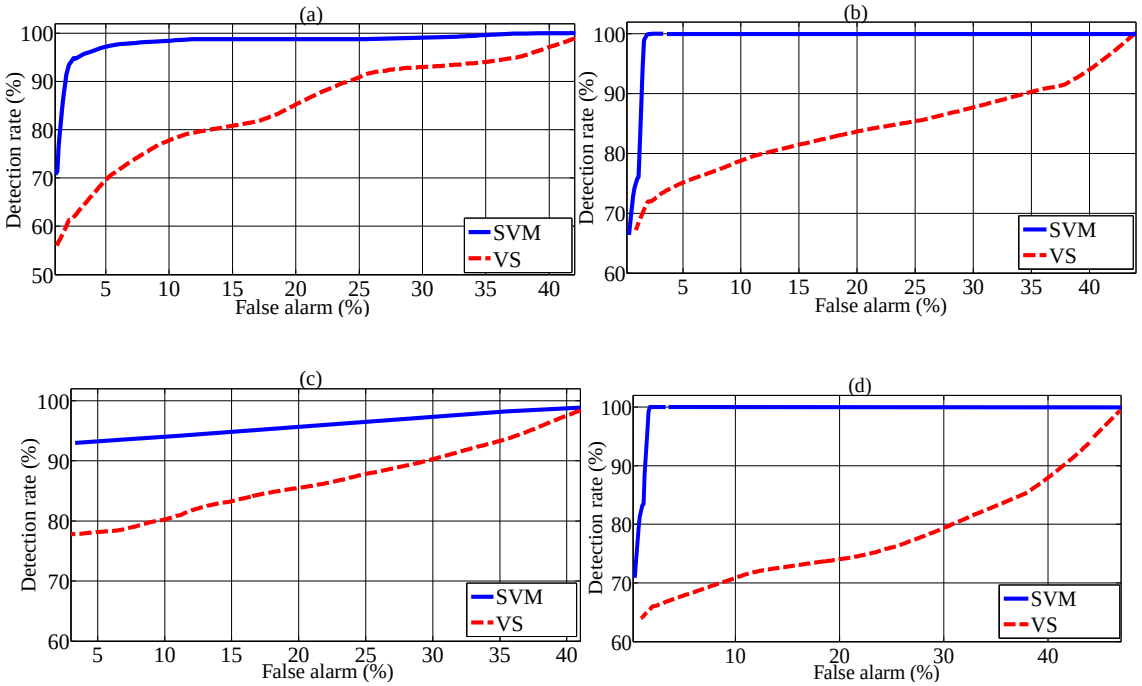

Fig. 4.19. ROC curves of VS relay and SVM-based approach under scenarios: (a) deficit of ΔP and deficit of ΔQ, (b) excess of ΔP and excess of ΔQ, (c) excess of ΔP and deficit of ΔQ, and (d) deficit of ΔP and excess of ΔQ.

4.5.1.2 Comparative Performance Analysis between VS relay and SVM Method on the basis of detection-time

Using the data of Table 4-III, islanding "detection time" of each event is determined for the conventional vector surge relay (VSR) as well as SVM relay (SVMR). But, the final value of detection time, as plotted in Fig. 4.20, is selected by taking the average value. To do so, at each ΔP level, 10-15 events are considered and their average detection time is selected as final detection time at that ΔP level. This same technique is followed for all combinations of power imbalance scenarios, which include deficit and excess of active power imbalance (ΔP) and reactive power imbalance (ΔQ). Thus, Figs. 4.20(a)-(d) are obtained and they illustrate the islanding detection time of SVMR and VSR. It is worth noting that setting value of VSR was kept at 10° during this comparative study, since this setting gives a reasonably good performance if a trade-off between DR and FA are taken into account (see Figs. 4.15 and 4.16). Similarly, 9 sample majority voting, which is demonstrated in Chapter 3 as a reliable decision-rule, is considered for SVMR. As shown in Figs. 4.20(a)-(d), SVMR relay can successfully operate under all possible combinations of power imbalance scenarios within 200 ms of the onset of islanding. However, SVMR requires a slightly higher detection time, i.e., 200-300 ms under the scenario (*b*), i.e., excess of ΔP and ΔQ with ΔP < 5% (see Fig.

4.20(b)). VSR needs larger detection time in comparison to SVMR for scenarios (*a*)-(*d*) when $\Delta P < 50\%$; however, for $\Delta P \geq 60\%$, it requires detection time of around 100-160 ms, which is slightly lower than SVMR that operates within 160-200 ms of islanding inception. Therefore, for an allowable islanding detection time of 200 ms and taking all possible combinations of ΔP and ΔQ into account, it can be concluded thatSVMR supersedes the performance of VS relay.

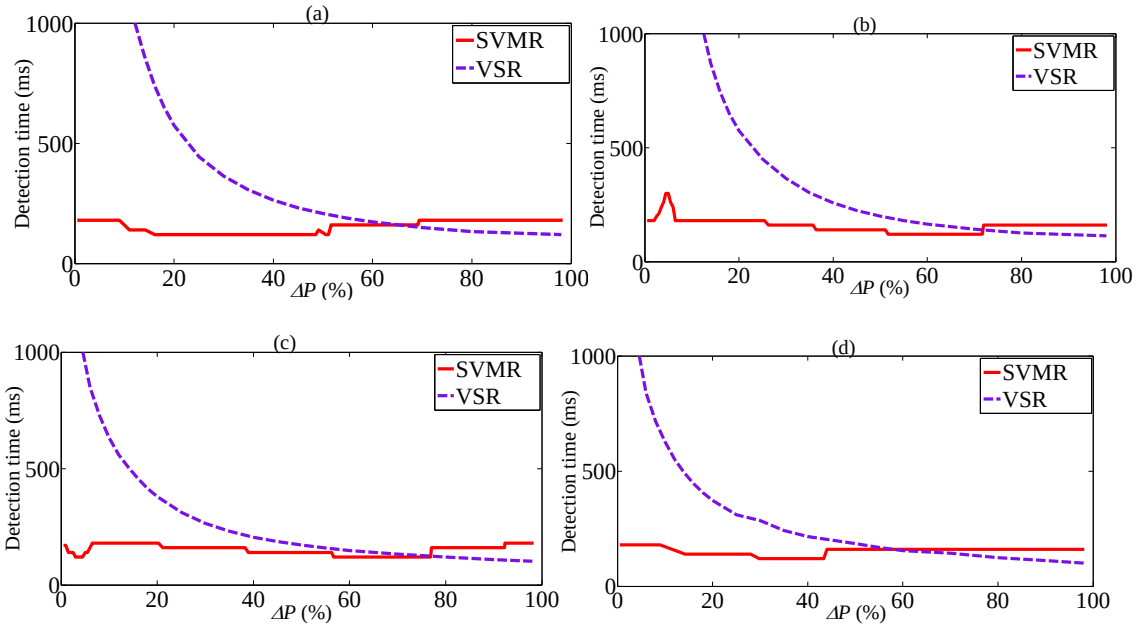

Fig. 4.20. Detection time of the SVM based relay (SVMR) and vector surge relay (VSR) under four possible combinations of power imbalance scenarios: (a) deficit of ΔP and deficit of ΔQ, (b) excess of ΔP and excess of ΔQ, (c) excess of ΔP and deficit of ΔQ, and (d) deficit of ΔP and excess of ΔQ.

4.5.2 Comparative Study between ROCOF relay and SVM based Approach

In this sub-section, ROCOF relay and SVM based method is compared using two criteria of performance evaluation as used in Section 4.5.1. The two performance criteria, which include the ROC curves and the assessment of the relays on the basis of detection-time of islanding, are presented in Sections 4.5.2.1 and 4.5.2.2, respectively.

4.5.2.1 Comparison of ROCOF Relay and SVM method using ROC curves

In order to conduct the comparative analysis between ROCOF and SVM-based approach, detection time of 200 ms is considered for both methods. Thus, using the common platform, i.e., same data of Table 4-III and equal detection time of 200 ms,

performance of ROCOF and SVM-based approachis compared. The Receiver Operating Characteristic (ROC) curves, as shown in Fig. 4.21, are used for this comparative analysis. Tuning the threshold setting of both methods, FA and DR are obtained which gives rise to the ROC curves. For instance, ROCOF relay-setting is varied from 0.1 Hz/s to 1.2 Hz/s, and at each relay-setting, FA and DR are considered for plotting the ROC curves of ROCOF relay. As illustrated in Fig.4.21, SVM-based approach produces significantly better performance than ROCOF relay for scenarios (*a*), (*b*), (*c*) and (*d*), which include all possible combinations of deficit and excess of active and reactive power imbalance scenarios soon after the inception of islanding. However, for scenarios (*a*)-(*d*), ROCOF relay can produce almost same DR of SVM method if FA of 42% or more, i.e., a risk of high percentage of nuisance tripping, is allowed in the system.

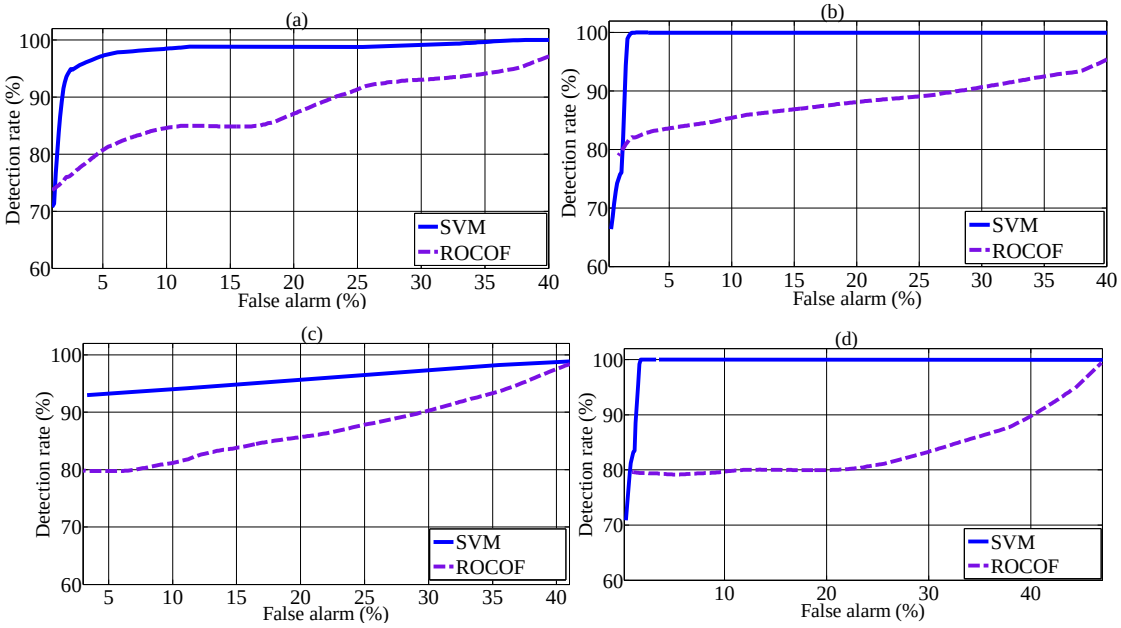

Fig. 4.21. ROC curves of ROCOF relay and SVM-based approach under scenarios: (a) deficit of ΔP and deficit of ΔQ, (b) excess of ΔP and excess of ΔQ, (c) excess of ΔP and deficit of ΔQ, and (d) deficit of ΔP and excess of ΔQ.

4.5.2.2 Comparison of ROCOF Relay and SVM method on the basis of detection-time of Islanding

Using the data of Table 4-III, islanding "detection time" of each event is determined for the conventional ROCOF relay as well as SVM relay (SVMR). But, the final value of detection time, which is plotted in Fig. 4.22, is selected by taking the average value as mentioned in Section 4.5.1.2. Thus, Figs. 4.22(a)-(d) are obtained. These figures

illustrate the islanding detection time of SVMR, and ROCOF relay, during all possible combinations of power imbalance scenarios. It is worth noting that ROCOF relay-setting was kept at 1.2 Hz/s during this comparative study, since this setting gives a reasonably good performance if a trade-off between DR and FA are taken into account (see Figs. 4.17 and 4.18).

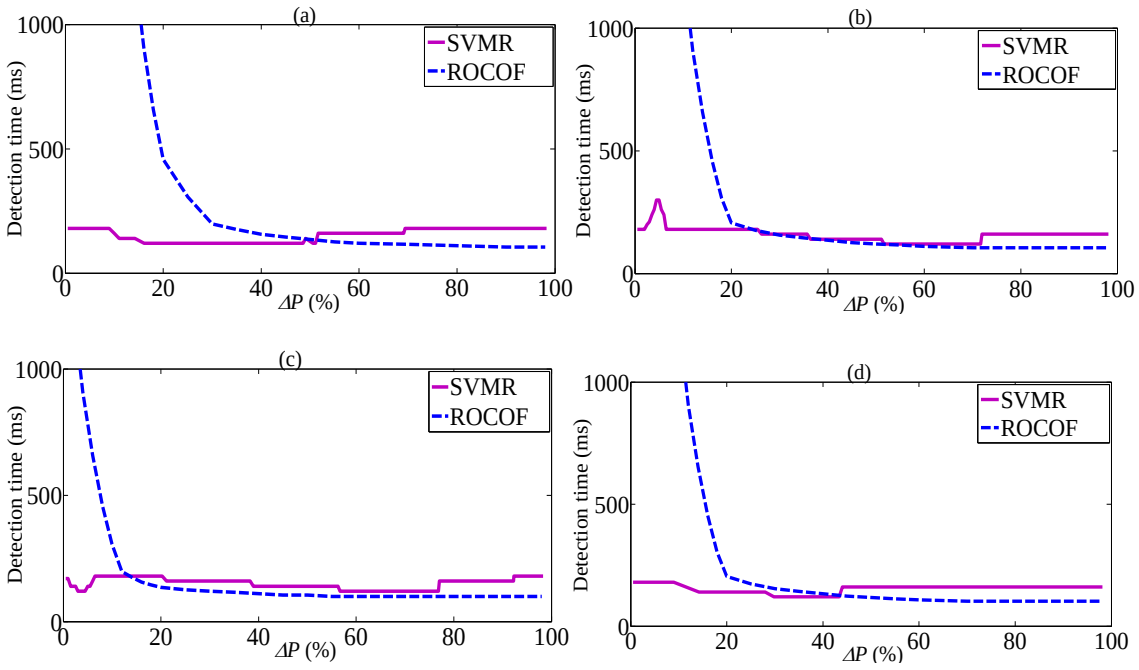

Fig. 4.22. Detection time of the SVM based relay (SVMR) and ROCOF relay; under four possible combinations of power imbalance scenarios: (a) deficit of ΔP and deficit of ΔQ, (b) excess of ΔP and excess of ΔQ, (c) excess of ΔP and deficit of ΔQ, and (d) deficit of ΔP and excess of ΔQ.

As shown in Figs. 4.22(a)-(d), SVMR relay can successfully operate under all possible combinations of power imbalance scenarios within 200 ms of the onset of islanding. ROCOF relay needs larger detection time in comparison to SVMR for scenarios (*a*), (*b*), (*d*) when $\Delta P < 20\%$, and for scenario (*c*) when $\Delta P < 12\%$; however, for $\Delta P \geq 20\%$, it requires detection time of around 100 ms, which is slightly lower than SVMR that operates within 160-200 ms of islanding inception. Therefore, considering an allowable islanding detection time of 200 ms along with all possible combinations of ΔP and ΔQ, SVMR supersedes the performance of ROCOF relay.

4.6 SUMMARY

This Chapter has presented performance evaluation of vector surge (VS) and rate-of-change-of-frequency (ROCOF) relays, and a comparative analysis of VS and ROCOF

relays with the support vector machines (SVM) based approach, employed in islanding detection of Distributed Generation (DG). The performance of VS and ROCOF relays was evaluated using the concept of NDZ; the comparative analysis was based on the receiver operating characteristic (ROC) curves obtained under all possible combinations of power imbalance scenarios, which may exist during the formation of an island. During the testing phase, a large number of islanding and non-islanding events were generated by simulating the probable practical scenarios in a test network of Australia. Test results demonstrate that SVM-based approach is more reliable and effective than VS and ROCOF relays, in terms of the detection rate (DR) and false alarm (FA). In summary, the following contributions are highlighted in this Chapter:

- Boundary limit of non-detection zone (NDZ), associated with VS and ROCOF relays, is established and formulated for constant *P* load. It has been further investigated for constant *Z* and constant *I* load.
- Boundary limit of NDZ of VS and ROCOF relays, at the presence of constant *Z*, constant *I* and constant *P* load along with four possible combinations of deficit and excess of active and reactive power imbalance scenarios, are investigated to obtain the pessimistic limit of NDZ for VS and ROCOF relays.
- Using an example test system, performance of VS and ROCOF relays is evaluated with variable relay-setting and detection time.
- Performance of VS and ROCOF relays is compared with the SVM based relay (SVMR) on the basis of detection-time of islanding; SVMR demonstrates comparatively better performance than VS and ROCOF relays.
- SVM-based approach is compared with VS and ROCOF relays on the basis of ROC curves, which explicitly show the superior performance of SVM-based method over VS and ROCOF relays.

Chapter 5

VOLTAGE DIPS/SAGS AND ITS ASSOCIATED PHASE-ANGLE JUMPS IN ELECTRICITY NETWORKS

5.1 INTRODUCTION

Over the last few years, the concept of power quality (PQ) has been changed significantly, due to technological progression and customer awareness of better services. A few years ago, the main PQ concerns were the reliability, i.e., the frequency of the discontinuity of electricity supply. At present, the problems related to PQ include voltage dips, fluctuations, temporary interruptions and harmonics [19]. The increased application of non-linear power electronic devices in electric power systems hastens the degradation of PQ, thereby necessitating more attention from electricity sector agents [20].

Voltage dip is usually considered a PQ problem of equal importance as long and short interruptions in the supply [21, 22]. They are generally defined as the short-duration reduction in root-mean-square (rms) voltage caused by switching and/or starting of electrical motors, generators and bulk loads, transformer energization and faults or short circuits in the power networks [23]. Even though power utilities and customers are exerting extensive efforts to improve the reliability of power networks, it has been very challenging to control the external factors that cause voltage dips.

Deregulation of energy market, economic benefits for distributed generation (DG) owners, and higher reliability through the reduction of outage intervals, have increased the penetration of local distributed generators, which are typically synchronous machines [11, 52]. This increased penetration of DG will have an impact on the PQ issues in a number of ways. The positive impact can be observed for certain disturbance levels, such as voltage dips, harmonics, and voltage fluctuations. However, utility

companies provide specific interconnection guidelines, and these local generators or DGs must comply with these guidelines/requirements [2]. Failure to meet these requirements will trip the DG; as a result, PQ issues, e.g., voltage dips may occur during the disconnection period of DG.

This Chapter investigates the voltage dips and its associated phase-angle jumps in power network due to various kinds of faults. The presence of synchronous type DG is also included in the voltage dip investigations. Seven types of voltage dips (A, B, D, F, E, C, and G) as proposed in [22], are taken into account during the study.

The remaining part of the Chapter is structured as follows. Section 5.2 describes the analytical expression of voltage dips due to balanced and unbalanced faults; the presence of DG is also included in the developed expressions. An illustrative example is presented in section 5.3 to validate the developed expressions. Section 5.4 highlights the severity of voltage dips for different fault-types, fault-location, size and location of DG. Section 5.5 presents a brief discussion addressing the importance of classification and characterization of voltage dips. Section 5.6 concludes the Chapter.

5.2 VOLTAGE DIPS AND PHASE-ANGLE JUMP WITH AND WITHOUT DG

Voltage dips may occur from motor-starting, transformer energizing, and short-circuits in the transmission and/or distribution system. In this section, voltage dips initiated by short-circuits are analysed. Firstly, an analytical expression of voltage is presented for a distribution network, where voltage dip occurs due to fault. To this end, a general expression of seven types of voltage dips (A, B, D, F, E, C and G), with and without DG, is developed.

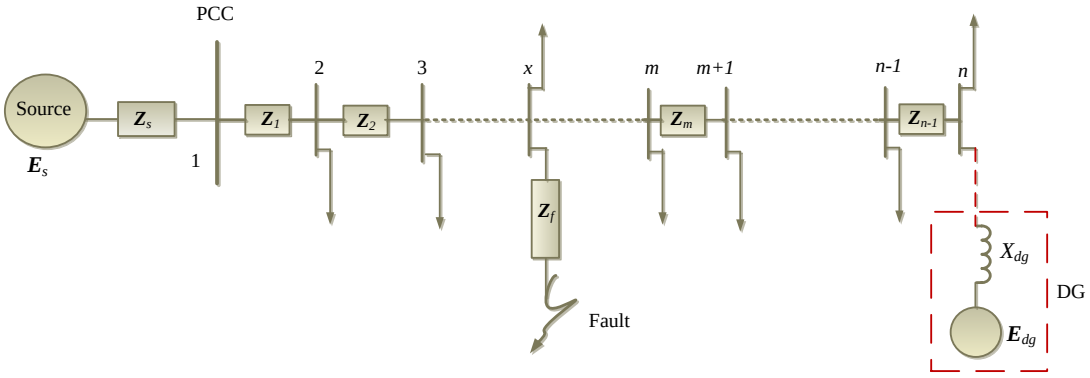

Fig. 5.1.Single line diagram of a distribution network model.

In order to determine the voltages at different buses of a test network, the distribution network model of Fig. 5.1 is considered. This model comprises source impedance ($\boldsymbol{Z}_s$) at the point of common coupling (PCC). The source voltage $\boldsymbol{E}_s$ and impedance $\boldsymbol{Z}_s$ are regarded as Thévenin equivalent of the upstream side. A total of n number of buses is shown in the model, where a fault (with fault impedance $\boldsymbol{Z}_f$) occurs at bus x. In this model, load currents are assumed to be negligible during fault (since fault currents are typically very high in comparison to load current). Synchronous Generator based DG is considered to analyse the impact of DG on voltage dips. It is to be noted that firstly, the general expressions of voltage dips associated with different types of faults and their corresponding types of dips are developed. Then, the contribution of DG is included to develop the expressions of voltage-dip and phase-angle jump during fault.

To formulate the general expressions of voltages during different types of faults, in Section 5.2.1, sequence-network diagram is formed considering the positive, negative and zero sequence impedance of the network. In Section 5.2.2, the 3-phase voltages during-fault (or the during-fault voltage) at a monitoring bus m are determined. Then, in Section 5.2.3, taking seven types of voltage dips into account, voltage-dip d_v is expressed as a function of sequence-impedance component of the network. Moreover, phase-angle jumps associated with different dip-types are presented. Lastly, Section 5.2.4 shows the derivation of the expressions of voltage-dip d_v and phase-angle jumps associated with different dip-types, when DG is connected to the network.

5.2.1 Sequence Network Diagrams for different types of Faults

Considering the test system of Fig. 5.1, voltage-current relationship can be given in terms of bus admittance matrix as

$$\begin{bmatrix} \boldsymbol{I}_1 \\ \boldsymbol{I}_2 \\ \boldsymbol{I}_x \\ .... \\ \boldsymbol{I}_m \\ ..... \\ \boldsymbol{I}_n \end{bmatrix} = \begin{bmatrix} \boldsymbol{Y}_{11} & \boldsymbol{Y}_{12} & ..... & \boldsymbol{Y}_{1x} & ..... & \boldsymbol{Y}_{1m} & ..... & \boldsymbol{Y}_{1n} \\ \boldsymbol{Y}_{21} & \boldsymbol{Y}_{22} & ..... & \boldsymbol{Y}_{2x} & ..... & \boldsymbol{Y}_{2m} & ..... & \boldsymbol{Y}_{2n} \\ ..... & & & & & & & \\ \boldsymbol{Y}_{x1} & \boldsymbol{Y}_{x2} & ..... & \boldsymbol{Y}_{xx} & ..... & \boldsymbol{Y}_{xm} & ..... & \boldsymbol{Y}_{xn} \\ ..... & & & & & & & \\ \boldsymbol{Y}_{m1} & \boldsymbol{Y}_{m2} & ..... & \boldsymbol{Y}_{mx} & ..... & \boldsymbol{Y}_{mm} & ..... & \boldsymbol{Y}_{mn} \\ ..... & & & & & & & \\ \boldsymbol{Y}_{n1} & \boldsymbol{Y}_{n2} & ..... & \boldsymbol{Y}_{nx} & ..... & \boldsymbol{Y}_{nm} & ..... & \boldsymbol{Y}_{nn} \end{bmatrix} \begin{bmatrix} \boldsymbol{V}_1 \\ \boldsymbol{V}_2 \\ \boldsymbol{V}_x \\ .... \\ \boldsymbol{V}_m \\ ..... \\ \boldsymbol{V}_n \end{bmatrix} \quad (5.1a)$$

Or

$$[\boldsymbol{I}] = [\boldsymbol{Y}_{BUS}][\boldsymbol{V}] \tag{5.1b}$$

Re-arranging Eq. (5.1b) yields

$$[\boldsymbol{V}] = [\boldsymbol{Y}_{BUS}]^{-1}[\boldsymbol{I}] = [\boldsymbol{Z}][\boldsymbol{I}] \tag{5.2}$$

where $\boldsymbol{Z}$ refers to the bus impedance matrix $\left([\boldsymbol{Z}] = [\boldsymbol{Y}_{BUS}]^{-1}\right)$ and the elements of $\boldsymbol{Z}$ are divided into two parts: driving point impedance and transfer impedance, which can be presented as below:

$$\boldsymbol{Z}_{kl} = \begin{cases} \text{driviving point impedance} & \text{when } k = l \\ \text{transfer impedance} & \text{when } k \neq l \end{cases}$$

The driving point impedance of a bus/node is equal to the Thévenin equivalent impedance of the network observed from that bus/node. Therefore, the driving point impedance or the diagonal elements of $\boldsymbol{Z}$ is applied to calculate the short-circuit current due to faults at different buses. In short-circuit studies, symmetrical components are assumed to be independent. In other words, assuming the network to be symmetrical, where an unsymmetrical fault takes place, the three sequence components, i.e., positive, negative and zero sequence components, are independent of each other.

For the test network of Fig. 5.1, the positive, negative and zero sequence impedance matrixes are built to develop the sequence network diagram associated with balanced and unbalanced faults. Therefore, three single-phase sequence network diagrams are required for individual consideration. These sequence diagrams are single-phase models of the power system and the impedance matrix can be used to model them. Using the method proposed in [113, 114], the three sequence bus impedance matrixes for the network can be easily obtained.

In order to build the sequence impedance matrix, the sequence impedance (positive, negative and zero sequence) encountered by the currents is investigated. It reveals that sequence currents depend on power system equipment, such as, transmission/distribution line, transformer, generator, etc. Both positive and negative sequence impedance of non-rotating apparatus, e.g., transmission/distribution line, is same. However, zero sequence impedance of overhead line usually lies between two to six times of positive sequence impedance, and it depends on grounding wires, tower footing resistance, etc. The leakage impedance of transformers represent the positive

and negative sequence impedance, whereas zero sequence impedance of transformers varies from open circuit to a low value based on the connection of transformer winding, the core construction and method of neutral grounding [115]. For evaluating the synchronous generator's performance, the positive sequence synchronous reactance, X_d, is used in steady state analysis, whereas subtransient reactance $\left(X_d^{''}\right)$and transient reactance $\left(X_d^{'}\right)$ is used in transient study. Negative and zero sequence impedance of synchronous machine are provided by the manufactures, based on their test results.

From the above discussion it can be concluded that the positive-sequence network is almost equal to the negative-sequence with two exceptions: a source is absent in the negative-sequence network and the reactance of the generator due to negative-sequence may be different from the positive one. The structure of positive-sequence impedance matrix $\left(\boldsymbol{Z}^P\right)$ is similar to the negative one $\left(\boldsymbol{Z}^N\right)$, but a small numerical difference may be found which is negligible. The zero-sequence impedance matrix is quite different from negative and positive ones. It has no voltage source and has discontinuities due to transformer winding connections; and the impedance values are different from positive ones.

Four major types of short-circuit faults are normally found in power systems, they are: a) balanced three-phase fault, b) single-phase/single-line to ground fault, c) phase-to-phase fault, and d) double line-to-ground fault. Fault a) is known as symmetrical or balanced fault whereas faults b), c) and d) are regarded as unsymmetrical or unbalanced faults. The connection diagrams of the hypothetical stubs for these four types of faults through a fault-impedance $\boldsymbol{Z}_f$ are shown in Fig. 5.2.

Now, considering a fault at bus *x* (with fault impedance $\boldsymbol{Z}_f$) of Fig. 5.1, the sequence network diagrams associated with the four types of faults are illustrated in Fig. 5.3. It should be noted that in Fig. 5.3, the superscripts *0*, *P* and *N* over the variables indicate the zero, positive and negative sequence components and $\boldsymbol{V}_a^{pref(x)}$ indicates *a*-phase voltage at faulted bus *x* prior to the fault.

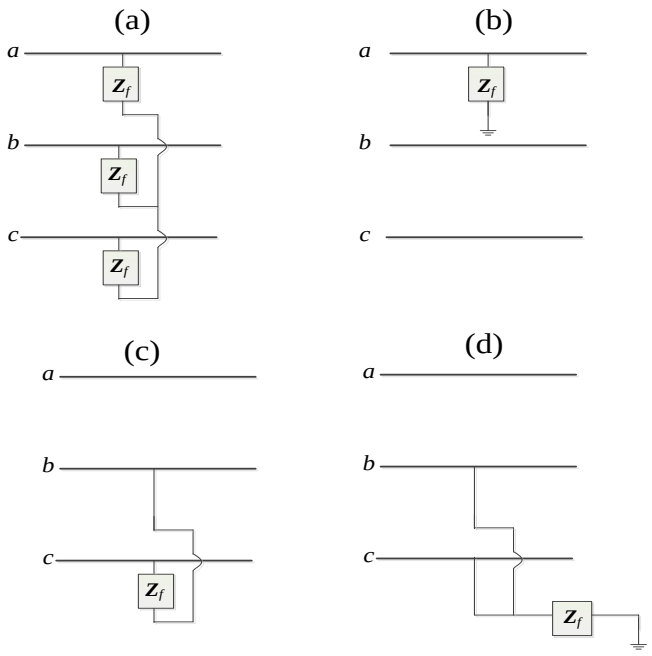

Fig. 5.2. Hypothetical connection diagrams for (a) 3-phase symmetrical fault, (b) single line-to-ground (SLG) fault, (c) phase-to-phase fault, and (d) double line-to-ground fault, through fault impedance.

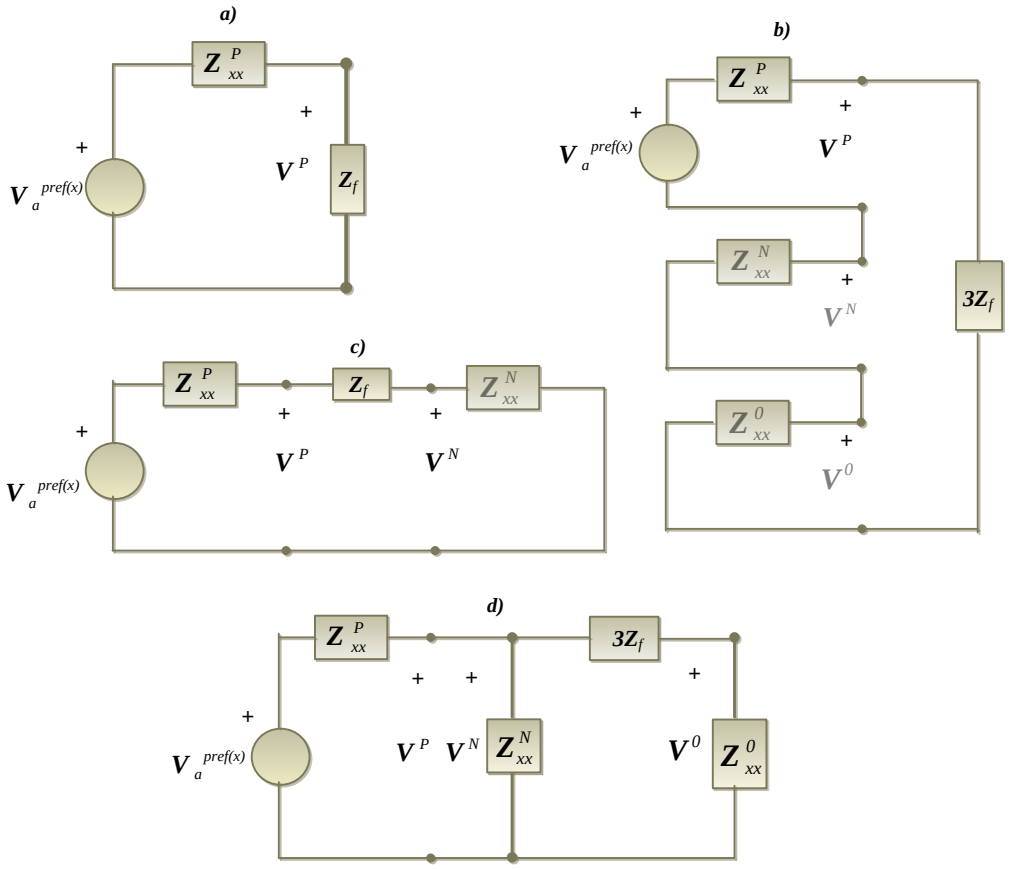

Fig. 5.3. Sequence network diagrams for (a) 3-phase symmetrical fault, (b) single line-to-ground (SLG) fault, (c) phase-to-phase fault, and (d) double line-to-ground fault.

5.2.2 Expression of phase-voltages during different types of Faults

Development of the expressions of 3-phase voltages during balanced dip (associated with balanced faults) and unbalanced dip (associated with unbalanced faults) is presented below:

i) Balanced voltage dip

Balanced dips are caused by three-phase faults. Considering a three-phase fault at bus *x* of Fig. 5.1 (with fault impedance $\boldsymbol{Z}_f$), voltage at node *m* (monitoring bus) during the fault is given by

$$\boldsymbol{V}^{mx} = \boldsymbol{V}^{pref(m)} + \Delta\boldsymbol{V}^{mx} \tag{5.3}$$

where $\boldsymbol{V}^{mx}$ = Voltage at monitoring bus *m* due to 3-phase fault at bus/node *x*,

$\boldsymbol{V}^{pref(m)}$ = Pre-fault voltage at monitoring bus *m*, and

$\Delta\boldsymbol{V}^{mx}$ = Change in voltage at monitoring bus *m* due to 3-phase fault at bus/node *x*.

Equation (5.3) shows that the voltage during the fault is equal to the pre-fault voltage at the monitoring bus plus the change of voltage due to the fault.

Now, during three-phase short-circuit at *x*, the current "injected" into *x* is given by (5.4), where $\boldsymbol{V}^{pref(x)}$ is the pre-fault voltage at bus *x*, $\boldsymbol{Z}_{xx}$ is the Thévenin impedance or the impedance seen from the faulted bus *x* into the network, and the minus sign is considered due to the direction of current. Only positive-sequence values are required to perform the calculations.

$$\boldsymbol{I}_x = -\frac{\boldsymbol{V}^{pref(x)}}{\boldsymbol{Z}_{xx} + \boldsymbol{Z}_f} \tag{5.4}$$

Once the "injected" current is known, the voltage-change at any bus *m* can be calculated using the transfer impedance between bus *m* and node *x*, denoted as $\boldsymbol{Z}_{mx}$. Thus, change in voltage is given by

$$\Delta\boldsymbol{V}^{mx} = -\boldsymbol{Z}_{mx}\frac{\boldsymbol{V}^{pref(x)}}{\boldsymbol{Z}_{xx} + \boldsymbol{Z}_f} \tag{5.5}$$

From (5.3) and (5.5), the during-fault voltage at bus *m*, due to 3-phase fault at *x*, is obtained as

$$\boldsymbol{V}^{mx} = \boldsymbol{V}^{pref(m)} - \boldsymbol{Z}_{mx}\,\frac{\boldsymbol{V}^{pref(x)}}{\boldsymbol{Z}_{xx} + \boldsymbol{Z}_{f}} \tag{5.6}$$

Equation (5.6) shows that the voltage-change at bus *m* due to a 3-phase fault at node *x* is given by the ratio of the transfer impedance to the driven point impedance at the faulted bus/node.

ii) Unbalanced voltage dip

Symmetrical components are used for the analysis of unbalanced voltage dips which are caused by unsymmetrical faults. As the sequence components are independent in symmetrical systems, the during-fault voltage for each sequence components can be determined by using (5.3). Before the fault, only a positive-sequence component $\left(\boldsymbol{V}^{P,pref}\right)$ exists in the node voltages; therefore, pre-fault voltage of negative and zero sequences are zero. The during-fault sequence voltages are given by

$$\boldsymbol{V}^{\boldsymbol{P}} = \boldsymbol{V}^{P,pref} + \Delta\boldsymbol{V}^{P} \tag{5.7a}$$

$$\boldsymbol{V}^{\boldsymbol{N}} = 0 + \Delta\boldsymbol{V}^{N} \tag{5.7b}$$

$$\boldsymbol{V}^{0} = 0 + \Delta\boldsymbol{V}^{0} \tag{5.7c}$$

Considering phase-*a* as the symmetrical phase, the phase voltages can be obtained by applying the symmetrical components transformation as presented below.

$$\begin{bmatrix}\boldsymbol{V}_a\\ \boldsymbol{V}_b\\ \boldsymbol{V}_c\end{bmatrix} = \begin{bmatrix}1 & 1 & 1\\ 1 & a^2 & a\\ 1 & a & a^2\end{bmatrix}\begin{bmatrix}\boldsymbol{V}^{0}\\ \boldsymbol{V}^{\boldsymbol{P}}\\ \boldsymbol{V}^{\boldsymbol{N}}\end{bmatrix} \tag{5.8}$$

From (5.7) and (5.8), the phase-voltages can be presented as

$$\boldsymbol{V}_a = \boldsymbol{V}^{P,pref} + \Delta\boldsymbol{V}^{P} + \Delta\boldsymbol{V}^{N} + \Delta\boldsymbol{V}^{0} \tag{5.9a}$$

$$\boldsymbol{V}_b = a^2\boldsymbol{V}^{P,pref} + a^2\Delta\boldsymbol{V}^{P} + a\,\Delta\boldsymbol{V}^{N} + \Delta\boldsymbol{V}^{0} \tag{5.9b}$$

$$\boldsymbol{V}_c = a\boldsymbol{V}^{P,pref} + a\,\Delta\boldsymbol{V}^{P} + a^2\Delta\boldsymbol{V}^{N} + \Delta\boldsymbol{V}^{0} \tag{5.9c}$$

(a) Unbalanced voltage dip due to single line-to-ground (SLG) fault

As shown in Fig. 5.3, due to single-phase or single line-to-ground (SLG) fault at bus *x*, the current injected into the positive, negative and zero sequence networks, is given by

$$\boldsymbol{I}_x^P = -\frac{\boldsymbol{V}_a^{pref(x)}}{\boldsymbol{Z}_{xx}^P + \boldsymbol{Z}_{xx}^N + \boldsymbol{Z}_{xx}^0 + 3\boldsymbol{Z}_f}; \boldsymbol{I}_x^P = \boldsymbol{I}_x^N = \boldsymbol{I}_x^0 \tag{5.10}$$

Now, the sequence voltage-changes at bus *m* due to fault at bus *x* are given by

$$\Delta\boldsymbol{V}^{P,mx} = -\boldsymbol{Z}_{mx}^P \frac{\boldsymbol{V}_a^{pref(x)}}{\boldsymbol{Z}_{xx}^P + \boldsymbol{Z}_{xx}^N + \boldsymbol{Z}_{xx}^0 + 3\boldsymbol{Z}_f} \tag{5.11a}$$

$$\Delta\boldsymbol{V}^{N,mx} = -\boldsymbol{Z}_{mx}^N \frac{\boldsymbol{V}_a^{pref(x)}}{\boldsymbol{Z}_{xx}^P + \boldsymbol{Z}_{xx}^N + \boldsymbol{Z}_{xx}^0 + 3\boldsymbol{Z}_f} \tag{5.11b}$$

$$\Delta\boldsymbol{V}^{0,mx} = -\boldsymbol{Z}_{mx}^0 \frac{\boldsymbol{V}_a^{pref(x)}}{\boldsymbol{Z}_{xx}^P + \boldsymbol{Z}_{xx}^N + \boldsymbol{Z}_{xx}^0 + 3\boldsymbol{Z}_f} \tag{5.11c}$$

The during-fault sequence voltages at node *m* are given by

$$\boldsymbol{V}^{P,mx} = \boldsymbol{V}_a^{pref(m)} - \boldsymbol{Z}_{mx}^P \frac{\boldsymbol{V}_a^{pref(x)}}{\boldsymbol{Z}_{xx}^P + \boldsymbol{Z}_{xx}^N + \boldsymbol{Z}_{xx}^0 + 3\boldsymbol{Z}_f} \tag{5.12a}$$

$$\boldsymbol{V}^{N,mx} = -\boldsymbol{Z}_{mx}^N \frac{\boldsymbol{V}_a^{pref(x)}}{\boldsymbol{Z}_{xx}^P + \boldsymbol{Z}_{xx}^N + \boldsymbol{Z}_{xx}^0 + 3\boldsymbol{Z}_f} \tag{5.12b}$$

$$\boldsymbol{V}^{0,mx} = -\boldsymbol{Z}_{mx}^0 \frac{\boldsymbol{V}_a^{pref(x)}}{\boldsymbol{Z}_{xx}^P + \boldsymbol{Z}_{xx}^N + \boldsymbol{Z}_{xx}^0 + 3\boldsymbol{Z}_f} \tag{5.12c}$$

Transforming back to phase components, the phase-voltages due to SLG faults are obtained as follows,

$$\boldsymbol{V}_a^{mx} = \boldsymbol{V}_a^{pref(m)} - \left(\boldsymbol{Z}_{mx}^P + \boldsymbol{Z}_{mx}^N + \boldsymbol{Z}_{mx}^0\right) \frac{\boldsymbol{V}_a^{pref(x)}}{\left(\boldsymbol{Z}_{xx}^P + \boldsymbol{Z}_{xx}^N + \boldsymbol{Z}_{xx}^0 + 3\boldsymbol{Z}_f\right)} \tag{5.13a}$$

$$\boldsymbol{V}_b^{mx} = a^2\boldsymbol{V}_a^{pref(m)} - \left(a^2\boldsymbol{Z}_{mx}^P + a\,\boldsymbol{Z}_{mx}^N + \boldsymbol{Z}_{mx}^0\right) \frac{\boldsymbol{V}_a^{pref(x)}}{\left(\boldsymbol{Z}_{xx}^P + \boldsymbol{Z}_{xx}^N + \boldsymbol{Z}_{xx}^0 + 3\boldsymbol{Z}_f\right)} \tag{5.13b}$$

$$\boldsymbol{V}_c^{mx} = a\boldsymbol{V}_a^{pref(m)} - \left(a\,\boldsymbol{Z}_{mx}^P + a^2\boldsymbol{Z}_{mx}^N + \boldsymbol{Z}_{mx}^0\right) \frac{\boldsymbol{V}_a^{pref(x)}}{\left(\boldsymbol{Z}_{xx}^P + \boldsymbol{Z}_{xx}^N + \boldsymbol{Z}_{xx}^0 + 3\boldsymbol{Z}_f\right)} \tag{5.13c}$$

(b) Unbalanced voltage dip due to phase-to-phase fault

In the analysis of phase-to-phase fault, only the negative and positive sequence networks participate. As shown in Fig. 5.3 (c), the positive- and negative-sequence

current at the fault location is equal in magnitude, but the direction is opposite. Equation (5.14) gives the injected currents in the sequence networks.

$$\boldsymbol{I}_x^P = -\frac{\boldsymbol{V}_a^{pref(x)}}{\boldsymbol{Z}_{xx}^P + \boldsymbol{Z}_{xx}^N + \boldsymbol{Z}_f}; \boldsymbol{I}_x^P = -\boldsymbol{I}_x^N \tag{5.14}$$

The change of positive- and negative-sequence voltage is given by

$$\Delta \boldsymbol{V}^{P,mx} = -\boldsymbol{Z}_{mx}^P \frac{\boldsymbol{V}_a^{pref(x)}}{\boldsymbol{Z}_{xx}^P + \boldsymbol{Z}_{xx}^N + \boldsymbol{Z}_f} \tag{5.15a}$$

$$\Delta \boldsymbol{V}^{N,mx} = \boldsymbol{Z}_{mx}^N \frac{\boldsymbol{V}_a^{pref(x)}}{\boldsymbol{Z}_{xx}^P + \boldsymbol{Z}_{xx}^N + \boldsymbol{Z}_f} \tag{5.15b}$$

Moreover, the change of zero-sequence voltage is zero. Thus, the phase-voltages are obtained by adding the pre-fault voltage to (5.15a) and then, performing the transformation of sequence components to phase components. This yields the phase-voltages, at bus *m* due to phase-to-phase faults at bus *x*, as given below,

$$\boldsymbol{V}_a^{mx} = \boldsymbol{V}_a^{pref(m)} + \left(\boldsymbol{Z}_{mx}^N - \boldsymbol{Z}_{mx}^P\right) \frac{\boldsymbol{V}_a^{pref(x)}}{\left(\boldsymbol{Z}_{xx}^P + \boldsymbol{Z}_{xx}^N + \boldsymbol{Z}_f\right)} \tag{5.16a}$$

$$\boldsymbol{V}_b^{mx} = a^2 \boldsymbol{V}_a^{pref(m)} + \left(a\,\boldsymbol{Z}_{mx}^N - a^2 \boldsymbol{Z}_{mx}^P\right) \frac{\boldsymbol{V}_a^{pref(x)}}{\left(\boldsymbol{Z}_{xx}^P + \boldsymbol{Z}_{xx}^N + \boldsymbol{Z}_f\right)} \tag{5.16b}$$

$$\boldsymbol{V}_c^{mx} = a\boldsymbol{V}_a^{pref(m)} + \left(a^2 \boldsymbol{Z}_{mx}^N - a\,\boldsymbol{Z}_{mx}^P\right) \frac{\boldsymbol{V}_a^{pref(x)}}{\left(\boldsymbol{Z}_{xx}^P + \boldsymbol{Z}_{xx}^N + \boldsymbol{Z}_f\right)} \tag{5.16c}$$

(c) Unbalanced voltage dip due to double-phase to ground fault

Following the diagram shown in Fig. 5.3 (d), the fault current due to two-phase-to-ground fault can be easily derived. The three sequence currents are different as the sequence networks are connected in parallel. Thus, the injected currents in the sequence networks are given by

$$\boldsymbol{I}_x^P = -\frac{\boldsymbol{V}_a^{pref(x)}}{\boldsymbol{Z}_{xx}^P + \dfrac{\boldsymbol{Z}_{xx}^N\left(\boldsymbol{Z}_{xx}^0 + 3\boldsymbol{Z}_f\right)}{\boldsymbol{Z}_{xx}^N + \boldsymbol{Z}_{xx}^0 + 3\boldsymbol{Z}_f}} = -\frac{\boldsymbol{V}_a^{pref(x)}\left(\boldsymbol{Z}_{xx}^N + \boldsymbol{Z}_{xx}^0 + 3\boldsymbol{Z}_f\right)}{\boldsymbol{Z}_{xx}^P\boldsymbol{Z}_{xx}^N + \boldsymbol{Z}_{xx}^P\left(\boldsymbol{Z}_{xx}^0 + 3\boldsymbol{Z}_f\right) + \boldsymbol{Z}_{xx}^N\left(\boldsymbol{Z}_{xx}^0 + 3\boldsymbol{Z}_f\right)} \tag{5.17a}$$

$$\boldsymbol{I}_x^N = \frac{\boldsymbol{V}_a^{pref(x)}\left(\boldsymbol{Z}_{xx}^0 + 3\boldsymbol{Z}_f\right)}{\boldsymbol{Z}_{xx}^P\boldsymbol{Z}_{xx}^N + \boldsymbol{Z}_{xx}^P\left(\boldsymbol{Z}_{xx}^0 + 3\boldsymbol{Z}_f\right) + \boldsymbol{Z}_{xx}^N\left(\boldsymbol{Z}_{xx}^0 + 3\boldsymbol{Z}_f\right)} \tag{5.17b}$$

$$\boldsymbol{I}_x^0 = \frac{\boldsymbol{V}_a^{pref(x)} \boldsymbol{Z}_{xx}^N}{\boldsymbol{Z}_{xx}^P \boldsymbol{Z}_{xx}^N + \boldsymbol{Z}_{xx}^P \left(\boldsymbol{Z}_{xx}^0 + 3\boldsymbol{Z}_f\right) + \boldsymbol{Z}_{xx}^N \left(\boldsymbol{Z}_{xx}^0 + 3\boldsymbol{Z}_f\right)} \tag{5.17c}$$

The nodal voltages can be calculated by means of sequence currents and the transfer impedances in the corresponding sequence. The positive-sequence voltage is the only sequence voltage that is present prior to the fault and is equal to the pre-fault voltage at phase *a*. Thus, the during fault sequence voltages are

$$\boldsymbol{V}^{P,mx} = \boldsymbol{V}_a^{pref(m)} - \boldsymbol{Z}_{mx}^P \frac{\boldsymbol{V}_a^{pref(x)} \left(\boldsymbol{Z}_{xx}^N + \boldsymbol{Z}_{xx}^0 + 3\boldsymbol{Z}_f\right)}{\boldsymbol{Z}_{xx}^P \boldsymbol{Z}_{xx}^N + \boldsymbol{Z}_{xx}^P \left(\boldsymbol{Z}_{xx}^0 + 3\boldsymbol{Z}_f\right) + \boldsymbol{Z}_{xx}^N \left(\boldsymbol{Z}_{xx}^0 + 3\boldsymbol{Z}_f\right)} \tag{5.18a}$$

$$\boldsymbol{V}^{N,mx} = \boldsymbol{Z}_{mx}^N \frac{\boldsymbol{V}_a^{pref(x)} \left(\boldsymbol{Z}_{xx}^0 + 3\boldsymbol{Z}_f\right)}{\boldsymbol{Z}_{xx}^P \boldsymbol{Z}_{xx}^N + \boldsymbol{Z}_{xx}^P \left(\boldsymbol{Z}_{xx}^0 + 3\boldsymbol{Z}_f\right) + \boldsymbol{Z}_{xx}^N \left(\boldsymbol{Z}_{xx}^0 + 3\boldsymbol{Z}_f\right)} \tag{5.18b}$$

$$\boldsymbol{V}^{0,mx} = \boldsymbol{Z}_{mx}^0 \frac{\boldsymbol{V}_a^{pref(x)} \boldsymbol{Z}_{xx}^N}{\boldsymbol{Z}_{xx}^P \boldsymbol{Z}_{xx}^N + \boldsymbol{Z}_{xx}^P \left(\boldsymbol{Z}_{xx}^0 + 3\boldsymbol{Z}_f\right) + \boldsymbol{Z}_{xx}^N \left(\boldsymbol{Z}_{xx}^0 + 3\boldsymbol{Z}_f\right)} \tag{5.18c}$$

Finally, the during-fault phase voltages are found by applying the symmetrical component transformation as follows,

$$\boldsymbol{V}_a^{mx} = \boldsymbol{V}_a^{pref(m)} + \boldsymbol{V}_a^{pref(x)} \frac{\left\{\left(\boldsymbol{Z}_{mx}^N - \boldsymbol{Z}_{mx}^P\right)\left(\boldsymbol{Z}_{xx}^0 + 3\boldsymbol{Z}_f\right) + \left(\boldsymbol{Z}_{mx}^0 - \boldsymbol{Z}_{mx}^P\right)\boldsymbol{Z}_{xx}^N\right\}}{\boldsymbol{Z}_{xx}^P \boldsymbol{Z}_{xx}^N + \boldsymbol{Z}_{xx}^P \left(\boldsymbol{Z}_{xx}^0 + 3\boldsymbol{Z}_f\right) + \boldsymbol{Z}_{xx}^N \left(\boldsymbol{Z}_{xx}^0 + 3\boldsymbol{Z}_f\right)} \tag{5.19a}$$

$$\boldsymbol{V}_b^{mx} = a^2 \boldsymbol{V}_a^{pref(m)} + \boldsymbol{V}_a^{pref(x)} \frac{\left\{\left(a\,\boldsymbol{Z}_{mx}^N - a^2 \boldsymbol{Z}_{mx}^P\right)\left(\boldsymbol{Z}_{xx}^0 + 3\boldsymbol{Z}_f\right) + \left(\boldsymbol{Z}_{mx}^0 - a^2 \boldsymbol{Z}_{mx}^P\right)\boldsymbol{Z}_{xx}^N\right\}}{\boldsymbol{Z}_{xx}^P \boldsymbol{Z}_{xx}^N + \boldsymbol{Z}_{xx}^P \left(\boldsymbol{Z}_{xx}^0 + 3\boldsymbol{Z}_f\right) + \boldsymbol{Z}_{xx}^N \left(\boldsymbol{Z}_{xx}^0 + 3\boldsymbol{Z}_f\right)} \tag{5.19b}$$

$$\boldsymbol{V}_c^{mx} = a\boldsymbol{V}_a^{pref(m)} + \boldsymbol{V}_a^{pref(x)} \frac{\left\{\left(a^2 \boldsymbol{Z}_{mx}^N - a\,\boldsymbol{Z}_{mx}^P\right)\left(\boldsymbol{Z}_{xx}^0 + 3\boldsymbol{Z}_f\right) + \left(\boldsymbol{Z}_{mx}^0 - a\,\boldsymbol{Z}_{mx}^P\right)\boldsymbol{Z}_{xx}^N\right\}}{\boldsymbol{Z}_{xx}^P \boldsymbol{Z}_{xx}^N + \boldsymbol{Z}_{xx}^P \left(\boldsymbol{Z}_{xx}^0 + 3\boldsymbol{Z}_f\right) + \boldsymbol{Z}_{xx}^N \left(\boldsymbol{Z}_{xx}^0 + 3\boldsymbol{Z}_f\right)} \tag{5.19c}$$

5.2.3 Voltage-dip and phase-angle jump for seven types of Dips

Seven types of voltage dips normally exist in electricity networks; they are A, B, D, F, E, C and G type, as discussed in Chapter 2. Dip-types A, B, and E are obtained due to 3-phase, single line-to-ground, and phase-to-phase faults, measured at the fault location. Dip-type C may result from phase-to-phase fault measured at the fault location. Dip-types D and F are obtained from the propagation of dip-types C and E via transformers. Dip-type G usually results from the propagation of dip-type F [31] and it is usually

found for double line-to-ground faults. Phasor representation of seven types of voltage dips with severely affected dip-phase is illustrated in Table 5-I.

TABLE 5-I

VOLTAGE PHASORS FOR SEVEN TYPES OF VOLTAGE DIPS

Dip-type	Severely affected dip-phase	Phasor re-presentation of voltages (solid arrow indicates voltages during dip)
A	*abc*-phase	Voltage phasors: 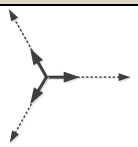
B	*a*-phase or *b*-phase or *c*-phase	Voltage phasors (severely affected *a*-phase): 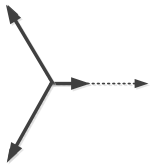
C	*ab*-phase or *bc*-phase or *ca*-phase	Voltage phasors (severely affected *bc*-phase): 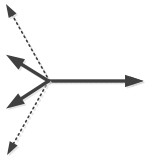
D	*a*-phase or *b*-phase or *c*-phase	Voltage phasors (severely affected *a*-phase): 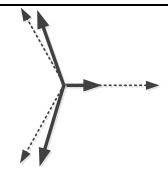
E	*ab*-phase or *bc*-phase or *ca*-phase	Voltage phasors (severely affected *bc*-phase): 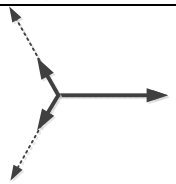
F	*a*-phase or *b*-phase or *c*-phase	Voltage phasors (severely affected *a*-phase): 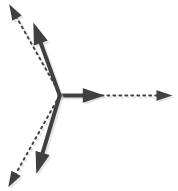
G	*ab*-phase or *bc*-phase or *ca*-phase	Voltage phasors (severely affected *bc*-phase): 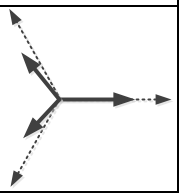

In summary, three types of dips are characterized with major drop in one of the phases (B, D, and F); they are called single phase voltage dips, see Table 5-I for illustration. Three dips are characterized with major drops in two of the phases and are called double phase dips (C, E, and G). The dip-type A is called a three-phase dip or

balanced or symmetrical dip. Now, the expression of voltage-dip d_v is derived for seven types of dips, assuming the pre-fault voltage at monitoring bus m and the faulted bus x is $1\angle 0°$.

(a) Voltage-dip d_v for type A

From (5.6), the expression of phase-a magnitude for type-A dip can be given by (assuming pre-fault voltages $=1\angle 0°$)

$$\left|\boldsymbol{V}_a^{mx}\right| = \left|1 - \frac{\boldsymbol{Z}_{mx}}{\boldsymbol{Z}_{xx} + \boldsymbol{Z}_f}\right| \tag{5.20}$$

Thus, for dip-type A, the expression of voltage-dip d_v, observed at monitoring bus m due to fault at bus x, is given by

$$d_v^{mx} = 1 - \left|\Omega_{\boldsymbol{A}}\right| \tag{5.21}$$

where $\Omega_{\boldsymbol{A}} = 1 - \dfrac{\boldsymbol{Z}_{mx}}{\boldsymbol{Z}_{xx} + \boldsymbol{Z}_f}$.

(b) Voltage-dip d_v for type B, D and F

Taking the phase-voltage a into account, from (5.13a), the expression of phase-a magnitude for dip-types B, D, and F can be given by (assuming pre-fault voltages = $1\angle 0°$)

$$\left|\boldsymbol{V}_a^{mx}\right| = \left|1 - \frac{\boldsymbol{Z}_{mx}^{P} + \boldsymbol{Z}_{mx}^{N} + \boldsymbol{Z}_{mx}^{0}}{\boldsymbol{Z}_{xx}^{P} + \boldsymbol{Z}_{xx}^{N} + \boldsymbol{Z}_{xx}^{0} + 3\boldsymbol{Z}_f}\right| \tag{5.22}$$

Thus, for dip-types B, D and F, the expressions of voltage-dip d_v, observed at monitoring bus m due to fault at bus x, are given by

$$d_v^{mx} = 1 - \left|\Omega_{\boldsymbol{BDF}}\right| \tag{5.23}$$

where $\Omega_{\boldsymbol{BDF}} = 1 - \dfrac{\boldsymbol{Z}_{mx}^{P} + \boldsymbol{Z}_{mx}^{N} + \boldsymbol{Z}_{mx}^{0}}{\boldsymbol{Z}_{xx}^{P} + \boldsymbol{Z}_{xx}^{N} + \boldsymbol{Z}_{xx}^{0} + 3\boldsymbol{Z}_f}$.

(c) Voltage-dip d_v for type E and C

Taking the phase-voltage *b* into account, from Eq. (5.16b), the expression of phase-*b* magnitude for dip-types E, and C can be given by (assuming pre-fault voltages $=1\angle 0°$)

$$\left|\boldsymbol{V}_b^{mx}\right| = \left| e^{j4\pi/3} + \frac{e^{j2\pi/3}\boldsymbol{Z}_{mx}^{N} - e^{j4\pi/3}\boldsymbol{Z}_{mx}^{P}}{\boldsymbol{Z}_{xx}^{P} + \boldsymbol{Z}_{xx}^{N} + \boldsymbol{Z}_f} \right| \tag{5.24}$$

Thus, for dip-types E and C, the expressions of voltage-dip d_v, observed at monitoring bus *m* due to fault at bus *x*, are given by

$$d_v^{mx} = 1 - \left|\Omega_{\boldsymbol{EC}}\right| \tag{5.25}$$

where $\Omega_{\boldsymbol{EC}} = e^{j4\pi/3} + \dfrac{e^{j2\pi/3}\boldsymbol{Z}_{mx}^{N} - e^{j4\pi/3}\boldsymbol{Z}_{mx}^{P}}{\boldsymbol{Z}_{xx}^{P} + \boldsymbol{Z}_{xx}^{N} + \boldsymbol{Z}_f}$.

(d) Voltage-dip d_v for type G

Considering the phase-voltage *b*, from Eq. (5.19b), the expression of phase-*b* magnitude for dip-type G can be given by (assuming pre-fault voltages $=1\angle 0°$)

$$\left|\boldsymbol{V}_b^{mx}\right| = \left| \boldsymbol{e}^{j4\pi/3} + \frac{\left\{\left(\boldsymbol{e}^{j2\pi/3}\boldsymbol{Z}_{mx}^{N} - \boldsymbol{e}^{j4\pi/3}\boldsymbol{Z}_{mx}^{P}\right)\left(\boldsymbol{Z}_{xx}^{0} + 3\boldsymbol{Z}_f\right) + \left(\boldsymbol{Z}_{mx}^{0} - \boldsymbol{e}^{j4\pi/3}\boldsymbol{Z}_{mx}^{P}\right)\boldsymbol{Z}_{xx}^{N}\right\}}{\boldsymbol{Z}_{xx}^{P}\boldsymbol{Z}_{xx}^{N} + \boldsymbol{Z}_{xx}^{P}\left(\boldsymbol{Z}_{xx}^{0} + 3\boldsymbol{Z}_f\right) + \boldsymbol{Z}_{xx}^{N}\left(\boldsymbol{Z}_{xx}^{0} + 3\boldsymbol{Z}_f\right)} \right| \tag{5.26}$$

Thus, for dip-type G, the expressions of voltage-dip d_v, observed at monitoring bus *m* due to fault at bus *x*, are given by

$$d_v^{mx} = 1 - \left|\Omega_{\boldsymbol{G}}\right| \tag{5.27}$$

where $\Omega_{\boldsymbol{G}} = \boldsymbol{e}^{j4\pi/3} + \dfrac{\left\{\left(\boldsymbol{e}^{j2\pi/3}\boldsymbol{Z}_{mx}^{N} - \boldsymbol{e}^{j4\pi/3}\boldsymbol{Z}_{mx}^{P}\right)\left(\boldsymbol{Z}_{xx}^{0} + 3\boldsymbol{Z}_f\right) + \left(\boldsymbol{Z}_{mx}^{0} - \boldsymbol{e}^{j4\pi/3}\boldsymbol{Z}_{mx}^{P}\right)\boldsymbol{Z}_{xx}^{N}\right\}}{\boldsymbol{Z}_{xx}^{P}\boldsymbol{Z}_{xx}^{N} + \boldsymbol{Z}_{xx}^{P}\left(\boldsymbol{Z}_{xx}^{0} + 3\boldsymbol{Z}_f\right) + \boldsymbol{Z}_{xx}^{N}\left(\boldsymbol{Z}_{xx}^{0} + 3\boldsymbol{Z}_f\right)}$.

The expressions of d_v for seven types of dips are summarized in Table 5-II. Along with the reduction of the voltage magnitude, as presented through the expressions of d_v^{mx}, remote fault also leads to a variation in the phase angle of the voltage. This variation of phase angle is known as phase-angle jump [116]. From Eq. (5.6) it can be observed that for symmetrical fault or type-A dip, phase-angle jump occurs when the

quotient $\frac{\boldsymbol{Z}_{mx}}{\boldsymbol{Z}_{xx}+\boldsymbol{Z}_f}$ is not a real number. However, for unsymmetrical fault or dip-types B, D, F, E, C, and G, the phase-angle jump of each phase-voltage are considered separately. From expressions (5.3)-(5.19), the phase-angle jumps corresponding to seven types of voltage dips can be easily derived, and these are given in Table 5-III. It is to be noted that for deriving the expressions of phase-angle jump, pre-fault voltage is assumed to be $1\angle 0°$. Moreover, due to fault at bus *x* and monitoring point at bus *m* of Fig. 5.1, the phase-angle jumps at *a*-, *b*-, and *c*-phase are denoted as $\Delta\mu_{\boldsymbol{a}}^{mx}$, $\Delta\mu_{\boldsymbol{b}}^{mx}$, and $\Delta\mu_{\boldsymbol{c}}^{mx}$, respectively.

TABLE 5-II

EXPRESSIONS OF VOLTAGE-DIP FOR SEVEN TYPES OF VOLTAGE DIPS

Dip-type	Voltage-dip (d_v) at monitoring node *m* due to fault at bus *x*
A	$d_v^{mx}=1-\lvert\Omega_{\boldsymbol{A}}\rvert$ where $\Omega_{\boldsymbol{A}}=1-\frac{\boldsymbol{Z}_{mx}}{\boldsymbol{Z}_{xx}+\boldsymbol{Z}_f}$
B, D, F	$d_v^{mx}=1-\lvert\Omega_{\boldsymbol{BDF}}\rvert$ where $\Omega_{\boldsymbol{BDF}}=1-\frac{\boldsymbol{Z}_{mx}^{P}+\boldsymbol{Z}_{mx}^{N}+\boldsymbol{Z}_{mx}^{0}}{\boldsymbol{Z}_{xx}^{P}+\boldsymbol{Z}_{xx}^{N}+\boldsymbol{Z}_{xx}^{0}+3\boldsymbol{Z}_f}$
E, C	$d_v^{mx}=1-\lvert\Omega_{\boldsymbol{EC}}\rvert$ where $\Omega_{\boldsymbol{EC}}=\boldsymbol{e}^{j4\pi/3}+\frac{\boldsymbol{e}^{j2\pi/3}\boldsymbol{Z}_{mx}^{N}-\boldsymbol{e}^{j4\pi/3}\boldsymbol{Z}_{mx}^{P}}{\boldsymbol{Z}_{xx}^{P}+\boldsymbol{Z}_{xx}^{N}+\boldsymbol{Z}_f}$
G	$d_v^{mx}=1-\lvert\Omega_{\boldsymbol{G}}\rvert$ where $\Omega_{\boldsymbol{G}}=\boldsymbol{e}^{j4\pi/3}+\frac{\left\{\left(\boldsymbol{e}^{j2\pi/3}\boldsymbol{Z}_{mx}^{N}-\boldsymbol{e}^{j4\pi/3}\boldsymbol{Z}_{mx}^{P}\right)\left(\boldsymbol{Z}_{xx}^{0}+3\boldsymbol{Z}_f\right)+\left(\boldsymbol{Z}_{mx}^{0}-\boldsymbol{e}^{j4\pi/3}\boldsymbol{Z}_{mx}^{P}\right)\boldsymbol{Z}_{xx}^{N}\right\}}{\boldsymbol{Z}_{xx}^{P}\boldsymbol{Z}_{xx}^{N}+\boldsymbol{Z}_{xx}^{P}\left(\boldsymbol{Z}_{xx}^{0}+3\boldsymbol{Z}_f\right)+\boldsymbol{Z}_{xx}^{N}\left(\boldsymbol{Z}_{xx}^{0}+3\boldsymbol{Z}_f\right)}$

TABLE 5-III

EXPRESSIONS OF PHASE-ANGLE JUMP FOR DIFFERENT DIP-TYPES

Dip-type	Phase-angle jump at monitoring node *m* due to fault at bus *x*
A	$\Delta\mu_a^{mx} = \left\lvert \arg\left\{ e^{j0} - \frac{Z_{mx}}{Z_{xx} + Z_f} \right\} \right\rvert = \Delta\mu_b^{mx} = \Delta\mu_c^{mx}$
B	$\Delta\mu_a^{mx} = \left\lvert \arg\left\{ e^{j0} - \frac{Z_{mx}^P + Z_{mx}^N + Z_{mx}^0}{Z_{xx}^P + Z_{xx}^N + Z_{xx}^0 + 3Z_f} \right\} \right\rvert$ $\Delta\mu_b^{mx} = \left\lvert \frac{4\pi}{3} - \arg\left\{ e^{j4\pi/3} - \frac{e^{j4\pi/3} Z_{mx}^P + e^{j2\pi/3} Z_{mx}^N + Z_{mx}^0}{Z_{xx}^P + Z_{xx}^N + Z_{xx}^0 + 3Z_f} \right\} \right\rvert$ $\Delta\mu_c^{mx} = \left\lvert \frac{2\pi}{3} - \arg\left\{ e^{j2\pi/3} - \frac{e^{j2\pi/3} Z_{mx}^P + e^{j4\pi/3} Z_{mx}^N + Z_{mx}^0}{Z_{xx}^P + Z_{xx}^N + Z_{xx}^0 + 3Z_f} \right\} \right\rvert$
E	$\Delta\mu_a^{mx} = \left\lvert \arg\left\{ e^{j0} + \frac{Z_{mx}^N - Z_{mx}^P}{Z_{xx}^P + Z_{xx}^N + Z_f} \right\} \right\rvert$ $\Delta\mu_b^{mx} = \left\lvert \frac{4\pi}{3} - \arg\left\{ e^{j4\pi/3} + \frac{e^{j2\pi/3} Z_{mx}^N - e^{j4\pi/3} Z_{mx}^P}{Z_{xx}^P + Z_{xx}^N + Z_f} \right\} \right\rvert$ $\Delta\mu_c^{mx} = \left\lvert \frac{2\pi}{3} - \arg\left\{ e^{j2\pi/3} + \frac{e^{j4\pi/3} Z_{mx}^N - e^{j2\pi/3} Z_{mx}^P}{Z_{xx}^P + Z_{xx}^N + Z_f} \right\} \right\rvert$
G	$\mu_a^{mx} = \left\lvert \arg\left[e^{j0} + \frac{\left\{ \left(Z_{mx}^N - Z_{mx}^P \right)\left(Z_{xx}^0 + 3Z_f \right) + \left(Z_{mx}^0 - Z_{mx}^P \right) Z_{xx}^N \right\}}{Z_{xx}^P Z_{xx}^N + Z_{xx}^P \left(Z_{xx}^0 + 3Z_f \right) + Z_{xx}^N \left(Z_{xx}^0 + 3Z_f \right)} \right] \right\rvert$ $\Delta\mu_b^{mx} = \left\lvert \frac{4\pi}{3} - \arg\left[e^{j4\pi/3} + \frac{\left\{ \left(e^{j2\pi/3} Z_{mx}^N - e^{j4\pi/3} Z_{mx}^P \right)\left(Z_{xx}^0 + 3Z_f \right) + \left(Z_{mx}^0 - e^{j4\pi/3} Z_{mx}^P \right) Z_{xx}^N \right\}}{Z_{xx}^P Z_{xx}^N + Z_{xx}^P \left(Z_{xx}^0 + 3Z_f \right) + Z_{xx}^N \left(Z_{xx}^0 + 3Z_f \right)} \right] \right\rvert$ $\Delta\mu_c^{mx} = \left\lvert \frac{2\pi}{3} - \arg\left[e^{j2\pi/3} + \frac{\left\{ \left(e^{j4\pi/3} Z_{mx}^N - e^{j2\pi/3} Z_{mx}^P \right)\left(Z_{xx}^0 + 3Z_f \right) + \left(Z_{mx}^0 - e^{j2\pi/3} Z_{mx}^P \right) Z_{xx}^N \right\}}{Z_{xx}^P Z_{xx}^N + Z_{xx}^P \left(Z_{xx}^0 + 3Z_f \right) + Z_{xx}^N \left(Z_{xx}^0 + 3Z_f \right)} \right] \right\rvert$

5.2.4 Voltage-dip d_v and phase-angle jump for seven types of Voltage Dips with DG

Table 5-II and 5-III summarize the expressions of voltage-dip and phase-angle jumps due to different types of dips. In these expressions, inclusion of DG was not considered. Considering a synchronous generator based DG connected at *n*-th bus of Fig. 5.1, the expressions of d_v (voltage-dip) and phase-angle jumps associated with balanced and unbalanced fault initiated dips are presented below.

i) Balanced voltage dip (Type A) with DG

Due to balanced or symmetrical fault at bus *x*, voltage at any monitoring bus *m* can be obtained. To do so, the test network of Fig. 5.1 is simplified to derive the during-fault voltage at *m* and the simplified equivalent network is shown in Fig. 5.4. Now, expressing the DG internal voltage as $\boldsymbol{E}_{DG}$, and applying superposition theorem at monitoring bus *m*, see Fig 5.4, voltage at bus *m* can be given by

$$\boldsymbol{V}^{mx} = \frac{\boldsymbol{E}_s \boldsymbol{Z}_f \left(\boldsymbol{Z}_{eq}^{mn} + \boldsymbol{Z}_{DG}\right) + \boldsymbol{E}_{DG}\left\{\boldsymbol{Z}_f\left(\boldsymbol{Z}_s + \boldsymbol{Z}_{eq}^{1x} + \boldsymbol{Z}_{eq}^{xm}\right) + \left(\boldsymbol{Z}_s + \boldsymbol{Z}_{eq}^{1x}\right)\boldsymbol{Z}_{eq}^{xm}\right\}}{\boldsymbol{Z}_f \boldsymbol{Z}_{eq}^{1x} + \left(\boldsymbol{Z}_{eq}^{mn} + \boldsymbol{Z}_{DG} + \boldsymbol{Z}_{eq}^{xm}\right)\left(\boldsymbol{Z}_s + \boldsymbol{Z}_f + \boldsymbol{Z}_{eq}^{1x}\right)} \quad (5.28)$$

where

$\boldsymbol{Z}_{eq}^{1x}$ = Equivalent impedance between bus *x* and PCC bus or bus *1*,

$\boldsymbol{Z}_{eq}^{mn}$ = Equivalent impedance between bus *m* and *n*,

$\boldsymbol{Z}_{eq}^{xm}$ = Equivalent impedance between bus *x* and *m*.

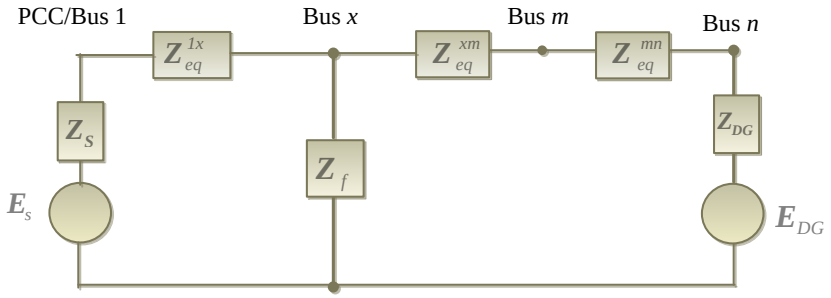

Fig. 5.4. Simplified network diagram of the test system of Fig. 5.1 for dip-type A associated with balanced 3-phase or symmetrical fault at bus *x*.

Taking the magnitude of phase-voltage *a* of (5.28) into account, voltage-dip (d_v) at monitoring bus *m* due to fault at bus *x* can be given by

$$d_v^{mx} = 1 - \left| \frac{\boldsymbol{E}_s \boldsymbol{Z}_f \left(\boldsymbol{Z}_{eq}^{mn} + \boldsymbol{Z}_{DG}\right) + \boldsymbol{E}_{DG}\left\{\boldsymbol{Z}_f\left(\boldsymbol{Z}_s + \boldsymbol{Z}_{eq}^{1x} + \boldsymbol{Z}_{eq}^{xm}\right) + \left(\boldsymbol{Z}_s + \boldsymbol{Z}_{eq}^{1x}\right)\boldsymbol{Z}_{eq}^{xm}\right\}}{\boldsymbol{Z}_f \boldsymbol{Z}_{eq}^{1x} + \left(\boldsymbol{Z}_{eq}^{mn} + \boldsymbol{Z}_{DG} + \boldsymbol{Z}_{eq}^{xm}\right)\left(\boldsymbol{Z}_s + \boldsymbol{Z}_f + \boldsymbol{Z}_{eq}^{1x}\right)} \right| \quad (5.29)$$

Besides, phase-angle jump associated with dip-type A can be easily obtained from (5.29), which is given by

$$\Delta\mu_a^{mx} = \arg\left\{ \frac{\boldsymbol{E}_s \boldsymbol{Z}_f \left(\boldsymbol{Z}_{eq}^{mn} + \boldsymbol{Z}_{DG}\right) + \boldsymbol{E}_{DG}\left\{\boldsymbol{Z}_f\left(\boldsymbol{Z}_s + \boldsymbol{Z}_{eq}^{1x} + \boldsymbol{Z}_{eq}^{xm}\right) + \left(\boldsymbol{Z}_s + \boldsymbol{Z}_{eq}^{1x}\right)\boldsymbol{Z}_{eq}^{xm}\right\}}{\boldsymbol{Z}_f \boldsymbol{Z}_{eq}^{1x} + \left(\boldsymbol{Z}_{eq}^{mn} + \boldsymbol{Z}_{DG} + \boldsymbol{Z}_{eq}^{xm}\right)\left(\boldsymbol{Z}_s + \boldsymbol{Z}_f + \boldsymbol{Z}_{eq}^{1x}\right)} \right\} \quad (5.30)$$

Expressions (5.28)-(5.30) are valid for the network topology shown in Fig. 5.1. In Fig. 5.1, DG is connected at remote end of a radial distribution feeder, and fault occurs between PCC bus and DG-connected bus. Thus, the simplified diagram of Fig. 5.4 is obtained and it is solved to get the during-fault (balanced) voltage at any monitoring bus *m* by applying superposition theorem. Similarly, for different positioning of DG along with different fault-location in the network, firstly, the simplified diagram needs to be obtained; then it can be solved to get the during-fault (balanced) voltage at any monitoring bus.

ii) Unbalanced voltage dip (Type B, D, F, E, C, and G) with DG

The presence of synchronous generator based DG in the network will obviously have an impact on the positive-, negative- and zero-sequence impedance matrix. Therefore, in order to develop the expressions of voltage-dip due to unbalanced faults with DG, the sequence impedance matrixes are taken into consideration. The positive-, negative- and zero-sequence impedance matrixes at the presence of synchronous generator based DG are shown in Fig. 5.5, which is acquired due to unbalanced fault at bus *x* of Fig. 5.1. Now, the description of symbols used in Fig. 5.5 is given below:

$\boldsymbol{Z}_{\boldsymbol{S}}^{P}, \boldsymbol{Z}_{\boldsymbol{S}}^{N}, \boldsymbol{Z}_{\boldsymbol{S}}^{0}$ are the positive-, negative-, and zero-sequence impedance of upstream source, respectively.

$\boldsymbol{Z}_{\boldsymbol{DG}}^{P}, \boldsymbol{Z}_{\boldsymbol{DG}}^{N}, \boldsymbol{Z}_{\boldsymbol{DG}}^{0}$ are the positive-, negative-, and zero-sequence impedance of synchronous generator based DG, respectively.

$\boldsymbol{Z}_{\boldsymbol{eq}}^{P,1x}, \boldsymbol{Z}_{\boldsymbol{eq}}^{N,1x}, \boldsymbol{Z}_{\boldsymbol{eq}}^{0,1x}$ are the positive-, negative-, and zero-sequence equivalent impedance between bus 1 and bus *x*.

$\boldsymbol{Z}_{\boldsymbol{eq}}^{P,xn}, \boldsymbol{Z}_{\boldsymbol{eq}}^{N,xn}, \boldsymbol{Z}_{\boldsymbol{eq}}^{0,xn}$ are the positive-, negative-, and zero-sequence equivalent impedance between bus *x* and bus *n*.

$\boldsymbol{Z}_{\boldsymbol{xx}}^{P'}, \boldsymbol{Z}_{\boldsymbol{xx}}^{N'}, \boldsymbol{Z}_{\boldsymbol{xx}}^{0'}$ are the positive-, negative-, and zero-sequence Thévenin equivalent impedance observed at bus *x*.

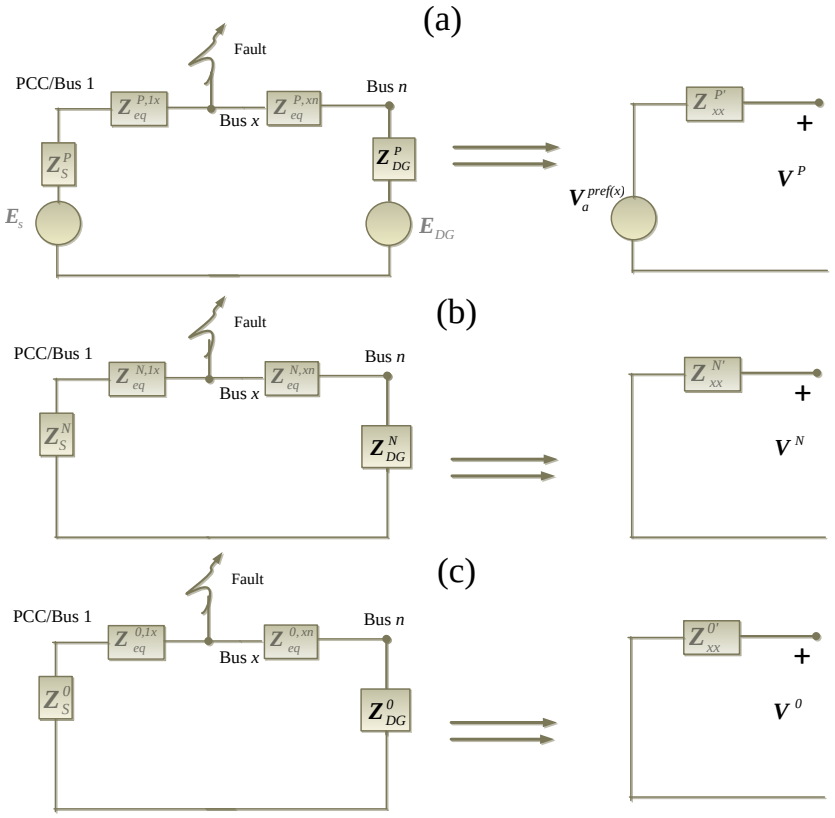

Fig. 5.5. (a) Positive-, (b) negative-, and (c) zero-sequence impedance diagrams of the test system of Fig. 5.1 for investigating voltage-dip associated with unbalanced fault at bus *x*.

Balanced faults as well as unbalanced faults including SLG, phase-to-phase, and double line-to-ground fault can be investigated by connecting the three sequence networks of Fig. 5.5 in the order as shown in Fig. 5.3. It is to be noted that from the equivalent network diagrams as illustrated in Fig. 5.5, calculation of Thévenin equivalent impedance $\left(\boldsymbol{Z}_{\boldsymbol{xx}}^{P'}, \boldsymbol{Z}_{\boldsymbol{xx}}^{N'}, \boldsymbol{Z}_{\boldsymbol{xx}}^{0'}\right)$ is a cumbersome task, especially for a large network with multiple DGs. Therefore, in order to make the task independent of network topology, bus impedance matrix is utilized. To this end, firstly, a minor modification, due to introduction of DG, is incorporated in the admittance matrix of (5.1) as follows

$$\left[\boldsymbol{Y}_{BUS}^{'}\right]=\begin{bmatrix} \boldsymbol{Y}_{11} & \boldsymbol{Y}_{12} \ldots\ldots\ldots\ldots\ldots \boldsymbol{Y}_{1x} \ldots\ldots\ldots \boldsymbol{Y}_{1m} \ldots\ldots\ldots\ldots\ldots\ldots \boldsymbol{Y}_{1n} \\ \boldsymbol{Y}_{21} & \boldsymbol{Y}_{22} \ldots\ldots\ldots\ldots\ldots \boldsymbol{Y}_{2x} \ldots\ldots\ldots \boldsymbol{Y}_{2m} \ldots\ldots\ldots\ldots\ldots\ldots \boldsymbol{Y}_{2n} \\ \ldots\ldots\ldots\ldots\ldots\ldots\ldots\ldots\ldots\ldots\ldots\ldots\ldots\ldots\ldots\ldots\ldots\ldots\ldots\ldots \\ \boldsymbol{Y}_{x1} & \boldsymbol{Y}_{x2} \ldots\ldots\ldots\ldots\ldots \boldsymbol{Y}_{xx} \ldots\ldots\ldots \boldsymbol{Y}_{xm} \ldots\ldots\ldots\ldots\ldots\ldots \boldsymbol{Y}_{xn} \\ \ldots\ldots\ldots\ldots\ldots\ldots\ldots\ldots\ldots\ldots\ldots\ldots\ldots\ldots\ldots\ldots\ldots\ldots\ldots\ldots \\ \boldsymbol{Y}_{m1} & \boldsymbol{Y}_{m2} \ldots\ldots\ldots\ldots\ldots \boldsymbol{Y}_{mx} \ldots\ldots\ldots \boldsymbol{Y}_{mm} \ldots\ldots\ldots\ldots\ldots\ldots \boldsymbol{Y}_{mn} \\ \ldots\ldots\ldots\ldots\ldots\ldots\ldots\ldots\ldots\ldots\ldots\ldots\ldots\ldots\ldots\ldots\ldots\ldots\ldots\ldots \\ \boldsymbol{Y}_{n1} & \boldsymbol{Y}_{n2} \ldots\ldots\ldots\ldots\ldots \boldsymbol{Y}_{nx} \ldots\ldots\ldots \boldsymbol{Y}_{nm} \ldots\ldots\ldots\ldots\ldots \boldsymbol{Y}_{nn}+\boldsymbol{Y}_{DG} \end{bmatrix} \tag{5.31}$$

Then, taking the inverse of the bus admittance matrix of (5.31), the bus impedance matrix is achieved; thus, the modified bus impedance matrix is denoted by a slight change in the notation (addition of a "dash" in the superscript of "impedance symbol") and it is given by $[\boldsymbol{Z}'] = [\boldsymbol{Y}_{BUS}']^{-1}$. Now, with the inclusion of DG, the positive-$(\boldsymbol{Z}^{P'})$, negative-$(\boldsymbol{Z}^{N'})$ and zero- $(\boldsymbol{Z}^{0'})$sequence impedance matrix are built as discussed in section 5.2.1. And, the sequence-impedance matrixes are described as: $\boldsymbol{Z}^{P'}$ = positive-sequence impedance matrix including DG's positive-sequence (X_{dg}^{P}) reactance while building the impedance matrix, $\boldsymbol{Z}^{N'}$ = negative-sequence impedance matrix including DG's negative-sequence (X_{dg}^{N}) reactance while building the impedance matrix, $\boldsymbol{Z}^{0'}$ = zero-sequence impedance matrix including DG's zero-sequence reactance (X_{dg}^{0}). Thus, with the introduction of DG, firstly, the sequence-impedance network is formed; then sequence network diagrams associated with different types of fault initiated dips are developed as discussed in Section 5.2.1. Afterwards, the expressions of voltage-dip d_v for seven dip-types are obtained, which are summarized in Table 5-IV. Moreover, the phase-angle jumps associated with these types of dips are presented in Table 5-V.

TABLE 5-IV

EXPRESSIONS OF VOLTAGE-DIP FOR SEVEN TYPES OF VOLTAGE DIPS WITH DG

Dip-type	Voltage-dip (d_v) at monitoring node *m* due to fault at bus *x*
A	$d_v^{mx} = 1 - \left\lvert \frac{\boldsymbol{E}_s \boldsymbol{Z}_f \left(\boldsymbol{Z}_{eq}^{mn} + \boldsymbol{Z}_{DG}\right) + \boldsymbol{E}_{DG}\left\{\boldsymbol{Z}_f\left(\boldsymbol{Z}_s + \boldsymbol{Z}_{eq}^{1x} + \boldsymbol{Z}_{eq}^{xm}\right) + \left(\boldsymbol{Z}_s + \boldsymbol{Z}_{eq}^{1x}\right)\boldsymbol{Z}_{eq}^{xm}\right\}}{\boldsymbol{Z}_f \boldsymbol{Z}_{eq}^{1x} + \left(\boldsymbol{Z}_{eq}^{mn} + \boldsymbol{Z}_{DG} + \boldsymbol{Z}_{eq}^{xm}\right)\left(\boldsymbol{Z}_s + \boldsymbol{Z}_f + \boldsymbol{Z}_{eq}^{1x}\right)} \right\rvert$ Or, $d_v^{mx} = 1 - \left\lvert \Omega_{\boldsymbol{A}}' \right\rvert$, where $\Omega_{\boldsymbol{A}}' = 1 - \frac{\boldsymbol{Z}_{mx}'}{\boldsymbol{Z}_{xx}' + \boldsymbol{Z}_f}$
B, D, F	$d_v^{mx} = 1 - \left\lvert \Omega_{\boldsymbol{BDF}}' \right\rvert$ where $\Omega_{\boldsymbol{BDF}}' = 1 - \frac{\boldsymbol{Z}_{mx}^{P'} + \boldsymbol{Z}_{mx}^{N'} + \boldsymbol{Z}_{mx}^{0'}}{\boldsymbol{Z}_{xx}^{P'} + \boldsymbol{Z}_{xx}^{N'} + \boldsymbol{Z}_{xx}^{0'} + 3\boldsymbol{Z}_f}$
E, C	$d_v^{mx} = 1 - \left\lvert \Omega_{\boldsymbol{EC}}' \right\rvert$ where $\Omega_{\boldsymbol{EC}}' = \boldsymbol{e}^{j4\pi/3} + \frac{\boldsymbol{e}^{j2\pi/3}\boldsymbol{Z}_{mx}^{N'} - \boldsymbol{e}^{j4\pi/3}\boldsymbol{Z}_{mx}^{P'}}{\boldsymbol{Z}_{xx}^{P'} + \boldsymbol{Z}_{xx}^{N'} + \boldsymbol{Z}_f}$
G	$d_v^{mx} = 1 - \left\lvert \Omega_{\boldsymbol{G}}' \right\rvert$ where $\Omega_{\boldsymbol{G}}' = \boldsymbol{e}^{j4\pi/3} + \frac{\left\{\left(\boldsymbol{e}^{j2\pi/3}\boldsymbol{Z}_{mx}^{N'} - \boldsymbol{e}^{j4\pi/3}\boldsymbol{Z}_{mx}^{P'}\right)\left(\boldsymbol{Z}_{xx}^{0'} + 3\boldsymbol{Z}_f\right) + \left(\boldsymbol{Z}_{mx}^{0'} - \boldsymbol{e}^{j4\pi/3}\boldsymbol{Z}_{mx}^{P'}\right)\boldsymbol{Z}_{xx}^{N'}\right\}}{\boldsymbol{Z}_{xx}^{P'}\boldsymbol{Z}_{xx}^{N'} + \boldsymbol{Z}_{xx}^{P'}\left(\boldsymbol{Z}_{xx}^{0'} + 3\boldsymbol{Z}_f\right) + \boldsymbol{Z}_{xx}^{N'}\left(\boldsymbol{Z}_{xx}^{0'} + 3\boldsymbol{Z}_f\right)}$

TABLE 5-V

EXPRESSIONS OF PHASE-ANGLE JUMP FOR DIFFERENT DIP-TYPES WITH DG

Dip-type	Phase-angle jump at monitoring node *m* due to fault at bus *x*
A	$\Delta\mu_a^{mx} = \left\lvert \arg\left\{ \boldsymbol{e}^{j0} - \frac{\boldsymbol{Z}_{mx}^{'}}{\boldsymbol{Z}_{xx}^{'} + \boldsymbol{Z}_f} \right\} \right\rvert = \Delta\mu_b^{mx} = \Delta\mu_c^{mx}$ Or, $\Delta\mu_a^{mx} = \arg\left\{ \frac{\boldsymbol{E}_s \boldsymbol{Z}_f \left(\boldsymbol{Z}_{eq}^{mn} + \boldsymbol{Z}_{DG}\right) + \boldsymbol{E}_{DG}\left\{\boldsymbol{Z}_f\left(\boldsymbol{Z}_s + \boldsymbol{Z}_{eq}^{1x} + \boldsymbol{Z}_{eq}^{xm}\right) + \left(\boldsymbol{Z}_s + \boldsymbol{Z}_{eq}^{1x}\right)\boldsymbol{Z}_{eq}^{xm}\right\}}{\boldsymbol{Z}_f \boldsymbol{Z}_{eq}^{1x} + \left(\boldsymbol{Z}_{eq}^{mn} + \boldsymbol{Z}_{DG} + \boldsymbol{Z}_{eq}^{xm}\right)\left(\boldsymbol{Z}_s + \boldsymbol{Z}_f + \boldsymbol{Z}_{eq}^{1x}\right)} \right\} = \Delta\mu_b^{mx} = \Delta\mu_c^{mx}$
B	$\Delta\mu_a^{mx} = \left\lvert \arg\left\{ \boldsymbol{e}^{j0} - \frac{\boldsymbol{Z}_{mx}^{P'} + \boldsymbol{Z}_{mx}^{N'} + \boldsymbol{Z}_{mx}^{0'}}{\boldsymbol{Z}_{xx}^{P'} + \boldsymbol{Z}_{xx}^{N'} + \boldsymbol{Z}_{xx}^{0'} + 3\boldsymbol{Z}_f} \right\} \right\rvert$ $\Delta\mu_b^{mx} = \left\lvert \frac{4\pi}{3} - \arg\left\{ \boldsymbol{e}^{j4\pi/3} - \frac{\boldsymbol{e}^{j4\pi/3}\boldsymbol{Z}_{mx}^{P'} + \boldsymbol{e}^{j2\pi/3}\boldsymbol{Z}_{mx}^{N'} + \boldsymbol{Z}_{mx}^{0'}}{\boldsymbol{Z}_{xx}^{P'} + \boldsymbol{Z}_{xx}^{N'} + \boldsymbol{Z}_{xx}^{0'} + 3\boldsymbol{Z}_f} \right\} \right\rvert$ $\Delta\mu_c^{mx} = \left\lvert \frac{2\pi}{3} - \arg\left\{ \boldsymbol{e}^{j2\pi/3} - \frac{\boldsymbol{e}^{j2\pi/3}\boldsymbol{Z}_{mx}^{P'} + \boldsymbol{e}^{j4\pi/3}\boldsymbol{Z}_{mx}^{N'} + \boldsymbol{Z}_{mx}^{0'}}{\boldsymbol{Z}_{xx}^{P'} + \boldsymbol{Z}_{xx}^{N'} + \boldsymbol{Z}_{xx}^{0'} + 3\boldsymbol{Z}_f} \right\} \right\rvert$
E	$\Delta\mu_a^{mx} = \left\lvert \arg\left\{ \boldsymbol{e}^{j0} + \frac{\boldsymbol{Z}_{mx}^{N'} - \boldsymbol{Z}_{mx}^{P'}}{\boldsymbol{Z}_{xx}^{P'} + \boldsymbol{Z}_{xx}^{N'} + \boldsymbol{Z}_f} \right\} \right\rvert$ $\Delta\mu_b^{mx} = \left\lvert \frac{4\pi}{3} - \arg\left\{ \boldsymbol{e}^{j4\pi/3} + \frac{\boldsymbol{e}^{j2\pi/3}\boldsymbol{Z}_{mx}^{N'} - \boldsymbol{e}^{j4\pi/3}\boldsymbol{Z}_{mx}^{P'}}{\boldsymbol{Z}_{xx}^{P'} + \boldsymbol{Z}_{xx}^{N'} + \boldsymbol{Z}_f} \right\} \right\rvert$ $\Delta\mu_c^{mx} = \left\lvert \frac{2\pi}{3} - \arg\left\{ \boldsymbol{e}^{j2\pi/3} + \frac{\boldsymbol{e}^{j4\pi/3}\boldsymbol{Z}_{mx}^{N'} - \boldsymbol{e}^{j2\pi/3}\boldsymbol{Z}_{mx}^{P'}}{\boldsymbol{Z}_{xx}^{P'} + \boldsymbol{Z}_{xx}^{N'} + \boldsymbol{Z}_f} \right\} \right\rvert$
G	$\mu_a^{mx} = \left\lvert \arg\left[\boldsymbol{e}^{j0} + \frac{\left\{\left(\boldsymbol{Z}_{mx}^{N'} - \boldsymbol{Z}_{mx}^{P'}\right)\left(\boldsymbol{Z}_{xx}^{0'} + 3\boldsymbol{Z}_f\right) + \left(\boldsymbol{Z}_{mx}^{0'} - \boldsymbol{Z}_{mx}^{P'}\right)\boldsymbol{Z}_{xx}^{N'}\right\}}{\boldsymbol{Z}_{xx}^{P'}\boldsymbol{Z}_{xx}^{N'} + \boldsymbol{Z}_{xx}^{P'}\left(\boldsymbol{Z}_{xx}^{0'} + 3\boldsymbol{Z}_f\right) + \boldsymbol{Z}_{xx}^{N'}\left(\boldsymbol{Z}_{xx}^{0'} + 3\boldsymbol{Z}_f\right)} \right] \right\rvert$ $\Delta\mu_b^{mx} = \left\lvert \frac{4\pi}{3} - \arg\left[\boldsymbol{e}^{j4\pi/3} + \frac{\left\{\left(\boldsymbol{e}^{j2\pi/3}\boldsymbol{Z}_{mx}^{N'} - \boldsymbol{e}^{j4\pi/3}\boldsymbol{Z}_{mx}^{P'}\right)\left(\boldsymbol{Z}_{xx}^{0'} + 3\boldsymbol{Z}_f\right) + \left(\boldsymbol{Z}_{mx}^{0'} - \boldsymbol{e}^{j4\pi/3}\boldsymbol{Z}_{mx}^{P'}\right)\boldsymbol{Z}_{xx}^{N'}\right\}}{\boldsymbol{Z}_{xx}^{P'}\boldsymbol{Z}_{xx}^{N'} + \boldsymbol{Z}_{xx}^{P'}\left(\boldsymbol{Z}_{xx}^{0'} + 3\boldsymbol{Z}_f\right) + \boldsymbol{Z}_{xx}^{N'}\left(\boldsymbol{Z}_{xx}^{0'} + 3\boldsymbol{Z}_f\right)} \right] \right\rvert$ $\Delta\mu_c^{mx} = \left\lvert \frac{2\pi}{3} - \arg\left[\boldsymbol{e}^{j2\pi/3} + \frac{\left\{\left(\boldsymbol{e}^{j4\pi/3}\boldsymbol{Z}_{mx}^{N'} - \boldsymbol{e}^{j2\pi/3}\boldsymbol{Z}_{mx}^{P'}\right)\left(\boldsymbol{Z}_{xx}^{0'} + 3\boldsymbol{Z}_f\right) + \left(\boldsymbol{Z}_{mx}^{0'} - \boldsymbol{e}^{j2\pi/3}\boldsymbol{Z}_{mx}^{P'}\right)\boldsymbol{Z}_{xx}^{N'}\right\}}{\boldsymbol{Z}_{xx}^{P'}\boldsymbol{Z}_{xx}^{N'} + \boldsymbol{Z}_{xx}^{P'}\left(\boldsymbol{Z}_{xx}^{0'} + 3\boldsymbol{Z}_f\right) + \boldsymbol{Z}_{xx}^{N'}\left(\boldsymbol{Z}_{xx}^{0'} + 3\boldsymbol{Z}_f\right)} \right] \right\rvert$

In Tables 5-III and 5-V, phase angle jumps associated with dip-types D, F and C are not shown, since these types of dips are generated due to propagation of dips through different types of transformer winding configurations; it is discussed briefly in the next Section. From the expressions shown in Tables 5-IV and 5-V, it is evident that DG will have an impact on the value of voltage-dip and phase-angle jump for symmetrical and unsymmetrical faults initiated (different types of)voltage dips. In the next section,

simulation of a test distribution network is conducted to validate the analytical expressions under different types of voltage dips with and without DG.

5.3 ILLUSTRATIVE EXAMPLE FOR VALIDATING THE ANALYTICAL EXPRESSIONS ASSOCIATED WITH VOLTAGE DIPS

In Section 5.3.1, a simulation study is conducted which explores different types of dips and their associated phase-angle jumps at different buses during different types of faults. Then, in Section 5.3.2, validation of the analytical expressions of Section 5.2 is carried out considering the common test system and experimental platform.

5.3.1 Simulation Study

Single line diagram of a simple radial distribution network is shown in Fig. 5.6. This test system is simulated to analyse the different types of fault-initiated dips at different buses of the system. The upstream side of the test system is represented by Thévenin equivalent of the utility grid, where voltage level and fault level is considered as 66 kV and 1000 MVA, respectively. It is connected to PCC bus through a 66/11 kV transformer. Three-phase loads are distributed along the distribution feeder. A synchronous generator type DG (capacity of 2 MW) equipped with automatic voltage regulator (AVR) is connected at the remote end of the distribution feeder, see Fig. 5.6. The details of the test network's parameters are presented in **Appendix A.2**.

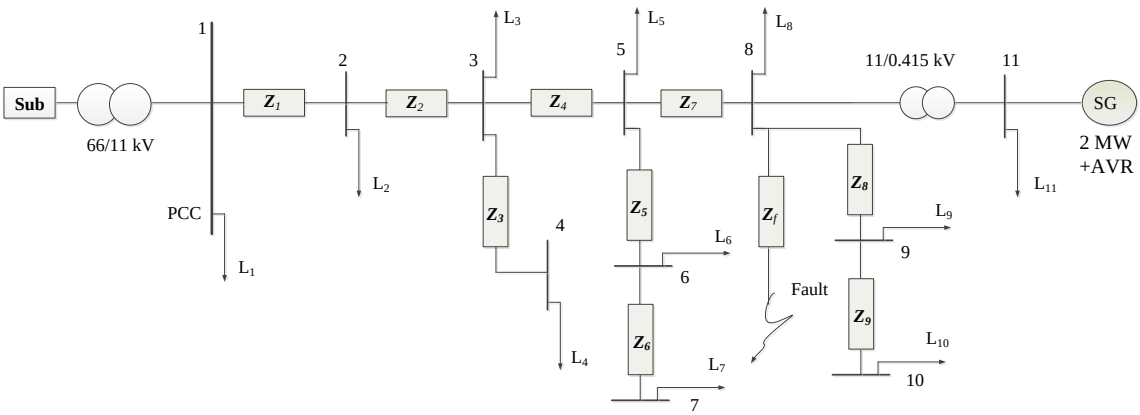

Fig. 5.6. Single line diagram of a radial distribution network with synchronous generator (SG) based DG.

Now, due to fault at any arbitrary bus(for this study, bus 8 is selected), voltages and their corresponding phase-angle at different buses are monitored. As discussed in

section 5.2, four types of faults are usually found in power system; they are Single line-to-ground (SLG) fault, phase-to-phase fault, double line-to-ground fault and symmetrical or balanced 3-phase fault. These faults are the primary reason for developing different types of dips. However, propagation of dips through different network elements can change the type of dips. For example, transformer winding connection and load-connection can influence the type of dips. A general discussion on transformer winding connection and load connections are presented below.

(a) Transformer Winding Connection

Transformer winding connections are classified into three types to explain the transfer of three-phase unbalanced voltage dips, as well as the change in voltage dip-type, from one voltage level to another [22].

- Type 1 – Transformers that do not change anything to the voltages. The primary voltages (per unit) are equal to the secondary per unit voltages. The only transformer configuration that falls under this type is the Wye Grounded-Wye grounded (Yg-Yg).
- Type 2 – Transformers that remove the zero-sequence voltage. Basically, the secondary voltage (pu) is equal to the primary voltage (pu) minus the zero-sequence component. The Delta-delta (Dd), Delta-zigzag (Dz) and the Wye-wye (with both windings ungrounded or with only one star point grounded) belong to this type.
- Type 3 – Transformers that changes line and phase voltages. Delta-wye (Dy), Wye-delta (Yd) and the Wye-zigzag (Yz) fit under this type.

(b) Load Connection

Three-phase loads in power networks are usually connected in two ways: wye-connected and delta-connected. These types of connectivity of loads, along with different combinations of fault-types and transformer-types, can also influence the type of dips.

In the simulation study, the seven types of dips, as discussed in Section 5.2.3, are generated by using the combinations of above three factors, i.e., fault type, winding connection of transformer, and load-connection. The combinations, which have been applied for generating the seven types of dips, are shown in Table 5-VI.

Table 5-VII illustrates the voltage-dip (d_v) and phase-angle jumps associated with seven types of dips. These dips are encountered at bus 10 of Fig. 5.6, due to fault at bus 8. Two scenarios are investigated in this simulation study; first scenario did not take DG into account, whereas the second scenario included the presence of DG at bus 11. From Table 5-VII it is evident that the presence of DG improves the voltage profile during dip, by showing comparatively less d_v than the d_v obtained when DG was not present. The reason is, the current provided by DG during fault, may keep the fault-current supplied by upstream side to a lesser amount resulting in less voltage drop at the monitored buses. Therefore, improvement of voltage-dip (d_v) is observed for all seven types of dips, see Table 5-VII. However, phase-angle jumps show slight difference for the two scenarios under all types of dips. It is due to the fact that DG-reactance influences the impedance matrix, and hence, phase-angle jumps are affected. To demonstrate the effect of voltage-dip and phase-angle jump with and without DG, Fig. 5.7 illustrates the instantaneous 3-phase voltages and its associated phase-angle, voltage-dip (d_v) for type-D dip with severely affected *a*-phase.

TABLE 5-VI

GENERATION OF SEVEN TYPES OF DIPS CONSIDERING DIFFERENT COMBINATIONS OF NETWORK ELEMENTS AND FAULTS [22]

Voltage Dip-type	Fault type	Transformer type			Load-connection	
		Type 1:Yg-Yg	Type 2:Dd	Type 3:Dy	Wye	Delta
A	3Φ	No effect on transformer type			No effect on load connection	
B	LG	Yes			Yes	
C	LG			Yes	Yes	
	LL		Yes		Yes	
D	LG		Yes		Yes	
	LL			Yes	Yes	
E	LLG	Yes			Yes	
F	LLG			Yes	Yes	
G	LLG		Yes		Yes	
				Yes		Yes

TABLE 5-VII

SEVEN TYPES OF VOLTAGE DIPS WITH AND WITHOUT DG OBSERVED AT BUS 10

Voltage Dip-type	Ground-truth (Severely affected dip-phase)	Without DG				With DG			
		Voltage-dip (d_v)	Phase-angle jump			Voltage-dip (d_v)	Phase-angle jump		
			$\lvert\Delta\mu_a\rvert^\circ$	$\lvert\Delta\mu_b\rvert^\circ$	$\lvert\Delta\mu_c\rvert^\circ$		$\lvert\Delta\mu_a\rvert^\circ$	$\lvert\Delta\mu_b\rvert^\circ$	$\lvert\Delta\mu_c\rvert^\circ$
A	*abc*-phase	0.9212	65.37	65.37	65.37	0.9122	67.06	67.06	67.06
B	*a*-phase	0.9488	68.75	15.14	13.59	0.945	70.22	14.93	13.91
C	*ca*-phase	0.4835	64	7	68	0.4801	60	5	63
D	*a*-phase	0.7544	70	25	28	0.7499	69	24	27
E	*ab*-phase	0.4777	58.91	58.74	0	0.4725	58.89	58.70	0
F	*a*-phase	0.7645	73	19	32	0.7605	71	17	28
G	*ab*-phase	0.9607	2	68.74	7	0.9577	3	70	8

Table 5-VII shows the voltage-dip (d_v) and phase-angle jump at one monitoring bus, i.e., at bus 10. To investigate the effect of voltage-dip and phase-angle jumps at all other buses in the distribution feeder, a SLG and phase-to-phase fault initiated B- and E-types dips are investigated and the results are illustrated in Tables 5-VIIIA and 5-VIIIB, respectively. Similar to the previous analysis as conducted for monitoring bus 10, the other buses also encounters the difference in voltage-dip (d_v) and phase-angle jumps with and without DG. However, buses in the proximity of fault encounter larger voltage-dip in comparison to the buses at farther away from the fault-point.

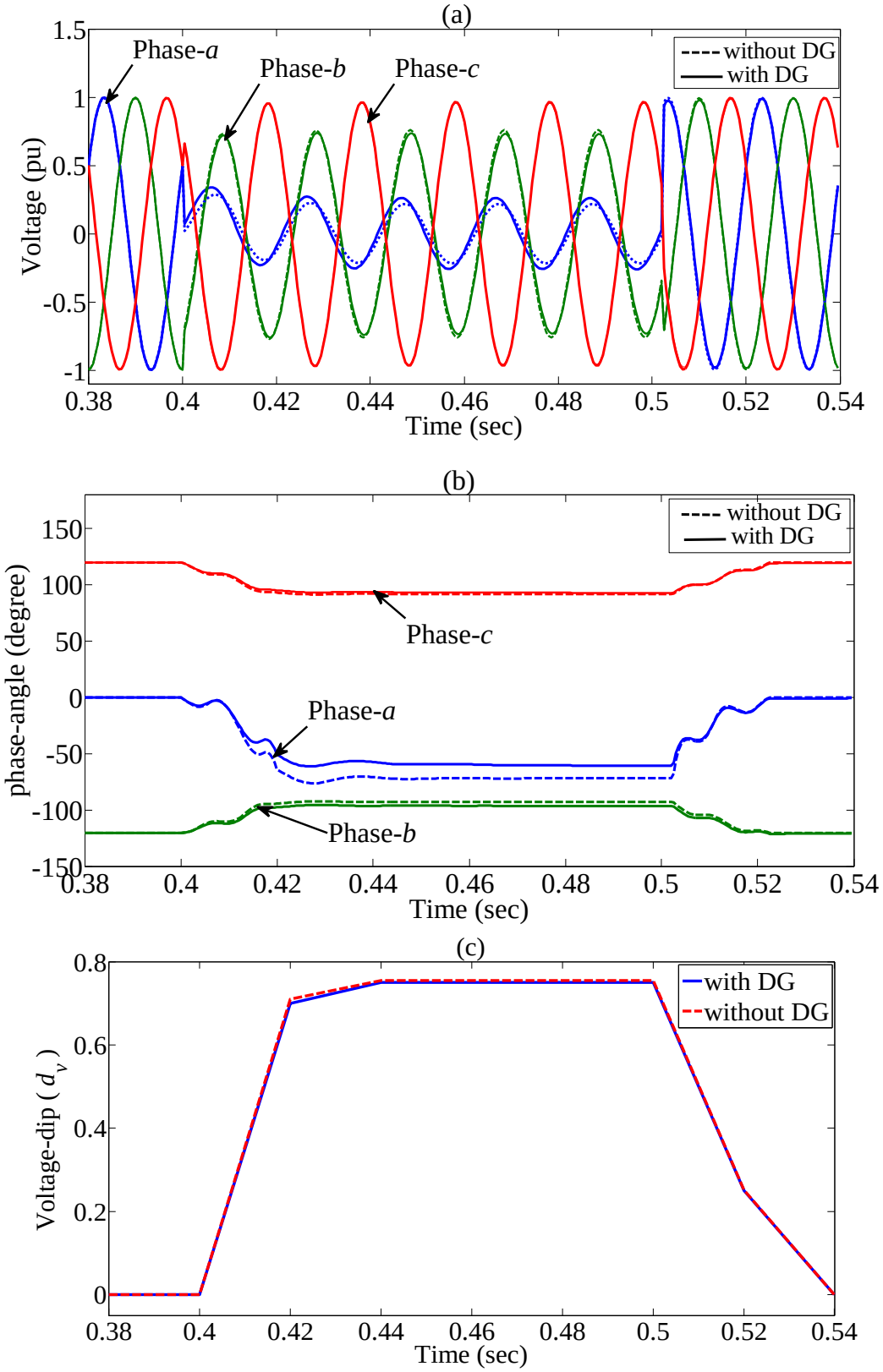

Fig. 5.7. (a) Instantaneous 3-phase voltages, (b) its phase-angles in time-domain, and (c) the associated voltage-dip (d_v), observed at bus 10 due to voltage dip D-type with severely affected *a*-phase.

TABLE 5-VIIIA

VOLTAGE DIPS AND PHASE-ANGLE JUMPS OBSERVED AT DIFFERENT BUSES DUE TO SLG FAULT AT BUS 8

Voltage Dip-type	Bus number	Without DG				With DG			
		Voltage-dip (d_v)	Phase-angle jump			Voltage-dip (d_v)	Phase-angle jump		
			$\lvert\Delta\mu_a\rvert^\circ$	$\lvert\Delta\mu_b\rvert^\circ$	$\lvert\Delta\mu_c\rvert^\circ$		$\lvert\Delta\mu_a\rvert^\circ$	$\lvert\Delta\mu_b\rvert^\circ$	$\lvert\Delta\mu_c\rvert^\circ$
B	1	0.059	1.42	1.44	1.86	0.058	1.42	1.17	1.81
B	2	0.108	2.59	1.44	1.86	0.109	2.60	1.16	1.79
B	3	0.4015	4.11	5.20	4.10	0.398	4.30	4.99	4.23
B	4	0.4015	4.11	5.20	4.10	0.398	4.30	4.99	4.23
B	5	0.6966	8.43	10.52	9.18	0.69	9.11	10.31	9.41
B	6	0.6966	8.43	10.52	9.18	0.695	9.11	10.31	9.41
B	7	0.6966	8.43	10.52	9.18	0.695	9.11	10.31	9.41
B	8	0.9488	68.75	15.14	13.59	0.945	70.22	14.93	13.91
B	9	0.9488	68.75	15.14	13.59	0.945	70.22	14.93	13.91
B	10	0.9488	68.75	15.14	13.59	0.945	70.22	14.93	13.91
B	11	0.9488	68.75	15.14	13.59	0.946	64.69	14.93	13.92

TABLE 5-VIIIB

VOLTAGE DIPS AND PHASE-ANGLE JUMPS OBSERVED AT DIFFERENT BUSES DUE TO PHASE-TO-PHASE FAULT AT BUS 8

Voltage Dip-type	Bus number	Without DG				With DG			
		Voltage-dip (d_v)	Phase-angle jump			Voltage-dip (d_v)	Phase-angle jump		
			$\lvert\Delta\mu_a\rvert^\circ$	$\lvert\Delta\mu_b\rvert^\circ$	$\lvert\Delta\mu_c\rvert^\circ$		$\lvert\Delta\mu_a\rvert^\circ$	$\lvert\Delta\mu_b\rvert^\circ$	$\lvert\Delta\mu_c\rvert^\circ$
E	1	0.0912	0	5.77	1.80	0.0897	0	5.80	1.77
E	2	0.1334	0	9.30	3.20	0.1315	0	9.34	3.15
E	3	0.2977	0	20.24	14.73	0.295	0	20.33	14.59
E	4	0.2977	0	20.24	14.73	0.295	0	20.33	14.59
E	5	0.4221	0	36.67	33.08	0.4182	0	36.77	32.90
E	6	0.4221	0	36.67	33.08	0.4182	0	36.77	32.90
E	7	0.4221	0	36.67	33.08	0.4182	0	36.77	32.90
E	8	0.4777	0	58.91	58.74	0.4725	0	58.89	58.70
E	9	0.4777	0	58.91	58.74	0.4725	0	58.89	58.70
E	10	0.4777	0	58.91	58.74	0.4725	0	58.89	58.70
E	11	0.4777	0	58.91	58.74	0.4723	0	57.99	57.65

5.3.2 Validation of Analytical Expressions of Voltage Dips with and without DG

In Section 5.3.1, the voltage-dip (d_v) and phase-angle jumps under different types of faults are calculated using the simulated results at different monitoring buses. To validate the expressions developed in Section 5.2, this sub-section explores the case by case study of different types of fault initiated dips and their associated phase-angle

jumps with and without DG employing the developed analytical expressions as well as through network simulations. To this end, voltage-dips and phase-angle jumps, as observed at bus 10 due to fault at bus 8, are calculated from the impedance matrix of the test network shown in Fig. 5.6 and the analytical expressions associated with balanced and unbalanced faults. The results can be seen in Tables 5-IXA and 5-IXB. Two scenarios, which include the presence of DG and the absence of DG, are taken into account in this study. To carry out the validation, the results obtained through simulation and analytical expressions are placed side by side. Less than 1% difference is found in the test results, which indicate the acceptability of the developed expressions of presented in Section 5.2.

TABLE 5-IXA

ANALYTICAL EXPRESSION AND SIMULATION-WISE VOLTAGE DIPS, PHASE-ANGLE JUMPS OBTAINED AT BUS 10 DUE TO FAULT AT BUS 8: WHEN DG IS NOT PRESENT

Voltage Dip-type	Ground-truth (Severely affected dip-phase)	Without DG (Analytical expression)				Without DG (Simulation)			
		Voltage-dip (d_v)	Phase-angle jump			Voltage-dip (d_v)	Phase-angle jump		
			$\lvert\Delta\mu_a\rvert^\circ$	$\lvert\Delta\mu_b\rvert^\circ$	$\lvert\Delta\mu_c\rvert^\circ$		$\lvert\Delta\mu_a\rvert^\circ$	$\lvert\Delta\mu_b\rvert^\circ$	$\lvert\Delta\mu_c\rvert^\circ$
A	*abc*-phase	0.924	67.77	67.77	67.77	0.9212	65.37	65.37	65.37
B	*a*-phase	0.9478	68.72	14.85	13.51	0.9488	68.75	15.14	13.59
E	*bc*-phase	0.4667	0	58.89	58.73	0.4777	0	58.91	58.74
G	*bc*-phase	0.9597	3	69	6	0.9607	2	68.74	7

TABLE 5-IXB

ANALYTICAL EXPRESSION AND SIMULATION-WISE VOLTAGE DIPS, PHASE-ANGLE JUMPS OBTAINED AT BUS 10 DUE TO FAULT AT BUS 8: WHEN DG IS PRESENT

Voltage Dip-type	Ground-truth (Severely affected dip-phase)	With DG (Analytical expression)				With DG (Simulation)			
		Voltage-dip (d_v)	Phase-angle jump			Voltage-dip (d_v)	Phase-angle jump		
			$\lvert\Delta\mu_a\rvert^\circ$	$\lvert\Delta\mu_b\rvert^\circ$	$\lvert\Delta\mu_c\rvert^\circ$		$\lvert\Delta\mu_a\rvert^\circ$	$\lvert\Delta\mu_b\rvert^\circ$	$\lvert\Delta\mu_c\rvert^\circ$
A	*abc*-phase	0.9147	68.24	68.24	68.24	0.9122	67.06	67.06	67.06
B	*a*-phase	0.9422	70.18	14.90	13.86	0.945	70.22	14.93	13.91
E	*bc*-phase	0.4625	0	58.86	58.67	0.4725	0	58.89	58.70
G	*bc*-phase	0.9571	4	71	9	0.9577	3	70	8

In order to conduct the further validation of the developed expressions, balanced 3-phase faults are taken into account. The during-fault bus voltages and phase-angle jumps at all buses in the distribution feeder are observed with and without DG. The voltage-dip (d_v) and phase-angle jumps at different buses obtained through simulations

are shown in Figs. 5.8 (a)-(b), whereas the d_v and phase-angle jumps obtained through analytical expressions are highlighted in Figs. 5.8 (c)-(d). Following the similar approach, unbalanced faults, such as, SLG and phase-to-phase faults, are investigated with and without DG using network simulations and analytical expressions; see Tables 5-XA, 5-XB, 5-XIA, 5-XIB for illustration. Less than 1% difference is found in all the test results, which is in line with the previous study.

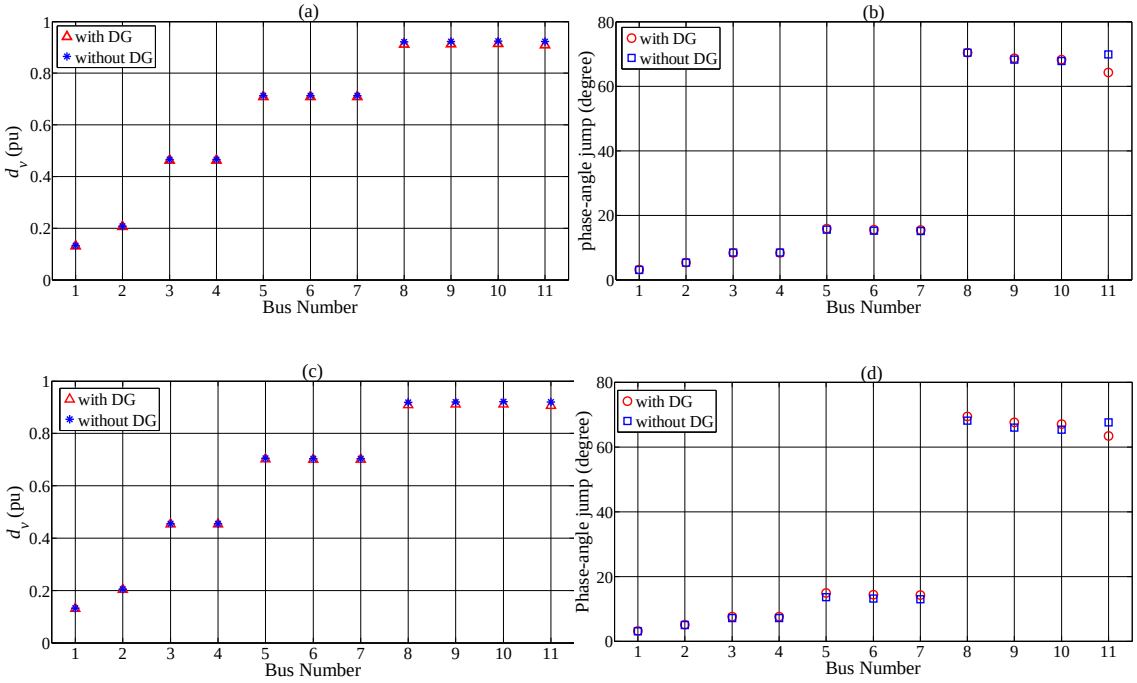

Fig. 5.8. Voltage-dip (d_v) and phase-angle jumps at bus 10 due to balanced 3-phase faults at bus 8; $d_v$obtained from (a) analytical expression and (b) simulation; phase-angle jumps obtained from (c) analytical expression and (d) simulation.

TABLE 5-XA

ANALYTICAL EXPRESSION AND SIMULATION-WISE VOLTAGE DIPS, PHASE-ANGLE JUMPS OBTAINED AT DIFFERENT BUSES DUE TO SLG FAULT AT BUS 8: WHEN DG IS NOT PRESENT

Voltage Dip-type	Bus number	Without DG (Analytical expression)				Without DG (Simulation)			
		Voltage-dip (d_v)	Phase-angle jump			Voltage-dip (d_v)	Phase-angle jump		
			$\lvert\Delta\mu_a\rvert^\circ$	$\lvert\Delta\mu_b\rvert^\circ$	$\lvert\Delta\mu_c\rvert^\circ$		$\lvert\Delta\mu_a\rvert^\circ$	$\lvert\Delta\mu_b\rvert^\circ$	$\lvert\Delta\mu_c\rvert^\circ$
B	1	0.0581	1.38	1.15	1.78	0.059	1.42	1.44	1.86
B	2	0.1069	2.56	1.15	1.78	0.108	2.59	1.44	1.86
B	3	0.3974	4.07	4.91	4.02	0.4015	4.11	5.20	4.10
B	4	0.3974	4.07	4.91	4.02	0.4015	4.11	5.20	4.10
B	5	0.6866	8.39	10.23	9.10	0.6966	8.43	10.52	9.18
B	6	0.6866	8.39	10.23	9.10	0.6966	8.43	10.52	9.18
B	7	0.6866	8.39	10.23	9.10	0.6966	8.43	10.52	9.18
B	8	0.9478	68.72	14.85	13.51	0.9488	68.75	15.14	13.59
B	9	0.9478	68.72	14.85	13.51	0.9488	68.75	15.14	13.59
B	10	0.9478	68.72	14.85	13.51	0.9488	68.75	15.14	13.59
B	11	0.9478	68.72	14.85	13.51	0.9488	68.75	15.14	13.59

TABLE 5-XB

ANALYTICAL EXPRESSION AND SIMULATION-WISE VOLTAGE DIPS, PHASE-ANGLE JUMPS OBTAINED AT DIFFERENT BUSES DUE TO SLG FAULT AT BUS 8: WHEN DG IS PRESENT

Voltage Dip-type	Bus number	With DG (analytical expression)				With DG (Simulation)			
		Voltage-dip (d_v)	Phase-angle jump			Voltage-dip (d_v)	Phase-angle jump		
			$\lvert\Delta\mu_a\rvert^\circ$	$\lvert\Delta\mu_b\rvert^\circ$	$\lvert\Delta\mu_c\rvert^\circ$		$\lvert\Delta\mu_a\rvert^\circ$	$\lvert\Delta\mu_b\rvert^\circ$	$\lvert\Delta\mu_c\rvert^\circ$
B	1	0.0575	1.38	1.14	1.77	0.058	1.42	1.17	1.81
B	2	0.106	2.56	1.13	1.75	0.109	2.60	1.16	1.79
B	3	0.3964	4.26	4.96	4.18	0.398	4.30	4.99	4.23
B	4	0.3964	4.26	4.96	4.18	0.398	4.30	4.99	4.23
B	5	0.6853	9.07	10.28	9.36	0.69	9.11	10.31	9.41
B	6	0.6853	9.07	10.28	9.36	0.695	9.11	10.31	9.41
B	7	0.6853	9.07	10.28	9.36	0.695	9.11	10.31	9.41
B	8	0.9422	70.18	14.90	13.86	0.945	70.22	14.93	13.91
B	9	0.9422	70.18	14.90	13.86	0.945	70.22	14.93	13.91
B	10	0.9422	70.18	14.90	13.86	0.945	70.22	14.93	13.91
B	11	0.9401	64.65	14.90	13.88	0.946	64.69	14.93	13.92

TABLE 5-XIA

ANALYTICAL EXPRESSION AND SIMULATION-WISE VOLTAGE DIPS, PHASE-ANGLE JUMPS OBTAINED AT DIFFERENT BUSES DUE TO PHASE-TO-PHASE FAULT AT BUS 8: WHEN DG IS NOT PRESENT

Voltage Dip-type	Bus number	Without DG (analytical expression)				Without DG (Simulation)			
		Voltage-dip (d_v)	Phase-angle jump			Voltage-dip (d_v)	Phase-angle jump		
			$\lvert\Delta\mu_a\rvert^\circ$	$\lvert\Delta\mu_b\rvert^\circ$	$\lvert\Delta\mu_c\rvert^\circ$		$\lvert\Delta\mu_a\rvert^\circ$	$\lvert\Delta\mu_b\rvert^\circ$	$\lvert\Delta\mu_c\rvert^\circ$
E	1	0.0802	0	5.74	1.79	0.0912	0	5.77	1.80
E	2	0.1224	0	9.27	3.19	0.1334	0	9.30	3.20
E	3	0.2867	0	20.22	14.72	0.2977	0	20.24	14.73
E	4	0.2867	0	20.22	14.72	0.2977	0	20.24	14.73
E	5	0.4111	0	36.65	33.07	0.4221	0	36.67	33.08
E	6	0.4111	0	36.65	33.07	0.4221	0	36.67	33.08
E	7	0.4111	0	36.65	33.07	0.4221	0	36.67	33.08
E	8	0.4667	0	58.89	58.73	0.4777	0	58.91	58.74
E	9	0.4667	0	58.89	58.73	0.4777	0	58.91	58.74
E	10	0.4667	0	58.89	58.73	0.4777	0	58.91	58.74
E	11	0.4667	0	58.89	58.73	0.4777	0	58.91	58.74

TABLE 5-XIB

ANALYTICAL EXPRESSION AND SIMULATION-WISE VOLTAGE DIPS, PHASE-ANGLE JUMPS OBTAINED AT DIFFERENT BUSES DUE TO PHASE-TO-PHASE FAULT AT BUS 8: WHEN DG IS PRESENT

Voltage Dip-type	Bus number	With DG (Analytical expression)				With DG (Simulation)			
		Voltage-dip (d_v)	Phase-angle jump			Voltage-dip (d_v)	Phase-angle jump		
			$\lvert\Delta\mu_a\rvert^\circ$	$\lvert\Delta\mu_b\rvert^\circ$	$\lvert\Delta\mu_c\rvert^\circ$		$\lvert\Delta\mu_a\rvert^\circ$	$\lvert\Delta\mu_b\rvert^\circ$	$\lvert\Delta\mu_c\rvert^\circ$
E	1	0.0797	0	5.77	1.75	0.0897	0	5.80	1.77
E	2	0.1215	0	9.31	3.12	0.1315	0	9.34	3.15
E	3	0.285	0	20.30	14.57	0.295	0	20.33	14.59
E	4	0.285	0	20.30	14.57	0.295	0	20.33	14.59
E	5	0.4082	0	36.74	32.88	0.4182	0	36.77	32.90
E	6	0.4082	0	36.74	32.88	0.4182	0	36.77	32.90
E	7	0.4082	0	36.74	32.88	0.4182	0	36.77	32.90
E	8	0.4625	0	58.86	58.67	0.4725	0	58.89	58.70
E	9	0.4625	0	58.86	58.67	0.4725	0	58.89	58.70
E	10	0.4625	0	58.86	58.67	0.4725	0	58.89	58.70
E	11	0.4623	0	57.95	57.62	0.4723	0	57.99	57.65

5.4 CHARACTERIZATION OF VOLTAGE DIPS

In this section, voltage dips are characterized by analysing the voltage-dip and phase-angle jumps at different buses under several scenarios, which include the fault-type, fault location, capacity (sizing) and location of DG in the distribution feeder.

i) Voltage dips characterization for different fault-types

Four types of faults, as discussed earlier, are analysed using the test network of Fig. 5.6. Voltage-dip (d_v) and phase-angle jumps at different buses are observed due to fault at bus 8. The analytical expressions derived in Section 5.2 are used for this dip-observation. The results are shown in Table 5-XII. It is to be noted that phase-angle jumps of one phase voltage, which shows the highest value, is presented in the Table 5-XII for different types of faults. However, the phase-angle jumps of other phase-voltages are also obtained from the network using developed expressions. From the test results it is evident that balanced 3-Φ faults yield the higher d_v than phase-to-phase faults. SLG faults result in higher d_v than balanced 3-Φ faults in the vicinity of fault location (i.e. adjacent to bus 8). Moreover, double line-to-ground faults show less d_v than balanced 3-Φ faults at monitoring bus 1 to 4, i.e., close to the upstream side.

TABLE 5-XII

VOLTAGE DIPS AT DIFFERENT BUSES FOR DIFFERENT FAULT-TYPES

Faulted node	Monitoring Bus	Fault-types							
		Balanced 3-phase fault		SLG (single line to ground) fault		Phase-to-phase fault		Double line-to-ground fault	
		Voltage-dip (d_v) in pu	Phase-angle jump (degree)	Voltage-dip (d_v) in pu	Phase-angle jump (degree)	Voltage-dip (d_v) in pu	Phase-angle jump (degree)	Voltage-dip (d_v) in pu	Phase-angle jump (degree)
8	1	0.1314	3.12	0.0575	1.38	0.0797	5.77	0.0947	6.11
	2	0.2067	5.33	0.106	2.56	0.1215	9.31	0.1567	10.31
	3	0.4624	8.36	0.3964	4.26	0.285	20.30	0.4445	22.30
	4	0.4626	8.37	0.3964	4.26	0.285	20.30	0.4445	22.30
	5	0.7088	15.87	0.6853	9.07	0.4082	36.74	0.7315	38.94
	6	0.7084	15.55	0.6853	9.07	0.4082	36.74	0.7315	38.94
	7	0.7085	15.45	0.6853	9.07	0.4082	36.74	0.7315	38.94
	8	0.9118	70.42	0.9422	70.18	0.4625	58.86	0.9577	59.86
	9	0.9138	68.66	0.9422	70.18	0.4625	58.86	0.9577	59.86
	10	0.9147	68.24	0.9422	70.18	0.4625	58.86	0.9577	59.86
	11	0.9093	64.28	0.9401	64.65	0.4623	57.95	0.9644	56.95

ii) Voltage dips characterization for different fault-location

In this study, fault locations are selected at bus 1, 5 and 8, and the associated voltage dips, phase-angle jumps are monitored at all buses; see table 5-XIII for illustration. It should be noted that SLG fault is considered in this study, since 70% (approximately) of the faults in the power system are SLG-types[115]. Voltage-dips (d_v) in the vicinity of faults show the highest value. For instance, when fault occurs at bus 5, then phase-voltages at bus 5 and its adjacent buses, which are bus 6 and 7, experience the most severe dip as shown in Table 5-XIII. However, fault occurred adjacent to upstream bus has less severe voltage dips. For example, when fault occurs at bus 1, which is nearest to the upstream side, then voltage-dip at a monitoring bus 4 experiences less dip in comparison to the fault that occurs at bus 8 located far away from upstream grid, see Table 5-XIII for more details.

TABLE 5-XIII

VOLTAGE DIPS AT DIFFERENT BUSES DUE TO FAULT AT DIFFERENT LOCATION

Fault-type	Monitoring Bus	Fault location					
		Bus 1		Bus 5		Bus 8	
		Voltage-dip (d_v) in pu	Phase-angle jump (degree)	Voltage-dip (d_v) in pu	Phase-angle jump (degree)	Voltage-dip (d_v) in pu	Phase-angle jump (degree)
SLG	1	0.4136	54.07	0.0807	2.02	0.0575	1.38
	2	0.4007	42.18	0.1485	3.84	0.106	2.56
	3	0.3906	40.54	0.5563	8.50	0.3964	4.26
	4	0.3906	40.54	0.5563	8.50	0.3964	4.26
	5	0.38	38.96	0.9209	69.29	0.6853	9.07
	6	0.38	38.96	0.9209	69.29	0.6853	9.07
	7	0.38	38.96	0.9209	69.29	0.6853	9.07
	8	0.3689	37.44	0.8991	54.84	0.9422	70.18
	9	0.3689	37.44	0.8991	54.84	0.9422	70.18
	10	0.3689	37.44	0.8991	54.84	0.9422	70.18
	11	0.3671	36.90	0.896	52.01	0.9401	64.65

iii) Voltage dips characterization at the presence of DG with different capacities

In this study, fault-location is considered at bus 8, and the capacity of synchronous generator based DG, which is placed at bus 11, is varied from 1 MW to 3 MW keeping unity power factor. The voltage-dips and their associated phase-angle jumps due to SLG fault is monitored at different buses. The test results are shown in Table 5-XIV. As the DG size increases, the injection of fault current from the DG also increases, which facilitate to improve the voltage profile during dip. Therefore, during the fault, less voltage-dip is found at different buses when 3 MW DG is connected instead of 1 or 2 MW DG; see Table 5-XIV for more details.

TABLE 5-XIV
VOLTAGE DIPS AT DIFFERENT BUSES CONSIDERING THE PRESENCE OF DG WITH DIFFERENT CAPACITIES

Fault-type	Faulted Bus	Monitoring Bus	DG Size					
			1 MW		2 MW		3 MW	
			Voltage-dip (d_v) in pu	Phase-angle jump (degree)	Voltage-dip (d_v) in pu	Phase-angle jump (degree)	Voltage-dip (d_v) in pu	Phase-angle jump (degree)
SLG	8	1	0.0578	1.38	0.0575	1.38	0.0572	1.38
		2	0.1064	2.56	0.106	2.56	0.1055	2.57
		3	0.3968	4.17	0.3964	4.26	0.3958	4.38
		4	0.3968	4.17	0.3964	4.26	0.3958	4.38
		5	0.6859	8.73	0.6853	9.07	0.6844	9.51
		6	0.6859	8.73	0.6853	9.07	0.6844	9.51
		7	0.6859	8.73	0.6853	9.07	0.6844	9.51
		8	0.945	69.50	0.9422	70.18	0.9385	70.97
		9	0.945	69.50	0.9422	70.18	0.9385	70.97
		10	0.945	69.50	0.9422	70.18	0.9385	70.97
		11	0.9439	66.54	0.9401	64.65	0.9349	62.48

iv) Voltage dips characterization at the presence of DG at different location

In this study, fault-location is considered at bus 5, and the location of synchronous generator based DG is selected at bus 3, 6 and 11. The size of the DG was 2 MW and it wasoperating at unity power factor. The test results are illustrated in Table 5-XV. From the test results it can be concluded that, placement of DG closer to the fault-location causes less severe voltage-dip adjacent to the faulted bus in comparison to the DG-placement farther away from the faulted node. In this test investigation, considering

faulted node as bus 5, bus 6 is the nearest location for DG placement; under this scenario, voltages at bus 6 and 7 of the distribution feeder encounters comparatively less voltage-dip than the scenario when DG is placed at bus 3 or bus 11. It should be noted that SLG fault is considered for this investigation.

TABLE 5-XV
VOLTAGE DIPS AT DIFFERENT BUSES CONSIDERING THE PRESENCE OF DG AT DIFFERENT LOCATION

Fault-type	Faulted node	Monitoring Bus	DG Location					
			Bus 3		Bus 6		Bus 11	
			Voltage-dip (d_v) in pu	Phase-angle jump (degree)	Voltage-dip (d_v) in pu	Phase-angle jump (degree)	Voltage-dip (d_v) in pu	Phase-angle jump (degree)
SLG	5	1	0.079	1.99	0.0806	2.02	0.0807	2.02
		2	0.1455	3.79	0.1484	3.85	0.1485	3.85
		3	0.5462	8.32	0.5563	8.50	0.5563	8.50
		4	0.5462	8.32	0.5563	8.50	0.5563	8.50
		5	0.9244	68.65	0.9208	69.30	0.9209	69.30
		6	0.9244	68.65	0.8989	54.79	0.9209	69.30
		7	0.9244	68.65	0.8989	54.79	0.9209	69.30
		8	0.9244	68.65	0.9208	69.30	0.8991	54.85
		9	0.9244	68.65	0.9208	69.30	0.8991	54.85
		10	0.9244	68.65	0.9208	69.30	0.8991	54.85
		11	0.9244	68.65	0.9208	69.30	0.896	52.02

5.5 DISCUSSION

This Chapter defines the during-fault voltage dips in terms of minimum magnitude of 3-phase voltages and the phase-angle jumps associated with the fault. This approach lacks the classification of voltage dips in terms of severely affected phase-voltages, and also the classification of seven types of voltage dips. However, the accurate diagnosis, characterization and classification of voltage dips are an important requirement for developing voltage-dips-mitigation techniques. Furthermore, classification of voltage dips plays an important role in the assessment of voltage dip ride-through capability and immunity specifications of electrical equipment. Therefore, an approach for classification and characterization of voltage dip/sag is presented in Chapter 6 highlighting the severely affected phase-voltages. This approach has a great potential to be used as a sag/swell monitoring tool or quick screening tool. However, this approach finds its limitation for the classification of some voltage dips, more specifically four-

types D, F, C, and G, which are affected by phase-angle jumps. Therefore, in Chapter 7, a detailed and innovative approach for classification and characterization of seven types of voltage dips is presented; the proposed detailed approach can effectively classify the dips even when the phase-voltages are affected by phase-angle jumps and rotation due to loading effects.

5.6 SUMMARY

This Chapter mainly investigates the voltage dips and its associated phase-angle jumps in power network due to four major types of faults, which include single line-to-ground (SLG), double line-to-ground, line-to-line or phase-to-phase and balanced 3-phase faults. The presence of synchronous generator type DG is also included in the voltage dip investigations. Seven types of voltage dips, namely, A, B, D, E, F, E, C and G, which are associated with these four types of faults, are analysed with and without DG. Firstly, analytical expressions of seven types of voltage-dip and their phase-angle jumps are developed. Then, a simulation study is conducted to validate the developed expressions. Simulation study demonstrates the acceptability of the developed expressions for investigating during-fault voltage dips at different buses in a test network with and without DG. Lastly, characterization of voltage dip is conducted under the influence of DG. The size of DG and its location are also examined to highlight the impact of DG during-fault. Moreover, the influence of fault-types and fault-location are observed during the investigation.

Chapter 6

DETECTION, CLASSIFICATION AND CHARACTERIZATION OF VOLTAGE DIPS AND SWELLS USING THREE-PHASE VOLTAGE ELLIPSE PARAMETERS

6.1 INTRODUCTION

Automatic analysis of voltage sags and swells is an essential requirement [31]. Many techniques have been developed for the detection and classification of sags and swells in electrical power distribution systems. Most of the existing standards and methods, as reported in [28], give conservative characterization for 3-phase unbalanced dips or sags, since these approaches can only characterize single-phase or three-phase balanced dips. Therefore, there is a need for new algorithms that can classify and characterize balanced and unbalanced sags and swells altogether keeping a higher level of accuracy for real-time usage.

This Chapter presents an algorithm for detection, classification and characterization of voltage dips (sags) and swells in electricity networks, using three-phase voltage ellipse parameters. The proposed method employs the instantaneous magnitude of three-phase voltage signals in three axes, which are separated from each other by 120°. Thus, resultant rotating vector, namely, three-phase voltage vector, traces an ellipse. Then, the parameters of the ellipse, which include minor axis, major axis and inclination angle, are used to develop the proposed algorithm for classification and characterization of voltage sags and swells. To detect the types of sags/swells (single-phase, phase-to-phase or three-phase) in real-time, cycle by cycle classification is carried out. To this end, the inclination angle is used to classify the types of sags/swells, whereas the minor and major axis are used to quantify the severity of sags/swells. The proposed method is validated using real data recorded by IEEE working group and some real data measured

from Belgian transmission grid. The method is further tested for the sags and swells generated due to balanced and unbalanced faults at different buses, in a test distribution network embedded with distributed generation (DG), and in a practical distribution network of Australia. This Chapter also demonstrates the capability of the proposed algorithm to be used as a real-time sag/swell monitoring tool.

The remaining part of the Chapter is organized as follows. Section 6.2 describes the algorithm of proposed approach for real-time detection, classification and characterization of voltage sags and swells using three-phase voltage ellipse parameters. Validation of the proposed approach is conducted in Section 6.3, using real data obtained from Belgian transmission grid and the real data recorded by IEEE 1159.2 working group [117]. Fault initiated sags and swells generated in a practical distribution network in Australia, are classified and characterized in Section 6.4. Section 6.5 demonstrates the development of the proposed algorithm as a real-time sag/swell monitoring tool. Section 6.6 and 6.7 present the discussions followed by conclusion.

6.2 PROPOSED APPROACH

In order to classify and characterize voltage sags and swells, the proposed approach employs three-phase voltage ellipse transformation using 3-phase voltages to obtain three parameters of an ellipse, which comprise the minor axis, major axis and inclination angle. In this section, the proposed approach is described in four sub-sections. Analytical formulation and visual representation of three-phase voltage ellipse and its corresponding parameters are presented in section 6.2.1 and 6.2.2 respectively. Shape of 3-phase voltage ellipses, under different types of sags and swells are determined and shown in section 6.2.3; the algorithm for classification and characterization of sags and swells is narrated in section 6.2.4.

6.2.1 Analytical formulation of Three-phase Voltage Ellipse

During the disturbances, phase angle differences among three-phase voltages may deviate from the nominal value of 120°. Therefore, voltage signals are pre-processed. To do so, voltage magnitude of three-phase voltages are extracted separately for a period of one cycle and prior to applying 3-phase voltage ellipse transformation, phase voltages are considered to be separated from each other by 120°. Then parameters of the ellipse, originated from 3-phase voltage ellipse transformation, are extracted.

Considering, phase angle differences among three-phase voltages before, during and after the disturbances as 120°, the phase voltages can be presented as:

$$v_a(t) = |\boldsymbol{V_a}|\cos(\omega t) \tag{6.1a}$$

$$v_b(t) = |\boldsymbol{V_b}|\cos(\omega t - 2\pi/3) \tag{6.1b}$$

$$v_c(t) = |\boldsymbol{V_c}|\cos(\omega t - 4\pi/3) \tag{6.1c}$$

Applying Clarke transformation in the three-phase voltages of (6.1) yields

$$\begin{bmatrix} E_\alpha(t) \\ E_\beta(t) \\ E_0(t) \end{bmatrix} = \frac{2}{3}\begin{bmatrix} 1 & -\frac{1}{2} & -\frac{1}{2} \\ 1 & \frac{\sqrt{3}}{2} & -\frac{\sqrt{3}}{2} \\ \frac{1}{2} & \frac{1}{2} & \frac{1}{2} \end{bmatrix}\begin{bmatrix} v_a(t) \\ v_b(t) \\ v_c(t) \end{bmatrix} \tag{6.2}$$

The first two components of (6.2) can be presented as a *3-phase voltage vector* in a complex plane as presented below,

$$\vec{\boldsymbol{E}}(\boldsymbol{t}) = E_\alpha(t) + jE_\beta(t) = \frac{2}{3}\begin{bmatrix} 1 & \boldsymbol{e}^{j\frac{2\pi}{3}} & \boldsymbol{e}^{j\frac{4\pi}{3}} \end{bmatrix}\begin{bmatrix} v_a(t) \\ v_b(t) \\ v_c(t) \end{bmatrix} \tag{6.3}$$

The third component, which represents the zero sequence voltage, can be presented as

$$E_0(t) = \frac{1}{3}\left(v_a(t) + v_b(t) + v_c(t)\right) \tag{6.4}$$

Expanding (6.1) using Euler's formula and then, placing it in expression (6.3) gives

$$\vec{\boldsymbol{E}}(\boldsymbol{t}) = \frac{2}{3}\begin{bmatrix} 1 & \boldsymbol{e}^{j\frac{2\pi}{3}} & \boldsymbol{e}^{j\frac{4\pi}{3}} \end{bmatrix}\begin{bmatrix} \frac{|\boldsymbol{V_a}|}{2}\left(e^{j\omega t} + e^{-j\omega t}\right) \\ \frac{|\boldsymbol{V_b}|}{2}\left(e^{j\omega t} + e^{-j\omega t}\right) \\ \frac{|\boldsymbol{V_c}|}{2}\left(e^{j\omega t} + e^{-j\omega t}\right) \end{bmatrix} \tag{6.5}$$

From (6.5), *3-phase voltage vector* can be formulated as

$$\vec{\boldsymbol{E}}(\boldsymbol{t}) = \frac{2}{3}\left[\left(\frac{|\boldsymbol{V_a}| + |\boldsymbol{V_b}| + |\boldsymbol{V_c}|}{2}\right)\boldsymbol{e}^{j\omega t} + \left(\frac{|\boldsymbol{V_a}|}{2} + \frac{|\boldsymbol{V_b}|}{2}\boldsymbol{e}^{j\frac{4\pi}{3}} + \frac{|\boldsymbol{V_c}|}{2}\boldsymbol{e}^{j\frac{8\pi}{3}}\right)\boldsymbol{e}^{-j\omega t}\right] \tag{6.6}$$

Eq. (6.6) is analogous to the ellipse represented as sum of positive and negative angular frequency phasors [118]:

$$\vec{E}(t) = E^{+}e^{j\omega t} + E^{-}e^{-j\omega t} \tag{6.7}$$

where $\boldsymbol{E}^{+} = \left|\boldsymbol{E}^{+}\right|e^{j\psi^{+}}$, $\boldsymbol{E}^{-} = \left|\boldsymbol{E}^{-}\right|e^{j\psi^{-}}$, and major axis ($A_{ma}$), minor axis ($A_{mi}$), inclination angle ($\psi$) are given by

$$A_{ma} = \left|\left|E^{+}\right| + \left|E^{-}\right|\right| \tag{6.8}$$

$$A_{mi} = \left|\left|E^{+}\right| - \left|E^{-}\right|\right| \tag{6.9}$$

$$\psi = 0.5\left(\psi^{+} + \psi^{-}\right) \tag{6.10}$$

TABLE 6-I

THREE-PHASE VOLTAGE ELLIPSE PARAMETERS DURING DIFFERENT TYPES OF DIPS AND SWELLS

Event	Dip/Swell Phase	3-Φ voltage ellipse parameters		
		ψ	A_{ma}	A_{mi}
Dip	A	$(\pi/2)\pm(\pi/12)$	V	$(2V_f + V)/3$
	B	$(\pi/6)\pm(\pi/12)$	V	$(2V_f + V)/3$
	C	$(5\pi/6)\pm(\pi/12)$	V	$(2V_f + V)/3$
	AB	$(\pi/3)\pm(\pi/12)$	$(V_f + 2V)/3$	V_f
	BC	$0\pm(\pi/12)$	$(V_f + 2V)/3$	V_f
	CA	$(2\pi/3)\pm(\pi/12)$	$(V_f + 2V)/3$	V_f
	ABC	-	V_f	V_f
Swell	A	$0\pm(\pi/12)$	$(2V_f + V)/3$	V
	B	$(2\pi/3)\pm(\pi/12)$	$(2V_f + V)/3$	V
	C	$(\pi/3)\pm(\pi/12)$	$(2V_f + V)/3$	V
	AB	$(5\pi/6)\pm(\pi/12)$	V_f	$(V_f + 2V)/3$
	BC	$(\pi/2)\pm(\pi/12)$	V_f	$(V_f + 2V)/3$
	CA	$(\pi/6)\pm(\pi/12)$	V_f	$(V_f + 2V)/3$
	ABC	-	V_f	V_f

Thus, by applying 3-phase voltage ellipse transformation on the pre-processed 3-phase voltages, three parameters: major axis, minor axis and inclination angle, can be obtained. In Table 6-I, analytical formula based three parameters, obtained from three-phase voltage ellipse transformation under different types of sags and swells, are presented using pre-processed voltages, where V_f and V indicates pu voltage of sag/swell phase and undisturbed phase respectively. More details of these analytical

formulations are given in the **Appendix B**.

6.2.2 Visual representation of Three-phase Voltage Ellipse

The proposed approach applies 3-phase voltage ellipse transformation on three pre-processed voltage signals. At first, instantaneous pre-processed voltages, as shown in (6.1), are represented by the tips of the vectors, which are obtained by mapping $v_a(t), v_b(t)$ and $v_c(t)$ in a_axis, b_axis and c_axis, respectively (see Fig. 6.1(a)). Thus, resultant of these three instantaneous vectors, denoted by $\vec{E}$ and named as three-phase voltage vector, rotates with time. Considering a time-duration of one cycle, the tip of rotating three-phase voltage vector traces an ellipse as illustrated in Fig. 6.1(a). By using the expressions (6.1)–(6.10) and mapping the ellipse in a complex plane, the major axis (A_{ma}), minor axis (A_{mi}) and inclination angle (ψ) can be obtained as demonstrated in Fig. 6.1(b).

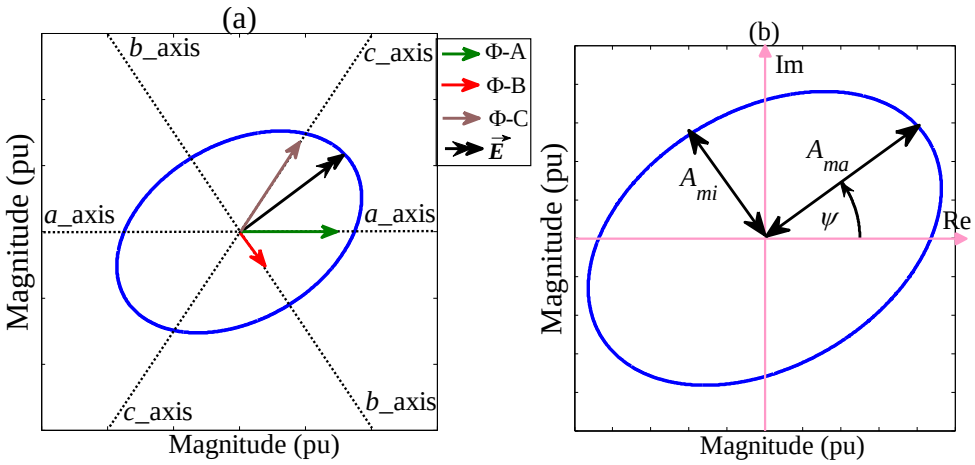

Fig. 6.1. (a) Generation of 3-Φ voltage ellipse from 3-Φ voltage vector $\vec{E}$; (b) 3-Φ voltage ellipse and its parameters: major axis (A_{ma}), minor axis (A_{mi}) and inclination angle (ψ), in a complex plane.

The variations of magnitudes of 3-phase voltages are reflected on the parameters of the ellipse and the decision boundary is set by the inclination angle as shown in Table 6-I. Phase angle jump is extracted separately to keep the information but it is not used as classification parameters since phase-angle jump may degrade the performance. For example, three-phase voltage signals, extracted during single phase fault in a DG embedded distribution network, are passed through the proposed approach with and without pre-processed voltages and it is shown in Fig. 6.2. From Figs. 6.2 (b)–(c), it is evident that due to large phase angle jump, single phase sag is incorrectly classified by inclination angle (A-sag is classified as AB-sag), when the proposed method uses the

input three-phase voltages which are not pre-processed. In contrast, the proposed method with pre-processed voltages classifies the A-sag correctly (see Table 6-I and Fig. 6.2 (c)).

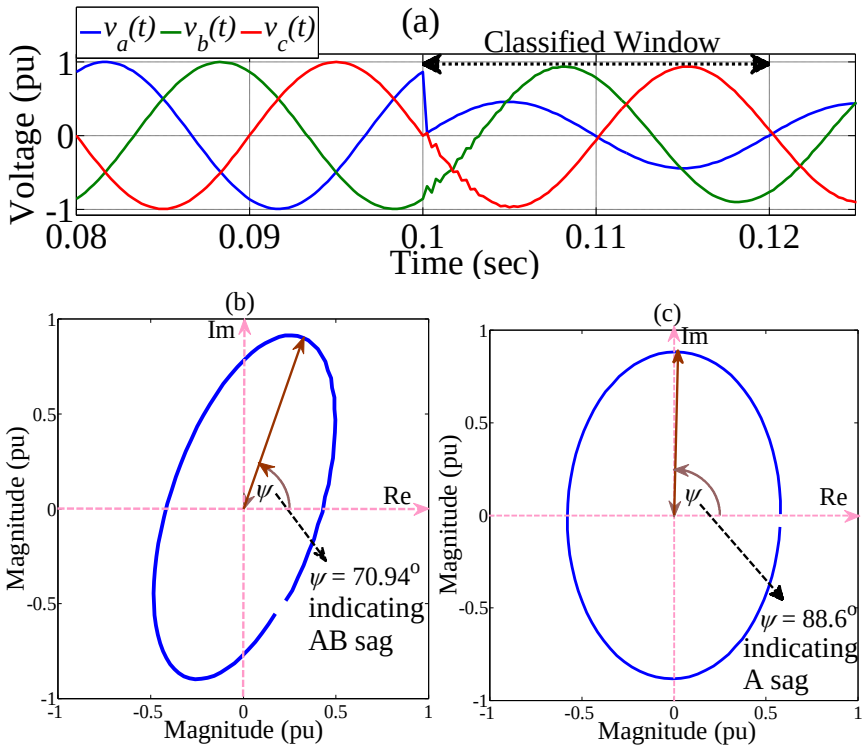

Fig. 6.2. Classification of single phase sag (A-phase sag of (a)) using proposed method: (b) without pre-processed 3-phase voltages and (c) with pre-processed 3-phase voltages.

6.2.3 Shape of Three-phase Voltage Ellipses during different types of Dips and Swells

The proposed approach transforms 3-phase voltages in one complex variable named 3-Φ voltage vector ($\vec{E}$). As observed, under normal condition, peak of the locus of $\vec{E}(t)$ represents a circle with radius equal to the nominal voltage, and for 3-phase sag, radius of the circle becomes smaller than the nominal voltage. Similarly, for three-phase swell, radius of the circle becomes larger than the nominal voltage. But, for single- or double-phase sag or swell, locus of three-phase voltage vector becomes an ellipse with different inclination angle depending on sag/swell severity, and drop/rise in phase voltages. Using pu values of 3-Φ voltages and applying the proposed approach, the shape of ellipses and their inclination angles (ψ) under different types of voltage sags/swells, are shown in Fig. 6.3. Note that Fig. 6.3 is drawn in a complex plane, where real and imaginary part of $\vec{E}(t)$ is mapped in *x*- and *y*-axis respectively.

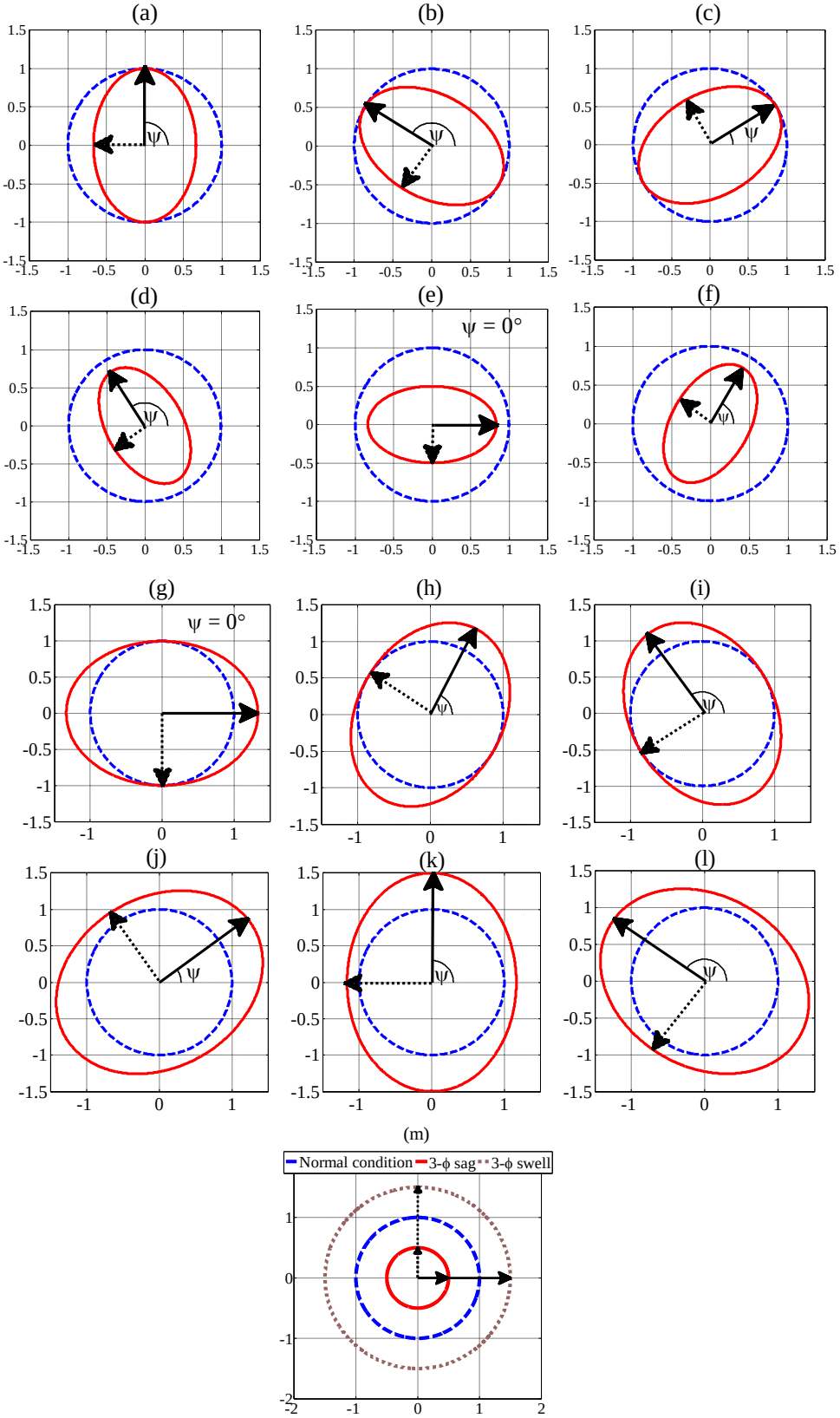

Fig. 6.3. Major axis (solid arrow), minor axis (dotted arrow), shape of ellipses under normal condition (dashed line) and under (a) A-phase sag, (b) C-phase sag, (c) B-phase sag, (d) CA-phase sag, (e) BC-phase sag, (f) AB-phase sag, (g) A-phase swell, (h) C-phase swell, (i) B-phase swell, (j) CA-phase swell, (k) BC-phase swell, (l) AB-phase swell, (m) ABC or 3-phase sag and swell.

6.2.4 Classification and Characterization of voltage Dips and Swells

In Section 6.2.4.1, an algorithm for classification of voltage dips and swells is presented. Then, characterization of voltage dips and swells is explored in Section 6.2.4.2.

6.2.4.1 Algorithm for Classification of Voltage Dips and Swells

Flowchart of Fig. 6.4 shows the algorithm of classification of sags and swells, using three-phase voltage signals within one cycle window length. At first, the complex phase voltages are extracted in each cycle of a sliding window using the DFT (Discrete Fourier Transform). Then, the phase voltage magnitude and phase angle, i.e. the voltage phasors, at power system frequency (50 Hz or 60 Hz), are extracted; this eliminates the harmonics of the input signal. Phase angle jump are calculated from the phasors and these are kept as information. Voltage magnitude (pu) of all three phasors are considered to be separated from each other by 120° and these voltage phasors are regarded as pre-processed voltages. Three parameters including major axis (A_{ma}), minor axis (A_{mi}) and inclination angle (ψ) are extracted by applying 3-phase voltage ellipse transformation on the pre-processed voltages.

Analysing the three-phase voltage ellipse parameters under different types of sags and swells, as presented in Table 6-I, it can be concluded that ABC sags, ABC swells and normal condition (no sag/swell) of the system can be easily classified. To do so, some threshold conditions can be applied on the three-phase voltage ellipse parameters. According to IEEE 1159.2 standard, V < 0.9 pu is considered as sag whereas V > 1.1 pu is defined as swell. Thus, for unbalanced sag and a dip-depth equal to 10% of the nominal voltage, the maximum value of (A_{mi}/A_{ma}) and the maximum value of A_{mi} are obtained as 0.933, which arecalculated from Table 6-I by putting V_f= 0.9 pu and V = 1 pu. Similarly, for unbalanced swell and a voltage rise of 10% of the nominal voltage, the minimum value of A_{ma} is obtained as 1.0667. Moreover, for balanced sag (ABC sag) and balanced swell (ABC swell), value of (A_{mi}/A_{ma}) is obtained as 1. Thus, by incorporating the necessary boundary conditions on the three-phase voltage parameters: (A_{mi}/A_{ma}), A_{ma} and A_{mi}; ABC sags, normal condition (no sag/swell) and ABC swells of the system can be classified as shown in Fig. 6.4. Besides, zero-sequence component parameter, as given by expression (6.4), can enhance the classification of normal condition, ABC dip and ABC swell. During these conditions, all three-phase voltages

are equal and they are separated from each other by 120°, which yields the theoretical value of zero-sequence component as zero, see (6.4). Thus, incorporating this additional zero-sequence parameter (E_0), classification of normal condition, ABC dip and ABC swell is conducted, see Fig. 6.4.

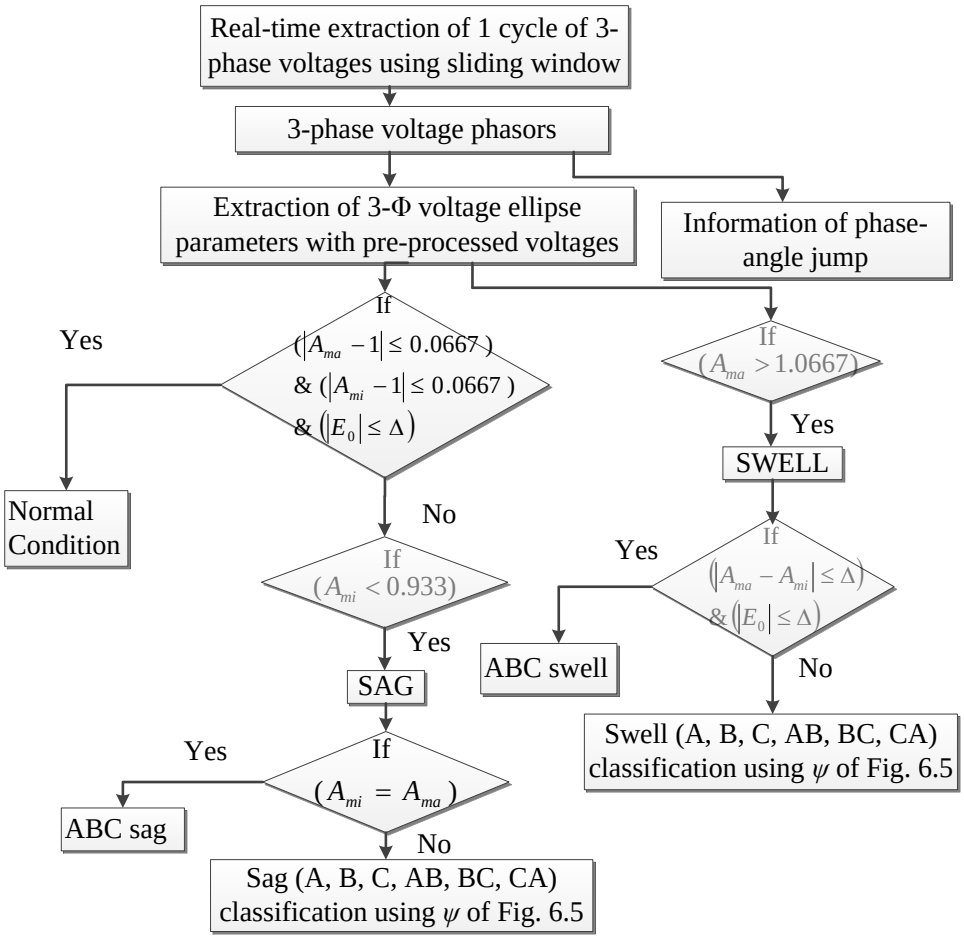

Fig. 6.4.Flowchart of the proposed algorithm.

In Fig. 6.4, taking IEEE 1159.2 standard into account, the normal condition is defined as a condition when the value of major and minor axis lies in the range of 0.933 to 1.0667. And, to distinguish swells, the condition: ($A_{ma} > 1.0667$) is applied considering the minimum value of major axis under 10% voltage rise of the nominal voltage. For ABC swells, theoretical value of (A_{mi}/A_{ma}) is obtained as 1, which implies the difference between A_{ma} and A_{mi} is zero. Therefore, to classify ABC swells, the difference between major and minor axis is considered to be less than or equal to Δ, where a typical value of $\Delta = 0.05$ is selected. Similarly, to classify ABC sags, the conditions: ($A_{mi} < 0.933$) and ($A_{mi} = A_{ma}$)are applied. Additionally, during this classification stage, the condition of zero-sequence component (E_0) is applied.

In the last stage of the flowchart, unbalanced or single and double-phase sags/swells (A, B, C, AB, BC, and CA) are classified by using one parameter – inclination angle (ψ). For this classification, the range of inclination angle as shown in Fig. 6.5, are considered.

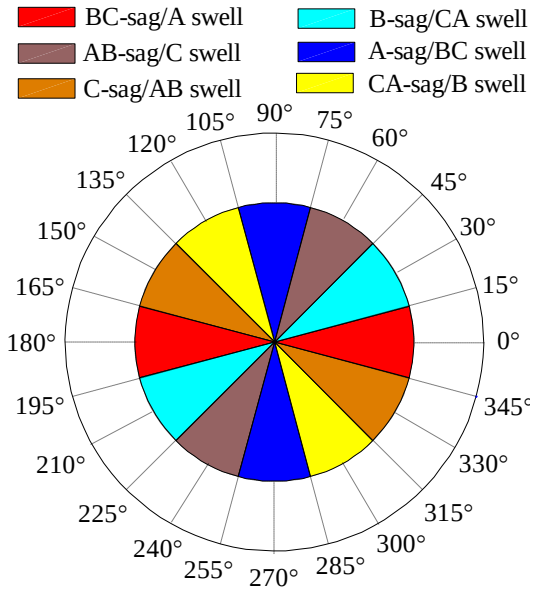

Fig. 6.5.Range of inclination angle (ψ) under different types of sags/swells.

6.2.4.2 Characterization of Voltage Dips and Swells

Once the different types of voltage dips and swells are classified, their severity can be characterized. For balanced three-phase (ABC) dip/swell, severity of dip/swell can be calculated from the major or minor axis of the ellipse, see Table 6-I. However, for unbalanced dip/swell, i.e., A, B, C, AB, BC, and CA dip/swell, severity of dips and swells can be evaluated from the two parameters – minor axis (A_{mi}) and major axis (A_{ma}), respectively. Since A_{mi} is a function of faulted or disturbed phase-voltage magnitude (V_f) as shown in Table 6-I, A_{mi} is considered as a characterization parameter for evaluating the severity of unbalanced voltage dips. Similarly, for unbalanced voltage swells, A_{ma} is selected as a characterization parameter since it is a function of V_f.Another technique to evaluate the gravity of dip/swell is to estimate the surface area of the ellipse in the complex plane. The decrease of the surface area of the ellipse is proportional to the dip gravity. Similarly, increase of the surface area of the ellipse is proportional to the swell gravity. For example, for a given dip-depth, three phase voltage dips are most severe, followed by double phase and single phase dips, which is reflected in the surface area of the ellipse.

6.3 VALIDATION OF THE PROPOSED APPROACH

The proposed method is validated with real data recorded by IEEE working group [117] and the real data obtained from [119].

6.3.1 Validation of the Proposed Method with real data provided by IEEE 1159.2 working group

Real data, recorded by IEEE 1159.2 working group[117], are used to validate the proposed algorithm. Fundamental frequency of the waveforms corresponding to the real data was 60 Hz. At first, complex phase voltages are extracted by applying DFT for one cycle window length. Then, the magnitudes of 3-phase voltages at ±60 Hz are obtained separately and passed through the proposed approach to extract the 3-Φ voltage ellipse parameters. Using these ellipse parameters, cycle by cycle classification and characterization is conducted. For the recorded waveforms, total 6 cycles are observed and classification results of third cycle (0.033 sec to 0.05 sec duration) are presented in Table 6-II. In Table 6-II, 2nd to 4th column shows the three-phase voltage ellipse parameters under different types of sags and swells whereas 5th column presents the "classification results". Table 6-II illustrates the successful classification of different types of sags and swells. Moreover, severity of sags and swells can also be quantified from the minor axis (A_{mi}) and major axis (A_{ma}) parameters respectively.

TABLE 6-II

CLASSIFICATION OF SAGS/SWELLS WITH REAL DATA RECORDED BY IEEE WORKING GROUP

Wave number	Sag and/or swell type (ground-truth)	3-Φ voltage ellipse parameters			Classification results
		A_{mi}	A_{ma}	$\psi°$	
wave 1	B sag	0.72	1.05	30.92	B sag
wave 2	C sag	0.56	0.99	149.51	C sag
wave 6a	C sag	0.45	0.72	145.29	C sag
wave 6b	C sag	0.35	0.65	147.64	C sag
wave 6c	AB sag	0.73	0.81	63.65	AB sag
wave 13	A sag	0.74	1.05	88.61	A sag
wave 14a	C sag and AB swell	0.44	1.10	150.29	C sag and AB swell
wave 14b	C sag and AB swell	0.46	1.09	150.39	C sag and AB swell
wave 14c	C sag and AB swell	0.45	1.07	150.77	C sag and AB swell
wave 15	C sag	0.68	1.04	151.61	C sag

For the application of the proposed approach as a monitoring tool, wave 15 of [117] is taken as an example. Cycle by cycle classification and characterization of wave 15, during 6 cycles of observation period, are illustrated in Fig. 6.6. As shown in Fig. 6.6(b), at each cycle, shapes of ellipse are plotted in a complex plane, and the ellipses represented by the dashed lines indicate the normal condition whereas ellipses marked by the solid lines specify the sag condition (in this case C sag). Moreover, deviation of minor axis (A_{mi}), from normal value of 1 pu, can be seen in Fig. 6.6(c), which characterizes the sag in terms of severity. In summary, the proposed algorithm is able to provide the exact type of sags and/or swells with severity indicator (A_{ma} and/or A_{mi}) as reported in Table 6-II. Moreover, the proposed method was also tested with adding noise (SNR ranging from 20 dB to 30 dB), and harmonic distortion (THD was varied from 1% to 20%); under these conditions, it was found that performance of the proposed method was not affected.

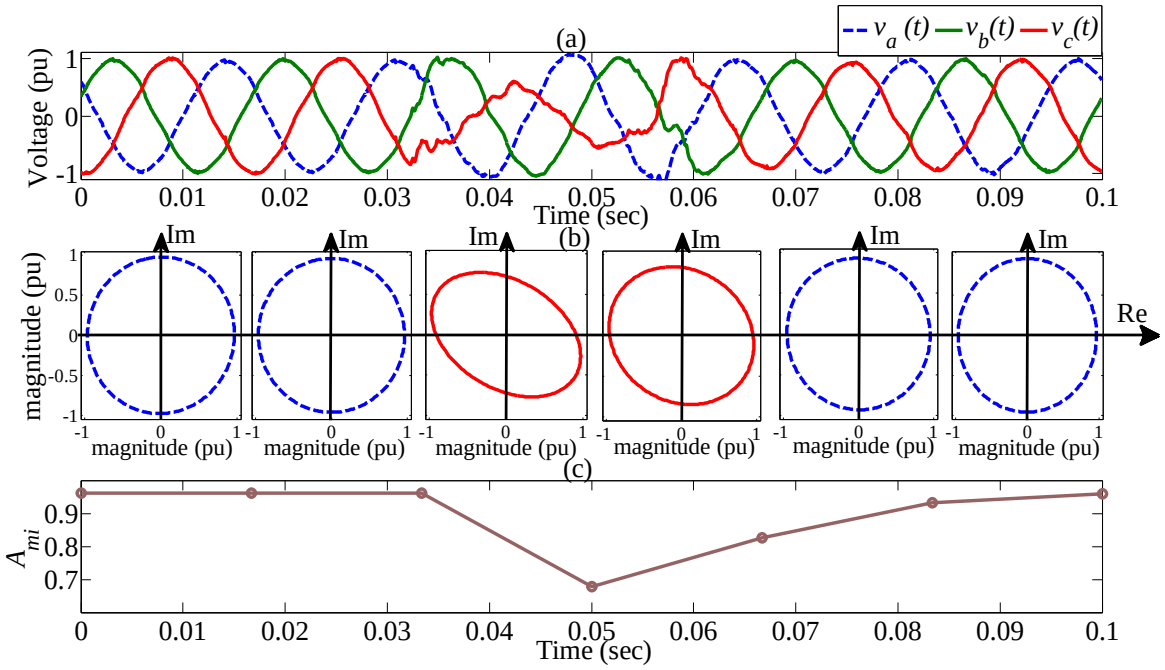

Fig. 6.6. (a) *wave 15*, (b) 3-Φ voltage ellipses at each cycle of *wave 15*, and (c) Minor axis (A_{mi}) as a function of time during 6 cycles of *wave 15*.

6.3.2 Validation of the Proposed Method using real data measured at Belgian transmission grid

To validate the proposed algorithm, voltage sags measured in Belgian transmission grid [119] are used. The phasors presented in Table 6-III are extracted from the waveform stored during the occurrence of voltage sag. Thus, one single phase sag (*Event 2*) and two double phase sags (*Event 1* and *Event 3*) are obtained for validation of the proposed approach. For classification of each type of sags, the three-phase voltage parameters including inclination angle, major axis and minor axis, are used as shown in the flowchart of Fig. 6.4. The results and their corresponding three-phase voltage ellipses in a complex plane, are presented in Table 6-IV and Fig. 6.7 respectively. Table 6-IV shows the successful classification of two double phase sags (BC-phase and CA-phase sag) and one single phase sag (A-phase sag), using the inclination angle (ψ) and the decision boundary shown in Fig. 6.5. Among these three types of sags, BC-phase sag is found to be the most severe sag as characterized by the minor axis.

TABLE 6-III

REAL DATA OBTAINED FROM BELGIAN TRANSMISSION GRID

Events	Type classified in [119] (ground-truth)	3-phase voltage phasors		
		$\boldsymbol{V_a}$	$\boldsymbol{V_b}$	$\boldsymbol{V_c}$
Event 1	C (CA-sag)	0.838∠5.2°	0.982∠-117.9°	0.876∠115.3°
Event 2	D (A-sag)	0.726∠1.7°	0.964∠-114.6°	0.958∠116.9°
Event 3	E (BC-sag)	0.977∠1.2°	0.286∠-166.6°	0.365∠124.2°

TABLE 6-IV

CLASSIFICATION OF SAGS/SWELLS WITH REAL DATA OF BELGIAN TRANSMISSION GRID

Events	3-phase voltage ellipse parameters			Classification results
	A_{mi}	A_{ma}	$\psi°$	
Event 1	0.85	0.94	111.82	CA-phase sag
Event 2	0.80	0.96	90.62	A-phase sag
Event 3	0.32	0.76	3.01	BC-phase sag

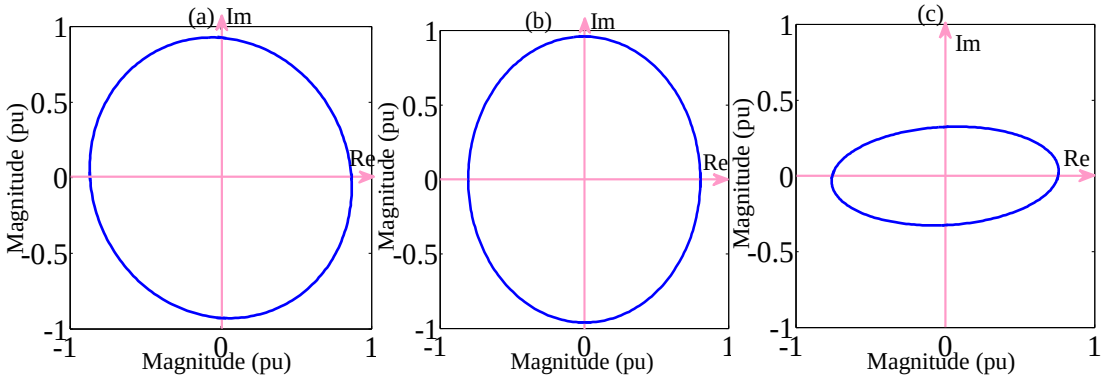

Fig. 6.7. 3-phase voltage ellipse during: (a) *Event 1*, (b) *Event 2*, (c) *Event 3*.

6.4 CASE STUDIES

Using the proposed approach, three cases, which include *Case 1*, *Case 2* and *Case 3*, are studied. *Case 1* incorporates a 12 bus test distribution network embedded with Synchronous Generator (SG) based DG. *Case 2* includes a practical distribution network of NSW, Australia. *Case 3* incorporates a typical mesh distribution network. Several test cases of voltage sags and swells, originated from faults at several buses in these distribution networks, have been detected, classified and characterized.

6.4.1 Case 1

A test distribution network shown in Fig. 6.8 has been simulated to test the proposed method for detection and classification of sags and swells. The simulated system is a radial distribution network with base-power of 24 MVA. It is comprised of a 132-kV, 50-Hz, subtransmission system with a short-circuit level of 1000 MVA, represented by a Thévenin equivalent (marked as Sub in the figure), which feeds a 33-kV distribution system through a 132/33-kV transformer. In this system, there are four 6-MVA synchronous generator (SG) connected to bus 6, 12, 10 and 8. These four DGs are connected to the network through 33/0.69 kV transformers. The lines are modelled as π section line. The synchronous generator is represented by a sixth-order three-phase model in the *d-q* rotor reference frame and it is equipped with an AVR (Automatic Voltage Regulator) represented by the IEEE—Type 1 model. More details of the network parameters are presented in **Appendix A.3.**

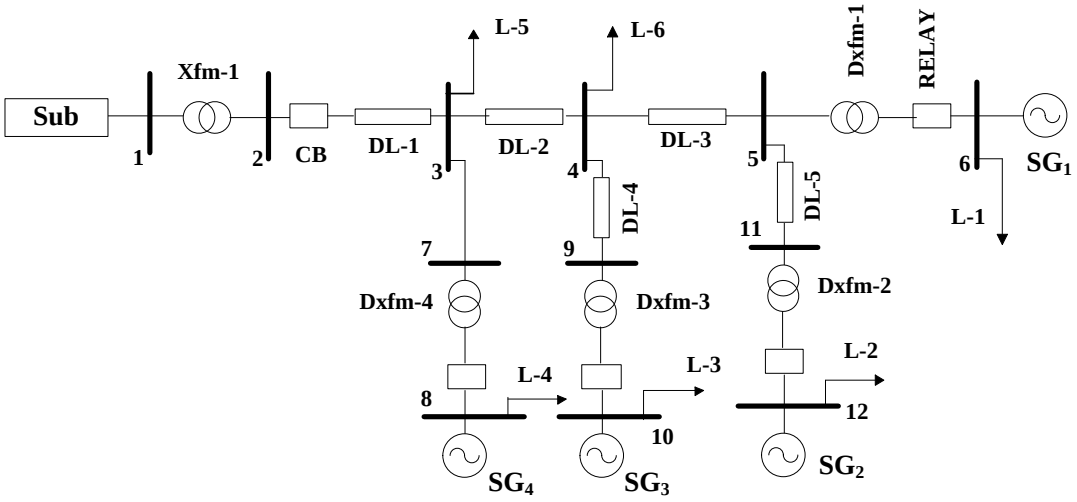

Fig. 6.8. Single line diagram of a 12 bus test distribution network.

The test system is simulated at 2 kHz sampling frequency and the relays are placed at transformer connection points of SG_1, SG_2, SG_3 and SG_4 respectively, to collect three-phase voltages. Several test cases of voltage sags and swells are generated by artificially creating balanced and unbalanced faults at bus number 11 and 4. Total 2 second time domain simulation is carried out where fault occurs soon after 1 second with fault duration of 5 cycles. And, a typical fault resistance of 0.001 ohm is considered. The voltage waveforms are collected from the relay connected at bus 6. By applying the proposed approach, cycle by cycle classification is carried out on the collected waveforms. The classification results of one cycle, which starts soon after the inception of faults, are presented in Table 6-VA.

From Table 6-VA, it is evident that for the fault at bus 11, balanced and unbalanced sags are classified correctly by the value of inclination angle (ψ) (see Fig. 6.5) and severity of sags can be realized from the value of minor axis (A_{mi}). Additionally, for the fault at bus 4, sag and swell are observed simultaneously where severity of sag and swell can be characterized from the value of minor axis (A_{mi}) and major axis (A_{ma}) respectively. The three-phase voltage ellipses under the sag/swell conditions of Table 6-VA are shown in Fig. 6.9. In Table 6-VA, the voltage sags are monitored from bus 6; however, the voltage sags encountered at bus 2, due to fault (balanced and unbalanced) at bus 11 and 4, are also classified and characterized as illustrated in Table 6-VB. The severity of voltage sags can be realized from the parameter A_{mi}. From Tables 6-VA and 6-VB, it is revealed that the severity of voltage sags observed from bus 2 is comparatively less than the voltage sags encountered at bus 6, due to similar type of

fault at bus 4 or bus 11. Moreover, AG fault at bus 11 did not cause a sag; therefore, the proposed approach classifies it as normal condition or "No-sag/swell" condition.

TABLE 6-VA

CLASSIFICATION AND CHARACTERIZATION OF FAULT INITIATED SAGS/SWELLS OBSERVED FROM BUS 6

Fault Type	Fault at Bus	3-Φ voltage ellipse parameters			Classified Sags/Swells
		A_{mi}	A_{ma}	$\psi°$	
AG	11	0.72	0.85	81.39	A-sag
BG	11	0.73	0.86	25.48	B-sag
CG	11	0.74	0.87	142.22	C-sag
AB	11	0.59	0.69	58.8	AB-sag
BC	11	0.59	0.69	3.56	BC-sag
CA	11	0.59	0.68	119.15	CA-sag
ABC	11	0.52	0.53	30.17	ABC-sag
AG	4	0.46	1.27	88.21	A-sag and BC-swell
BG	4	0.46	1.24	27.95	B-sag and CA-swell
CG	4	0.46	1.27	148.36	C-sag and AB-swell

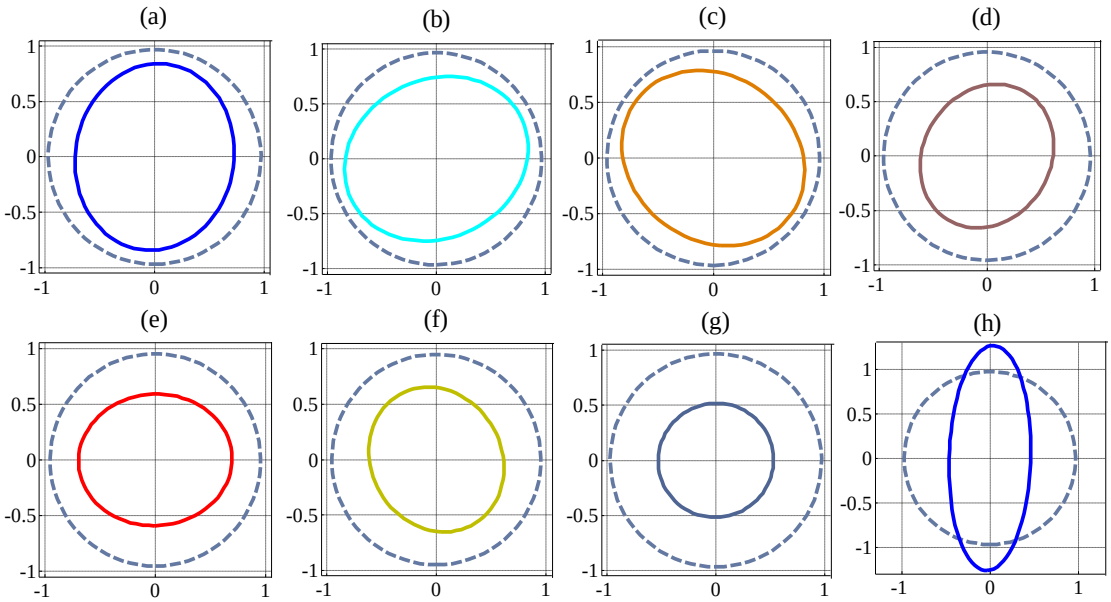

Fig. 6.9. Three-phase voltage ellipses observed under normal condition (dashed line) and under: (a) A-sag, (b) B-sag, (c) C-sag, (d) AB-sag, (e) BC-sag, (f) CA-sag, (g) ABC-sag, (h) A-sag and BC-swell.

TABLE 6-VB

CLASSIFICATION AND CHARACTERIZATION OF FAULT INITIATED SAGS/SWELLS OBSERVED FROM BUS 2

Fault Type	Fault at Bus	3-Φ voltage ellipse parameters			Classified Sags/Swells encountered at bus 2
		A_{mi}	A_{ma}	$\psi°$	
AG	11	0.94	1.01	90.66	No-sag/swell
AB	11	0.88	0.95	60.78	AB-sag
ABC	11	0.83	0.85	89.77	ABC-sag
AG	4	0.89	1.00	90.3	A-sag
BG	4	0.90	0.99	37.01	B-sag
CG	4	0.90	0.99	143.65	C-sag

6.4.2 Case 2

In this study, several test cases of balanced and unbalanced fault initiated sags, at several buses in a rural distribution network of Australia, have been detected, classified and characterized.

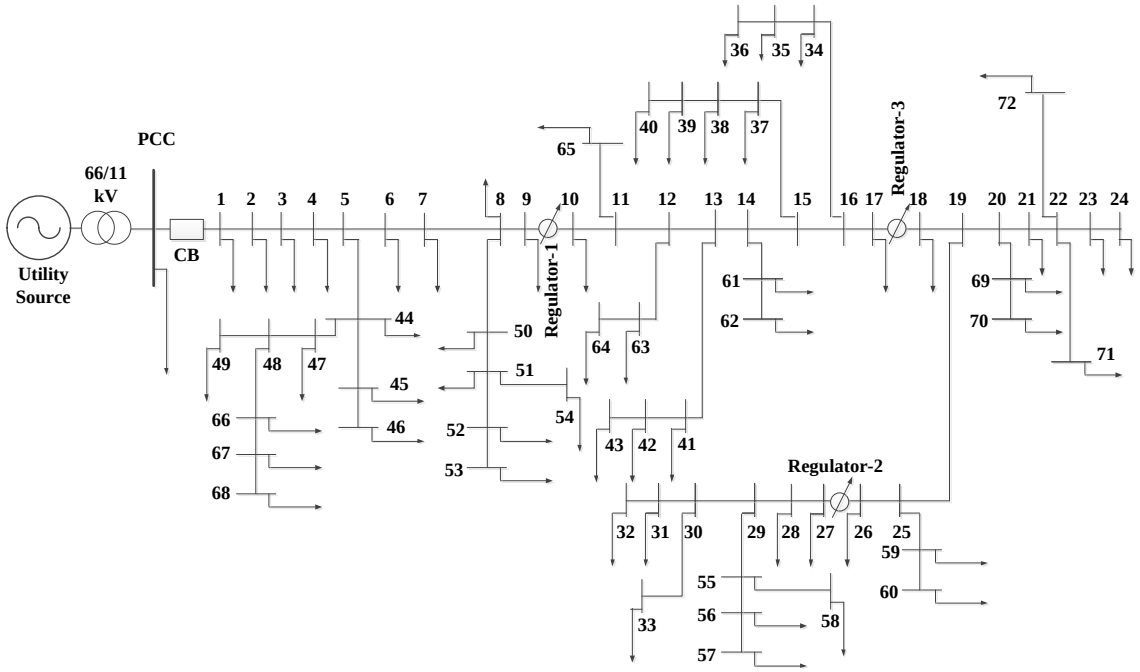

Fig. 6.10.A test distribution network in Australia.

Fig. 6.10 shows an 11 kV rural distribution network extracted from the New South Wales distribution networks, Australia. The system is simulated in SIMPOWER SIMULINK to generate the fault initiated sags. The simulated system is a radial

distribution network with base power of 100 MVA. It is comprised of a 66-kV, 50-Hz, subtransmission system with a short-circuit level of 1000 MVA, represented by a utility source, which feeds an 11-kV rural distribution feeder through a 66/11-kV transformer. Total load of 4 MW has been distributed at several buses of the distribution network. More details of the network parameters, such as, loads, distribution lines, etc., are presented in **Appendix A.4.**

Symmetrical faults or ABC faults and non-symmetrical faults, such as, single phase faults (AG: A-phase-to-ground, BG: B-phase-to-ground, CG: C-phase-to-ground) and double phase faults (AB: line-A-to-line-B, BC: line-B-to-line-C, CA: line-C-to-line-A) are simulated at two arbitrarily selected buses, bus 66 and bus 37, of the test network shown in Fig. 6.10. These faults initiated sags are monitored from different monitoring ends i.e. from bus 49, 46, 8, 70, 62 and 43. Total 2 second time domain simulation is carried out where fault occurs soon after 1 second with fault duration of 5 cycles. And, a typical fault resistance of 0.001 ohm is considered. By applying the proposed approach, the classification results of one cycle, which starts soon after the inception of faults, are presented in Table 6-VI and Table 6-VII. Moreover, Fig. 6.11 shows the visual presentation of the three-phase voltage ellipses corresponding to the sags of Table 6-VI.

Figs. 6.4-6.5 and Tables 6-VI and 6-VII show that voltage sags can be classified by the inclination angle (ψ) and the sag severity can be characterized by the minor axis (A_{mi}). From Tables 6-VI and 6-VII, it can be observed that a sag monitored in the vicinity of the fault-location has a lower A_{mi} value than a sag monitored at relatively distant end. For example, when a fault occurs at bus 66 (see Fig. 6.10), bus 49 is nearer than bus 46 in terms of electrical distance from the fault-location. Therefore, for different types of sags, A_{mi} value obtained at monitoring bus 49 gives a lower value (see Table 6-VI and Fig. 6.11). Besides, sags encountered at buses 8 and 70, which are relatively farther than buses 49 and 46 (in terms of electrical distance from the fault-location at bus 66), indicates less severity than the sags occurring at buses 49 and 46. Some events, such as single-phase faults at bus 66, did not cause a sag at bus 8 or 70; hence, it is correctly classified as a "No-sag" condition, see Table 6-VI. Similarly, the A_{mi} value obtained from monitoring bus 62 is lower than the A_{mi} value obtained from monitoring bus 43, when the fault occurs at bus 37, see Table 6-VII for illustration. Moreover, the sag at bus 8, which is relatively farther than bus 62 or 43, indicates less severity than the sag observed at buses 62 and 43. In contrast, A_{mi} at bus 70 indicates

more severe voltage sag than the sags realized at buses 62 and 43, since bus 70 is relatively nearer to the fault-location (bus 37), see Table 6-VII.

TABLE 6-VI

CLASSIFICATION AND CHARACTERIZATION OF FAULT INITIATED DIPS/SWELLS: FAULT AT BUS 66

Fault Type	Monitoring Bus	3-Φ voltage ellipse parameters			Classified Sags/Swells
		A_{mi}	A_{ma}	ψ°	
AG	49	0.76	0.98	88.14	A-sag
	46	0.86	1.01	87.32	A-sag
	8	0.94	1.01	83.47	No-sag
	70	0.94	1.02	79.08	No sag
BG	49	0.76	0.97	29.43	B-sag
	46	0.86	0.99	29.30	B-sag
	8	0.95	0.99	32.05	No sag
	70	0.96	0.99	24.3	No sag
CG	49	0.76	0.97	147.07	C-sag
	46	0.86	1.00	145.45	C-sag
	8	0.94	1.00	128.42	No sag
	70	0.95	1.00	121.95	No sag
AB	49	0.73	0.91	52.10	AB-sag
	46	0.82	0.96	49.10	AB-sag
	8	0.91	0.99	51.88	AB-sag
	70	0.92	1.00	81.85	AB-sag
BC	49	0.74	0.90	170.46	BC-sag
	46	0.83	0.95	167.14	BC-sag
	8	0.92	0.98	165.1	BC-sag
	70	0.93	0.99	166.23	BC-sag
CA	49	0.73	0.91	109.74	CA-sag
	46	0.83	0.97	106.08	CA-sag
	8	0.9	1.00	105.2	CA-sag
	70	0.91	1.00	105.1	CA-sag
ABC	49	0.63	0.64	81.67	ABC-sag
	46	0.76	0.77	68.81	ABC-sag
	8	0.87	0.89	89.87	ABC-sag
	70	0.88	0.90	89.64	ABC-sag

TABLE 6-VII

CLASSIFICATION AND CHARACTERIZATION OF FAULT INITIATED DIPS/SWELLS: FAULT AT BUS 37

Fault Type	Monitoring Bus	3-Φ voltage ellipse parameters			Classified Sags/Swells
		A_{mi}	A_{ma}	$\psi°$	
AG	62	0.62	0.93	88.08	A-sag
	43	0.67	0.95	88.14	A-sag
	8	0.79	0.96	86.32	A-sag
	70	0.55	0.92	85.35	A-sag
BG	62	0.63	0.92	28.82	B-sag
	43	0.67	0.94	28.97	B-sag
	8	0.81	0.95	29.43	B-sag
	70	0.56	0.90	26.29	B-sag
CG	62	0.62	0.92	147.20	C-sag
	43	0.67	0.94	147.15	C-sag
	8	0.81	0.95	141.68	C-sag
	70	0.56	0.90	143.83	C-sag
AB	62	0.61	0.87	53.48	AB-sag
	43	0.65	0.89	53.63	AB-sag
	8	0.85	0.97	59.45	AB-sag
	70	0.67	0.92	53.65	AB-sag
BC	62	0.61	0.86	172.16	BC-sag
	43	0.66	0.88	172.20	BC-sag
	8	0.86	0.95	172.81	BC-sag
	70	0.68	0.90	170.79	BC-sag
CA	62	0.60	0.87	111.78	CA-sag
	43	0.65	0.89	111.83	CA-sag
	8	0.84	0.97	110.36	CA-sag
	70	0.67	0.92	109.97	CA-sag
ABC	62	0.42	0.42	91.69	ABC-sag
	43	0.50	0.50	93.10	ABC-sag
	8	0.72	0.74	89.73	ABC-sag
	70	0.38	0.39	88.51	ABC-sag

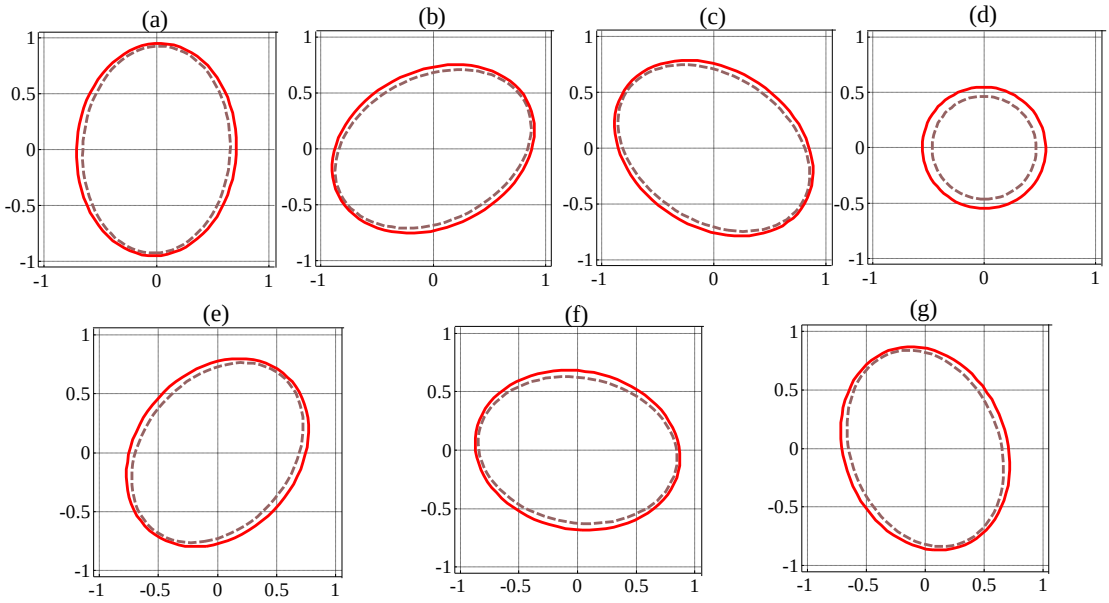

Fig. 6.11. Three-phase voltage ellipses observed at monitoring bus 46 (solid line) and 49 (dashed line) due to faults at bus 66 results in: (a) A-sag, (b) B-sag, (c) C-sag, (d) ABC-sag, (e) AB-sag, (f) BC-sag, and (g) CA-sag.

6.4.3 Case 3

In *Case 3*, the detection, classification and characterization of balanced and unbalanced fault initiated sags are conducted in a typical mesh distribution network. Fig. 6.12 shows an 11 kV mesh distribution network, simulated in SIMPOWER SIMULINK to generate the fault initiated sags. The simulated system is comprised of an 11-kV, 50-Hz, subtransmission system with a short-circuit level of 1000 MVA, represented by a source. A total load of 600 kW is distributed at buses 1, 2, 3, 4, and 5 of the distribution network. Three synchronous type DGs, each with a capacity of 250 kW, are placed at buses 3, 4, and 5. Symmetrical and unsymmetrical faults are simulated at two arbitrarily selected buses: bus 3 and bus 5 of the test network of Fig. 6.12. These faults initiated sags are monitored from different monitoring ends i.e. from bus 1, 4 and 5. A fault occurs 0.2 second after the start of the simulation and lasts for 5 cycles. The classification of sags and characterization of sags and swells using the proposed approach are presented in Table 6-VIII. Test results indicate that all fault-initiated sags are classified correctly from different monitoring points. It is to be noted though that the phase-voltages observed at bus 1, which is close to the upstream side or source side, did not encounter sag due to AB-phase fault at bus 3; therefore, it is correctly classified as "No-sag" or normal condition by the proposed approach.

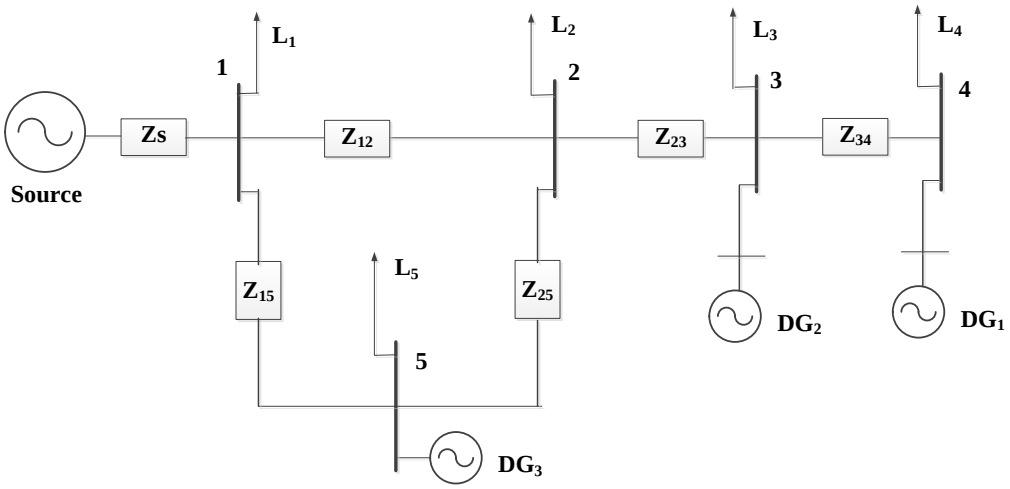

Fig. 6.12.A typical mesh distribution network.

TABLE 6-VIII

CLASSIFICATION AND CHARACTERIZATION OF FAULT INITIATED SAGS/SWELLS IN A MESH DISTRIBUTION NETWORK

Fault Type	Fault at bus	Monitoring bus	3-Φ voltage ellipse parameters			Classified Sags/Swells
			A_{mi}	A_{ma}	$\psi°$	
AG	3	1	0.92	1.01	89.84	A-sag
		4	0.36	1.03	89.56	A-sag
		5	0.81	1.02	89.69	A-sag
AB		1	0.92	0.98	69.2	No-sag
		4	0.47	0.79	61.46	AB-sag
		5	0.80	0.93	63.56	AB-sag
ABC		1	0.89	0.91	90	ABC-sag
		4	0.04	0.04	95	ABC-sag
		5	0.72	0.74	90.02	ABC-sag
AG	5	1	0.85	1.01	89.9	A-sag
		4	0.66	1.03	89.45	A-sag
		5	0.33	1.02	89.88	A-sag
AB		1	0.84	0.95	64.08	AB-sag
		4	0.66	0.87	62.63	AB-sag
		5	0.49	0.82	61.13	AB-sag
ABC		1	0.78	0.79	90	ABC-sag
		4	0.49	0.50	90.77	ABC-sag
		5	0	0	99	ABC-sag

6.5 MONITORING OF VOLTAGE SAG/SWELL IN REAL-TIME USING PROPOSED APPROACH

This Section presents a tool for voltage sag/swell monitoring in electricity network. The proposed tool can be used for real-time monitoring of voltage sag/swell if the following facilities are available in the network:

- Time synchronization among all monitoring nodes is readily available according to the IEEE Standard C37.118–2005 [120].
- The monitoring system requires the instantaneous 3-phase voltages at every 1 cycle. Therefore, reliable input data, in the form of 3-phase instantaneous voltage signals, is required to be sent to the proposed algorithm embedded tool in real-time. These can be obtained using potential transformer (PT), which provides an excellent reproduction of primary voltage, both transient and steady-state [1], and reliable communication channel, such as, TCP/IP, switched Ethernet, high-speed wide area networks, etc. Illustration of such reliable communication channels can be found in IEC61850 standard [121], which is employed for substation automation.

In short, if the facilities, such as, real-time data transfer, data synchronization and level of data reliability, etc., are available in an electricity network which is to be monitored, then the proposed tool can be installed in a monitoring station to analyse the voltage sag/swell in real-time. Taking the availability of the above facilities into consideration, this Section demonstrates a real-time sag/swell monitoring tool. To this end, a total of 14.42 seconds time-domain simulation is carried out using the test network of Fig. 6.8. Several types of sags and swells are generated by artificially creating different types of faults at buses 11 and 4, with a time interval of 1.3 seconds and fault duration of 5 cycles. The snapshot of instantaneous 3-phase voltages during normal condition, balanced and unbalanced sags and swells are shown in Fig. 6.13. The snapshot of real-time sag and swell monitoring tool along with log report are shown in Fig. 6.14.

In Fig. 6.14, "Real-time Sag Monitoring" tool demonstrates the three-phase voltage ellipses generated in real-time after processing the time-domain instantaneous 3-phase voltages through the proposed approach. The ellipses, corresponding to the balanced and unbalanced sags, are created in their respective square blocks. In each block, "time (sec)" indicates the instant of the sag or normal condition; and "A_{ma}", "A_{mi}" specifies the value of major and minor axis during that instant. Similarly, "Real-time Swell

Monitoring" tool demonstrates the shape and behaviour of three-phase voltage ellipses under normal and disturbed conditions. The whole scenario can be visualized through a video. The video can be viewed from the following link:

https://drive.google.com/file/d/0B4lp0bqMwpWrajlvU0ZVR1NtM28/edit?usp=sharing

TABLE 6-IX

LOG REPORT OBTAINED FROM CLASSIFICATION OF SAGS/SWELLS USING PROPOSED APPROACH IN REAL-TIME

Fault/Event Type	Fault/Event occurrence time (sec)	Observed and classified sag/swell		
		Dip/swell type	Detection time (sec)	
			From	To
AG fault	0.1-0.2	A-sag	0.1	0.2
		ABC-sag	0.2	0.22
BG fault	1.5-1.6	B-sag	1.5	1.62
		ABC-sag	1.62	1.64
CG fault	2.9-3.0	C-sag	2.9	3.0
		ABC-sag	3.0	3.04
ABC fault	4.3-4.4	ABC-sag	4.3	4.46
AB fault	5.7-5.8	AB-sag	5.7	5.8
		ABC-sag	5.8	5.86
BC fault	7.1-7.2	BC-sag	7.1	7.22
		ABC-sag	7.22	7.26
CA fault	8.5-8.6	CA-sag	8.5	8.62
		ABC-sag	8.62	8.66
ABC-swell	9.9-10	ABC-swell	9.9	10
CG fault	11.2-11.3	AB-swell	11.2	11.3
		C-sag	11.2	11.3
AG fault	12.5-12.6	BC-swell	12.5	12.6
		A-sag	12.5	12.6
BG fault	13.8-13.9	CA-swell	13.8	13.9
		B-sag	13.8	13.9

In Fig. 6.14, "Log Report of Sag-Swell" is also shown and it is obtained by storing the real-time data: "time (sec)" and "three-phase voltage ellipse parameters", in a log file. The log report can be a useful record for off-line analysis of sag/swell data in electricity networks. Table 6-IX summarizes this log report and it highlights the classification results of different types of sag/swell, which are initiated by different types of faults as discussed earlier. Moreover, duration of sag/swell is also obtained from the "Detection time (sec)" of sag/swell occurrence. From Table 6-IX, it can be

observed that during the transition of A-sag to normal condition, ABC-sag is found. For instance, duration of AG fault is 0.1-0.2 sec, and the classified sag is A-sag followed by the detection time ranging from 0.1 to 0.2 sec. However, ABC-sag is found from 0.2 to 0.22 sec, i.e., during the transition of A-sag to normal condition, which is evident from Fig. 6.13 and hence, it is reflected in the classification results of Table 6-IX. Similar observation is found for B-, C-, ABC-, AB-, BC-, and CA-sag conditions.

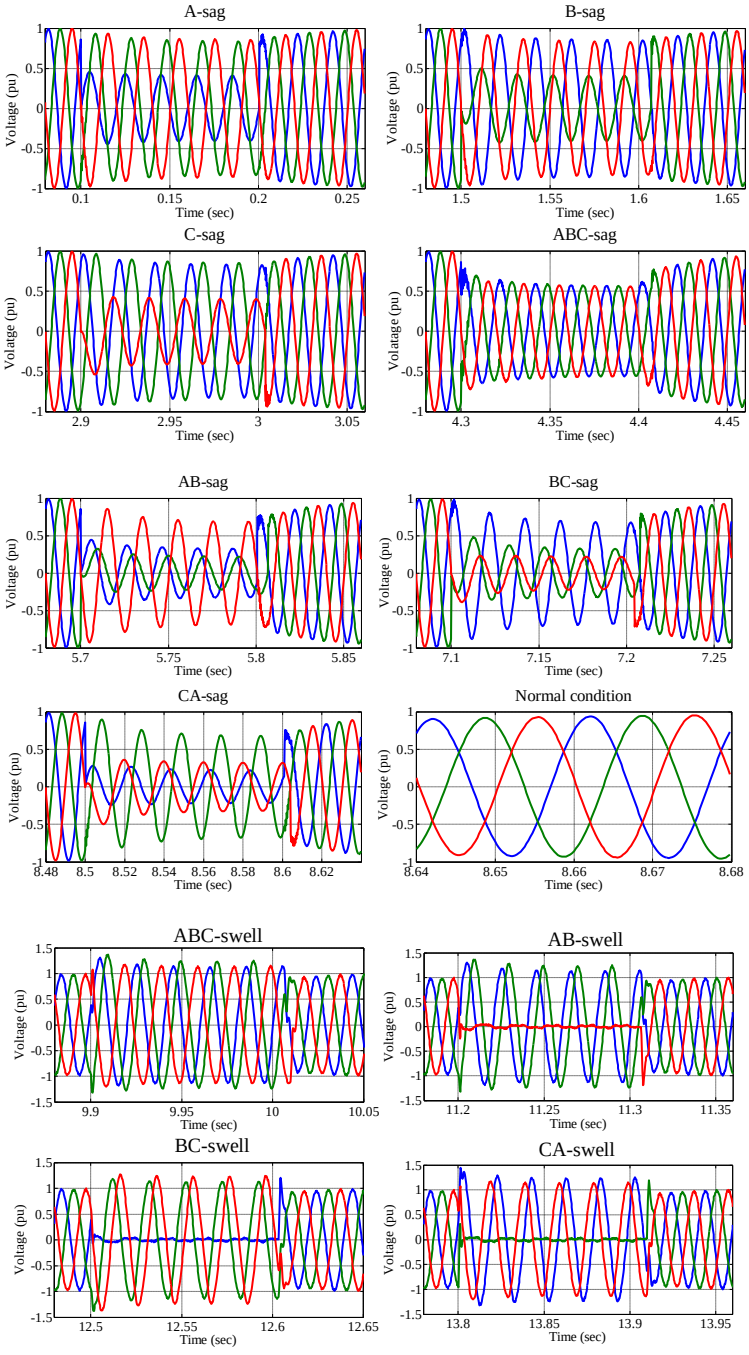

Fig. 6.13.Instantaneous 3-phase voltages observed at a monitoring point during different types of faults and under normal condition.

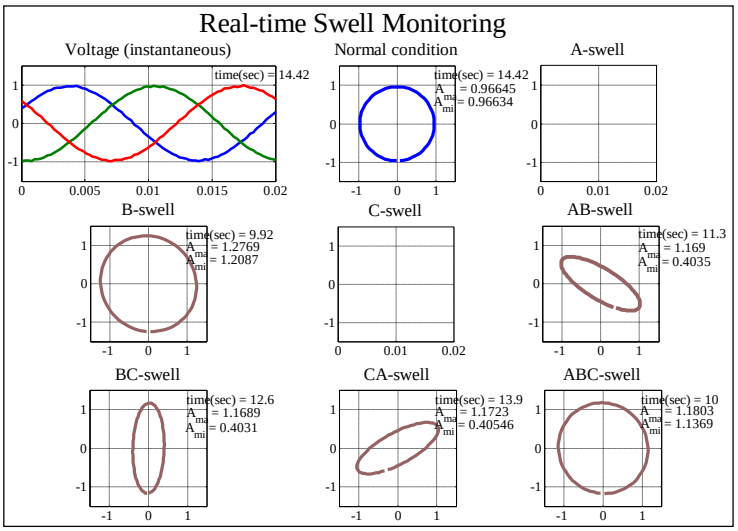

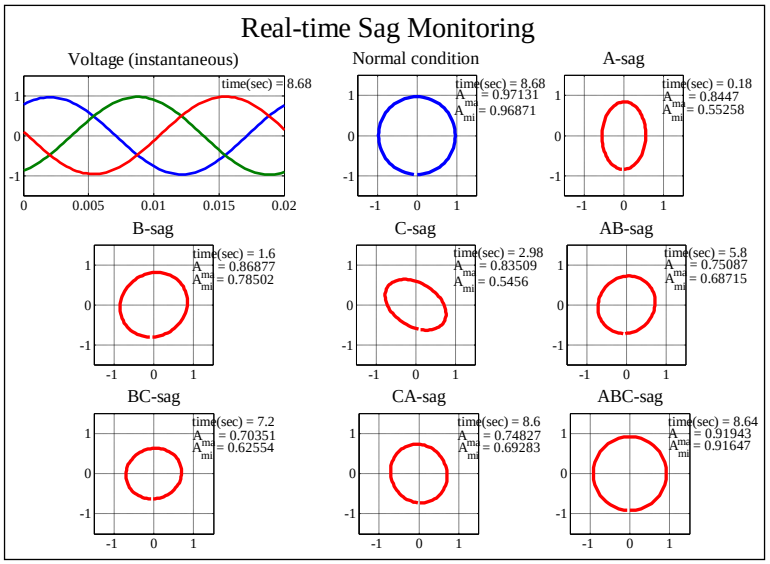

LOG REPORT OF SAG-SWELL

	Timestamp (sec)	Ami	Ama	Inclination angle (degree)
A-SAG	0.1000	0.6113	0.9340	88.4768
A-SAG	0.1200	0.5799	0.8844	88.5894
A-SAG	0.1400	0.5640	0.8614	88.6501
A-SAG	0.1600	0.5565	0.8505	88.6781
A-SAG	0.1800	0.5526	0.8447	88.6936
ABC-SAG	0.2000	0.8742	0.8976	90.8157
B-SAG	1.5000	0.5670	0.9421	29.2486
B-SAG	1.5200	0.5802	0.8885	28.8391
B-SAG	1.5400	0.5627	0.8608	28.9214
B-SAG	1.5600	0.5543	0.8484	28.9452
B-SAG	1.5800	0.5500	0.8420	28.9499
B-SAG	1.6000	0.7850	0.8688	29.5152
ABC-SAG	1.6200	0.9244	0.9277	101.1046
C-SAG	2.9000	0.6146	0.9335	149.4237
C-SAG	2.9200	0.5751	0.8796	149.1845
C-SAG	2.9400	0.5585	0.8544	149.0425
C-SAG	2.9600	0.5501	0.8418	148.9924
C-SAG	2.9800	0.5456	0.8351	148.9688
ABC-SAG	3.0000	0.8220	0.8757	143.7159

Fig. 6.14.Snapshot of real-time sag and swell monitoring tool, and the log report for off-line analysis.

6.6 DISCUSSIONS

In this Chapter, the three-phase voltage ellipse is formed by considering two orthogonal components in a complex plane. These two components are obtained through Clarke's transformation. The third component, i.e., the zero-sequence component, is applied as a parameter for the classification algorithm in conjunction with the ellipse parameters.

The proposed three-phase voltage ellipse method is simple to use as an online tool and provides a quick screening of voltage dip/swell. It has some limitations in classifying the types of voltage dips, which are influenced by phase angle jump, specially the types D, F, C, and G, as presented in[22]. However, pre-processed voltages, which are applied in the three-phase voltage ellipse method, can identify the D, F type dips as double-phase dips and C, G type dips as single-phase dips correctly. In short, the method can classify and characterize voltage dip/swell in terms of the severity of dip/swell-phase voltages. According to[22], different types of voltage dips are originated due to propagation of dips through different network elements, such as, transformers of different types (e.g. delta-wye, wye-delta etc.). Transformers cause phase-angle shift of voltages along with change of voltage magnitudes; thus, making the classification task even more complex. Therefore, the detailed classification of voltage dips and swells would require the events to be classified in terms of severity of dip/swell-phase as well as with the identification of dip/swell-type. Taking this into consideration, a new and detailed approach using 3D polarization ellipse parameters is proposed in the next chapter (**Chapter 7**) to classify and characterize voltage dips and swells of different types.

6.7 SUMMARY

A new algorithm for classification and characterization of voltage sags and swells is proposed in this Chapter. It is based on the shape of three-phase voltage ellipse which is defined by the three parameters of ellipse: major axis, minor axis and inclination angle. Prior to applying the three-phase voltage ellipse transformations on 3-phase voltages, voltage phasors are pre-processed in order to ignore the impact of phase angle jump, which may deteriorate the performance of classification. Then three-phase voltage ellipse parameters are extracted which are used to classify and characterize voltage sags

and swells. The proposed method is validated with real data, and simulated data (sags and swells) during balanced and unbalanced faults in test distribution networks (radial and mesh networks) as well as in a practical distribution network of Australia. Moreover, this chapter also exhibits the development of the proposed algorithm as a real-time sag/swell monitoring tool. Based on the validation with recorded waveforms and demonstration of the approach as a sag-swell monitoring tool, the proposed method would be an important tool for real-time detection and classification of voltage sags and swells in electricity networks.

Chapter 7

DETECTION, CLASSIFICATION AND CHARACTERIZATION OF VOLTAGE DIPS AND SWELLS USING 3D POLARIZATION ELLIPSE PARAMETERS

7.1 INTRODUCTION

Voltage dips are usually characterized by the minimum voltage magnitude and total duration [24-27]. According to [28], these standards can be effective for the characterization of single-phase and 3-phase balanced voltage dips; however, these approaches fail to characterize unbalanced voltage dips, including single- and double-phase dips. To resolve this problem, Bollen proposed a seven-type dip classification [22], referred to as ABC classification. Bollen and Zhang also proposed a symmetrical component based technique to classify and characterize voltage dips [23, 29]. In [30], it was reported that the symmetrical component technique has some limitations in characterizing unbalanced voltage sags originating from large dynamic loads. In [31], a space vector method was presented wherein the ellipse inclination angle was used to classify single-phase and double-phase voltage dips. However, this method is not suitable for classification of voltage dips for the case of large phase angle jump.

This Chapter presents a new method for classification and characterization of voltage dips and swells in electricity networks. The proposed method exploits unique signatures and parameters of three phase voltage signals extracted from the polarization ellipse in three-dimensional (3D) co-ordinates. Five ellipse parameters, which include azimuthal angle, elevation, tilt, semi-minor axis and semi-major axis, are used to classify and characterize voltage dips and swells. Seven types of voltage dips, which include a total of 19 groups of dips incorporating different kinds of balanced (three-phase dips) and unbalanced (single-phase or double-phase) dips, are identified and successfully classified using the 3D polarization ellipse parameters. Two types of voltage swells,

which include a total of 6 groups, are also classified using the proposed method.Cycle by cycle classification is carried out in this approach. The proposed method is validated using real measurement data, recorded waveforms provided by the IEEE 1159.2 working group, and the data of unbalanced dips associated with phase angle jumps, voltage drops and rotations due to loading effects. The advantage of this method is that it can cope with large angle jumps, and it has the capability to detect both voltage dips and swells.

The remainder of the Chapter is structured as follows. Section 7.2 describes the behaviour of the *Polarization Ellipse* (PE) parameters under the different types of voltage dips. The proposed approach for the classification and characterization of voltage dips and swells is developed in Section 7.3. Section 7.4 presents the experimental validation and results. Section 7.5 concludes the Chapter.

7.2 CHARACTERIZATION OF 3-PHASE VOLTAGE WAVEFORMS USING POLARIZATION ELLIPSE

In the next subsections, the polarization ellipse is obtained by mapping the three phase voltage signals onto three perpendicular axes of a Cartesian co-ordinate system. Then five ellipse parameters, namely azimuthal angle (φ), elevation angle (θ), tilt angle (ψ), semi-minor axis (A_y) and semi-major axis (A_x) are extracted for different types of voltage dips. Moreover, expressions of θ and φ are developed for seven types of voltage dips.

7.2.1 Polarization Ellipse in 3-D

The instantaneous three-phase voltage signals received at a monitoring end of a transmission or distribution network can be presented as

$$v_{\Phi}(t) = |\boldsymbol{V}_{\Phi}| \cos(\omega t + \alpha_{\Phi}) \tag{7.1}$$

where $\Phi = a, b,$ and c denotes phase-*a*, phase-*b* and phase-*c*, respectively. These instantaneous voltages can be represented by the vectors in 3D space, which are obtained by mapping $v_a(t), v_b(t)$ and $v_c(t)$ on the X, Y and Z co-ordinates, respectively. The tip of the resultant vector, denoted by $\boldsymbol{R}$, traces an ellipse in 3D space, as illustrated in Fig. 7.1.

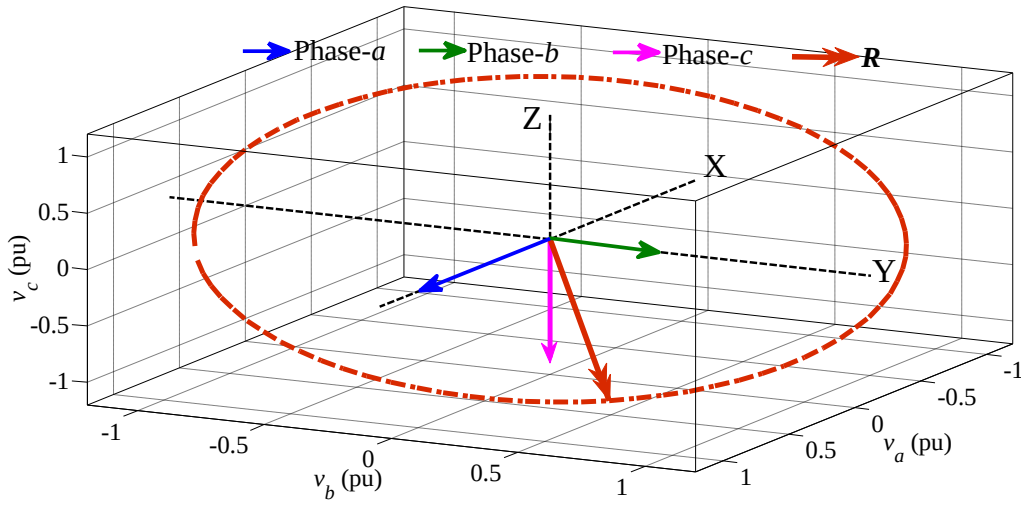

Fig. 7.1. Instantaneous voltage vectors of phase-*a*, phase-*b*, phase-*c*, and their resultant rotating vector ***R*;** dash-dot line highlights the locus ofthe tip of ***R***.

The phenomenon of obtaining the plane from the locus of resultant rotating vector ***R*** (see Fig. 7.1) is analogous to the polarization plane obtained from 3D time-varying electromagnetic fields. The parameters of the ellipse can be obtained from the phasor representations of the 3-phase voltages: $\boldsymbol{V}_a = |\boldsymbol{V}_a| e^{j\alpha_a}$, $\boldsymbol{V}_b = |\boldsymbol{V}_b| e^{j\alpha_b}$, and $\boldsymbol{V}_c = |\boldsymbol{V}_c| e^{j\alpha_c}$. Altogether, these 3 phasors can be presented in a compact form as: $\boldsymbol{V} = \left[|\boldsymbol{V}_a| e^{j\alpha_a} \quad |\boldsymbol{V}_b| e^{j\alpha_b} \quad |\boldsymbol{V}_c| e^{j\alpha_c} \right]^T$.

The normal vector (***U***) of the polarization plane is parallel to the cross-product, i.e., $j\boldsymbol{V} \times \boldsymbol{V}^*$[122]. Thus, ***U*** is obtained as:

$$\boldsymbol{U} \equiv (\boldsymbol{U}_X, \boldsymbol{U}_Y, \boldsymbol{U}_Z)$$

where

$$\boldsymbol{U}_X = -2|\boldsymbol{V}_b||\boldsymbol{V}_c|\sin(\alpha_b - \alpha_c) \tag{7.2a}$$

$$\boldsymbol{U}_Y = -2|\boldsymbol{V}_c||\boldsymbol{V}_a|\sin(\alpha_c - \alpha_a) \tag{7.2b}$$

$$\boldsymbol{U}_Z = -2|\boldsymbol{V}_a||\boldsymbol{V}_b|\sin(\alpha_a - \alpha_b) \tag{7.2c}$$

From the normal vector ***U***, azimuthal angle φ and elevation angles θ can be derived as (see Fig. 7.2):

$$\theta = \arctan\left(\frac{\sqrt{\boldsymbol{U}_X^2 + \boldsymbol{U}_Y^2}}{\boldsymbol{U}_Z} \right) \tag{7.3}$$

$$\varphi = \arctan\left(\boldsymbol{U}_Y / \boldsymbol{U}_X \right) \tag{7.4}$$

Now,using Cartesian to spherical coordinate conversion [123], the transverse signal components are represented as:

$$\boldsymbol{S}_{\theta} = \boldsymbol{V}_{\boldsymbol{a}} \cos\theta\cos\varphi + \boldsymbol{V}_{\boldsymbol{b}} \cos\theta\sin\varphi - \boldsymbol{V}_{\boldsymbol{c}} \sin\theta \tag{7.5a}$$

$$\boldsymbol{S}_{\varphi} = -\boldsymbol{V}_{\boldsymbol{a}} \sin\varphi + \boldsymbol{V}_{\boldsymbol{b}} \cos\varphi \tag{7.5b}$$

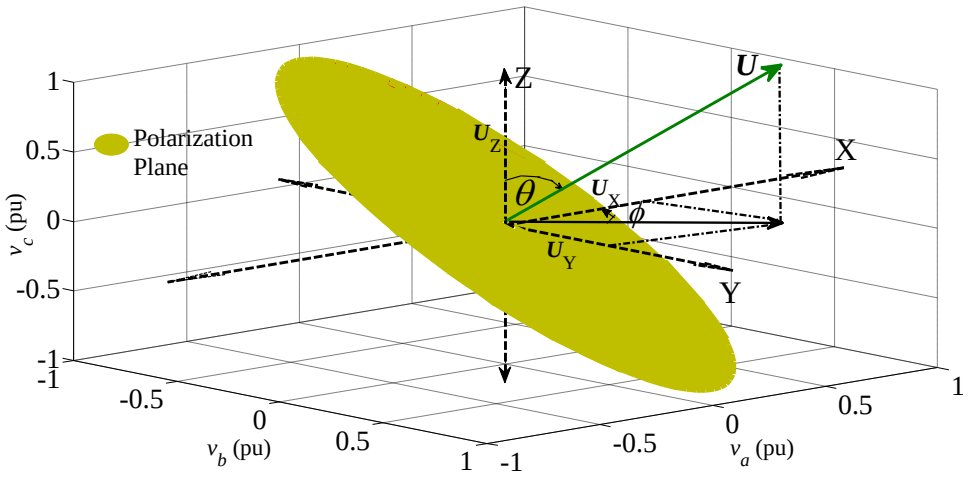

Fig. 7.2. PE parameters: θ and φ, extracted from 3D representation of 3-Φ voltage signals in polarization concept.

With $\boldsymbol{S}_{\theta}$ and $\boldsymbol{S}_{\varphi}$, which are analogous to the two electric field components of a plane electromagnetic wave [124], the elliptical polarization parameters can be obtained from the planar 2D ellipse (see Fig. 7.3). To extract the ellipse parameters, namely ellipticity, tilt, and the major and minor semi-axes, the Stokes' parameters incorporated in Poincare sphere are used. Equation (7.6) describes the relationships between the polarization ellipse parameters and Stokes' parameters given in [124]:

$$\begin{bmatrix} h_0 \\ h_1 \\ h_2 \\ h_3 \end{bmatrix} = \begin{bmatrix} |\boldsymbol{S}_{\theta}|^2 + |\boldsymbol{S}_{\varphi}|^2 \\ |\boldsymbol{S}_{\theta}|^2 - |\boldsymbol{S}_{\varphi}|^2 \\ 2|\boldsymbol{S}_{\theta}||\boldsymbol{S}_{\varphi}|\cos\delta \\ 2|\boldsymbol{S}_{\theta}||\boldsymbol{S}_{\varphi}|\sin\delta \end{bmatrix} = \begin{bmatrix} h_0 \\ h_0\cos 2\tau\cos 2\psi \\ h_0\cos 2\tau\sin 2\psi \\ h_0\sin 2\tau \end{bmatrix} \tag{7.6}$$

where $\delta = arg(\boldsymbol{S}_{\varphi}) - arg(\boldsymbol{S}_{\theta})$, h_0, h_1, h_2, h_3 are the Stokes' parameters, τ is the ellipticity angle and ψ is the tilt angle. From the relationship of (7.6), the tilt angle (ψ)is obtained as:

$$|\psi| = \left| \frac{1}{2} \arctan \frac{2|\boldsymbol{S}_{\theta}||\boldsymbol{S}_{\varphi}|\cos(\delta)}{|\boldsymbol{S}_{\theta}|^2 - |\boldsymbol{S}_{\varphi}|^2} \right| \tag{7.7}$$

From Fig. 7.3 and Eq. (7.6), the major and minor semi-axes (A_x) and (A_y) can be derived as

$$A_y = \left| \sqrt{|\boldsymbol{S}_\theta|^2 + |\boldsymbol{S}_\varphi|^2} \sin\left(\frac{1}{2} \arcsin \frac{2|\boldsymbol{S}_\theta||\boldsymbol{S}_\varphi|\sin(\delta)}{|\boldsymbol{S}_\theta|^2 + |\boldsymbol{S}_\varphi|^2} \right) \right| \tag{7.8}$$

$$A_x = \left| \sqrt{|\boldsymbol{S}_\theta|^2 + |\boldsymbol{S}_\varphi|^2} \cos\left(\frac{1}{2} \arcsin \frac{2|\boldsymbol{S}_\theta||\boldsymbol{S}_\varphi|\sin(\delta)}{|\boldsymbol{S}_\theta|^2 + |\boldsymbol{S}_\varphi|^2} \right) \right| \tag{7.9}$$

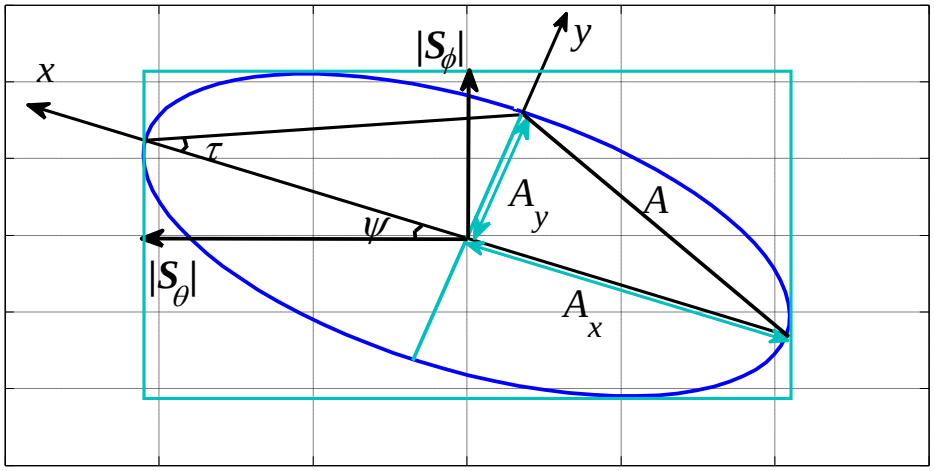

Fig. 7.3. PE parameters: A_y, A_x and ψ, obtained from classical 2D representation of polarization plane.

In the next subsection, the five parameters of the 3D PE, namely θ, φ, $|\psi|$, A_y and A_x, are presented for different dip types.

7.2.2 Polarization Ellipse Parameters under seven types of Dips

In this subsection, the five parameters, φ, θ, $|\psi|$, $A_y$and A_x, are used to characterize three-phase voltage dips caused by different types of faults or other incidents (e.g. starting of induction motor). Table 7-I presents the seven types of voltage dips identified in [22]. In this table, the phasor voltages are expressed as a function of the dip-depth d, and the phasor diagram illustrates the phase voltages before (dotted arrow) and during (solid arrows) the voltage sags or dips.

Due to faults or other disturbances, the phase angle differences among the three phase voltages may deviate from the nominal value of 120°. Moreover, a significant change in phase angle jump could deteriorate the performance of voltage dip classification [30]. Therefore, in the proposed method, the PE parameters are obtained from the projected voltage phasors for a period of one cycle. As an example, the extraction of projected

voltage phasors of type D (see Table 7-I) is demonstrated in Fig. 7.4. The in-phase and out-of-phase projection of 3-phase voltages on a-, b- and c-axis are shown for d = 0.5. In general, to extract the projected voltages, the three phasors $(V_a\angle\alpha_a, V_b\angle\alpha_b, V_c\angle\alpha_c)$ are obtained in each cycle, and the angle deviations of α_a, α_b and α_c from a-, b- and c-axis, respectively, are calculated. The in-phase $(V_{a\_in}, V_{b\_in}, V_{c\_in})$ and out-of-phase $(V_{a\_out}, V_{b\_out}, V_{c\_out})$ projected voltages are obtained as follows:

$$\boldsymbol{V}_{a\_in} = |\boldsymbol{V}_a|\cos(\alpha_a - 0)\angle 0 \tag{7.10a}$$

$$\boldsymbol{V}_{b\_in} = |\boldsymbol{V}_b|\cos(\alpha_b - 4\pi/3)\angle 4\pi/3 \tag{7.10b}$$

$$\boldsymbol{V}_{c\_in} = |\boldsymbol{V}_c|\cos(\alpha_c - 2\pi/3)\angle 2\pi/3 \tag{7.10c}$$

$$\boldsymbol{V}_{a\_out} = |\boldsymbol{V}_a|\sin(\alpha_a - 0)\angle \pi/2 \tag{7.11a}$$

$$\boldsymbol{V}_{b\_out} = |\boldsymbol{V}_b|\sin(\alpha_b - 4\pi/3)\angle 11\pi/6 \tag{7.11b}$$

$$\boldsymbol{V}_{c\_out} = |\boldsymbol{V}_c|\sin(\alpha_c - 2\pi/3)\angle 7\pi/6 \tag{7.11c}$$

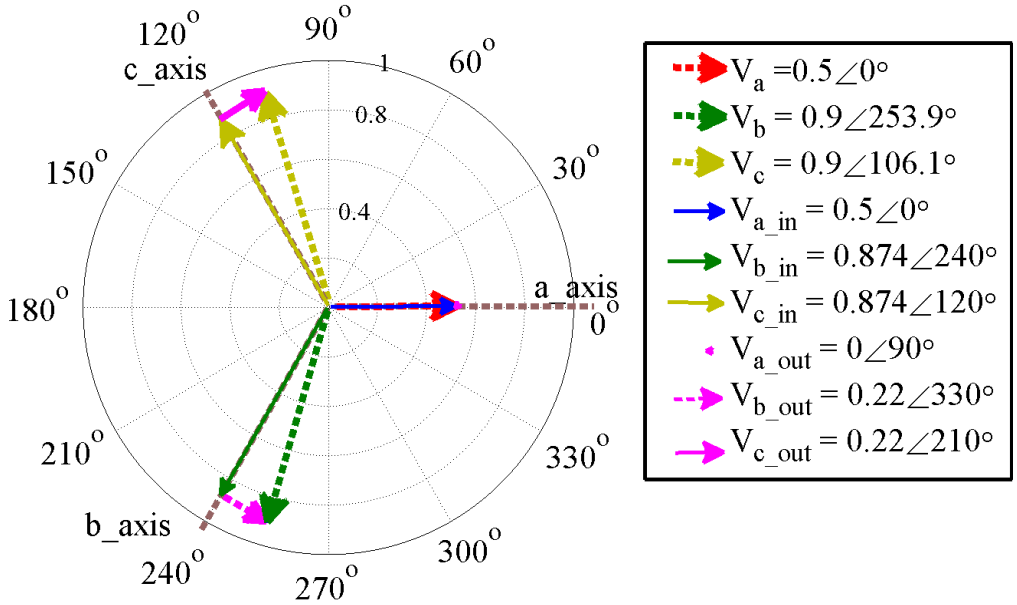

Fig. 7.4. Extraction of in-phase and out-of-phase projected voltages on a-axis, b-axis and c-axis for dip-type D with dip-depth d = 0.5.

The five PE parameters (θ,φ, $|\psi|$,A_y and A_x) are extracted from in-phase projected 3-phase voltages expressed by (7.10). A sixth PE parameter, denoted as A_y^{out}, is extracted from the semi-minor axis obtained from out-of-phase projected 3-phase voltages given

in (7.11). The dip-wise expressions of two PE parameters (θ and φ) are reported in Table 7-II. Mathematical derivations of these expressions are presented in **Appendix C**.

TABLE 7-I

PHASOR PRESENTATION OF 3-PHASE VOLTAGES FOR SEVEN TYPES OF DIPS

Dip-type	Voltage Phasors	Vector diagram
A	$\boldsymbol{V}_a = (1-d)$ $\boldsymbol{V}_b = -0.5(1-d)\left(1+j\sqrt{3}\right)$ $\boldsymbol{V}_c = -0.5(1-d)\left(1-j\sqrt{3}\right)$	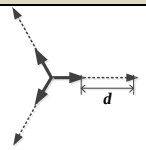
B	$\boldsymbol{V}_a = (1-d)$ $\boldsymbol{V}_b = -0.5\left(1+j\sqrt{3}\right)$ $\boldsymbol{V}_c = -0.5\left(1-j\sqrt{3}\right)$	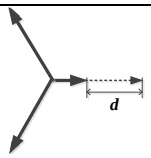
C	$\boldsymbol{V}_a = 1$ $\boldsymbol{V}_b = -0.5-0.5(1-d)\left(j\sqrt{3}\right)$ $\boldsymbol{V}_c = -0.5+0.5(1-d)\left(j\sqrt{3}\right)$	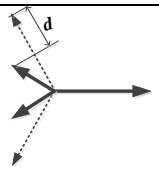
D	$\boldsymbol{V}_a = (1-d)$ $\boldsymbol{V}_b = -0.5(1-d)-0.5\left(j\sqrt{3}\right)$ $\boldsymbol{V}_c = -0.5(1-d)+0.5\left(j\sqrt{3}\right)$	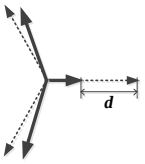
E	$\boldsymbol{V}_a = 1$ $\boldsymbol{V}_b = -0.5(1-d)\left(1+j\sqrt{3}\right)$ $\boldsymbol{V}_c = -0.5(1-d)\left(1-j\sqrt{3}\right)$	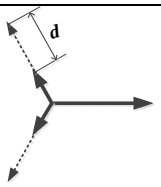
F	$\boldsymbol{V}_a = (1-d)$ $\boldsymbol{V}_b = -0.5(1-d)-\left(\frac{1}{3}+\frac{1-d}{6}\right)\left(j\sqrt{3}\right)$ $\boldsymbol{V}_c = -0.5(1-d)+\left(\frac{1}{3}+\frac{1-d}{6}\right)\left(j\sqrt{3}\right)$	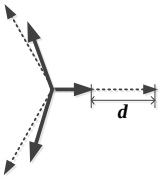
G	$\boldsymbol{V}_a = \frac{2}{3}+\frac{1-d}{3}$ $\boldsymbol{V}_b = -\frac{1}{3}-\frac{1}{6}(1-d)-0.5(1-d)\left(j\sqrt{3}\right)$ $\boldsymbol{V}_c = -\frac{1}{3}-\frac{1}{6}(1-d)+0.5(1-d)\left(j\sqrt{3}\right)$	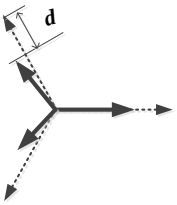

TABLE 7-II

DIP-WISE EXPRESSIONS OF TWO POLARIZATION ELLIPSE PARAMETERS

Affected dip-phase	Dip-type	Elevation angle (θ)	Azimuthal angle (φ)
abc	A	$\pi - \tan^{-1}\left(\sqrt{2}\right)$	$-3\pi/4$
a	B	$\pi - \tan^{-1}\left(\frac{\sqrt{1+(1-d)^2}}{1-d}\right)$	$-\pi + \tan^{-1}(1-d)$
b			$-\pi + \tan^{-1}(1/(1-d))$
a	D	$\pi - \tan^{-1}\left(\frac{\sqrt{17d^2-40d+32}}{4(1-d)}\right)$	$-\pi + \tan^{-1}((4-4d)/(4-d))$
b			$-\pi + \tan^{-1}((4-d)/(4-4d))$
a	F	$\pi - \tan^{-1}\left(\frac{\sqrt{8-12d+5d^2}}{2-2d}\right)$	$-\pi + \tan^{-1}((2-2d)/(2-d))$
b			$-\pi + \tan^{-1}((2-d)/(2-2d))$
c	B	$\pi - \tan^{-1}\left(\sqrt{2}-\sqrt{2}d\right)$	$-3\pi/4$
	D	$\pi - \tan^{-1}\left(4\sqrt{2}(1-d)/(4-d)\right)$	
	F	$\pi - \tan^{-1}\left(2\sqrt{2}(1-d)/(2-d)\right)$	
ab	E	$\pi - \tan^{-1}\left(\sqrt{2}/(1-d)\right)$	$-3\pi/4$
	C	$\pi - \tan^{-1}\left(4\sqrt{2}/(4-3d)\right)$	
	G	$\pi - \tan^{-1}\left(2\sqrt{2}(3-d)/(6-5d)\right)$	
bc	E	$\pi - \tan^{-1}\left(\sqrt{1+(1-d)^2}\right)$	$-\pi + \tan^{-1}(1/(1-d))$
ca			$-\pi + \tan^{-1}(1-d)$
bc	C	$\pi - \tan^{-1}\left(\frac{\sqrt{9d^2-24d+32}}{4}\right)$	$-\pi + \tan^{-1}(4/(4-3d))$
ca			$-\pi + \tan^{-1}((4-3d)/4)$
bc	G	$\pi - \tan^{-1}\left(\frac{\sqrt{72-84d+29d^2}}{6-2d}\right)$	$-\pi + \tan^{-1}((6-2d)/(6-5d))$
ca			$-\pi + \tan^{-1}((6-5d)/(6-2d))$

In the next Section, the algorithm and procedure of classification and characterization of voltage dips and swells are presented.

7.3 CLASSIFICATION AND CHARACTERIZATION OF VOLTAGE DIPS AND SWELLS

For the seven types of dips presented in Table 7-I, there are a total of 19 groups (see Table 7-IIIA) covering all possible combinations of dip-affected phase voltages. In

Table 7-IIIA, a notation convention has been employed to describe the different voltage dip groups: the letters *a*, *b* and *c* on the left side of the word "dip" indicate the class of dip and the capital letters on the right side indicate the dip-type. For example, *ab*_dip_E refers to E type dip with severely affected *ab*-phase or class of *ab*-Φ. Similarly, Table 7-IIIB presents two types of voltage swells, which include 6 swell groups.

TABLE 7-IIIA

GROUPS OF DIPS

Serial No.	Groups of dips	Classes of dips	Dip-type	Severely affected dip-Φ
1	*abc*_dip_A	*abc*-Φ or 3-Φ	A	*abc*
2-4	*a*_dip_B, *a*_dip_D, *a*_dip_F	*a*-Φ	B, D, F	*a*
5-7	*b*_dip_B, *b*_dip_D, *b*_dip_F	*b*-Φ	B, D, F	*b*
8-10	*c*_dip_B, *c*_dip_D, *c*_dip_F	*c*-Φ	B, D, F	*c*
11-13	*ab*_dip_E, *ab*_dip_C, *ab*_dip_G	*ab*-Φ	E, C, G	*ab*
14-16	*bc*_dip_E, *bc*_dip_C, *bc*_dip_G	*bc*-Φ	E, C, G	*bc*
17-19	*ca*_dip_E, *ca*_dip_C, *ca*_dip_G	*ca*-Φ	E, C, G	*ca*

TABLE 7-IIIB

GROUPS OF SWELLS

Serial No.	Groups of swells	Group name	Swell-type	Severely affected swell-Φ
1	*A*_swell_I	*a*-Φ swell	I	*a*
2	*B*_swell_I	*b*-Φ swell	I	*b*
3	*C*_swell_I	*c*-Φ swell	I	*c*
4	*AB*_swell_H	*ab*-Φ swell	H	*ab*
5	*BC*_swell_H	*bc*-Φ swell	H	*bc*
6	*CA*_swell_H	*ca*-Φ swell	H	*ca*

Numerical values of four PE parameters, $|\psi|$, A_y, A_x, and A_y^{out} , are obtained from Eqs. (7.2)–(7.9), by varying the dip-depth *d* (from 0.1 pu to 1 pu). Similarly, the numerical values of the other two PE parameters, θ and φ, are acquired from the expressions given in Table 7-II. Thus, six PE parameters are obtained. By analysing these parameters for *abc*_dip_A, it is observed that the 3-Φ or *abc*-phase dips can be easily classified by applying a threshold condition on the ratio of the semi-minor to the semi-major axis (A_y/A_x) and another threshold condition on semi-minor axis (A_y). According to IEEE 1159.2 standard, a voltage less than 0.9 pu is considered as a dip, whereas a voltage

greater than 1.1 pu is defined as swell. In the proposed approach, for a dip-depth equal to 10% of the nominal voltage i.e. for d = 0.1 pu, the ratio of (A_y/A_x) is obtained as 0.933. Taking IEEE 1159.2 standard into account, for minimum allowable voltage magnitude, i.e., for $|\boldsymbol{V}_a|=|\boldsymbol{V}_b|=|\boldsymbol{V}_c|=0.9\,\text{pu}$, A_y is obtained as 1.1023 and for maximum allowable voltage limit, i.e., for $|\boldsymbol{V}_a|=|\boldsymbol{V}_b|=|\boldsymbol{V}_c|=1.1$ pu, $A_y$yields 1.286. Thus, by incorporating the necessary boundary condition on the PE parameters, A_x and A_y, voltage dip, normal condition (no dip) and voltage swell of the system can be classified as shown in Fig. 7.5. In the next subsection, i.e., in Section 7.3.1, an algorithm for classification of voltage dips is presented. Then, classification of voltage swells is explored in Section 7.3.2. Characterization of voltage dips and swells are presented in Section 7.3.3.

7.3.1 Voltage Dip Classification

The flowchart of Fig. 7.5 shows the algorithm of dip classification using three phase voltage signals within one cycle window length. As illustrated in Fig. 7.5, the whole classification methodology is carried out in three stages. In the first stage, *abc*_dip_A type is classified by applying the necessary threshold conditions as discussed above. It should be noted that in the first stage, two PE parameters, A_y and A_x are obtained by considering the actual voltage magnitudes of 3-Φ voltages; the phase angle differences among the 3-phase voltages are assumed to be separated by 120°.

At the commencement of the second stage, six PE parameters are extracted from in-phase and out-of-phase projected phasors. The dip affected phase is classified in this stage. To this end, $|\psi|$ versus φ are considered for six classes of dips: single phase dips (*a*-Φ, *b*-Φ and *c*-Φ dip) and double phase dips (*ab*-Φ, *bc*-Φ and *ca*-Φ dip). The optimum decision boundaries among these six classes of dips are obtained as the curve bisecting two adjacent regions. To do so, at first, the curves ($|\psi|$ as a function of φ) relating the "classes of dips" presented in Table 7-IIIA, are obtained from Eqs. (7.2)–(7.5), Eq. (7.7) and the voltage phasors shown in Table 7-I for $0.1<d<1$. These curves are denoted as $|\psi|_a(\varphi)$, $|\psi|_b(\varphi)$, $|\psi|_c(\varphi)$, $|\psi|_{ab}(\varphi)$, $|\psi|_{bc}(\varphi)$and $|\psi|_{ca}(\varphi)$, where the different subscripts represent the "classes of dips". As an example, the two curves $|\psi|_c(\varphi)$and$|\psi|_{ab}(\varphi)$ are given by

$$|\psi|_c(\varphi)=\pi/2, \quad \text{and} \quad |\psi|_{ab}(\varphi)=0.$$

The other four curves $|\psi|_a(\varphi)$, $|\psi|_b(\varphi)$, $|\psi|_{ca}(\varphi)$ and $|\psi|_{bc}(\varphi)$ are represented by Eq. (7.7), where the variables $\boldsymbol{S}_\theta$, $\boldsymbol{S}_\varphi$ and the range of φ are shown in Table 7-IV. Figure 7.6 illustrates the six decision boundaries separating the different classes. For instance, decision boundary $D_{c-ca}(\varphi)$ separating *c*-Φ and *ca*-Φ classes is given by

$$D_{c-ca}(\varphi) = 0.5|\psi|_c(\varphi) + 0.5|\psi|_{ca}(\varphi) \tag{7.12}$$

The other five decision boundaries,which include $D_{c-bc}(\varphi)$, $D_{a-ab}(\varphi)$, $D_{b-bc}(\varphi)$, $D_{a-ca}(\varphi)$ and $D_{b-ab}(\varphi)$, are obtained in the same manner. As Fig. 7.6 shows, if φ< -135°, then $D_{c-ca}(\varphi)$, $D_{a-ca}(\varphi)$ and $D_{a-ab}(\varphi)$ are employed, which implies that the class of dip can be *a*-Φ or *c*-Φ or *ca*-Φ or *ab*-Φ. Similarly, for $\varphi \geq$ -135°, the decision boundaries $D_{b-bc}(\varphi)$, $D_{b-ab}(\varphi)$, and $D_{c-bc}(\varphi)$ are applied. Thus, six classes of dips are classified.

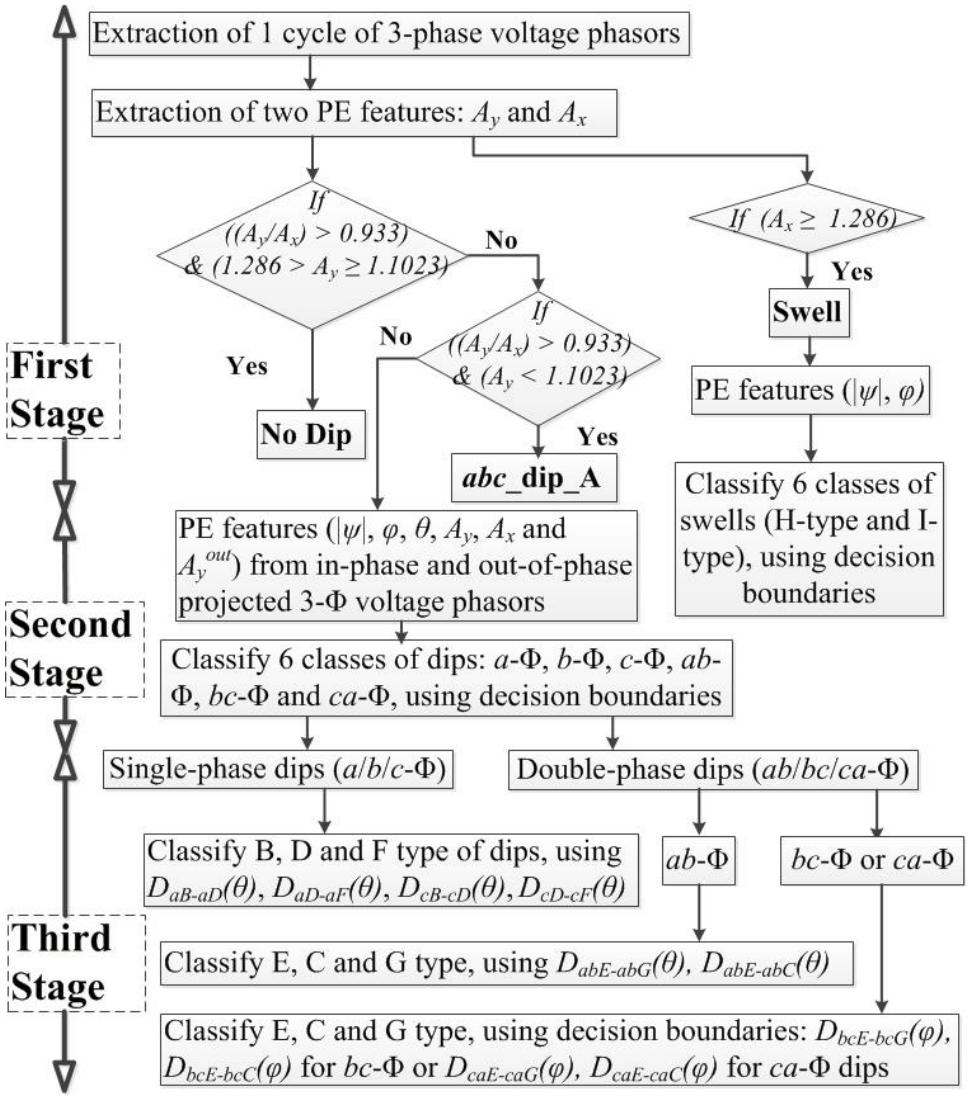

Fig. 7.5.Flowchart of the 3D polarization ellipse method.

TABLE 7-IV

CURVES FOR CLASSIFYING SIX CLASSES OF DIPS

Curves	S_θ	S_φ	Range of φ
$\lvert\psi\rvert_{ca}(\varphi)$	$0.5\tan\varphi\left\{\sqrt{1+\cos^2\varphi}\left(1-j\sqrt{3}\right)\right\}$	$-\dfrac{0.5\left(1+\sin^2\varphi+j\sqrt{3}\cos^2\varphi\right)}{\cos\varphi}$	$-180^{O} \le \varphi < -135^{O}$
$\lvert\psi\rvert_{a}(\varphi)$	$0.5\left\{\sqrt{1+\sin^2\varphi}\left(1-j\sqrt{3}\right)\right\}$		
$\lvert\psi\rvert_{b}(\varphi)$	$0.5\left\{\sqrt{1+\cos^2\varphi}\left(1-j\sqrt{3}\right)\right\}$	$-\dfrac{0.5\left(1+\sin^2\varphi+j\sqrt{3}\cos^2\varphi\right)}{\sin\varphi}$	$-135^{O} \le \varphi \le -90^{O}$
$\lvert\psi\rvert_{bc}(\varphi)$	$0.5\cot\varphi\left\{\sqrt{1+\sin^2\varphi}\left(1-j\sqrt{3}\right)\right\}$		

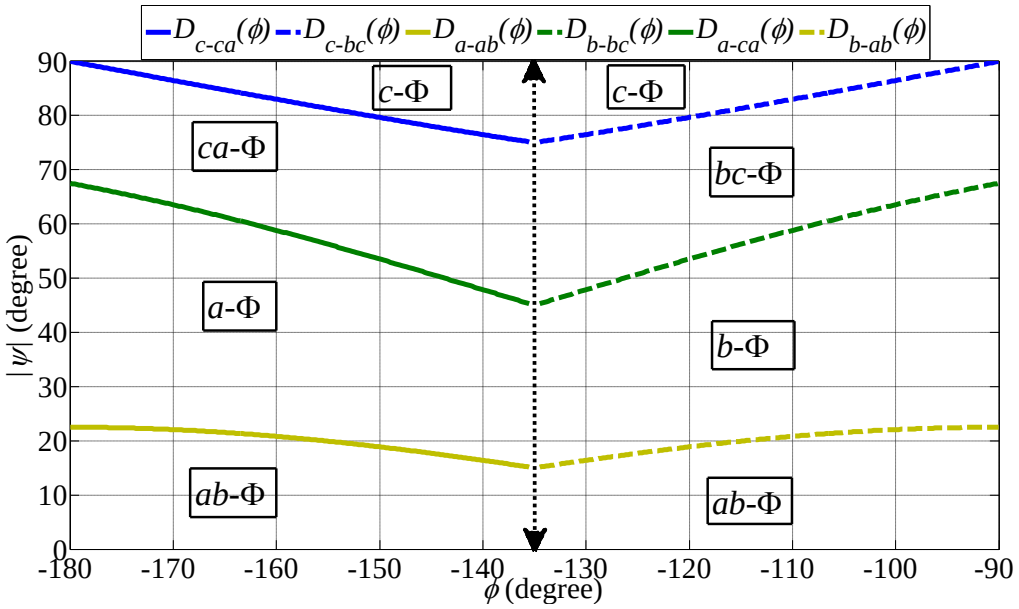

Fig. 7.6. Decision boundaries: $D_{c-ca}(\varphi)$, $D_{c-bc}(\varphi)$, $D_{a-ab}(\varphi)$, $D_{b-bc}(\varphi)$, $D_{a-ca}(\varphi)$, and $D_{b-ab}(\varphi)$, establishing the classified zone of six classes of dips, which include *a*-Φ, *b*-Φ, *c*-Φ, *ab*-Φ, *bc*-Φ, and *ca*-Φ; double arrow dotted line acts as a logical separator among the classes of dips.

In the third stage, the dip-type is classified for single-Φ (B, D and F type) and double-Φ (E, C and G type) dips. For classifying B, D and F types of single-Φ dips, the curves (A_x as a function of θ), obtained from (7.2)–(7.5), (7.9) and the phasors of Table 7-I for $0.1<d<1$, are used. The equations of these curves are represented by (7.9), where the variables $\boldsymbol{S}_\theta$, $\boldsymbol{S}_\varphi$ and the range of θ are reported in Table 7-V. These equations show the behaviour of PE parameters A_x and θ under B, D and F types of single-phase dips. In Table 7-V, the curves, representing B, D and F types of *a*-Φ, *b*-Φ and *c*-Φ dips, are denoted as $A_{x,aB}(\theta)$, $A_{x,aD}(\theta)$, $A_{x,aF}(\theta)$, $A_{x,bB}(\theta)$, $A_{x,bD}(\theta)$, $A_{x,bF}(\theta)$, $A_{x,cB}(\theta)$, $A_{x,cD}(\theta)$ and $A_{x,cF}(\theta)$ respectively. Moreover, Fig. 7.7 shows the decision boundaries, used for the

classification of B, D and F types of dips. As an example, the decision boundary $D_{aB-aD}(\theta)$, separating *a*_dip_*B* from *a*_dip_*D*, is given by

$$D_{aB-aD}(\theta) = 0.5A_{x,aB}(\theta) + 0.5A_{x,aD}(\theta) \tag{7.13}$$

Similarly, the expressions for $D_{aD-aF}(\theta)$, $D_{cB-cD}(\theta)$ and $D_{cD-cF}(\theta)$ are obtained. Using the equations of these decision boundaries, the B, D and F type dips can be easily classified (see Fig. 7.7).

TABLE 7-V

CURVES USED FOR THE CLASSIFICATION OF DIP-TYPE:B, D AND F

Curves	S_θ	S_φ	Range of θ
$A_{x,\,aB}(\theta)$ $A_{x,\,bB}(\theta)$	$\dfrac{0.5\left(1-j\sqrt{3}\right)}{\sin\theta}$	$\dfrac{0.5\left(1+j\sqrt{3}\left(1-2\cos^2\theta\right)\right)}{\sin\theta\sqrt{1-2\cos^2\theta}}$	$90^{\mathrm{O}} \le \theta \le 125^{\mathrm{O}}$
$A_{x,\,aD}(\theta)$ $A_{x,\,bD}(\theta)$	$\dfrac{1.5\left(1-j\sqrt{3}\right)\sqrt{1-2\cos^2\theta}}{\sin\theta\left(4\sqrt{1-2\cos^2\theta}+\cos\theta\right)}$	$\dfrac{1.5\left(1+j\sqrt{3}\right)\left(1-2\cos^2\theta\right)}{\sin\theta\left(4\sqrt{1-2\cos^2\theta}+\cos\theta\right)}$	
$A_{x,\,aF}(\theta)$ $A_{x,\,bF}(\theta)$	$\dfrac{1.5\left(1-j\sqrt{3}\right)\sqrt{1-2\cos^2\theta}}{\sin\theta\left(2\sqrt{1-2\cos^2\theta}+\cos\theta\right)}$	$\dfrac{1.5\left(1+j\sqrt{3}\right)\left(1-2\cos^2\theta\right)}{\sin\theta\left(2\sqrt{1-2\cos^2\theta}+\cos\theta\right)}$	
$A_{x,\,cB}(\theta)$	$-0.5\left(1-j\sqrt{3}\right)/\left(\sqrt{2}\cos\theta\right)$	$0.5\times\sqrt{1.5}\times\left(\sqrt{3}+j\right)$	$125^{\mathrm{O}} < \theta \le 180^{\mathrm{O}}$
$A_{x,\,cD}(\theta)$	$-\dfrac{1.5\left(1-j\sqrt{3}\right)}{4\sqrt{2}\cos\theta+\sin\theta}$	$\dfrac{1.5\cos\theta\left(3+j\sqrt{3}\right)}{4\sqrt{2}\cos\theta+\sin\theta}$	
$A_{x,\,cF}(\theta)$	$-\dfrac{0.5\left(1-j\sqrt{3}\right)}{2\sqrt{2}\cos\theta+\sin\theta}$	$\dfrac{0.5\cos\theta\left(3+j\sqrt{3}\right)}{2\sqrt{2}\cos\theta+\sin\theta}$	

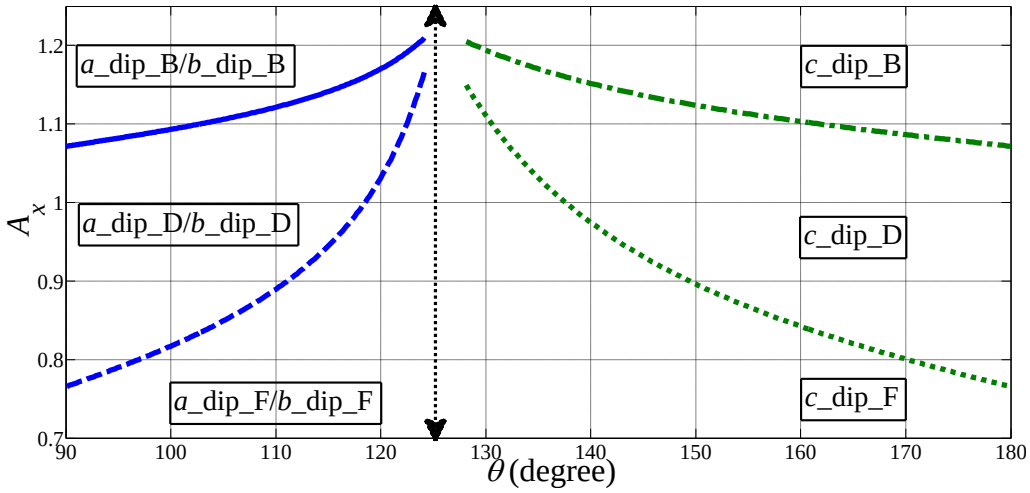

Fig. 7.7. Decision boundaries: $D_{aB-aD}(\theta)$ (solid line), $D_{aD-aF}(\theta)$ (dash line), $D_{cB-cD}(\theta)$ (dash dotted line), $D_{cD-cF}(\theta)$ (dotted line) establishing the classified zone of B, D and F types of single-Φ dips; double arrow dotted line acts as a logical separator between *a*/*b*-Φ class and *c*-Φ class of dips.

Double-Φ dips (E, C and G type) are classified in two steps. First E and C type dips are bundled together as E/C type, the E/C and G types are classified. In the second step, the dips E and C are classified. In order to make a distinction among E, C and G types of *ab*-Φ dips, at first, E/C and G type are classified. To do so, A_x relating *ab*-Φ dips of the E, C, and G types are generated from Eqs. (7.2)–(7.5), Eq. (7.9) and the corresponding phasors of Table 7-I for 0.1<*d*<1; these are denoted as $A_{x,abE}(\theta)$, $A_{x,abC}(\theta)$ and $A_{x,abG}(\theta)$ respectively. The curves $A_{x,abE}(\theta)$, $A_{x,abC}(\theta)$ and $A_{x,abG}(\theta)$ are presented by (7.9), where the variables $\boldsymbol{S}_\theta$, $\boldsymbol{S}_\varphi$ and the range of θ are shown in Table 7-VI. Hence, the decision boundary is expressed as,

$$D_{abE-abG}(\theta) = 0.5A_{x,abE}(\theta) + 0.5A_{x,abG}(\theta) \tag{7.14}$$

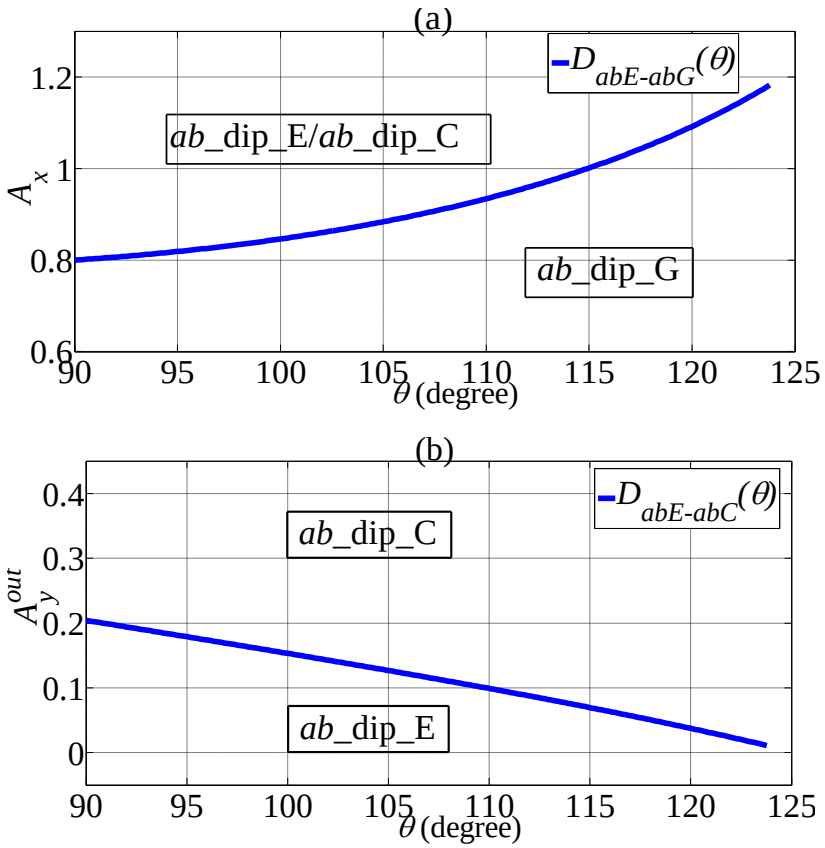

Fig. 7.8. Classified zone of *ab*-Φ dips using decision boundaries: (a) $D_{abE-abG}(\theta)$ for E/C and G types; (b) $D_{abE-abC}(\theta)$ for E and C types.

Secondly, the classification of *ab*_dip_E and *ab*_dip_C is conducted by obtaining the curves derived from Eqs. (7.2)-(7.5), Eq. (7.8) and the corresponding phasors of Table 7-I for 0.1<*d*<1. In this case, A_y^{out} is obtained through the proposed PE technique

applied to the out-of-phase phasor voltages. To this end, A_y^{out} related to *ab*-Φ dips of type E and C type are generated from (7.8); they are denoted as $A_{y,abE}^{out}(\theta)$ and $A_{y,abC}^{out}(\theta)$, respectively. Thus, $A_{y,abE}^{out}(\theta)$ is obtained as $A_{y,abE}^{out}=0$ and $A_{y,abC}^{out}(\theta)$ is represented by (7.8) followed by $\boldsymbol{S}_\theta$, $\boldsymbol{S}_\varphi$ and the range of θ as reported in Table 7-VI. The decision boundary is denoted as $D_{abE-abC}(\theta)$. The decision boundaries $D_{abE-abG}(\theta)$ and $D_{abE-abC}(\theta)$, corresponding to the first and second steps of classifying E, C and G type of *ab*-Φ dips, are presented in Figs. 7.8 (a) and 7.8(b), respectively.

TABLE 7-VI

CURVES USED FOR CLASSIFYING E, C AND G TYPE OF AB-Φ DIPS

Curves	$\boldsymbol{S}_\theta$	$\boldsymbol{S}_\varphi$	Range of θ
$A_{x,\,abE}(\theta)$	$0.5\left(1-j\sqrt{3}\right)/\sin\theta$	$-0.5\times\cos\theta\left(3+\boldsymbol{j}\sqrt{3}\right)/\sin\theta$	$90^{O} \le \theta \le 125^{O}$
$A_{x,\,abC}(\theta)$			
$A_{x,\,abG}(\theta)$	$\dfrac{1.5\left(1-j\sqrt{3}\right)}{2\sqrt{2}\cos\theta+5\sin\theta}$	$-\dfrac{1.5\cos\theta\left(3+j\sqrt{3}\right)}{2\sqrt{2}\cos\theta+5\sin\theta}$	
$A_{y,\,abC}^{out}(\theta)$	$-\dfrac{\sin\theta+\sqrt{2}\cos\theta}{\sqrt{3}\sin\theta}$	$-\dfrac{0.5\left(1+j\sqrt{3}\right)\left(\sin\theta+\sqrt{2}\cos\theta\right)}{\sqrt{3}\sin\theta}$	

Following similar steps for classifying *ab*-Φ dips of type E, C and G, the *bc*-Φ and *ca*-Φ dips are distinguished by the decision boundaries obtained from the curves: $A_{x,bcE}(\varphi)$, $A_{x,bcC}(\varphi)$, $A_{x,bcG}(\varphi)$, $A_{x,caE}(\varphi)$, $A_{x,caC}(\varphi)$, $A_{x,caG}(\varphi)$, $A_{y,bcC}^{out}(\varphi)$, $A_{y,bcE}^{out}(\varphi)$, $A_{y,caE}^{out}(\varphi)$ and $A_{y,caC}^{out}(\varphi)$. It should be noted that $A_{y,bcE}^{out}(\varphi)$ and $A_{y,caE}^{out}(\varphi)$ are obtained as $A_{y,bcE}^{out}=A_{y,caE}^{out}=0$. The rest of the curvesare derived from Eqs. (7.8) and (7.9), and the variables presented in Table 7-VII. The curves corresponding to the decision boundaries of *bc*-Φ and *ca*-Φ dips are shown in Fig. 7.9. The detailed derivations of the decision boundaries, corresponding to voltage dips of seven types, are presented in **Appendix D.**

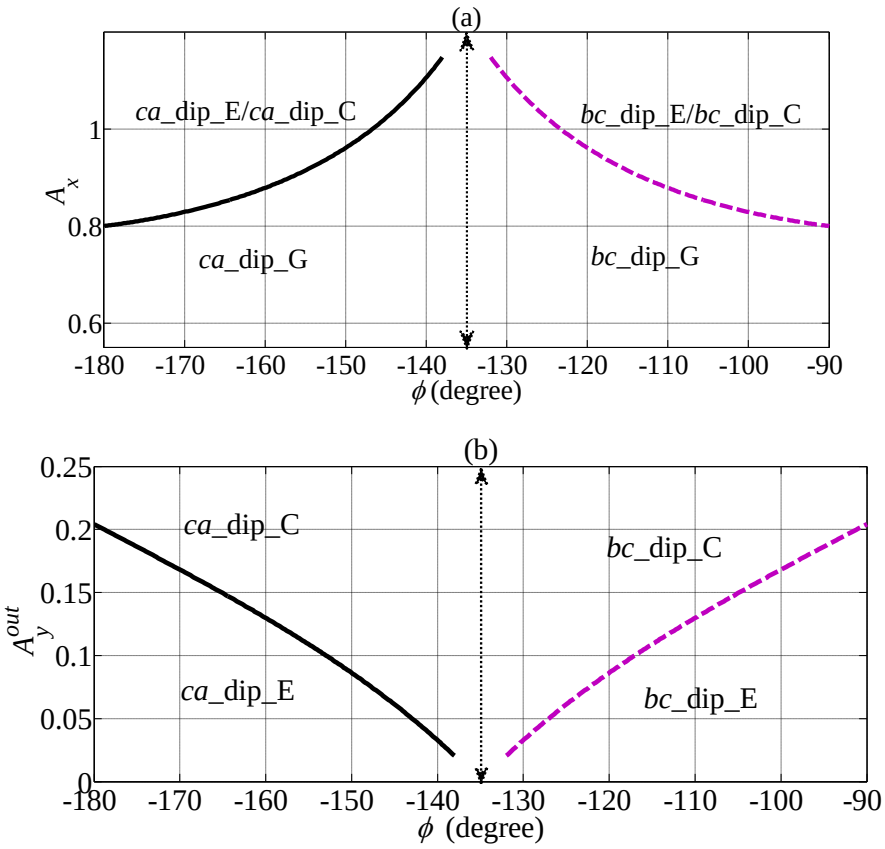

Fig. 7.9. (a) Decision boundaries $D_{caE-caG}(\varphi)$ (solid line), $D_{bcE-bcG}(\varphi)$ (dash line) establishing the classified zone of E/C and G-type of *ca*-Φ, and *bc*-Φ class of dips, (b) Decision boundaries $D_{caE-caC}(\varphi)$ (solid line), $D_{bcE-bcC}(\varphi)$ (dash line) establishing the classified zone of E and C-type of *ca*-Φ, and *bc*-Φ class of dips; double arrow dotted line acts as a logical separator between *bc*-Φ and *ca*-Φ class of dips.

TABLE 7-VII

CURVES USED FOR CLASSIFYING E, C AND G TYPE OF BC-Φ AND CA-Φ DIPS

Curves	S_θ	S_φ	Range of φ
$A_{x,\,bcE}(\varphi)$ $A_{x,\,bcC}(\varphi)$	$\frac{(1-j\sqrt{3})\cos\varphi\sqrt{1+\sin^2\varphi}}{2\sin\varphi}$	$-\frac{1+j\sqrt{3}\cos^2\varphi+\sin^2\varphi}{2\sin\varphi}$	$-\frac{3\pi}{4} < \varphi \le -\frac{\pi}{2}$
$A_{x,\,bcG}(\varphi)$	$-\frac{1.5(1-j\sqrt{3})\cos\varphi\sqrt{1+\sin^2\varphi}}{2\cos\varphi-5\sin\varphi}$	$-\frac{1.5\cos\theta(3+j\sqrt{3})}{2\sqrt{2}\cos\theta+5\sin\theta}$	
$A_{y,\,bcC}^{out}(\varphi)$	$\frac{\sqrt{3}(1-j\sqrt{3})(\sin\varphi-\cos\varphi)}{6\sin\varphi}$	$\frac{\sqrt{3}(1+j\sqrt{3})(\sin\varphi-\cos\varphi)}{6\sin\varphi}$	
$A_{x,\,caE}(\varphi)$ $A_{x,\,caC}(\varphi)$	$0.5(1-j\sqrt{3})\tan\varphi\sqrt{1+\cos^2\varphi}$	$-\frac{(1+j\sqrt{3}\cos^2\varphi+\sin^2\varphi)}{2\cos\varphi}$	$-\pi \le \varphi \le -\frac{3\pi}{4}$
$A_{x,\,caG}(\varphi)$	$\frac{1.5(1-j\sqrt{3})\sin\varphi\sqrt{1+\cos^2\varphi}}{5\cos\varphi-2\sin\varphi}$	$-\frac{1.5(1+j\sqrt{3}\cos^2\varphi+\sin^2\varphi)}{5\cos\varphi-2\sin\varphi}$	
$A_{y,\,caC}^{out}(\varphi)$	$\frac{\sqrt{3}(1-j\sqrt{3})(\cos\varphi-\sin\varphi)}{6\cos\varphi}$	$\sqrt{3}(\cos\varphi-\sin\varphi)/3\cos\varphi$	

7.3.2 Voltage Swell Classification

The proposed method is used for classification of voltage swells, which include two types of voltage swells: H- and I-type, as reported in [31] and presented in Table 7-VIII. The I-type swell includes the single-Φ voltage swells, *a*-Φ, *b*-Φ, and *c*-Φ swells, whereas the H-type includes the double-Φ voltage swell, i.e., *ab*-Φ, *bc*-Φ, and *ca*-Φ swell, as shown in Table 7-IIIB. As shown in Fig. 7.5, the six swell groups are classified by following similar approach to that of classifying six classes of voltage dips. To this end, the equations required for the decision boundaries are denoted as $|\psi|_A(\varphi)$, $|\psi|_B(\varphi)$, $|\psi|_C(\varphi)$, $|\psi|_{AB}(\varphi)$, $|\psi|_{BC}(\varphi)$ and $|\psi|_{CA}(\varphi)$, where subscript letter "*A*" represents *a*-Φ swell, "*B*" represents *b*-Φ swell and so on. The equations ($|\psi|$ as a function of φ) relating the "groups of swells" presented in Table 7-IIIB, are obtained from Eqs. (7.2)–(7.5), Eq. (7.7) and the voltage phasors shown in Table 7-VIII. Thus, the Eqs.of two curves $|\psi|_{AB}(\varphi)$and$|\psi|_C(\varphi)$ are derived as: $|\psi|_{AB}(\varphi)=\pi/2$, and $|\psi|_C(\varphi)=0$. The other four curves, $|\psi|_A(\varphi)$, $|\psi|_B(\varphi)$, $|\psi|_{CA}(\varphi)$ and $|\psi|_{BC}(\varphi)$are represented by (7.7), where the variables $\boldsymbol{S}_\theta$, $\boldsymbol{S}_\varphi$ and the range of φ are shown in Table 7-IX. From these expressions, the equations of decision boundaries, which bisect two adjacent swell regions, are obtained; see Fig. 7.10 for illustration. The six groups of swells are classified using the expressions of these decision boundaries. The detailed derivations of these decision boundaries, corresponding to voltage swells, are presented in **Appendix E.**

TABLE 7-VIII

PHASOR PRESENTATION OF 3-PHASE VOLTAGES FOR TWO TYPES OF SWELLS

Swell-type	Voltage Phasors	Vector diagram
H	$\boldsymbol{V}_a = (1-d)$ $\boldsymbol{V}_b = -0.5(1+d) - 0.5\left(j\sqrt{3}\right)$ $\boldsymbol{V}_c = -0.5(1+d) + 0.5\left(j\sqrt{3}\right)$	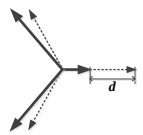
I	$\boldsymbol{V}_a = (1+2d)$ $\boldsymbol{V}_b = -0.5(1-d) - 0.5\left(j\sqrt{3}\right)$ $\boldsymbol{V}_c = -0.5(1-d) + 0.5\left(j\sqrt{3}\right)$	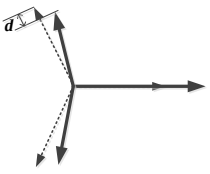

TABLE 7-IX

CURVES FOR CLASSIFYING SIX GROUPS OF SWELLS

Curves	S_θ	S_φ	Range of φ
$\lvert\psi\rvert_B(\varphi)$	$\frac{1.5\sin\varphi\left\{\sqrt{1+\cos^2\varphi}\left(1-\boldsymbol{j}\sqrt{3}\right)\right\}}{\cos\varphi+2\sin\varphi}$	$-\frac{1.5\left(1+\sin^2\varphi+j\sqrt{3}\cos^2\varphi\right)}{\cos\varphi+2\sin\varphi}$	$-180^{O} \le \varphi < -135^{O}$
$\lvert\psi\rvert_{BC}(\varphi)$	$0.5\left\{\sqrt{1+\sin^2\varphi}\left(1-j\sqrt{3}\right)\right\}$	$-0.5\left(1+\sin^2\varphi+j\sqrt{3}\cos^2\varphi\right)/\cos\varphi$	
$\lvert\psi\rvert_{CA}(\varphi)$	$0.5\left\{\sqrt{1+\cos^2\varphi}\left(1-j\sqrt{3}\right)\right\}$	$-0.5\left(1+\sin^2\varphi+j\sqrt{3}\cos^2\varphi\right)/\sin\varphi$	$-135^{O} \le \varphi \le -90^{O}$
$\lvert\psi\rvert_A(\varphi)$	$\frac{1.5\cos\varphi\left\{\sqrt{1+\sin^2\varphi}\left(1-j\sqrt{3}\right)\right\}}{2\cos\varphi+\sin\varphi}$	$-\frac{1.5\left(1+\sin^2\varphi+j\sqrt{3}\cos^2\varphi\right)}{2\cos\varphi+\sin\varphi}$	

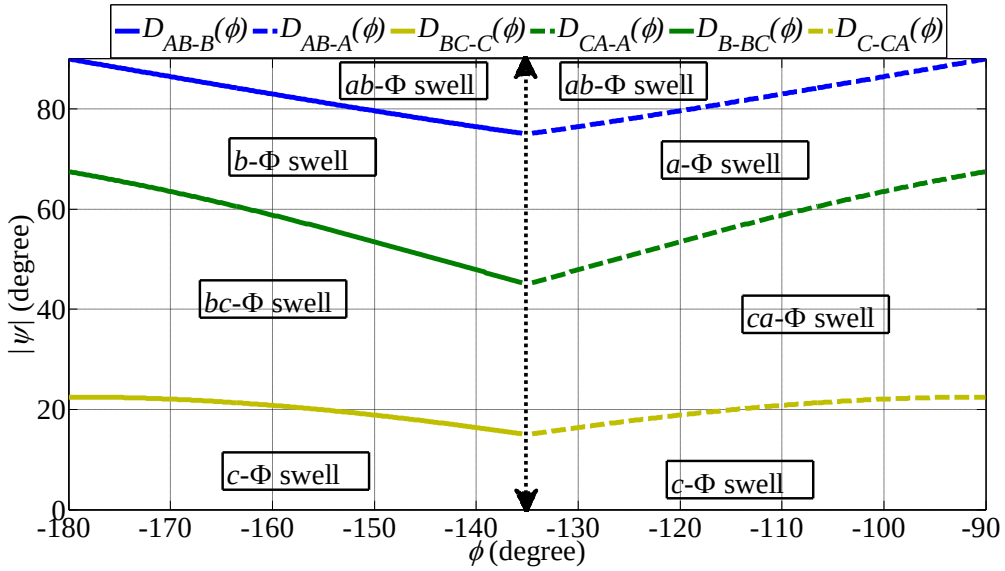

Fig. 7.10. Decision boundaries, $D_{AB-B}(\varphi)$, $D_{AB-A}(\varphi)$, $D_{BC-C}(\varphi)$, $D_{CA-A}(\varphi)$, $D_{B-BC}(\varphi)$, and $D_{C-CA}(\varphi)$, establishing the classified zone of six groups of swells, which include *a*-Φ, *b*-Φ, *c*-Φ, *ab*-Φ, *bc*-Φ, and *ca*-Φ; double arrow dotted line acts as a logical separator among the groups of swells.

7.3.3 Characterization of Voltage Dips and Swells

Upon completion of the classification task, the severity of voltage dips can be characterized using the dip-depth *d*. In Table 7-II, PE parameter θ and φ are expressed as a function of *d*; therefore, *d* can be easily calculated from the expressions corresponding to the dip-type which is obtained through the classification.For example, if an event is classified as *a*_dip_D with PE parameters θ =121.2° and φ = –142.9°, then *d* can be calculated from the expressions of θ and φ corresponding to *a*-Φ dip

(affected dip-phase is *a*) and type D, as shown in Table 7-II. The calculation is presented below:

$$\varphi = -\pi + tan^{-1}\left((4-4d)/(4-d)\right);$$
$$\Rightarrow -142.9 = -180 + tan^{-1}\left((4-4d)/(4-d)\right);$$
$$\Rightarrow d = 0.3005$$

From the above calculation it is evident that the event, which is classified as *a*-Φ dip and type D, has encountered a dip-depth of 0.3 pu. To derive the general expressions of dip-depth d as a function of θ or φ, considering dip-types B, D, F, E, C, and G, the expressions of Table 7-II are re-arranged and summarized in Table 7-X. For A-type dip, all three-phase voltages are reduced in equal amount; hence, dip-depth can be easily obtained as $d = 1 - |\boldsymbol{V}_{\Phi}|$, where $\Phi = a$ or b or c.

TABLE 7-X

EXPRESSIONS OF DIP-DEPTH AS A FUNCTION OF POLARIZATION ELLIPSE PARAMETERS

Affected dip-phase	Dip-type	Dip-depth (d)
a	B	$1-\tan(\pi+\varphi)$
b		$1-\cot(\pi+\varphi)$
a	D	$(1-\tan(\pi+\varphi))/(1-0.25\tan(\pi+\varphi))$
b		$(1-\tan(\pi+\varphi))/(0.25-\tan(\pi+\varphi))$
a	F	$(1-\tan(\pi+\varphi))/(1-0.5\tan(\pi+\varphi))$
b		$(1-\tan(\pi+\varphi))/(0.5-\tan(\pi+\varphi))$
c	B	$1-\tan(\pi-\theta)/\sqrt{2}$
	D	$\left(\sqrt{2}-\tan(\pi-\theta)\right)/\left(\sqrt{2}-0.25\tan(\pi-\theta)\right)$
	F	$\left(\sqrt{2}-\tan(\pi-\theta)\right)/\left(\sqrt{2}-0.5\tan(\pi-\theta)\right)$
ab	E	$1-\sqrt{2}/\tan(\pi-\theta)$
	C	$4/3-4\sqrt{2}/(3\tan(\pi-\theta))$
	G	$\left(6\sqrt{2}-6\tan(\pi-\theta)\right)/\left(2\sqrt{2}-5\tan(\pi-\theta)\right)$
bc	E	$1-\cot(\pi+\varphi)$
ca		$1-\tan(\pi+\varphi)$
bc	C	$(4-4\cot(\pi+\varphi))/3$
ca		$(4-4\tan(\pi+\varphi))/3$
bc	G	$(6-6\tan(\pi+\varphi))/(2-5\tan(\pi+\varphi))$
ca		$(6-6\tan(\pi+\varphi))/(5-2\tan(\pi+\varphi))$

According to IEEE 1159.2 standard, definition of voltage dip involves the dip-depth d to lie within 0.1 to 1 pu. Thus, concurrent operation of cycle by cycle

classificationand extraction of *d*, will allow to detect the onset of voltage dip in real-time. For example, if *d* is monitored continuously, under normal condition its value will be close to 0; if *d* is found within 0.1 to 1 pu, then dip-inception can be detected. Another technique to evaluate the gravity of dip/swell is to estimate the surface area of the ellipse. The decrease of the surface area of the ellipse is proportional to the dip gravity. Similarly, increase of the surface area of the ellipse is proportional to the swell gravity. For example, for a given dip-depth, three phase voltage dips are the most severe, followed by double phase and single phase dips, which is reflected in the surface are of the ellipse obtained in 3D co-ordinates.

7.4 VALIDATION AND TEST RESULTS

The proposed method is validated with recorded waveforms provided by IEEE 1159.2 [117], real measurement data given in [119], and unbalanced dips associated with phase angle jump.

7.4.1 Voltage Dip Classification from recorded waveforms

IEEE 1159.2 working group recorded several test waveforms, which include balanced and unbalanced voltage sags influenced by industrial power electronic equipment [117]. Most of these recorded waveforms are used to validate the proposed method.

The phase voltages may be influenced by noise and harmonic distortion due to the presence of power electronic devices and other electrical equipment. The impact of noise can be seen in Fig. 7.11, which shows one of the recorded waveforms *wave 15*[117]. To extract the ellipse parameters, the DFT (Discrete Fourier Transform) is applied to one cycle long window. The phase voltage magnitude and phase angle at the fundamental frequency (in this case ±60 Hz), are extracted and passed through the proposed polarization ellipse technique for dip classification. The proposed algorithm operates on a sliding time-window of 1 cycle length and each of the recorded waveforms has 3-phase voltage signals of six cycle duration. Therefore, if voltage dip or swell is found within any window frame passing through the six cycles of voltage signal, it is detected; otherwise it is classified as normal condition. However, to test the proposed method, normal condition of the recorded waveforms is not shown; only the classification results within one cycle window frame, starting at the inception of voltage sags, are considered and presented in Table 7-XI. For instance, 3-Φ voltage phasors of

third cycle (0.033 to 0.05 sec duration) are considered for the voltage dip-classification of *wave 15* and marked as classified window. Similarly, voltage phasors of other recorded waveforms are classified as shown in Table 7-XI.

TABLE 7-XI

CLASSIFICATION OF VOLTAGE DIPS WITH RECORDED WAVEFORMS

Wave number	Classes of dips (ground-truth)	Polarization Ellipse parameters				Test results (classes of dips)
		A_y/A_x	A_y	$\varphi°$	$\lvert\psi\rvert°$	
wave 1	*b*-Φ	0.72	0.93	-117.9	38.3	*b*-Φ
wave 2	*c*-Φ	0.65	0.79	-135.2	89.7	*c*-Φ
wave 3a	*a*-Φ	0.59	0.49	-173.2	43.1	*a*-Φ
wave 5	*ca*-Φ	0.77	0.47	-145.5	69.5	*ca*-Φ
wave 6a	*c*-Φ	0.67	0.59	-135.2	89.7	*c*-Φ
wave 7	*a*-Φ	0.59	0.49	-173.5	42.9	*a*-Φ
wave 8	*a*-Φ	0.61	0.41	-165.4	41.2	*a*-Φ
wave 11a	*b*-Φ	0.9	0.66	-129.8	40.8	*b*-Φ
wave 12	3-Φ or *abc*-Φ	0.99	0.72	-	-	3-Φ or *abc*-Φ
wave 13	*a*-Φ	0.74	0.95	-150.4	35.7	*a*-Φ
wave 14c	*c*-Φ	0.59	0.77	-134.2	89.1	*c*-Φ
wave 15	*c*-Φ	0.70	0.89	-134.2	88.8	*c*-Φ

It is observed that the test recorded waveforms are suffered from voltage dips in single-phase or two-phases or 3-phases; the ground-truth for the "classes of dips" is presented in column 2 of Table 7-XI. These recorded waveforms are passed through the proposed multi-stage classification algorithm. Firstly, the PE parameters are extracted for each of the recorded waveforms, see columns 3-6 of Table 7-XI. Then, using the decision boundaries as highlighted in Fig. 7.6 and the PE parameters $|\psi|$ and φ of Table 7-XI, classes of dips are identified. For *wave 12*, *abc*-Φ or 3-Φ balanced dip is identified by applying the conditions on PE parameters (A_y/A_x)and A_y,see Fig. 7.5. The classification results, as presented in 7th column of Table 7-XI, specify the successful classification of all the test recorded waveforms with 100% accuracy. In summary, the proposed algorithm is able to provide the exact "classes of dips" as reported in the results of recorded waveforms. Moreover, dip-depth can be monitored in real-time by applying a sliding data-window of one-cycle as illustrated in Fig. 7.11. Thus, dip-inception time and severity of dip can be realized in real-time.

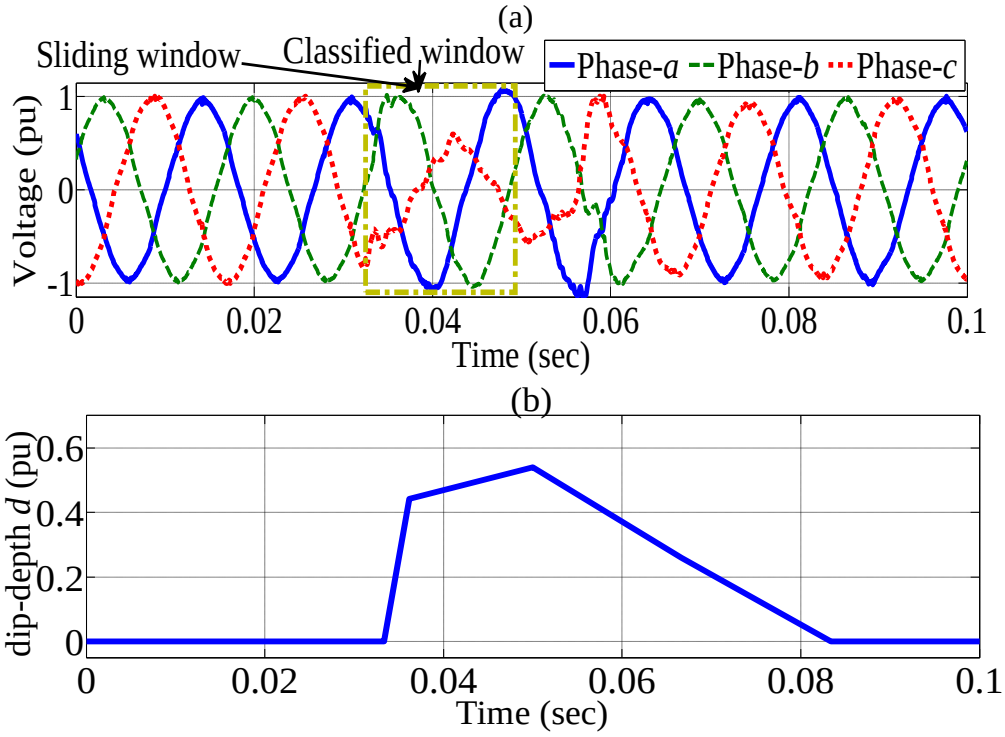

Fig. 7.11. (a) Recorded waveform *wave 1*5 collected from [117], (b) real-time monitoring of voltage dips for *wave 15* using dip-depth *d*.

7.4.2 Validation of the Proposed Method using real measurement Data

Voltage dips, measured in Belgian transmission grid as presented in [119], and voltage swell, recorded from a medium voltage network [31], are used to validate the proposed algorithm. The phasors, illustrated in Table 7-XII, are extracted from the waveform stored during the occurrence of a voltage dip or swell. For classification of each type of dips/swells, the in-phase and out-of-phase projected voltage phasors are obtained by following the procedure presented in Fig. 7.4; the projected phasors are then passed through the proposed polarization ellipse technique. The whole classification process is conducted in three stages as described in Section 7.3. The first stage is disregarded since the PE parameters (A_y/A_x),A_x and $A_y$do not fall in the groups of balanced dip or no dip condition (see Fig. 7.5 and Table 7-XIII). Therefore, in order to explore the last two stages of classification, the waveform of dip-type D is taken as an example. Applying the PE parameters, $|\psi|$ and φ, see Fig. 7.6, reveals that the "class of dip" is a-Φ. Likewise, applying the PE parameters — A_x and θ in Fig. 7.7, implies that the type of dip is D. Other two types of dips, Cand E, are classified and characterized using similar approach. Upon completion of the classification task, characterization of the dips is conducted by extracting dip-depth d as discussed in Section 7.3.3. Among

these three types of dips, *bc*_dip_E type is found to be the most severe dip as indicated by the dip-depth value, see Table 7-XIII. Moreover, for H-type swell, using the PE parameters, $|\psi|$ and φ, see Fig. 7.10, reveals that the "group of swell" is *ab*-Φ which is denoted as *AB*_swell_H type. This H-type of swell also experiences a dip in *c*-phase and its severity can be determined from the *d* value, see Table 7-XIII. In summary, the test results, as presented in Table 7-XIII, specify the successful classification of *bc*_dip_E type, *ca*_dip_C type, *a*_dip_D type and *AB*_swell_H type of events.

TABLE 7-XII

PHASORS OF 3-PHASE VOLTAGES RECORDED DURING DIPS/SWELLS

Type	$\boldsymbol{V_a}$	$\boldsymbol{V_b}$	$\boldsymbol{V_c}$
C	0.838∠5.2°	0.982∠-117.9°	0.876∠115.3°
D	0.726∠1.7°	0.964∠-114.6°	0.958∠116.9°
E	0.977∠1.2°	0.286∠-166.6°	0.365∠124.2°
H	1.52∠-15.1°	1.56∠-135°	0.08∠118.2°

TABLE 7-XIII

CLASSIFICATION OF VOLTAGE DIPS/SWELLS WITH RECORDED DATA

Dip/Swell type	Polarization Ellipse parameters					Classified dips/swells	Dip-depth (d)
	A_y/A_x	A_x	$\theta°$	$\varphi°$	$\lvert\psi\rvert°$		
C	0.91	1.15	126.1	-139.6	55.9	*ca*_dip_C	0.199
D	0.85	1.17	121.2	-142.9	34.7	*a*_dip_D	0.3
E	0.4	0.99	117.9	-101.4	77.1	*bc*_dip_E	0.798
H	0.58	1.822	175.6	-135.7	89.3	*AB*_swell_H	0.95

7.4.3 Validation of the Proposed Method using unbalanced voltage Dips associated with phase-angle jump

According to [30], the impedance angle or maximum phase angle jump of -10° to +10° is found in typical transmission system faults, whereas phase angle jump of -40° to -60° occur with faults in distribution lines. In agreement with this, the real cases, which are considered in this subsection, possess phase angle jump of less than 60°.

In [23] and [30], several test events of voltage dips including single-Φ and double-Φ dips are presented. Among those test events, six critical events, which include large phase angle jump and rotation due to loading effects, are used to validate the proposed algorithm. These six events are presented in Table 7-XIV. Event 1 is associated with

single-Φ voltage dip [23]. Event 2 illustrates the scenario when phase "a" experiences a dip of fifty percent with a phase-angle jump of –30° in a solidly grounded systems [30]. Event 3 represents a similar case to Event 2 with a larger phase-angle jump, i.e., –40° [30]. Event 4 represents the "bc" phase dip incorporating 50% voltage drop along with phase-angle jump of –40°. Event 5 and 6 are originated from Event 4 by considering the dynamics of the load associated with voltage drops and rotation [30]. Using the proposed algorithm, it is revealed in column 6 of Table 7-XIV that single-Φ and double-Φ dips have been classified correctly. The classified dip-types of all six events are also shown in column 7 of Table 7-XIV. Comparative analysis between space vector method presented in [31] and the proposed PE method are conducted on the basis of classification results of these six critical events. Among these six events, space vector method fails to classify four critical events (Events 3-6 as highlighted in Table 7-XIV) influenced by large phase-angle jump; whereas the proposed PE method has successfully classified all six events. Moreover, the proposed method was tested with adding noise (SNR ranging from 20 dB to 30 dB), see Table 7-XV, and harmonic distortion (THD was varied from 1% to 20%); under these conditions, it was found that performance of the proposed method was not affected.

TABLE 7-XIV

CLASSIFICATION OF UNBALANCED VOLTAGE DIPS ASSOCIATED WITH PHASE-ANGLE JUMP, VOLTAGE DROP AND ROTATION DUE TO LOAD EFFECTS

Events	V_a	V_b	V_c	"Classes" of dips (ground-truth)	Classified dips (Proposed PE method)		Classified "Classes" of dips using [31]
					"Classes"	Dip-type	
Event 1	0.316∠-11°	0.842∠-103.0°	0.848∠97.7°	*a*-Φ	*a*-Φ	D	*a*-Φ
Event 2	0.497∠-30°	1.003∠-120°	1.003∠120°	*a*-Φ	*a*-Φ	B	*a*-Φ
Event 3	0.497∠-40°	1.003∠-120°	1.003∠120°	*a*-Φ	*a*-Φ	B	*ab*-Φ
Event 4	1.00∠0°	0.847∠-157.1°	0.397∠123°	*bc*-Φ	*bc*-Φ	E	*c*-Φ
Event 5	0.85∠0°	0.717∠-157.0°	0.338∠124°	*bc*-Φ	*bc*-Φ	G	*c*-Φ
Event 6	0.851∠-20°	0.781∠-177.1°	0.339∠103°	*bc*-Φ	*bc*-Φ	G	*c*-Φ

TABLE 7-XV

Events	"Classes" of dips (ground-truth)	Classified dips					
		No noise		SNR 30 dB		SNR 20 dB	
		"Classes"	Dip-type	"Classes"	Dip-type	"Classes"	Dip-type
Event 1	*a*-Φ	*a*-Φ	D	*a*-Φ	D	*a*-Φ	D
Event 2	*a*-Φ	*a*-Φ	B	*a*-Φ	B	*a*-Φ	B
Event 3	*a*-Φ	*a*-Φ	B	*a*-Φ	B	*a*-Φ	B
Event 4	*bc*-Φ	*bc*-Φ	E	*bc*-Φ	E	*bc*-Φ	E
Event 5	*bc*-Φ	*bc*-Φ	G	*bc*-Φ	G	*bc*-Φ	G
Event 6	*bc*-Φ	*bc*-Φ	G	*bc*-Φ	G	*bc*-Φ	G

7.5 SUMMARY

A new method for classification and characterization of voltage dips and swells is proposed in this Chapter. Using the proposed approach, a total of seven types (A, B, D, F, E, C, and G) of dips, which include 19 possible groups of dips, are classified and characterized. Two types of voltage swells (H- and I-type), which include a total of 6 groups, are also classified using the developed method. The proposed method is designed based on the Polarization Ellipse (PE) parameters, in 3D co-ordinates, extracted from three phase voltage signals. Six PE parameters are extracted from in-phase and out-of-phase projected voltage phasors on a-, b- and c-axis. Based on the PE parameters, the expressions corresponding to seven types of dips and two types of swells, and their decision boundaries are developed. Using the decision boundaries and PE parameters, three-stage classification algorithm is proposed. The proposed algorithm can effectively classify the balanced dips, six classes (single-Φ and double-Φ dips) and their corresponding types of dips (B, D, F, E, C and G). Moreover, the developed analytical expressions of decision boundaries require less computation time for cycle by cycle classification. Therefore, the speed of the proposed algorithm is expected to be fast. The proposed algorithm is validated with recorded waveforms extracted from IEEE 1159.2 working group report and real measurement data of Belgian transmission grid. Besides, the proposed PE algorithm is able to classify the unbalanced dips associated with phase angle jump. Thus, the proposed method has a great potential to be used as an important tool for classification and characterization of voltage dips and swells in electricity networks.

Chapter 8

CHARACTERIZING VOLTAGE DIPS AND SWELLS DURING AND SUBSEQUENT TO ISLANDING SCENARIOS — A SPECIAL CASE STUDY

8.1 INTRODUCTION

The presence of DG strengthens the distribution system and introduces a damping for disturbances. For example, by using active control on the voltage at the terminals of the generator units, voltage fluctuations and voltage dips can be mitigated. However, utilitiesmay have specific interconnection guidelines for these local generators or DGs and they must comply with these guidelines/requirements for integration to the utility networks[2]. Controllers of these DGs do not need to control the grid frequency but can support voltage of the system, when they remain in grid-connected (i.e. in parallel operation mode). On the other hand, DG needs to control the voltage and frequency when they tend to operate in a stable stand-alone mode in a power system island. Stand-alone operation of DG may be triggered by islanding, which is defined as a situation when a segment of the distribution system is isolated from the utility-grid due to faults or other disturbances, and yet that isolated segment remains energized by DGs [2]. Stand-alone islanded operation increases the reliability, and therefore, several researchers have investigated the islanded operation of DG under micro-grid environment [125-127]. In [127], the authors have raised several issues for further investigation in the context of micro-grid. Two such issues are reliability of islanding detection, and voltage quality issues relevant to the sensitive loads inside the islanded network. In Chapter 3, an SVM based islanding detection method is proposed and the performance of the method is assessed under critical conditions emphasizing the reliability of the islanding detection process; further details of the SVM base method can be found in [106, 128]. However, the second issue, i.e., voltage quality issues, such as voltage dips, which may occur due to islanding and its subsequent scenarios including transitional state, island

stabilization state, and grid-reconnection state, have not been critically examined. Besides, widespread expansion of DG integration in future grid may increase the occurrence of voltage dips caused by these post-islanding scenarios, which may raise a concern in the future. Therefore, classification and characterization of voltage dips, due to these scenarios, are required to be critically investigated.

This Chapter investigates the voltage dips and swells associated with pre- and post-islanding scenarios of a distribution network embedded with DG under different network contingencies and conditions. To carry out this investigation, the 3D polarization ellipse technique, as proposed in Chapter 7, is employed for the classification and characterization of voltage dips and swells.

The remainder of the Chapter is structured as follows. Section 8.2 describes the test system employed for the study of voltage dips and swells associated with pre- and post-islanding scenarios. Section 8.3 characterizes thevoltage dips and swells arising due to pre- and post-islanding scenarios, which include the transitional state of islanding, disconnection of DG or establishment of island with proper controlling action, grid re-connection state, etc.;the 3D polarization ellipse parameters are applied for this characterization. Section 8.4concludes the Chapter.

8.2 TEST SYSTEM

Fig. 8.1 shows the single line diagram of a test distribution network of New South Wales, Australia, which will be used for the simulation study of pre- and post-islanding scenarios. The test system is an 11-kV radial distribution network having base-power of 100 MVA. It is connected to a subtransmission system of upstream grid-side through a 66/11-kV transformer. The subtransmission system is a 66-kV, 50-Hz system with short-circuit (SC) level of 1000 MVA;it is represented by a **Utility Source** in Fig. 8.1. In the test system, there is one 6-MVA synchronous generator (SG) used as DG and it is connected to bus 8 through 11/0.415 kV transformer. The SG is represented by a sixth-order 3-phase model in the *d-q* rotor reference frame and it is equipped with a steam-turbine governor and an exciter represented by the IEEE—Type 1 model. Exciter and governor of the synchronous generator are controlled in such a way that it allows the flexibility of operating the SG in grid-connected mode or stand-alone mode. The distribution lines are modelled as π-section line. Loads,shown in each buses of the distribution feeder, are modelled as constant impedance load. A total of 18 MW load is

distributed along the distribution feeder. Some loads are considered as noncritical loads, and they can be disconnected or connected according to the requirement of island stabilization state or grid-reconnection state. The relay is placed at transformer connection point of the DG to collect three-phase voltages.More details of the test system parameters are presented in **Appendix A.4** and the data of DG is presented in **Appendix A.3**.

The simulation system also includes measurement circuitry; including frequency estimation block, angle tracking block and instantaneous voltage measurement block. The frequency estimation block is implemented based on a cycle-to-cycle calculation of the time interval between two consecutive rising zero-crossing of the voltage waveform. The angle tracking block measures the real-time angle-difference between the two sides of Circuit Breaker (CB) connecting the grid-side and DG-side. Instantaneous voltage measurement block collects the instantaneous 3-phase voltages from DG end. These phase-voltages are processed using the proposed approach to classify and characterize voltage dips during dynamic and steady state operating conditions followed by islanding.

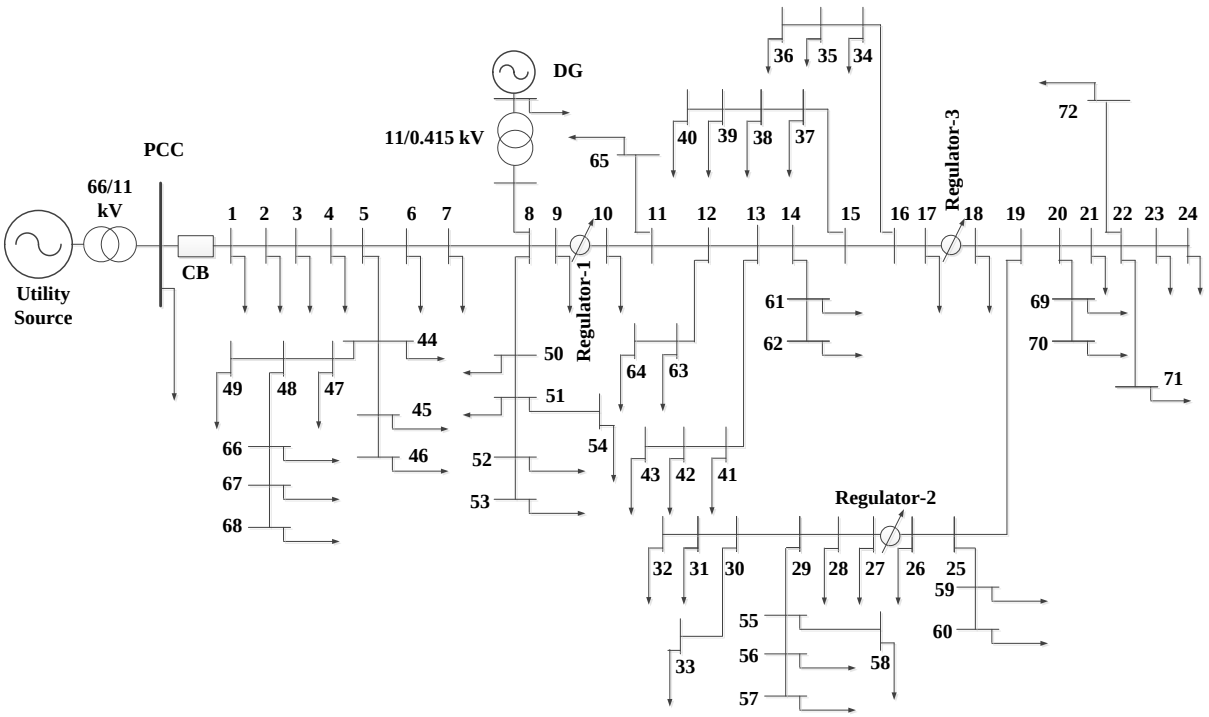

Fig. 8.1. Single line diagram of a test distribution system of Australia used for the simulation study.

8.3 CHARACTERIZATION OF VOLTAGE DIPS AND SWELLS DURING AND SUBSEQUENT TO ISLANDING SCENARIOS

This Section deals with the characterization of voltage dips caused by islanding and its subsequent scenarios. The scenarios include transitional state of islanding, stabilization of islanding and grid-reconnection of island. Under these scenarios, voltage dips are characterized and classified. To this end, the 3D PE algorithm, which is proposed in Chapter 7, is applied to classify the voltage dips and swells, and severity of dips is measured by dip-depth *d*. In Section8.3.1, pre-islanding scenarios are briefly discussed followed by the simulation study of the test system of Fig. 8.1. In Section 8.3.2, post-islanding scenarios are narrated followed by the classification and characterization of voltage dips using 3D PEalgorithm throughout the simulation study of the test system.

8.3.1 Pre-islanding Scenarios

Different switching incidents, e.g., unplanned or pre-planned switching incidents can give rise to islanding situation. Pre-planned islanding may result in minimal transients during the islanding period, if proper sharing between loads and DG units in the island are maintained. On the contrary, unplanned islanding does not allow maintaining the balance between load and generation in the island in a planned way. Therefore, severe transients may be found due to unplanned islanding. In this study, unplanned islanding is considered while conducting several case studies using the 11-kV test system of Fig. 8.1. The case studies include the classification and characterization of voltage dips originated from different types of permanent faults under grid connected environment. These permanent faults, which initiate the islanding phenomenon, are described as pre-islanding scenarios which include 1) Single line-to-ground (SLG) fault, 2) phase-to-phase fault and 3) balanced 3-phase fault. Using the test system of Fig. 8.1, a study forinvestigating these pre-islanding scenarios is carried out through simulations and described below.

1) *Single line-to-ground (SLG) fault*: A permanent SLG fault, i.e.,*a*-phase to ground fault, occurs on the 11-kV line (Bus 1 of Fig. 8.1) at t = 4.3 sec. The fault is cleared by the operation of CB, 10 cycles after the fault inception, e.g., at t= 4.5 sec, and an islanded zone is formed due to the fault mentioned above. The islanding phe-

nomenon is detected 10 cycles after the CB's open, e.g., at t = 4.7 sec, soon after that the control strategy of the DG units is activated to allow the stable islanded operation which will be elaborately discussed under the post-islanding scenarios of Sections8.3.2 and 8.3.3. Fig. 8.2 shows the transients during the fault, fault clearing, separation and onset of islanding. During the fault, voltage severely drops, see Figs. 8.2 (a) and 8.2 (c), and this impact is reflected in the characterization parameter *d*, which is obtained by using the proposed 3D PE algorithm, see Figs.8.2 (b) and 8.2 (d). It should be noted that Fig. 8.2(a) shows the terminal voltage of DG, whereas Fig. 8.2(c) shows the terminal voltage of a bus located at remote end from the DG. The characterization parameter *d* shown in Figs. 8.2(b) and 8.2(d) represents the voltage dips at DG end and remote end, respectively. Moreover, classification of voltage dip yields the F-type dip with severely affected *a*-phase (*a*_dip_F) at DG end, see Fig. 8.2 (b), whereas D-type dip with severely affected *a*-phase (*a*_dip_D) is observed at remote end, see Fig. 8.2 (d) for illustration. Similar observation is found for *b*-phase to ground and *c*-phase to ground faults.

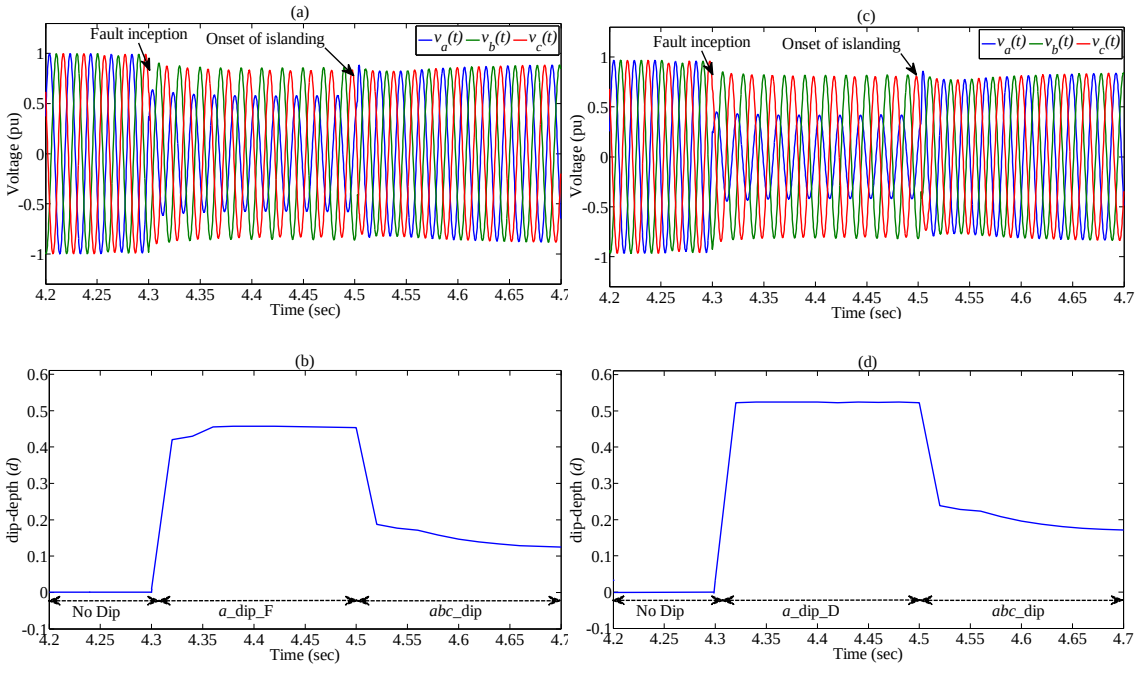

Fig. 8.2. (a) Pre-islanding (due to SLG fault) voltage observed at DG end and (b) its corresponding dip-depth parameter; (c) pre-islanding (due to SLG fault) voltage observed at remote end from DG and (d) its corresponding dip-depth parameter.

2) *Phase-to-phase fault*: This case study is identical to the previous case except that the fault is phase-to-phase. Therefore, just like the previous case, a permanent phase-to-

phase fault, i.e., *a*-phase to *b*-phase fault, is forced to occur on the 11-kV line (bus 1 of Fig. 8.1) at t = 4.3 sec. Study results are illustrated in Fig. 8.3 for phase-to-phase fault, e.g., *a*-phase to *b*-phase fault. Voltage dips encountered at DG end and remote end during these transients are successfully classified (*ab*_dip_C) and characterized as illustrated in Figs. 8.3(b) and 8.3(d). Similar observation is found for *b*-phase to *c*-phase and *c*-phase to *a*-phase faults.

3) *Balanced 3-phase fault*: This case study investigates the islanded operation and its electrical transients due to a permanent balanced 3-phase fault on the 11-kV line. The time intervals corresponding to fault clearing and islanding detection are the same as those of the previous case studies except that system islanding is detected within 8 cycles (as opposed to 10 cycles in the previous cases). In this case, islanding detection within 8 cycles is possible because of the severe voltage drop due to the 3-phasefault; it allows the features, used for islanding detection, to deviate significantly and thereby accelerating the detection process [106, 128]. Figs. 8.4(a) and8.4(c) show the system transients at DG end and remote end, respectively, during the pre-islanding period.Voltage dips during these transients are classified (*abc*_dip) and characterizedusing the proposed approach as shown in Figs. 8.4(b) and 8.4(d).

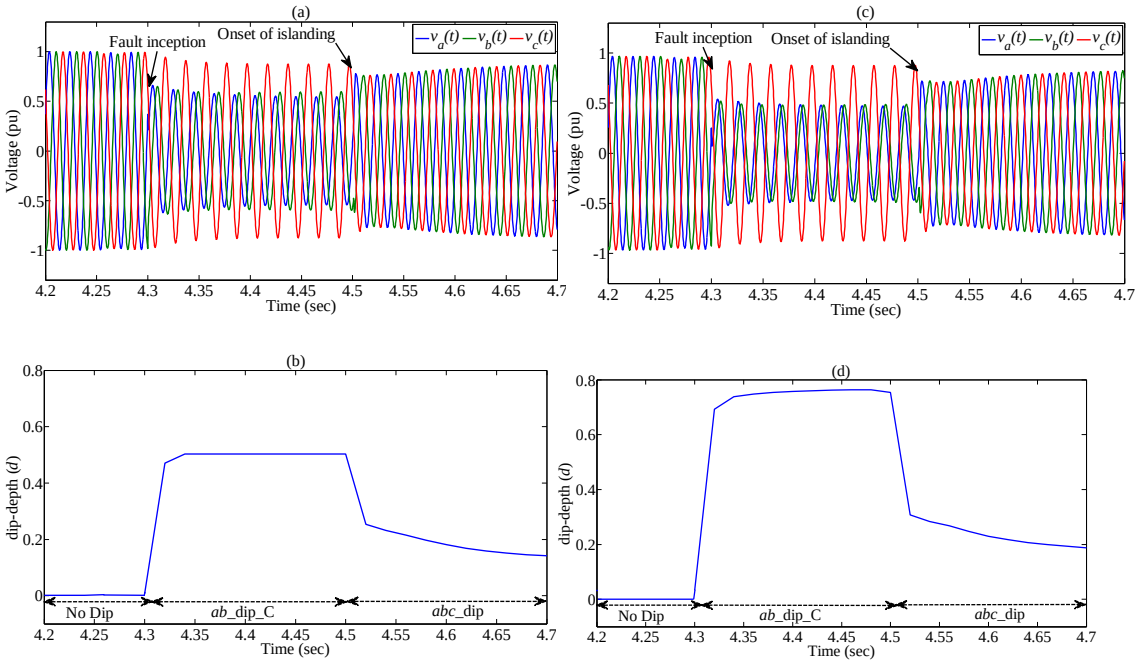

Fig. 8.3. (a) Pre-islanding (due to phase-to-phase fault) voltage observed at DG end and (b) its corresponding dip-depth parameter; (c) pre-islanding (due to phase-to-phase) voltage observed at remote end from DG and (d) its corresponding dip-depth parameter.

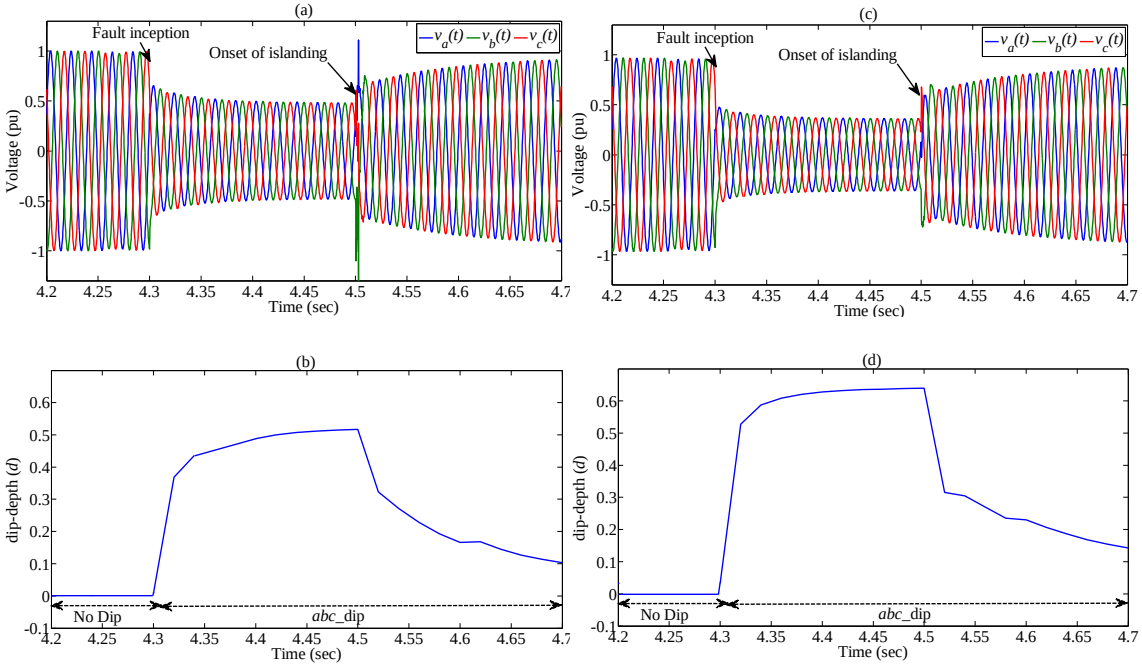

Fig. 8.4. (a) Pre-islanding (due to balanced3-phase fault) voltage observed at DG end and (b)its corresponding dip-depth parameter; (c) pre-islanding (due to balanced3-phase fault) voltage observed at remote end from DG and (d) its corresponding dip-depth parameter.

8.3.2 Post-islanding Scenarios

In this sub-section, post-islanding scenarios are briefly described through three states: 1) transitional state, 2) island stabilization state, and 3) grid-reconnection state. It is to be noted that the voltage dips associated with post-islanding scenarios arising from the anti-islanding operations are investigated in detail in [129], whereas this study explores the voltage dips associated with island stabilization states leading towards the micro-grid and then, returning to grid-reconnection state when fault is cleared.

1) *Transitional state of Islanding:*Transitional state is defined as a state which starts soon after the onset of islanding and ends as soon as islanding is detected. The islanding detection is conducted by islanding detection tool or relay. As presented in[106, 128], 10 cycles of post-islanding data are required to detect islanding. Therefore, in this study, 10 cycles of time duration is considered as transitional state duration.

Operating conditions prior to islanding or grid-connected mode and the type of DG, influence the severity of post-islanding scenarios. In agreement with this, voltage dips during the transitional state also experience an impact based on the type of DG and operating mode of DG. In this study, synchronous type DG, governed by biomassbased steam turbine, (biodiesel or diesel engine, or gas turbine can also be considered) and an

exciter, which can be operated either in voltage control mode or power factor control mode, is considered. As reported in [130], in grid-connected mode, speed governor needs to be operated in droop control mode and the exciter in power factor control mode. Conversely, stabilization of islanding requires the speed governor to be operated in isochronous mode and the exciter in voltage control mode. Therefore, transition of operating modes need to be performed as soon as islanding is detected. During the transitional state, islanding is not detected and hence, the exciter and governor of synchronous DG operate in grid-connected mode. Moreover, the power imbalance between load and generation in the island influences the voltage dips or swells. If, inside the formed island, there is a deficit of active power imbalance, i.e., load is higher than the generation of DG, then voltage dips are expected to occur. Similarly, for excess of active power imbalance, voltage swells are expected during the transitional state.

2) *Stabilization of Islanding state:* After the transitional state of islanding,continuity of electrical supply is ensured by stabilizing the island. To do so, the balance between load and generation is required to be maintained. By applying the load shedding approach and proper control mode on exciter (isochronous mode) and prime mover (droop-control mode), the islanding state can be stabilized[131].

3) *Grid-reconnection state:*After the onset of islanding, reconnection of the islanded network to the utility grid is allowed when restoration of the main grid and the islanded-side is attained. Grid restoration is ascertained when the system voltages and frequencies, return to a normal operating range, and are maintained in that normal state for a considerable period of time, e.g., five minutes [2]. To carry out this reconnection, proper synchronization between the islanded-side and the grid-side is required. Limits have been imposed for acceptable range of errors corresponding to voltage magnitude, frequency and phase-angle between the islanded-side and the main grid. For islanded network, energized with DG units ranging from 1.5-MW to 10-MW, reconnection is allowed if voltage error lies below 3%, frequency error is less than 0.1 Hz, and phase-angle error lies below 10° [2]. Obeying these limits ensures the reconnection of the stabilized islanded side with utility grid-side; this results in minimal transients in the grid-reconnection scenario.

8.3.3 Simulation Study for the Characterization of Voltage Dips under post-islanding scenarios

In this study, unplanned islanding is considered while conducting several case studies using the test system of Fig. 8.1. The case studies include the classification and characterization of voltage dips originated from the post-islanding scenarios which encompass the transitional state, island stabilization state and the grid-reconnection state. In general, throughout these case studies, characterization of voltage dips is illustrated during the steady state response and the dynamic response of the system under post-islanding scenarios. To this end, a simulation study has been carried out for the duration of 21.5 sec to investigate the behaviour of the system during post islanding scenarios. Fig. 8.5 shows the behaviour during transitional state and island stabilization state, and Fig. 8.6 shows the system behaviour during grid-reconnection state. The simulation procedure and characterization of voltage sags/swells under these post-islanding scenarios are described below.

To investigate the voltage dips during the transitional state and island stabilization state, the test system of Fig. 8.1 is simulated by opening CB, which yields the onset of islanding. While simulating the islanding scenario, deficit of active power imbalance is considered, and as expected, voltage dips are obtained in the transitional state and island stabilization state. At t = 4.5 second, islanding occurs andat t = 4.7 s the event is detected by using the method proposed in[106, 128]. Then, control of island operation is maintained by using the load-shedding approach, where indirect communication between loads and generators uses the frequency and knowledge of the generators' droop-characteristic as presented in [131]. The generator's capacity is 6 MW and loads inside the formed island are 18 MW. During grid connected mode, the excess active power load was fed by upstream grid. Therefore, during islanding period, deficit of active power occurs, and it drives the frequency to 44 Hz (see Fig. 8.5(a)), which in turn increases the possibility of instability in the islanded system. Hence, to keep the system stable, load-shedding is conducted gradually from 4.7-4.8 s. Since 12 MW load and generation imbalance exists in the islanded system, a total of 12 MW noncritical loads are disconnected to retain the frequency and voltage in stable state. Switching operation for load-balancing is conducted during the subsequent 5 cycles of transitional state, which lies within 4.7 to 4.8 seconds. Moreover, from Figs. 8.5 (a)-(b), it is revealed that at t =9.5 s, the frequency and rotor angle of the DG is stabilized, i.e., the island state is

stabilized. Three-phase voltage signals, obtained during these transitional and island stabilization states, are passed through the proposed 3D polarization ellipse method. Fig. 8.5(c) illustrates the characterization of voltage dips using the dip-depth (*d*) parameter on real-time basis. If *d*surpasses0.1 pu, then dip is observed; otherwise no dip is observed as indicated in Fig. 8.5(c). For the purpose of visualization, classification results are also shown in Fig. 8.5(c). During the most part of island stabilization state no dip is observed; however, the transient of voltage is reflected in one of the 3D PE parameters: normalized A_y, which can be observed from Fig. 8.5(d). Besides, classification of dips is presented in Table 8-I, which shows a balanced or *abc*_dip during the transitional state and a small fraction of island-stabilization state.

As illustrated in Fig. 8.5, island is stabilized at 9.5 s which can be observed from the frequency and rotor angle at DG connection point. At t = 20.1 s, grid-reconnection is conducted by re-connecting the breaker (CB) between the grid-side and islanded network. It should be noted that prior to performing the grid-reconnection, the parameters: voltage, frequency, phase sequence and phase angle between grid-side and stabilized island side were kept within the standard limit as presented in [2]. To do so, voltage, frequency and phase sequence were monitored continuously, and at t = 9.5 s the errors corresponding to these parameters were found within acceptable range. But, phase angle error was found to be deviated by more than 10°. However, using the controllable voltage source as grid-source, phase-angle error or phase-angle difference between grid and islanded-side was adjusted before re-connection took place. As shown in Fig. 8.6, at t = 19 s phase-angle adjustment starts and at t = 20 s the adjusted voltage, frequency, rotor-angle and phase-angle errors are found within acceptable limits which permits the grid-reconnection. At t = 20.1 s grid-reconnection are forced to occur and the DG terminal voltage is monitored continuously. At t = 21 s the system reaches to steady-state condition as observed from the DG terminal voltage. The steady condition is further verified by the frequency and rotor angle at DG end, see Figs. 8.6 (b)-(c). During grid-reconnection period, no voltage dips are observed. However, the slight variation of voltages, during the transient period of grid-reconnection state, is reflected in the normalizedA_y parameter as shown in Fig. 8.6(d). Moreover, classification results of grid-reconnection state are presented in Table 8-I.

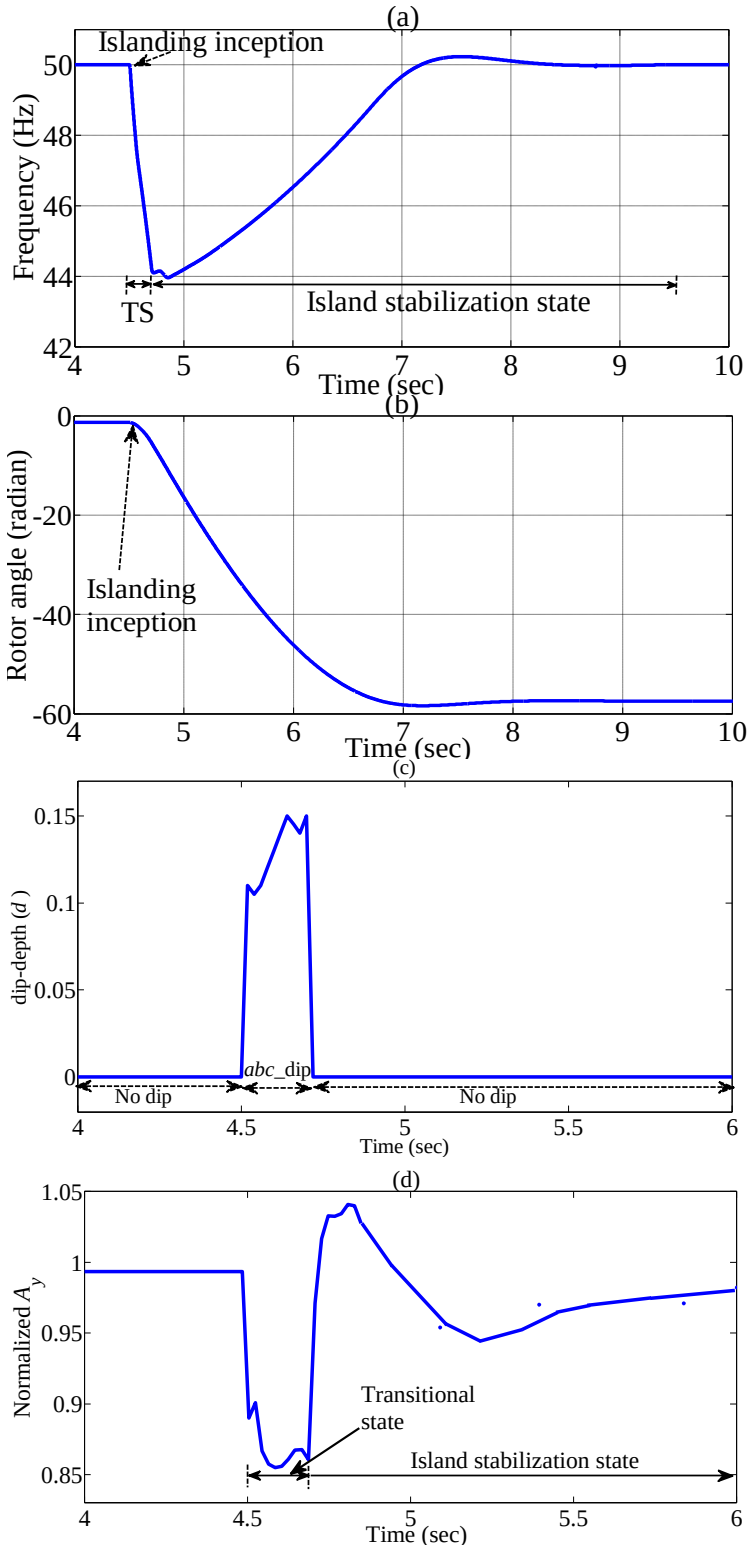

Fig. 8.5. (a) Frequency, (b) rotor angle, (c) characterization of voltage dip using dip-depthand (d) normalized A_y, during transitional state and stabilization state of islanding.

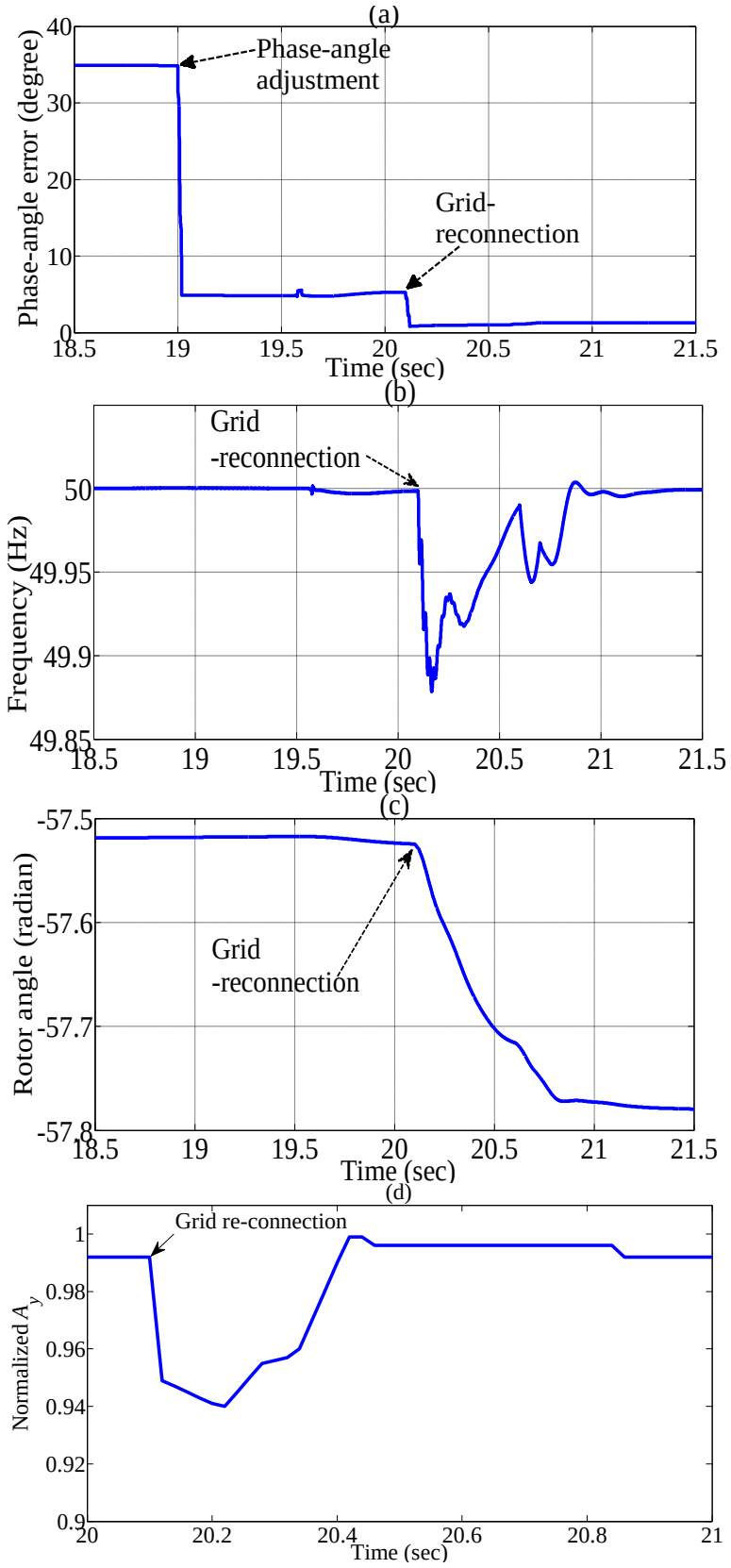

Fig. 8.6. (a) Phase-angle error adjustment at t = 19 s, and grid-reconnection at t = 20.1 s; (b) frequency, (c) rotor angle, and (d) characterization of grid-reconnection scenario using normailzed A_y, observed at DG end.

TABLE 8-I
CLASSIFICATION RESULTS DURING POST-ISLANDING SCENARIOS

Scenarios	Time	Classification results
Transitional state of islanding	4.5-4.7 s	*abc*_dip
Island stabilization state	4.7-4.8 s	*abc*_dip
	4.8-9.5 s	No dip
Grid-reconnection state	20.1-21 s	No dip

In the above study, grid-reconnection is observed after maintaining the phase-angle error within standard permissible limit. However, if there is an absence of phase-angle error adjustment mechanism, and grid-reconnection takes place, then voltage transients (with voltage swell)can also be observed using the proposed 3D polarization ellipse method.

It is worth-noting that,for the simulation study demonstrated in this Section, various operations followed by the post-islanding scenarios are forced to happen within very short time-durations. For practical scenarios, the time-durations may be different depending on the standard agreement set by the utility, customer and DG operator. However, the proposed 3D polarization can effectively perform to characterize the voltage dips and swells irrespective of the time-durations of the scenarios.

8.4 SUMMARY

Introduction of distributed generation (DG) may provide special benefits in a number of ways. For example, it can strengthen the distribution system in terms of load carrying capacity and voltage support, and introduce a damping for the voltage disturbance, such as, voltage dips, harmonics, etc. On the contrary, penetration of DG may give rise to islanding event, which can have adverse effects if it is not properly detected. Development of reliable islanding detection methods, allows the flexibility of stand-alone operation of synchronous generator based DG under islanded mode. This stand-alone operation is achieved by appropriate switching operation of the controllers from grid-parallel mode to stand-alone mode. Conversely, when grid-restoration or reconnection is permitted, reverse switching operation, i.e., stand-alone mode to grid-parallel mode, is employed. If islanding is detected properly, then depending on the agreement set by the utility and/or customer, DG is disconnected, or remains connected that result in a micro-grid. However, for both cases, voltage dips and swells may occur, which are encountered during and subsequent period of islanding.

To investigate the voltage dips associated with the islanding event of distributed generation (DG) and its subsequent operations, this chapter conducted the classification and characterization of voltage dips using the 3D polarization ellipse algorithm.Islanding and its subsequent scenarios are simulated using a test distribution network embedded with synchronous generator (SG) based DG, for which voltage dips are characterized.To this end, the3D polarization ellipse parameters and the proposed method of Chapter 7, which can characterize (using the dip-depth parameter *d*) as well as classify seven types of voltage dips, is employed. The pre-islanding voltage dips, which could be triggered by balanced or unbalanced faults,have been classified and characterized. Moreover, three states of post-islanding scenarios, which is composed of transitional state, island stabilization state, and grid-reconnection state, are also characterized. In summary, using the proposed 3D PE method, this Chapter has mainly focused on characterization of the voltage dips and swells associated with a special case, which can be found during pre- and post-islanding scenarios.

CHAPTER 9

CONCLUSIONS AND DIRECTIONS FOR FUTURE WORKS

This thesis has developed comprehensive and realistic approaches for solving two critical issues in electricity network using voltage and its associated features: 1) Anti-islanding protection of distributed generation with special emphasis on critical islanding events, and 2) classification and characterization of voltage dips and swells. General conclusions of the thesis and directions of future works are provided below.

9.1 CONCLUDING REMARKS

A brief literature review, to address the two critical issues, islanding detection and characterization of voltage dips/swells, are presented in **Chapter 2**. A review on islanding detection schemes as presented in existing literatures and non-detection zone of conventional relays is carried out and presented. Classification of different types of voltage dips and swells, their phasor representation, and propagation of voltage dips through different network elements, e.g., transformers, causing transformation of dip-types, are described. Importance and requirement of new islanding detection schemes and voltage dips/swells characterization methods are also highlighted. Existing studies in literature facilitate to construct the basis of the work presented in this thesis.

A novel approach, which involves multiple features and a support vector machine (SVM) classifier,has been developedin **Chapter 3** for islanding detection of distributed generation. The developed approach uses multiple features extracted from the network variables including voltage, frequency and rotor angle. These variables show distinguishable behaviour for classifying the islanding and non-islanding events as presented through analytical expressions as well as simulations. Five features, extracted from these variables using sliding data-window, are used to train the SVM with linear, Gaussian RBF and polynomial kernels. The islanding events, considering all possible combinations of power imbalance scenarios with special emphasis on the critical events

associated with NDZ of conventional relays, are taken into account during the training period. Thus, the trained SVM ensures the successful classification of islanding events both outside and inside the NDZ as demonstrated using the simulation results.

In **Chapter 4**,an analytical approach that providethe expressions of boundary limit of NDZ for rate-of-change-of-frequency (ROCOF) and vector surge (VS) relays is developed using the concept of critical active power imbalance inside the islanded segment. These analytic expressions are useful for the performance study of ROCOF and VS relays for islanding detection. For example, the time required for the ROCOF and VS relays to trigger under different power imbalance conditions can be easily obtained from these expressions. Similarly, if VS and ROCOF relays are required to operate within specific time (e.g., 200 ms) of onset of islanding, the minimum amount of power imbalance can be easily determined. Extensive simulation is conducted to verify these expressions as well as to investigate the performance of VS and ROCOF relays under deficit and excess of active and reactive power imbalance. Three types of load, which include constant impedance, constant current and constant power load, are also considered during these simulation studies. Moreover, a comparative study of VS and ROCOF relays with SVM based approach is conducted considering the performance indicators, namely detection rate and false alarm, under different network contingencies. Test results demonstrate the superiority of SVM based method over ROCOF and VS relays.

Chapter 5 mainly investigates the voltage dips and its associated phase-angle jumps in power network due to four major types of faults. The presence of synchronous generator type DG is also included in the voltage dip investigation. Seven types of voltage dips, namely, A, B, D, E, F, E, C and G, are analysed with and without DG. Firstly, analytical expressions of seven types of voltage-dip and their phase-angle jumps are developed. Simulation study demonstrates the acceptability of the developed expressions for investigating voltage dips at different buses during the occurrence of fault in a test network with and without DG. Also, characterization of voltage dip is conducted under the influence of DG. The size of DG and its location are examined to highlight the impact of DG during fault. Moreover, the influence of fault-types and fault-location are studied during the investigation.

A new approach has been developed in **Chapter 6** for classifying and characterizing voltage sags and swells. To this end, three-phase voltage ellipse parameters are used where, inclination angle is used to classify sags/swells, and minor and major axis are used to characterize the severity of sags and swells, respectively. The developed approach provides the flexibility of applying it as an online monitoring tool. Moreover, offline record of the voltage data can also be analysed using the approach as per utility and/or customer requirements. This helps quantify the quality of voltage, in terms of sags and swells, their levels and propagation at different points of the networks.

A novel approach, using polarization ellipse (PE) parameters in 3D co-ordinates, is developed in **Chapter 7** for classifying and characterizing voltage dips and swells of different types**.** A multi-stage classification algorithm, incorporating the decision boundaries derived for different types of dips and swells, is applied in the classification process. The proposed strategy is able to provide a good level of accuracy for the classification and characterization of the critical voltage dips associated with phase angle jump, rotation of phase-voltages due to loading effects, etc. The decision boundaries applied in this strategy are derived using simple analytical expressions; as a result, the approach requires less computation time for cycle by cycle classification. Therefore, the proposed approach can be used as a real-time voltage dip/swell monitoring tool and suitable for online implementation.

Chapter 8 mainly demonstrates the applicability of 3D polarization ellipse technique proposed in **Chapter 7**. A special case study, which includes the islanding event of distributed generation (DG) and its subsequent operations, is conducted to investigate the voltage dips and swells. Islanding and its subsequent scenarios are simulated using a test distribution network embedded with synchronous generator (SG) based DG, and the voltage dips are characterized using 3D PE technique. The pre-islanding voltage dips, which could be triggered by balanced or unbalanced faults, are classified and characterized. Moreover, three states of post-islanding scenarios, which are composed of transitional state, island stabilization state, and grid-reconnection state, are classified and characterized and results are presented.

9.2 DIRECTIONS FOR FUTURE WORKS

General directions for future work are provided below.

- The SVM based approach was described in **Chapter 3** for islanding detection of distributed generation (DG). The type of DG which was used throughout the thesis was synchronous-type DG. Therefore, the proposed approach can be extended for inverter-based and asynchronous or induction generator based DG. Since in the SVM based approach, only time-domain voltage signal is required to extract the features, the extension of the proposed approach for other types of DG is expected to be feasible.

- Islanding is a critical protection issue for the safe operation of future micro-grid or smart-grid. Hence, islanding detection method needs to provide reliability with the possibility of limited amount of nuisance tripping. In the SVM based approach, simulated data, considering all possible combinations of power imbalance, are used to train the SVM. Real data, collected from practical network during islanding events, can enhance the reliability of SVM based method.

- In **Chapter 4**, analytical formulae, for establishing the NDZ of VS and ROCOF relays, are developed to investigate the performance of these relays in islanding detection. Some constraints have been imposed while deriving those analytic expressions or formulae. For instance, classical model of synchronous generator (SG) is used to develop the expressions. Replacing the classical model of SG with higher order, e.g., sixth-order three-phase model in the *d-q* rotor reference frame, more precise and accurate expressions can be obtained. Thus, the derived expressions could be made more precise for analysing the performance of ROCOF and VS relay.

- In **Chapter 5**, analytical expressions of phase-voltages associated with four major types of faults, which include balanced and unbalanced faults, are developed. Steady-state analysis is carried out to develop these expressions. Incorporating dynamic analysis of the power systems, more precise expressions, which may facilitate to explain the transient phenomenon during voltage dips/swells, can be obtained.

- The 3D polarization ellipse (PE) approach, as presented in **Chapter 7**,can be extended to classify some other power quality events, such as, voltage interruption, flicker, etc. Using the parameters of PE, and considering the definition of voltage interruption and flicker, a simple classifier can be designed to classify these events.

Moreover, using 3D PE parameters along with multiple voltage features, a comprehensive classifier, for example, multi-class SVM can be designed to classify and characterize power quality events as reported in IEEE 1159 standard.

- In **Chapter 8**, the applicability of the proposed 3D polarization ellipse technique is demonstrated by a special case study, which is associated with pre- and post-islanding scenarios. However, the application of the proposed approach can be extended and tested for various case studies (including practical scenarios). For example, customers, adjacent to an industrial area, may be affected by voltage dips due to starting of heavy loads, e.g., motor-start. By explaining this scenario, i.e., how frequently and severely different types of voltage dips occur, emphasizing its importance and describing some factors that affect it, the realistic problems can be assessed and the necessary pre-emptive actions can be taken thereby.

REFERENCES

[1] J. L. Blackburn and T. J. Domin. (2006). *Protective Relaying : Principles and Applications, Third Edition (3 ed.)*. Available: http://UOW.eblib.com/patron/FullRecord.aspx?p=283277

[2] "IEEE Standard for Interconnecting Distributed Resources with Electric Power Systems," *IEEE Std 1547-2003*, pp. 1-28, 2003.

[3] "IEEE Application Guide for IEEE Std 1547(TM), IEEE Standard for Interconnecting Distributed Resources with Electric Power Systems," *IEEE Std 1547.2-2008*, pp. 1-217, 2009.

[4] H. G. Far, A. J. Rodolakis, and G. Joos, "Synchronous distributed generation islanding protection using intelligent relays," *Smart Grid, IEEE Transactions on*, vol. 3, pp. 1695-1703, 2012.

[5] L. Kumpulainen and K. Kauhaniemi, "Analysis of the impact of distributed generation on automatic reclosing," in *Power Systems Conference and Exposition, 2004. IEEE PES*, 2004, pp. 603-608.

[6] H. H. Zeineldin and M. M. Salama, "Impact of load frequency dependence on the NDZ and performance of the SFS islanding detection method," *Industrial Electronics, IEEE Transactions on*, vol. 58, pp. 139-146, 2011.

[7] A. Yafaoui, B. Wu, and S. Kouro, "Improved active frequency drift anti-islanding detection method for grid connected photovoltaic systems," *Power Electronics, IEEE Transactions on*, vol. 27, pp. 2367-2375, 2012.

[8] H. Karimi, A. Yazdani, and R. Iravani, "Negative-sequence current injection for fast islanding detection of a distributed resource unit," *Power Electronics, IEEE Transactions on*, vol. 23, pp. 298-307, 2008.

[9] "IEEE Guide for Interfacing Dispersed Storage and Generation Facilities With Electric Utility Systems," *ANSI/IEEE Std 1001-1988*, pp. 0-1, 1989.

[10] W. J. S. Rogers, "The parallel operation of generating plant within a regional electricity company's distribution network," in *Parallel Operation of Generating Plant within a Public Electricity Supply Network, IEE Colloquium on*, 1991, pp. 1/1-1/9.

[11] *Impact of increasing contribution of dispersed generation on the power system: final report*: CIGRE, 1999.

[12] C. W. G. 4, "Dispersed Generation," CIRED, Tech. Rep., Liege, Belgium 1999.

[13] W. Freitas, W. Xu, C. M. Affonso, and Z. Huang, "Comparative analysis between ROCOF and vector surge relays for distributed generation applications," *Power Delivery, IEEE Transactions on*, vol. 20, pp. 1315-1324, 2005.

[14] K. El-Arroudi, G. Joos, I. Kamwa, and D. T. McGillis, "Intelligent-based approach to islanding detection in distributed generation," *Power Delivery, IEEE Transactions on*, vol. 22, pp. 828-835, 2007.

[15] K. El-Arroudi and G. Joos, "Data mining approach to threshold settings of islanding relays in distributed generation," *Power Systems, IEEE Transactions on*, vol. 22, pp. 1112-1119, 2007.

[16] S. Samantaray, K. El-Arroudi, G. Joós, and I. Kamwa, "A fuzzy rule-based approach for islanding detection in distributed generation," *Power Delivery, IEEE Transactions on*, vol. 25, pp. 1427-1433, 2010.

[17] M. S. Thomas and P. P. Terang, "Islanding detection using decision tree approach," in *Power Electronics, Drives and Energy Systems (PEDES) & 2010 Power India, 2010 Joint International Conference on*, 2010, pp. 1-6.

[18] A. Pigazo, M. Liserre, R. A. Mastromauro, V. M. Moreno, and A. Dell'Aquila, "Wavelet-based islanding detection in grid-connected PV systems," *Industrial Electronics, IEEE Transactions on,* vol. 56, pp. 4445-4455, 2009.
[19] B. Panigrahi and V. R. Pandi, "Optimal feature selection for classification of power quality disturbances using wavelet packet-based fuzzy k-nearest neighbour algorithm," *IET generation, transmission & distribution,* vol. 3, pp. 296-306, 2009.
[20] "IEEE Guide for Identifying and Improving Voltage Quality in Power Systems," *IEEE P1250/D13 January 2011,* pp. 1-68, 2011.
[21] M. F. McGranaghan, D. R. Mueller, and M. J. Samotyj, "Voltage sags in industrial systems," *IEEE Transactions on industry applications,* vol. 29, pp. 397-403, 1993.
[22] M. H. Bollen, *Understanding power quality problems,* vol. 3: IEEE press New York, 2000.
[23] L. Zhang and M. H. Bollen, "Characteristic of voltage dips (sags) in power systems," *Power Delivery, IEEE Transactions on,* vol. 15, pp. 827-832, 2000.
[24] "Voltage Characteristics of the Electricity Supplied by Public Distri-bution Systems," *European/British Standard EN (EuroNorms) BS/EN 50160, CLC, BTTF 68-6.,* Nov. 1994.
[25] "IEEE Recommended Practice for Monitoring Electric Power Quality," *IEEE Std 1159-2009 (Revision of IEEE Std 1159-1995)*, pp. c1-81, 2009.
[26] "Electricity Supply-Quality Supply, Part 2: Minimum Standards," *South African Bureau of Standard. NRS 048-2,* 1996, 2002.
[27] *Int. Electrotechnical Vocabulary (IEV)*, IEC Standard 60050, 1999.
[28] S. s. Z. Djokic, J. V. Milanovic, D. J. Chapman, and M. F. McGranaghan, "Shortfalls of existing methods for classification and presentation of voltage reduction events," *IEEE Transactions on Power Delivery,* vol. 20, pp. 1640-1649, 2005.
[29] M. H. Bollen and L. Zhang, "Different methods for classification of three-phase unbalanced voltage dips due to faults," *Electric power systems research,* vol. 66, pp. 59-69, 2003.
[30] M. H. Bollen, "Algorithms for characterizing measured three-phase unbalanced voltage dips," *Power Delivery, IEEE Transactions on,* vol. 18, pp. 937-944, 2003.
[31] V. Ignatova, P. Granjon, and S. Bacha, "Space vector method for voltage dips and swells analysis," *Power Delivery, IEEE Transactions on,* vol. 24, pp. 2054-2061, 2009.
[32] V. N. Vapnik, *Statistical learning theory*: Wiley, 1998.
[33] N. Cristianini and J. Shawe-Taylor, *An Introduction to Support Vector Machines and Other Kernel-based Learning Methods*: Cambridge University Press, 2000.
[34] P. G. Axelberg, I.-H. Gu, and M. H. Bollen, "Support vector machine for classification of voltage disturbances," *Power Delivery, IEEE Transactions on,* vol. 22, pp. 1297-1303, 2007.
[35] X. Ding, "Synchronised Phasor Measurement and Islanding Operation of Distributed Generation," Ph.D., Faculty of Engineering and Power System, Queen's University, Belsfast, 2006.
[36] H. Jouybari-Moghaddam, S. Hosseinian, and B. Vahidi, "An introduction to active distribution networks islanding issues," in *Electrical Power Distribution Networks (EPDC), 2012 Proceedings of 17th Conference on*, 2012, pp. 1-6.

[37] C. F. Ten, "Loss of mains detection and amelioration on electrical distribution networks," Ph.D., University of Manchester, 2011.
[38] W. Xu, K. Mauch, and S. Martel, "An assessment of distributed generation islanding detection methods and issues for Canada," *CANMET Energy Technology Centre-Varennes, Natural Resources Canada, QC-Canada, Tech. Rep. CETC-Varennes*, vol. 74, 2004.
[39] E. Ltd, "Assessment of islanded operation of distribution networks and measures for protection," ETSU K/EL/00235/REP,2001.
[40] X. Ding and P. A. Crossley, "Islanding detection for distributed generation," in *Power Tech, 2005 IEEE Russia*, 2005, pp. 1-4.
[41] A. Ishibashi, M. Imai, K. Omata, S. Sato, T. Takagi, Y. Nakachi, *et al.*, "New type of islanding detection system for distributed generation based on voltage angle difference between utility network and distributed generation site," 2004.
[42] Z. Y. R. Walling, N. Miller, P. Du, K. Nelson, "Facility Microgrids," NREL/SR-560-38019, 2005.
[43] R. Walling and N. Miller, "Distributed generation islanding-implications on power system dynamic performance," in *Power Engineering Society Summer Meeting, 2002 IEEE*, 2002, pp. 92-96.
[44] J. Yin, L. Chang, and C. Diduch, "Recent developments in islanding detection for distributed power generation," in *Power Engineering, 2004. LESCOPE-04. 2004 Large Engineering systems Conference on*, 2004, pp. 124-128.
[45] P. Hopewell, N. Jenkins, and A. Cross, "Loss-of-mains detection for small generators," *IEE Proceedings-Electric Power Applications*, vol. 143, pp. 225-230, 1996.
[46] P. O'kane and B. Fox, "Loss of mains detection for embedded generation by system impedance monitoring," in *Developments in Power System Protection, Sixth International Conference on (Conf. Publ. No. 434)*, 1997, pp. 95-98.
[47] P. O'Kane, B. Fox, and D. Morrow, "Impact of embedded generation on emergency reserve," *IEE Proceedings-Generation, Transmission and Distribution*, vol. 146, pp. 159-163, 1999.
[48] N. Strath, "Islanding Detection in Power Systems," Ph.D., Department of Industrial Electrical Engineering and Automation, Lund University, Lund, 2005.
[49] S. Salman and D. King, "Monitoring changes in system variables due to islanding condition and those due to disturbances at the utilities' network," in *Transmission and Distribution Conference, 1999 IEEE*, 1999, pp. 460-465.
[50] "Technical Report of NECA for Frequency operating standards determination," Sep. 2001. [Available online] http://www.neca.com.au/Files/RP_Final_Determination_Sep_2001.pdf.
[51] C. Bright, "COROCOF: comparison of rate of change of frequency protection. A solution to the detection of loss of mains," 2001.
[52] N. Jenkins and I. o. E. Engineers, *Embedded Generation*: Institution of Engineering and Technology, 2000.
[53] M. Geidl, *Protection of power systems with distributed generation: state of the art*: ETH, Eidgenössische Technische Hochschule Zürich, EEH Power Systems Laboratory, 2005.
[54] A. Beddoes, P. Thomas, and M. Gosden, "Loss of mains protection relay performances when subjected to network disturbances/events," in *Electricity Distribution, 2005. CIRED 2005. 18th International Conference and Exhibition on*, 2005, pp. 1-5.

[55] W. Freitas, W. Xu, Z. Huang, and J. Vieira, "Characteristics of vector surge relays for distributed synchronous generator protection," *Electric power systems research*, vol. 77, pp. 170-180, 2007.
[56] F. Noor, R. Arumugam, and M. Vaziri, "Unintentional islanding and comparison of prevention techniques," in *Power Symposium, 2005. Proceedings of the 37th Annual North American*, 2005, pp. 90-96.
[57] W. Freitas and W. Xu, "False operation of vector surge relays," *Power Delivery, IEEE Transactions on*, vol. 19, pp. 436-438, 2004.
[58] N. Lidula and A. Rajapakse, "A pattern recognition approach for detecting power islands using transient signals—Part I: Design and implementation," *Power Delivery, IEEE Transactions on*, vol. 25, pp. 3070-3077, 2010.
[59] M. Hanif, U. Dwivedi, M. Basu, and K. Gaughan, "Wavelet based islanding detection of DC-AC inverter interfaced DG systems," in *Universities Power Engineering Conference (UPEC), 2010 45th International*, 2010, pp. 1-5.
[60] S.-I. Jang and K.-H. Kim, "An islanding detection method for distributed generations using voltage unbalance and total harmonic distortion of current," *Power Delivery, IEEE Transactions on*, vol. 19, pp. 745-752, 2004.
[61] K.-H. Chao and C.-L. Chiu, "An intelligent islanding detection method based-on extension theory for photovoltaic power generation systems," in *Computer Communication Control and Automation (3CA), 2010 International Symposium on*, 2010, pp. 171-174.
[62] W.-Y. Chang, "An Islanding Detection Method for Grid-Connected Inverter of Distributed Renewable Generation System," in *Power and Energy Engineering Conference (APPEEC), 2011 Asia-Pacific*, 2011, pp. 1-4.
[63] W.-Y. Chang, "A hybrid islanding detection method for distributed synchronous generators," in *Power Electronics Conference (IPEC), 2010 International*, 2010, pp. 1326-1330.
[64] D. Martin, K.-H. Wu, C.-L. Chen, and J.-S. Lai, "Phase lock loop design and novel test schemes for islanding detection," in *Power Electronics and ECCE Asia (ICPE & ECCE), 2011 IEEE 8th International Conference on*, 2011, pp. 1793-1800.
[65] S. Samantaray, T. M. Pujhari, and B. Subudhi, "A new approach to Islanding detection in Distributed Generations," in *Power Systems, 2009. ICPS'09. International Conference on*, 2009, pp. 1-6.
[66] A. Samui and S. Samantaray, "Assessment of ROCPAD relay for islanding detection in distributed generation," *Smart Grid, IEEE Transactions on*, vol. 2, pp. 391-398, 2011.
[67] J. Yin, C. P. Diduch, and L. Chang, "Islanding detection using proportional power spectral density," *Power Delivery, IEEE Transactions on*, vol. 23, pp. 776-784, 2008.
[68] S.-H. Lee and J.-W. Park, "New islanding detection method for inverter-based distributed generation considering its switching frequency," *Industry Applications, IEEE Transactions on*, vol. 46, pp. 2089-2098, 2010.
[69] S. Samantaray, A. Samui, and B. C. Babu, "S-transform based cumulative sum detector (CUSUM) for islanding detection in Distributed Generations," in *Power Electronics, Drives and Energy Systems (PEDES) & 2010 Power India, 2010 Joint International Conference on*, 2010, pp. 1-6.
[70] O. N. Faqhruldin, E. El-Saadany, and H. Zeineldin, "Evaluation of islanding detection techniques for inverter-based distributed generation," in *Power and Energy Society General Meeting, 2012 IEEE*, 2012, pp. 1-7.

[71] O. Faqhruldin, "A Universal Islanding Detection Technique for Distributed Generation Using Pattern Recognition," M.Sc. Thesis, University of Waterloo, Waterloo, Ontario, Canada, 2013.
[72] J. C. M. Vieira, W. Freitas, X. Wilsun, and A. Morelato, "An Investigation on the Nondetection Zones of Synchronous Distributed Generation Anti-Islanding Protection," *Power Delivery, IEEE Transactions on*, vol. 23, pp. 593-600, 2008.
[73] K. Bhattacharya, M. H. Bollen, and J. E. Daalder, "Operation of restructured power systems," 2001.
[74] R. C. Dugan, M. F. McGranaghan, S. Santoso, and H. W. Beaty, *Electrical Power Systems Quality, Third Edition*: McGraw-Hill Education, 2012.
[75] V. E. Wagner, A. A. Andreshak, and J. P. Staniak, "Power quality and factory automation," *Industry Applications, IEEE Transactions on*, vol. 26, pp. 620-626, 1990.
[76] *Electromagnetic Compatibility (EMC), Part 2: Environment, Section 8: Voltage Dips and Short Interruptions on Public Electric Power Supply Systems With Statistical Measurement*, IEC Standard 61 000-2-8, 2000.
[77] *Voltage Characteristics of the Electricity Supplied by Public Distribution Systems*, European/British Standard EN (EuroNorms) BS/EN 50160, CLC, BTTF 68-6, Nov. 1994.
[78] *Electricity Supply—Quality of Supply, Part 1: Overview of Implementation of Standards and Procedures*, South African Bureau of Standards NRS 048-1, 1996, 2002.
[79] *IEEE Recommended Practice for Evaluating Electric Power System Compatibility With Electronic Process Equipment*, IEEE Standard 1346, 1998.
[80] *IEEE Recommended Practice for Powering and Grounding Sensitive Electronic Equipment (Emerald Book)*, IEEE Standard 1100, 1992.
[81] *Recommended Practice for Monitoring Electric Power Quality*, IEEE Standard 1159, 1995.
[82] *Electromagnetic Compatibility (EMC), Part 4: Testing and Measurement Techniques, Section 30: Power Quality Measurement Techniques*, IEC Standard 61000-4-30, 2003.
[83] *Voltage sags and short interruptions on public electric power supply systems with statistical measurement results*: IEC 61000-2-8, 2002.
[84] D. S. Dorr, M. B. Hughes, T. M. Gruzs, R. E. Jurewicz, and J. L. McClaine, "Interpreting recent power quality surveys to define the electrical environment," *Industry Applications, IEEE Transactions on*, vol. 33, pp. 1480-1487, 1997.
[85] D. Sabin, A. Dettloff, and F. Goodman, "Overview of Detroit Edison's voltage dip performance agreements," in *Proc. 5th Int. Conf. Electrical Power Quality Utililization. Kraków, Poland*, 1999, pp. 53-58.
[86] K. Stockman, F. D'hulster, K. Verhaege, M. Didden, and R. Belmans, "Ride-through of adjustable speed drives during voltage dips," *Electric Power Systems Research*, vol. 66, pp. 49-58, 2003.
[87] S. Z. Djokic, J. V. Milanovic, and D. S. Kirschen, "Sensitivity of AC coil contactors to voltage sags, short interruptions, and undervoltage transients," *Power Delivery, IEEE Transactions on*, vol. 19, pp. 1299-1307, 2004.
[88] P. Pohjanheimo, *A probabilistic method for comprehensive voltage sag management in power distribution systems*: Helsinki University of Technology, 2003.
[89] F. C. Pereira, O. Souto, J. De Oliveira, A. Vilaca, and P. Ribeiro, "An analysis of costs related to the loss of power quality," in *Harmonics and Quality of*

Power Proceedings, 1998. Proceedings. 8th International Conference On, 1998, pp. 777-782.

[90] D. Lineweber and S. McNulty, *The cost of power disturbances to industrial & digital economy companies*: EPRI, 2001.

[91] P. K. Ray, S. R. Mohanty, and N. Kishor, "Classification of Power Quality Disturbances Due to Environmental Characteristics in Distributed Generation System," *Sustainable Energy, IEEE Transactions on*, vol. 4, pp. 302-313, 2013.

[92] D. Surender, D. K. Jain, and A. Kumar, "Power quality issues of embedded generation," in *Power India Conference, 2006 IEEE*, 2006, p. 4 pp.

[93] J. V. Milanovic, H. Ali, and M. T. Aung, "Influence of distributed wind generation and load composition on voltage sags," *Generation, Transmission & Distribution, IET*, vol. 1, pp. 13-22, 2007.

[94] L. Zhang, "Three-phase unbalance of voltage dips," Licentiate thesis, Chalmers University of Technology, Dept Electric Power Engineering, Gothenburg, Sweden, 1999.

[95] P. Heine and M. Lehtonen, "Voltage sag distributions caused by power system faults," *Power Systems, IEEE Transactions on*, vol. 18, pp. 1367-1373, 2003.

[96] M. Didden, E. De Jaeger, W. D'haeseleer, and R. Belmans, "How to connect a voltage sag-measuring device: Phase to phase or phase to neutral?," *Power Delivery, IEEE Transactions on*, vol. 20, pp. 1174-1181, 2005.

[97] R. Chouhy Leborgne, G. Olguin, and M. Bollen, "The influence of pq-monitor connection on voltage dip measurements," in *2004 IEE MedPower Conference Cyprus*, 2004.

[98] E. Styvaktakis, M. H. Bollen, and I. Y. Gu, "Expert system for classification and analysis of power system events," *Power Delivery, IEEE Transactions on*, vol. 17, pp. 423-428, 2002.

[99] D. Gallo, C. Landi, and M. Luiso, "Accuracy analysis of algorithms adopted in voltage dip measurements," *Instrumentation and Measurement, IEEE Transactions on*, vol. 59, pp. 2652-2659, 2010.

[100] L. Conrad, K. Little, and C. Grigg, "Predicting and preventing problems associated with remote fault-clearing voltage dips," *Industry Applications, IEEE Transactions on*, vol. 27, pp. 167-172, 1991.

[101] P. Thakur, A. Singh, and R. Bansal, "A novel way to distinguish single phase dips through potential gradient method," *Electric Power Components and Systems*, vol. 40, pp. 336-347, 2012.

[102] M. Bollen and E. Styvaktakis, "Characterization of Three-Phase Unbalanced Dips (as easy as one-two-three?)," in *Harmonics and Quality of Power, 2000. Proceedings. Ninth International Conference on*, 2000, pp. 81-86.

[103] S. Abe, *Support Vector Machines for Pattern Classification*: Springer London, Limited, 2010.

[104] W. Freitas, Z. Huang, and W. Xu, "A practical method for assessing the effectiveness of vector surge relays for distributed generation applications," *Power Delivery, IEEE Transactions on*, vol. 20, pp. 57-63, 2005.

[105] J. C. Vieira, W. Freitas, and D. Salles, "Characteristics of voltage relays for embedded synchronous generators protection," *IET Generation, Transmission & Distribution*, vol. 1, pp. 484-491, 2007.

[106] M. R. Alam, K. Muttaqi, and A. Bouzerdoum, "An Approach for assessing the effectiveness of multiple-feature-based SVM method for islanding detection of distributed generation," *Industry Application Society, IEEE Transactions on*, vol. 50, pp. 2844-2852, 2014.

[107] R. K. Tripathy, A. Acharya, and S. K. Choudhary, "Gender Classification from ECG Signal Analysis using Least Square Support Vector Machine," *American Journal of Signal Processing,* vol. 2, pp. 145-149, 2012.
[108] P. Castello, P. Ferrari, A. Flammini, C. Muscas, and S. Rinaldi, "An IEC 61850-Compliant distributed PMU for electrical substations," in *Applied Measurements for Power Systems (AMPS), 2012 IEEE International Workshop on*, 2012, pp. 1-6.
[109] S. Samantaray, B. C. Babu, and P. Dash, "Probabilistic neural network based islanding detection in distributed generation," *Electric Power Components and Systems,* vol. 39, pp. 191-203, 2011.
[110] J. Vieira, W. Freitas, Z. Huang, W. Xu, and A. Morelato, "Formulas for predicting the dynamic performance of ROCOF relays for embedded generation applications," *IEE Proceedings-Generation, Transmission and Distribution,* vol. 153, pp. 399-406, 2006.
[111] C. L. Wadhwa, *Electrical Power Systems*: New Age International, 2005.
[112] C. Ten and P. Crossley, "Evaluation of ROCOF relay performances on networks with distributed generation," in *Developments in Power System Protection, 2008. DPSP 2008. IET 9th International Conference on*, 2008, pp. 523-528.
[113] H. E. Brown, *Solution of large networks by matrix methods*: Wiley, 1975.
[114] W. D. Stevenson, "Elements of power system analysis," 1975.
[115] J. Das, *Power system analysis: short-circuit load flow and harmonics*: CRC press, 2002.
[116] M. H. Bollen, "Fast assessment methods for voltage sags in distribution systems," *Industry Applications, IEEE Transactions on,* vol. 32, pp. 1414-1423, 1996.
[117] "IEEE 1159.2 Working Group, Test waveforms [online]. Available: grouper.ieee.org/groups/1159/2/testwave.html."
[118] E. Collett, *Polarized Light in Fiber Optics*: PolaWave Group, 2003.
[119] M. H. Bollen, P. Goossens, and A. Robert, "Assessment of voltage dips in HV-networks: deduction of complex voltages from the measured rms voltages," *Power Delivery, IEEE Transactions on,* vol. 19, pp. 783-790, 2004.
[120] *IEEE Standard for Synchrophasor Measurements for Power Systems*, IEEE Std C37.118.1-2011 (Revision of IEEE Std C37.118-2005).
[121] *IEC Communication networks and systems for power utility automation*, IEC 61850, Ed. 2, 2011.
[122] T. Carozzi, R. Karlsson, and J. Bergman, "Parameters characterizing electromagnetic wave polarization," *Physical Review E,* vol. 61, p. 2024, 2000.
[123] P. H. Moon and D. E. Spencer, *Field Theory Handbook: Including Coordinate Systems, Differential Equations, and Their Solutions/by Parry Moon and Domina Eberle Spencer*: Springer-Verlag, 1961.
[124] Y. Yang, R. Tao, and Y. Wang, "A new SINR equation based on the polarization ellipse parameters," *Antennas and Propagation, IEEE Transactions on,* vol. 53, pp. 1571-1577, 2005.
[125] A. Bagnasco, B. Delfino, G. Denegri, and S. Massucco, "Management and dynamic performances of combined cycle power plants during parallel and islanding operation," *Energy Conversion, IEEE Transactions on,* vol. 13, pp. 194-201, 1998.
[126] R. H. Lasseter and P. Paigi, "Microgrid: a conceptual solution," in *Power Electronics Specialists Conference, 2004. PESC 04. 2004 IEEE 35th Annual*, 2004, pp. 4285-4290.

[127] P. Piagi and R. H. Lasseter, "Autonomous control of microgrids," in *Power Engineering Society General Meeting, 2006. IEEE*, 2006, p. 8 pp.
[128] M. Alam, K. Muttaqi, and A. Bouzerdoum, "A Multifeature-Based Approach for Islanding Detection of DG in the Subcritical Region of Vector Surge Relays."
[129] F. C. Trindade, K. V. do Nascimento, and J. Vieira, "Investigation on voltage sags caused by DG anti-islanding protection," *IEEE transactions on power delivery*, vol. 28, pp. 972-980, 2013.
[130] F. C. Trindade, P. C. Meira, W. Freitas, and J. C. Vieira, "Control systems analysis of industrial plants with synchronous generators during islanded operation," in *Power and Energy Society General Meeting, 2010 IEEE*, 2010, pp. 1-8.
[131] M. Banejad, G. Ledwich, and M. A. Kashem, "Operation of power system islands," in *Australian Universities Power Engineering Conference (AUPEC)*, Tasmania, Australia, 25-28 Sep. 2005.

APPENDIX A

Test System

A.1 A Practical Power Network Extracted from New South Wales Electricity Networks

Test system (Fig. 3.9) data:

a) Transmission network side

Gen: Rated kV=132, V_{base}=132 kV, SC MVA=1000, f=50 Hz.

SM-1, SM-3 and SM-4: rated MVA=5, rated kV=132, V_{base}=132 kV, f=50 Hz, 2 pole pairs, H=2.9 s, X_d=2.86, $X_d^{'}$=0.7, $X_d^{''}$=0.22, X_q=2, $X_q^{''}$=0.2, $T_{d0}^{'}$=3.4, $T_{d0}^{''}$=0.01, $T_{q0}^{''}$= 0.05, R_S=0.0052.

SM-2: rated MVA=100, rated kV=132, V_{base}=132 kV, f=50 Hz, 2 pole pairs, H=10.12 s, X_d=1.25, $X_d^{'}$=0.23, $X_d^{''}$=0.12, X_q=1.22, $X_q^{''}$=0.12, $T_{d0}^{'}$=4.7, $T_{d0}^{''}$=0.06, $T_{q0}^{''}$=0.21, R_S = 0.0014.

Exciter of SM-1, SM-2, SM-3 and SM-4: T_r(s) = 0.02, K_a = 300, T_a(s) = 0.001, K_e = 1, T_e(s) = 0, K_f = 0.001, T_f(s) = 0.1, V_{RMAX}(pu) = 11.5 and V_{RMIN}(pu) = -11.5.

Equivalent inductance of Transformers:

Xfm-1 = 0.013H, Xfm-2 = 0.017H, Xfm-3 = 0.034H, Xfm-4 = 0.055H, Xfm-5 = 0.0634H, Xfm-6 = 0.055H, Xfm-7 = 0.029H, Xfm-8 = 0.057H.

b) Distribution network side:

Xfm-9: rated MVA = 100, rated kV = 132/33, *f* = 50 Hz, R_1 = 0.00375 pu, X_1 = 0.1 pu, R_m = 500 pu, X_m = 500 pu.

SG1, SG2 and SG3: rated MVA = 6, rated kV = 0.69, V_{base} = 0.69 kV, *f* = 50 Hz, 2 pole pairs, H = 1.5 s, X_d = 1.4, $X_d^{'}$ = 0.23, $X_d^{''}$ = 0.12, X_q = 1.37, $X_q^{''}$ = 0.12, $T_{d0}^{'}$ = 5.5, $T_{d0}^{''}$ = 0.05, $T_{q0}^{'}$ = 1.25, $T_{q0}^{''}$ = 0.19, R_S = 0.0014.

Exciter of SG1, SG2 and SG3: T_r(s) = 0.005, K_a = 270, T_a(s) = 0.1, K_e = 1, T_e(s) = 0.65, K_f = 0.048, T_f(s) = 0.95, V_{RMAX}(pu) = 7 and V_{RMIN}(pu) = -4.

Dxfm-1, Dxfm-2, Dxfm-3: rated MVA = 30, rated kV = 33/0.69, *f* = 50 Hz, R_1 = 0.00375 pu, X_1 = 0.1 pu, R_m = 500 pu, X_m = 500 pu.

L-1, L-2 and L-3: 1.5 MW, 0.5 MVAR; *L-4:* 13.5 MW, 2.1 MVAR;

DL-1, DL-2 and DL-3: R_0 = 0.413 Ω/km, R_1 = 0.1153 Ω/km, X_{0L} = 1.043 Ω/km, X_{1L} = 0.33 Ω/km, X_{0C} = 1.574 μΩ/km, X_{1C} = 3.6 μΩ/km, Length = 10 km.

A.2 Data of A test Distribution Network

TABLE A.2
TEST SYSTEM DATA (FIG. 5.6)

Network Elements	Parameters	Value	Network Elements	Parameters	Value
Thévenin equivalent data (*Sub*)	V_{base} (kV)	66	Loads data (L_1, L_2, L_3 ,L_4, L_5, L_6, L_7, L_8, L_9 , L_{10}, L_{11})	P_L	100 kW (each)
	Rated kV	66			
	SC MVA	1000			
	Frequency	50 Hz		Q_L	40 kVAr (each)
Transformer data	Rated kV	66/11 kV(Yg/Yg)	Distribution Transformer data	Rated kV	11/0.415(Yg /Yg)
	Rated MVA	50		Rated MVA	5
	Frequency	50 Hz		Frequency	50 Hz
	Resistance (pu)	0.00375		Resistance (pu)	0.00375
	Inductance	0.1 pu		Inductance	0.1 pu
Lines data (Z_1, Z_2, Z_3 ,Z_4, Z_5, Z_6, Z_7, Z_8, Z_9)	Resistance	0.4 Ω/km	Synchronous generator data	Frequency	50 Hz
	Inductive reactance	1.6 Ω/km		V_{base} (kV) or Rated kV	0.415
	Line Length	2 km		Rated MVA	2
Exciter of Synchronous generator	T_r (s)	0.005		Pole pairs	2
	K_a	200		H (s)	1.5
	T_a (s)	0.001		X_d (pu)	1.4
	K_e	1		X_d' (pu)	0.23
	T_e (s)	0		X_d'', X_q''	0.12
	K_f	0.001		T_{d0}' (s)	5.5
				T_{d0}'' (s)	0.05
	T_f (s)	0.1		T_{q0}' (s)	1.25
				T_{q0}'' (s)	0.19
	V_{RMAX} (pu)	7		Stator resistance	0.0014 pu
	V_{RMIN} (pu)	0		Leakage reactance	0.05 pu

A.3 Data of A test Distribution Network

TABLE A.3
TEST SYSTEM DATA (FIG. 6.8)

Network Elements	Parameters	Value	Network Elements	Parameters	Value
Thévenin equivalent data (*Sub*)	V_{base} (kV)	132	Loads data (L-1, L-2, L-3,L-4)	P_L	3 MW
	Rated kV	132		Q_L	0.5 MVAr
	SC MVA	1000	Loads data (L-5, L-6)	P_L	6 MW
	Frequency	50 Hz		Q_L	1.4 MVAr
Transformer data (*Xfm-1*)	Rated kV	132/33 (Δ/Yg)	Transformers data (*Dxfm-1, Dxfm-2, Dxfm-3, Dxfm-4*)	Rated kV	33/0.69 (Δ/Yg)
	Rated MVA	100		Rated MVA	30
	Frequency	50 Hz		Frequency	50 Hz
	Resistance (pu)	0.00375		Resistance (pu)	0.00375
	Inductance	0.1 pu		Inductance	0.1 pu
Lines data (*DL-1, DL-2, DL-3, DL-4, DL-5*)	Resistance	0.4 Ω/km	Synchronous generator data *(SG1, SG2, SG3, and SG4)*	Frequency	50 Hz
	Inductive reactance	1.6 Ω/km		V_{base} (kV) or Rated kV	0.69
	Line Length	10 km		Rated MVA	6
Exciter of *SG1, SG2, SG3,* and *SG4*	T_r (s)	0.005		Pole pairs	2
	K_a	200		H (s)	1.5
	T_a (s)	0.001		X_d (pu)	1.4
	K_e	1		X_d' (pu)	0.23
	T_e (s)	0		X_d'', X_q''	0.12
	K_f	0.001		T_{d0}' (s)	5.5
				T_{d0}'' (s)	0.05
	T_f (s)	0.1		T_{q0}' (s)	1.25
				T_{q0}'' (s)	0.19
	V_{RMAX} (pu)	7		Stator resistance	0.0014 pu
	V_{RMIN} (pu)	0		Leakage reactance	0.05 pu

A.4 A Practical Distribution Network Extracted from New South Wales Electricity Networks

TABLE A.4.1
LOADS OF THE SYSTEM OF FIG. 6.10

Load bus	P (kW)	Q (kVAR)
1	60	15
2	100	25
3	70	20
4	100	10
6	50	35
7	100	20
8	70	20
9	100	15
10	60	20
17	100	20
21	50	15
23	100	25
24	60	15
26	100	25
27	70	20
28	100	10
31	60	35
32	70	20
33	60	20
34	75	15
35	60	20
36	70	20
37	60	15
38	70	25
39	60	15
40	70	25
41	45	20
42	60	10
43	40	35
44	60	20
45	40	20
46	60	15
47	40	20
49	70	20
50	40	15
51	60	25
52	40	15
53	85	25
54	75	20
56	80	10
57	75	35
58	80	20
59	100	20
60	70	15
61	90	20
62	60	20
63	185	15
64	80	25
65	185	15
66	60	25
69	185	20
72	90	10

TABLE A.4.2
IMPEDANCE DATA OF THE SYSTEM OF FIG. 6.10

From node	To node	Resistance (Ω)	Reactance (Ω)
PCC	1	0.028	0.090862
1	3	2.099	2.8944
3	5	7.830	5.1479
5	8	5.858	5.8750
5	44	15.210	5.6598
44	45	8.692	3.2342
44	47	4.356	4.2253
45	46	2.143	1.6650
47	48	13.011	4.5424
48	66	5.060	1.5377
48	49	2.345	0.9425
66	67	3.250	0.7540
67	68	10.035	7.3511
8	51	13.286	1.5112
51	54	8.048	2.0266
51	53	8.007	0.2795
8	9	5.141	3.3802
10	11	1.377	0.9054
11	12	4.459	2.9318
11	65	17.680	7.5998
12	64	11.801	7.6172
12	13	6.086	4.0010
13	43	10.428	4.6708
13	14	6.086	4.0010
14	62	11.451	2.2981
14	15	4.066	2.6731
15	40	12.535	5.1364
15	16	3.948	1.4262
16	36	2.472	0.9312
16	17	8.958	5.8895
18	19	3.896	0.4964
19	24	13.410	9.0760
19	32	11.546	4.6708
19	60	8.057	4.0010
19	29	5.039	2.2981
29	57	4.056	1.4244
20	70	6.046	2.6263
22	72	3.066	1.0807

A.5 Data of A test Distribution Network

TABLE A.5
TEST SYSTEM DATA (FIG. 4.5)

Network Elements	Parameters	Value
Thévenin equivalent data (*Sub*)	V_{base} (kV) or rated kV	132
	SC MVA	1000
	Frequency	50 Hz
Transformer data (*Connected between Bus 1 and Bus 2*)	Rated kV	132/33 (Δ/Y_g)
	Rated MVA	100
	Frequency	50 Hz
	Resistance (pu)	0.00375
	Inductance	0.1 pu
Lines data (*DL-1, DL-2*)	Resistance	0.4 Ω/km
	Inductive reactance	1.6 Ω/km
	Line Length	10 km
Exciter of Synchronous generator	T_r (s)	0.005
	K_a	200
	T_a (s)	0.001
	K_e	1
	T_e (s)	0
	K_f	0.001
	T_f (s)	0.1
	V_{RMAX} (pu)	7
	V_{RMIN} (pu)	0
Transformer data (*Connected at Bus 5*)	Rated kV	33/0.69 (Δ/Yg)
	Rated MVA	30
	Frequency	50 Hz
	Resistance (pu)	0.00375
	Inductance	0.1 pu
Synchronous generator data	Frequency	50 Hz
	Vbase (kV) or Rated kV	0.69
	Rated MVA	30
	Pole pairs	2
	H (s)	1.5
	X_d (pu)	1.4
	$X_d^{'}$ (pu)	0.23
	$X_d^{''}$, $X_q^{''}$	0.12
	$T_{d0}^{'}$ (s)	5.5
	$T_{d0}^{''}$ (s)	0.05
	$T_{q0}^{'}$ (s)	1.25
	$T_{q0}^{''}$ (s)	0.19
	Stator resistance	0.0014 pu
	Leakage reactance	0.05 pu

APPENDIX B

Three-phase Voltage-ellipse Parameters under Voltage Dips and Swells

B.1 Formulation of 3-phase Voltage-ellipse parameters under Voltage Dips/Sags

Theoretical value of 3-phase Voltage-ellipse parameters under different types of sags are obtained as follows

1) A-sag:

Phase-voltage magnitudes: $|\boldsymbol{V}_a|=V_f$, $|\boldsymbol{V}_b|=|\boldsymbol{V}_c|=V$ for $V>V_f$

From (6.6), $\vec{E}(t)=\frac{1}{3}\left[\left(V_f+2V\right)e^{j\omega t}+\left(V_f+Ve^{j\frac{4\pi}{3}}+Ve^{j\frac{8\pi}{3}}\right)e^{-j\omega t}\right]$

From (6.7), $|E^+|=\frac{1}{3}\left(V_f+2V\right),\ \psi^+=0,|E^-|=\frac{1}{3}\left(V-V_f\right),\ \psi^-=\pi$

Thus, from (6.8), (6.9) and (6.10) $A_{ma}=V,\ A_{mi}=(2V_f+V)/3$, $\psi=\pi/2$

2) B-sag:

Phase-voltage magnitudes: $|\boldsymbol{V}_b|=V_f$, $|\boldsymbol{V}_a|=|\boldsymbol{V}_c|=V$ for $V>V_f$

From (6.6), $\vec{E}(t)=\frac{1}{3}\left[\left(V_f+2V\right)e^{j\omega t}+\left(V+V_fe^{j\frac{4\pi}{3}}+Ve^{j\frac{8\pi}{3}}\right)e^{-j\omega t}\right]$

From (6.7), $|E^+|=\frac{1}{3}\left(V_f+2V\right),\ \psi^+=0,|E^-|=\frac{1}{3}\left(V-V_f\right),\ \psi^-=\pi/3$

Thus, from (6.8), (6.9) and (6.10) $A_{ma}=V,\ A_{mi}=(2V_f+V)/3$, $\psi=\pi/6$

3) C-sag:

Phase-voltage magnitudes: $|\boldsymbol{V}_c|=V_f$, $|\boldsymbol{V}_a|=|\boldsymbol{V}_b|=V$ for $V>V_f$

From (6.6), $\vec{E}(t)=\frac{1}{3}\left[\left(V_f+2V\right)e^{j\omega t}+\left(V+Ve^{j\frac{4\pi}{3}}+V_fe^{j\frac{8\pi}{3}}\right)e^{-j\omega t}\right]$

From (6.7), $|E^+|=\frac{1}{3}\left(V_f+2V\right),\ \psi^+=0,|E^-|=\frac{1}{3}\left(V-V_f\right),\ \psi^-=5\pi/3$

Thus, from (6.8), (6.9) and (6.10) $A_{ma}=V,\ A_{mi}=(2V_f+V)/3$, $\psi=5\pi/6$

4) AB-sag:

Phase-voltage magnitudes: $|\boldsymbol{V}_c|=V$, $|\boldsymbol{V}_a|=|\boldsymbol{V}_b|=V_f$ for $V>V_f$

From (6.6), $\vec{E}(t)=\frac{1}{3}\left[(2V_f+V)e^{j\omega t}+\left(V_f+V_f e^{j\frac{4\pi}{3}}+Ve^{j\frac{8\pi}{3}}\right)e^{-j\omega t}\right]$

From (6.7), $|E^+|=\frac{1}{3}(2V_f+V)$, $\psi^+=0$, $|E^-|=\frac{1}{3}(V-V_f)$, $\psi^-=2\pi/3$

Thus, from (6.8), (6.9) and (6.10) $A_{ma}=(V_f+2V)/3$, $A_{mi}=V_f$, $\psi=\pi/3$

5) BC-sag:

Phase-voltage magnitudes: $|\boldsymbol{V}_a|=V$, $|\boldsymbol{V}_b|=|\boldsymbol{V}_c|=V_f$ for $V>V_f$

From (6.6), $\vec{E}(t)=\frac{1}{3}\left[(2V_f+V)e^{j\omega t}+\left(V+V_f e^{j\frac{4\pi}{3}}+V_f e^{j\frac{8\pi}{3}}\right)e^{-j\omega t}\right]$

From (6.7), $|E^+|=\frac{1}{3}(2V_f+V)$, $\psi^+=0$, $|E^-|=\frac{1}{3}(V-V_f)$, $\psi^-=0$

Thus, from (6.8), (6.9) and (6.10) $A_{ma}=(V_f+2V)/3$, $A_{mi}=V_f$, $\psi=0$

6) CA-sag:

Phase-voltage magnitudes: $|\boldsymbol{V}_b|=V$, $|\boldsymbol{V}_a|=|\boldsymbol{V}_c|=V_f$ for $V>V_f$

From (6.6), $\vec{E}(t)=\frac{1}{3}\left[(2V_f+V)e^{j\omega t}+\left(V_f+Ve^{j\frac{4\pi}{3}}+V_f e^{j\frac{8\pi}{3}}\right)e^{-j\omega t}\right]$

From (6.7), $|E^+|=\frac{1}{3}(2V_f+V)$, $\psi^+=0$, $|E^-|=\frac{1}{3}(V-V_f)$, $\psi^-=4\pi/3$

Thus, from (6.8), (6.9) and (6.10) $A_{ma}=(V_f+2V)/3$, $A_{mi}=V_f$, $\psi=2\pi/3$

7) ABC-sag:

Phase-voltage magnitudes: $|\boldsymbol{V}_a|=|\boldsymbol{V}_b|=|\boldsymbol{V}_c|=V_f$ for $V>V_f$

From (6.6), $\vec{E}(t)=\left[V_f\, e^{j\omega t}+0.e^{-j\omega t}\right]$; from (6.7), $|E^+|=V_f$, $|E^-|=0$

Thus, from (6.8) and (6.9) $A_{ma}=V_f$, $A_{mi}=V_f$

B.2 Formulation of 3-phase Voltage-ellipse parameters under Voltage Swells

Theoretical value of 3-phase Voltage-ellipse parameters under different types of swells are obtained as follows

1) A-swell:

Phase-voltage magnitudes: $|\boldsymbol{V}_a|=V_f$, $|\boldsymbol{V}_b|=|\boldsymbol{V}_c|=V$ for $V_f > V$

From (6.6), $\vec{E}(t)=\frac{1}{3}\left[\left(2V+V_f\right)e^{j\omega t}+\left(V_f+Ve^{j\frac{4\pi}{3}}+Ve^{j\frac{8\pi}{3}}\right)e^{-j\omega t}\right]$

From (6.7), $|E^+|=\frac{1}{3}\left(2V+V_f\right)$, $\psi^+=0$, $|E^-|=\frac{1}{3}\left(V_f-V\right)$, $\psi^-=0$

Thus, from (6.8), (6.9) and (6.10) $A_{ma}=(V+2V_f)/3$, $A_{mi}=V$, $\psi=0$

2) B-swell:

Phase-voltage magnitudes: $|\boldsymbol{V}_b|=V_f$, $|\boldsymbol{V}_a|=|\boldsymbol{V}_c|=V$ for $V_f > V$

From (6.6), $\vec{E}(t)=\frac{1}{3}\left[\left(2V+V_f\right)e^{j\omega t}+\left(V+V_fe^{j\frac{4\pi}{3}}+Ve^{j\frac{8\pi}{3}}\right)e^{-j\omega t}\right]$

From (6.7), $|E^+|=\frac{1}{3}\left(2V+V_f\right)$, $\psi^+=0$, $|E^-|=\frac{1}{3}\left(V_f-V\right)$, $\psi^-=4\pi/3$

Thus, from (6.8), (6.9) and (6.10) $A_{ma}=(V+2V_f)/3$, $A_{mi}=V$, $\psi=2\pi/3$

3) C-swell:

Phase-voltage magnitudes: $|\boldsymbol{V}_c|=V_f$, $|\boldsymbol{V}_a|=|\boldsymbol{V}_b|=V$ for $V_f > V$

From (6.6), $\vec{E}(t)=\frac{1}{3}\left[\left(2V+V_f\right)e^{j\omega t}+\left(V+Ve^{j\frac{4\pi}{3}}+V_fe^{j\frac{8\pi}{3}}\right)e^{-j\omega t}\right]$

From (6.7), $|E^+|=\frac{1}{3}\left(2V+V_f\right)$, $\psi^+=0$, $|E^-|=\frac{1}{3}\left(V_f-V\right)$, $\psi^-=2\pi/3$

Thus, from (6.8), (6.9) and (6.10) $A_{ma}=(V+2V_f)/3$, $A_{mi}=V$, $\psi=\pi/3$

4) AB-swell:

Phase-voltage magnitudes: $|\boldsymbol{V}_c|=V$, $|\boldsymbol{V}_a|=|\boldsymbol{V}_b|=V_f$ for $V_f > V$

From (6.6), $\vec{E}(t)=\frac{1}{3}\left[\left(V+2V_f\right)e^{j\omega t}+\left(V_f+V_fe^{j\frac{4\pi}{3}}+Ve^{j\frac{8\pi}{3}}\right)e^{-j\omega t}\right]$

From (6.7), $|E^+|=\frac{1}{3}(V+2V_f)$, $\psi^+=0$, $|E^-|=\frac{1}{3}(V_f-V)$, $\psi^-=5\pi/3$

Thus, from (6.8), (6.9) and (6.10) $A_{ma}=V_f$, $A_{mi}=(2V+V_f)/3$, $\psi=5\pi/6$

5) BC-swell:

Phase-voltage magnitudes: $|\boldsymbol{V}_a|=V$, $|\boldsymbol{V}_b|=|\boldsymbol{V}_c|=V_f$ for $V_f>V$

From (6.6), $\vec{E}(t)=\frac{1}{3}\left[(2V_f+V)e^{j\omega t}+\left(V+V_f e^{j\frac{4\pi}{3}}+V_f e^{j\frac{8\pi}{3}}\right)e^{-j\omega t}\right]$

From (6.7), $|E^+|=\frac{1}{3}(2V_f+V)$, $\psi^+=0$, $|E^-|=\frac{1}{3}(V_f-V)$, $\psi^-=\pi$

Thus, from (6.8), (6.9) and (6.10) $A_{ma}=V_f$, $A_{mi}=(2V+2V_f)/3$, $\psi=\pi/2$

6) CA-swell:

Phase-voltage magnitudes: $|\boldsymbol{V}_b|=V$, $|\boldsymbol{V}_a|=|\boldsymbol{V}_c|=V_f$ for $V_f>V$

From (6.6), $\vec{E}(t)=\frac{1}{3}\left[(V+2V_f)e^{j\omega t}+\left(V_f+Ve^{j\frac{4\pi}{3}}+V_f e^{j\frac{8\pi}{3}}\right)e^{-j\omega t}\right]$

From (6.7), $|E^+|=\frac{1}{3}(V+2V_f)$, $\psi^+=0$, $|E^-|=\frac{1}{3}(V_f-V)$, $\psi^-=\pi/3$

Thus, from (6.8), (6.9) and (6.10) $A_{ma}=V_f$, $A_{mi}=(2V+V_f)/3$, $\psi=\pi/6$

APPENDIX C

Formulation of Polarization Ellipse parameters, elevation angle (θ) and azimuthal angle (φ), under different types of Voltage dips

Seven types (A, B, D, F, E, C, and G) of voltage dips comprise 19 groups of dips. The phasor diagram representing these 19 groups of dips are illustrated in Fig. C.1, where dip-depth is denoted by *d* and three phase voltages before and during the occurrence of dip is represented by dotted and solid arrow line, respectively.

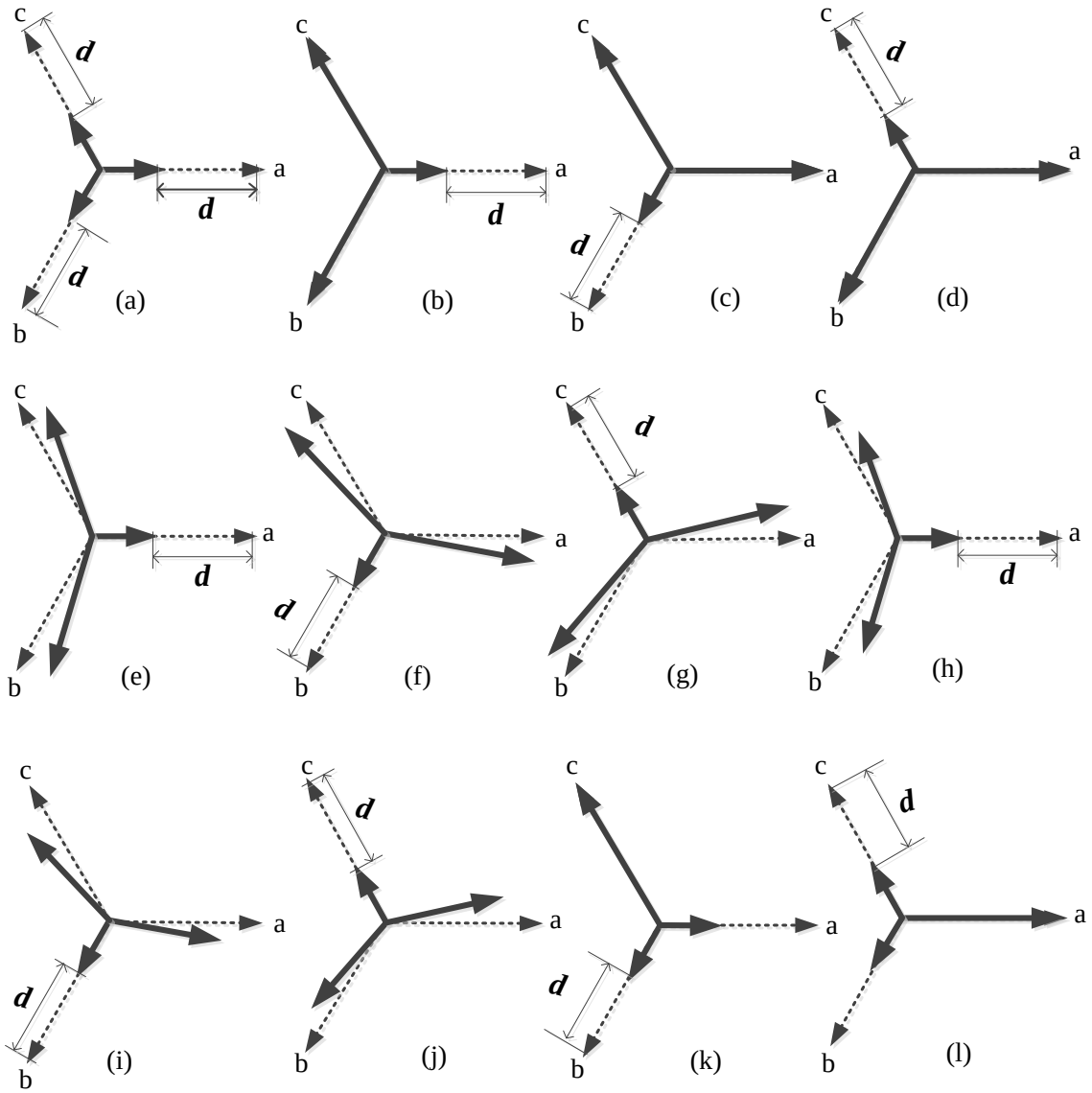

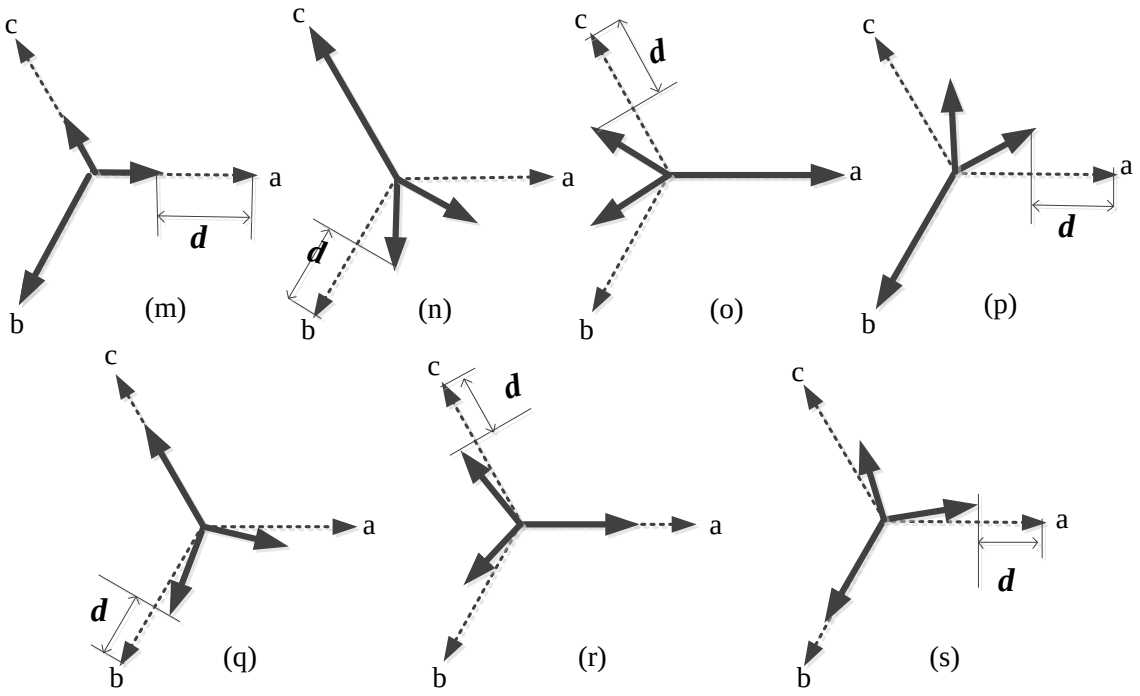

Fig. C.1. Phasor diagram representing 19 groups of dips: (a) A-type, (b) *a*_dip_B, (c) *b*_dip_B, (d) *c*_dip_B, (e) *a*_dip_D, (f) *b*_dip_D, (g) *c*_dip_D, (h) *a*_dip_F, (i) *b*_dip_F, (j) *c*_dip_F, (k) *ab*_dip_E, (l) *bc*_dip_E, (m) *ca*_dip_E, (n) *ab*_dip_C, (o) *bc*_dip_C, (p) *ca*_dip_C, (q) *ab*_dip_G, (r) *bc*_dip_G, and (s) *ca*_dip_G.

For the formulation of θ and φ, the projected voltage magnitudes on a-axis, b-axis and c-axis, are considered. The a-, b- and c-axes are separated by 120°, where $\alpha_a = 0°$, $\alpha_b = 240°$, and $\alpha_c = 120°$. Fig. 7.4 illustrates the procedure of extracting the projected voltage phasors, denoted as V_{a_in}, V_{b_in} and V_{c_in}, using Eqs. 7.10(a)–(c). Then, magnitude of the projected phasors, i.e., $|V_{a\_in}|$, $|V_{b\_in}|$ and $|V_{c\_in}|$ are mapped onto three perpendicular axes of an XYZ Cartesian co-ordinate system; θ and φ are obtained from the polarized plane in 3D co-ordinates using Eqs. (7.3)–(7.4).

1) *a*_dip_B

3-phase voltage phasors

$$\boldsymbol{V_a} = (1-d);\ \boldsymbol{V_b} = -0.5\left(1+\mathrm{j}\sqrt{3}\right);\ \boldsymbol{V_c} = -0.5\left(1-\mathrm{j}\sqrt{3}\right)$$

$$\left|\boldsymbol{V_{a\_in}}\right| = 1-d;\ \left|\boldsymbol{V_{b\_in}}\right| = \left|\boldsymbol{V_{c\_in}}\right| = 1$$

X, Y and Z component of normal vector U to the polarized plane:

$$\boldsymbol{U_X} = -2\left|\boldsymbol{V_{b\_in}}\right|\left|\boldsymbol{V_{c\_in}}\right|\sin(\alpha_b - \alpha_c) = -\sqrt{3}$$

$$\boldsymbol{U_Y} = -2\left|\boldsymbol{V_{c\_in}}\right|\left|\boldsymbol{V_{a\_in}}\right|\sin(\alpha_c - \alpha_a) = -\sqrt{3}(1-d)$$

$$\boldsymbol{U}_Z = -2\left|\boldsymbol{V}_{a\_in}\right|\left|\boldsymbol{V}_{b\_in}\right|\sin(\alpha_a - \alpha_b) = -\sqrt{3}(1-d)$$

Thus, the elevation (θ) and azimuthal (φ) angles are obtained as

$$\theta = \text{angle}\left(\boldsymbol{U}_z + \boldsymbol{j}\sqrt{\boldsymbol{U}_x^2 + \boldsymbol{U}_y^2}\right) = \text{angle}\left\{-\sqrt{3}(1-d) + j\sqrt{3}\sqrt{1+(1-d)^2}\right\} = \pi - \arctan\left(\frac{\sqrt{1+(1-d)^2}}{1-d}\right)$$

$$\varphi = \text{angle}\left(\boldsymbol{U}_x + \boldsymbol{j}\boldsymbol{U}_y\right) = \text{angle}\left\{-\sqrt{3} - j\sqrt{3}(1-d)\right\} = -\pi + \arctan(1-d)$$

2) *b*_dip_B

3-phase voltage phasors

$$\boldsymbol{V}_a = 1,\ \boldsymbol{V}_b = -0.5\left(1 + \text{j}\sqrt{3}\right)(1-d),\ \boldsymbol{V}_c = -0.5\left(1 - \text{j}\sqrt{3}\right)$$

$$\left|\boldsymbol{V}_{b\_in}\right| = 1-d;\ \left|\boldsymbol{V}_{a\_in}\right| = \left|\boldsymbol{V}_{c\_in}\right| = 1$$

X, Y and Z component of normal vector *U* to the polarized plane:

$$\boldsymbol{U}_X = -2\left|\boldsymbol{V}_{b\_in}\right|\left|\boldsymbol{V}_{c\_in}\right|\sin(\alpha_b - \alpha_c) = -\sqrt{3}(1-d)$$

$$\boldsymbol{U}_Y = -2\left|\boldsymbol{V}_{c\_in}\right|\left|\boldsymbol{V}_{a\_in}\right|\sin(\alpha_c - \alpha_a) = -\sqrt{3}$$

$$\boldsymbol{U}_Z = -2\left|\boldsymbol{V}_{a\_in}\right|\left|\boldsymbol{V}_{b\_in}\right|\sin(\alpha_a - \alpha_b) = -\sqrt{3}(1-d)$$

Thus, the elevation (θ) and azimuthal (φ) angles are obtained as

$$\theta = \text{angle}\left(\boldsymbol{U}_z + \boldsymbol{j}\sqrt{\boldsymbol{U}_x^2 + \boldsymbol{U}_y^2}\right) = \text{angle}\left\{-\sqrt{3}(1-d) + j\sqrt{3}\sqrt{1+(1-d)^2}\right\} = \pi - \arctan\left(\frac{\sqrt{1+(1-d)^2}}{1-d}\right)$$

$$\varphi = \text{angle}\left(\boldsymbol{U}_x + \boldsymbol{j}\boldsymbol{U}_y\right) = \text{angle}\left\{-\sqrt{3}(1-d) - j\sqrt{3}\right\} = -\pi + \arctan\left(\frac{1}{1-d}\right)$$

3) *c*_dip_B

3-phase voltage phasors

$$\boldsymbol{V}_a = 1,\ \boldsymbol{V}_b = -0.5\left(1 + \text{j}\sqrt{3}\right),\ \boldsymbol{V}_c = -0.5\left(1 - \text{j}\sqrt{3}\right)(1-d)$$

$$\left|\boldsymbol{V}_{c\_in}\right| = 1-d;\ \left|\boldsymbol{V}_{a\_in}\right| = \left|\boldsymbol{V}_{b\_in}\right| = 1$$

X, Y and Z component of normal vector *U* to the polarized plane:

$$\boldsymbol{U}_X = -2\left|\boldsymbol{V}_{b\_in}\right|\left|\boldsymbol{V}_{c\_in}\right|\sin(\alpha_b - \alpha_c) = -\sqrt{3}(1-d)$$

$$\boldsymbol{U}_Y = -2\left|\boldsymbol{V}_{c\_in}\right|\left|\boldsymbol{V}_{a\_in}\right|\sin(\alpha_c - \alpha_a) = -\sqrt{3}(1-d)$$

$$\boldsymbol{U}_Z = -2\left|\boldsymbol{V}_{a\_in}\right|\left|\boldsymbol{V}_{b\_in}\right|\sin(\alpha_a - \alpha_b) = -\sqrt{3}$$

Thus, the elevation (θ) and azimuthal (φ) angles are obtained as

$$\theta = \text{angle}\left(\boldsymbol{U}_z + \boldsymbol{j}\sqrt{\boldsymbol{U}_x^2 + \boldsymbol{U}_y^2}\right) = \text{angle}\left\{-\sqrt{3} + j\sqrt{3}\sqrt{2}(1-d)\right\} = \pi - \arctan\left(\sqrt{2} - \sqrt{2}d\right)$$

$$\varphi = \text{angle}\left(\boldsymbol{U}_x + \boldsymbol{j}\boldsymbol{U}_y\right) = \text{angle}\left\{-\sqrt{3}(1-d) - j\sqrt{3}(1-d)\right\} = -3\pi/4$$

4) *a*_dip_D

3-phase voltage phasors

$$\boldsymbol{V}_a = 1-d,\ \boldsymbol{V}_b = -0.5(1-d) - \mathrm{j}\frac{\sqrt{3}}{2},\ \boldsymbol{V}_c = -0.5(1-d) + \mathrm{j}\frac{\sqrt{3}}{2}$$

$$\left|\boldsymbol{V}_{a\_in}\right| = 1-d;$$

$$\left|\boldsymbol{V}_{b\_in}\right| = \left|\boldsymbol{V}_b\right|\cos\left(\pi/3 - \tan^{-1}\left(\frac{\sqrt{3}}{1-d}\right)\right) = \left(\frac{1}{2}\sqrt{3+(1-d)^2}\right)\left(\frac{1}{2}\frac{4-d}{\sqrt{3+(1-d)^2}}\right) = 1-0.25d;$$

$$\left|\boldsymbol{V}_{c\_in}\right| = \left|\boldsymbol{V}_c\right|\cos\left(\pi/3 - \tan^{-1}\left(\frac{\sqrt{3}}{1-d}\right)\right) = \left(\frac{1}{2}\sqrt{3+(1-d)^2}\right)\left(\frac{1}{2}\frac{4-d}{\sqrt{3+(1-d)^2}}\right) = 1-0.25d;$$

X, Y and Z component of normal vector *U* to the polarized plane:

$$\boldsymbol{U}_X = -2\left|\boldsymbol{V}_{b\_in}\right|\left|\boldsymbol{V}_{c\_in}\right|\sin(\alpha_b - \alpha_c) = -\sqrt{3}(1-0.25d)^2$$

$$\boldsymbol{U}_Y = -2\left|\boldsymbol{V}_{c\_in}\right|\left|\boldsymbol{V}_{a\_in}\right|\sin(\alpha_c - \alpha_a) = -\sqrt{3}(1-0.25d)(1-d)$$

$$\boldsymbol{U}_Z = -2\left|\boldsymbol{V}_{a\_in}\right|\left|\boldsymbol{V}_{b\_in}\right|\sin(\alpha_a - \alpha_b) = -\sqrt{3}(1-0.25d)(1-d)$$

$$\theta = \mathrm{angle}\left(\boldsymbol{U}_z + \boldsymbol{j}\sqrt{\boldsymbol{U}_x^2 + \boldsymbol{U}_y^2}\right) = \pi - \arctan\left(\frac{\sqrt{(1-d)^2 + (1-0.25d)^2}}{1-d}\right) = \pi - \arctan\left(\frac{\sqrt{32-40d+17d^2}}{4(1-d)}\right)$$

$$\varphi = \mathrm{angle}\left(\boldsymbol{U}_x + \boldsymbol{j}\boldsymbol{U}_y\right) = \mathrm{angle}\left\{-\sqrt{3}(1-0.25d)^2 - j\sqrt{3}(1-0.25d)(1-d)\right\} = -\pi + \arctan\left(\frac{4-4d}{4-d}\right)$$

5) *b*_dip_D

Following the formulation procedure as presented for *a*_dip_D, the projected voltage magnitudes of 3-phase voltages for *b*_dip_D are obtained as

$$\left|\boldsymbol{V}_{b\_in}\right| = 1-d;\ \left|\boldsymbol{V}_{a\_in}\right| = \left|\boldsymbol{V}_{c\_in}\right| = 1-0.25d;$$

X, Y and Z component of normal vector *U* to the polarized plane:

$$\boldsymbol{U}_X = -2\left|\boldsymbol{V}_{b\_in}\right|\left|\boldsymbol{V}_{c\_in}\right|\sin(\alpha_b - \alpha_c) = -\sqrt{3}(1-0.25d)(1-d)$$

$$\boldsymbol{U}_Y = -2\left|\boldsymbol{V}_{c\_in}\right|\left|\boldsymbol{V}_{a\_in}\right|\sin(\alpha_c - \alpha_a) = -\sqrt{3}(1-0.25d)^2$$

$$\boldsymbol{U}_Z = -2\left|\boldsymbol{V}_{a\_in}\right|\left|\boldsymbol{V}_{b\_in}\right|\sin(\alpha_a - \alpha_b) = -\sqrt{3}(1-0.25d)(1-d)$$

$$\theta = \mathrm{angle}\left(\boldsymbol{U}_z + \boldsymbol{j}\sqrt{\boldsymbol{U}_x^2 + \boldsymbol{U}_y^2}\right) = \pi - \arctan\left(\frac{\sqrt{(1-d)^2 + (1-0.25d)^2}}{1-d}\right) = \pi - \arctan\left(\frac{\sqrt{32-40d+17d^2}}{4(1-d)}\right)$$

$$\varphi = \mathrm{angle}\left(\boldsymbol{U}_x + \boldsymbol{j}\boldsymbol{U}_y\right) = \mathrm{angle}\left\{-\sqrt{3}(1-0.25d)(1-d) - j\sqrt{3}(1-0.25d)^2\right\} = -\pi + \arctan\left(\frac{4-d}{4-4d}\right)$$

6) *c*_dip_D

Following the formulation procedure as presented for *a*_dip_D, the projected voltage magnitudes of 3-phase voltages for *c*_dip_D are obtained as

$$\left|\boldsymbol{V}_{c\_in}\right| = 1-d;\ \left|\boldsymbol{V}_{a\_in}\right| = \left|\boldsymbol{V}_{b\_in}\right| = 1-0.25d;$$

X, Y and Z component of normal vector *U* to the polarized plane:

$$\boldsymbol{U}_X = -2\left|\boldsymbol{V}_{b\_in}\right|\left|\boldsymbol{V}_{c\_in}\right|\sin(\alpha_b - \alpha_c) = -\sqrt{3}(1-0.25d)(1-d)$$

$$\boldsymbol{U}_Y = -2\left|\boldsymbol{V}_{c\_in}\right|\left|\boldsymbol{V}_{a\_in}\right|\sin(\alpha_c-\alpha_a)=-\sqrt{3}(1-0.25d)(1-d)$$

$$\boldsymbol{U}_Z = -2\left|\boldsymbol{V}_{a\_in}\right|\left|\boldsymbol{V}_{b\_in}\right|\sin(\alpha_a-\alpha_b)=-\sqrt{3}(1-0.25d)^2$$

$$\theta=\text{angle}\left(\boldsymbol{U}_z+\boldsymbol{j}\sqrt{\boldsymbol{U}_x^2+\boldsymbol{U}_y^2}\right)=\pi-\arctan\left(\frac{(1-d)\sqrt{2}}{1-0.25d}\right)=\pi-\arctan\left(\frac{4\sqrt{2}(1-d)}{4-d}\right)$$

$$\varphi=\text{angle}\left(\boldsymbol{U}_x+\boldsymbol{j}\boldsymbol{U}_y\right)=\text{angle}\left\{-\sqrt{3}(1-0.25d)(1-d)-j\sqrt{3}(1-0.25d)(1-d)\right\}=-3\pi/4$$

7) *a*_dip_F

3-phase voltage phasors

$$\boldsymbol{V}_a=1-d,\ \boldsymbol{V}_b=-0.5(1-d)-\text{j}\frac{\sqrt{3}}{6}(3-d),\ \boldsymbol{V}_c=-0.5(1-d)+\text{j}\frac{\sqrt{3}}{6}(3-d)$$

$$\left|\boldsymbol{V}_{a\_in}\right|=1-d;$$

$$\left|\boldsymbol{V}_{b\_in}\right|=\left|\boldsymbol{V}_b\right|\cos\left(\pi/3-\tan^{-1}\left(\frac{3-d}{\sqrt{3}-\sqrt{3}d}\right)\right)=\left(\frac{\sqrt{d^2-3d+3}}{\sqrt{3}}\right)\left(\frac{\sqrt{3}(2-d)}{2\sqrt{d^2-3d+3}}\right)=1-0.5d;$$

$$\left|\boldsymbol{V}_{c\_in}\right|=\left|\boldsymbol{V}_c\right|\cos\left(\pi/3-\tan^{-1}\left(\frac{3-d}{\sqrt{3}-\sqrt{3}d}\right)\right)=\left(\frac{\sqrt{d^2-3d+3}}{\sqrt{3}}\right)\left(\frac{\sqrt{3}(2-d)}{2\sqrt{d^2-3d+3}}\right)=1-0.5d;$$

X, Y and Z component of normal vector *U* to the polarized plane:

$$\boldsymbol{U}_X = -2\left|\boldsymbol{V}_{b\_in}\right|\left|\boldsymbol{V}_{c\_in}\right|\sin(\alpha_b-\alpha_c)=-\sqrt{3}(1-0.5d)^2$$

$$\boldsymbol{U}_Y = -2\left|\boldsymbol{V}_{c\_in}\right|\left|\boldsymbol{V}_{a\_in}\right|\sin(\alpha_c-\alpha_a)=-\sqrt{3}(1-0.5d)(1-d)$$

$$\boldsymbol{U}_Z = -2\left|\boldsymbol{V}_{a\_in}\right|\left|\boldsymbol{V}_{b\_in}\right|\sin(\alpha_a-\alpha_b)=-\sqrt{3}(1-0.5d)(1-d)$$

$$\theta=\text{angle}\left(\boldsymbol{U}_z+\boldsymbol{j}\sqrt{\boldsymbol{U}_x^2+\boldsymbol{U}_y^2}\right)=\pi-\arctan\left(\frac{\sqrt{8-12d+5d^2}}{2(1-d)}\right)$$

$$\varphi=\text{angle}\left(\boldsymbol{U}_x+\boldsymbol{j}\boldsymbol{U}_y\right)=\text{angle}\left\{-\sqrt{3}(1-0.5d)^2-j\sqrt{3}(1-0.5d)(1-d)\right\}=-\pi+\arctan\left(\frac{2-2d}{2-d}\right)$$

8) *b*_dip_F

Following the formulation procedure as presented for *a*_dip_F, the projected voltage magnitudes of 3-phase voltages for *b*_dip_F are obtained as

$$\left|\boldsymbol{V}_{b\_in}\right|=1-d;\ \left|\boldsymbol{V}_{a\_in}\right|=\left|\boldsymbol{V}_{c\_in}\right|=1-0.5d;$$

X, Y and Z component of normal vector *U* to the polarized plane is obtained as

$$\boldsymbol{U}_X = -\sqrt{3}(1-0.5d)(1-d)=\boldsymbol{U}_Z;\ \ \boldsymbol{U}_Y = -\sqrt{3}(1-0.5d)^2$$

$$\theta=\text{angle}\left(\boldsymbol{U}_z+\boldsymbol{j}\sqrt{\boldsymbol{U}_x^2+\boldsymbol{U}_y^2}\right)=\pi-\arctan\left(\frac{\sqrt{8-12d+5d^2}}{2(1-d)}\right)$$

$$\varphi=\text{angle}\left(\boldsymbol{U}_x+\boldsymbol{j}\boldsymbol{U}_y\right)=\text{angle}\left\{-\sqrt{3}(1-0.5d)(1-d)-j\sqrt{3}(1-0.5d)^2\right\}=-\pi+\arctan\left(\frac{2-d}{2-2d}\right)$$

9) *c*_dip_F

Following the formulation procedure as presented for *a*_dip_F, the projected voltage magnitudes of 3-phase voltages for *c*_dip_F are obtained as

$$|\boldsymbol{V}_{c\_in}| = 1-d;\ |\boldsymbol{V}_{a\_in}| = |\boldsymbol{V}_{b\_in}| = 1-0.5d;$$

X, Y and Z component of normal vector *U* to the polarized plane is obtained as

$$\boldsymbol{U}_X = -\sqrt{3}(1-0.5d)(1-d) = \boldsymbol{U}_Y;\ \ \boldsymbol{U}_Z = -\sqrt{3}(1-0.5d)^2$$

$$\theta = \text{angle}\left(\boldsymbol{U}_z + \boldsymbol{j}\sqrt{\boldsymbol{U}_x^2 + \boldsymbol{U}_y^2}\right) = \pi - \arctan\left(\frac{2\sqrt{2}(1-d)}{2-d}\right)$$

$$\varphi = \text{angle}\left(\boldsymbol{U}_x + \boldsymbol{j}\boldsymbol{U}_y\right) = \text{angle}\left\{-\sqrt{3}(1-0.5d)(1-d) - j\sqrt{3}(1-0.5d)(1-d)\right\} = -3\pi/4$$

10) *ab*_dip_E

3-phase voltage phasors

$$\boldsymbol{V}_a = (1-d);\boldsymbol{V}_b = -0.5(1-d)\left(1+\text{j}\sqrt{3}\right);\ \boldsymbol{V}_c = -0.5\left(1-\text{j}\sqrt{3}\right)$$

$$|\boldsymbol{V}_{a\_in}| = |\boldsymbol{V}_{b\_in}| = 1-d\ ;\ |\boldsymbol{V}_{c\_in}| = 1$$

X, Y and Z component of normal vector *U* to the polarized plane:

$$\boldsymbol{U}_X = -2|\boldsymbol{V}_{b\_in}||\boldsymbol{V}_{c\_in}|\sin(\alpha_b - \alpha_c) = -\sqrt{3}(1-d)$$

$$\boldsymbol{U}_Y = -2|\boldsymbol{V}_{c\_in}||\boldsymbol{V}_{a\_in}|\sin(\alpha_c - \alpha_a) = -\sqrt{3}(1-d)$$

$$\boldsymbol{U}_Z = -2|\boldsymbol{V}_{a\_in}||\boldsymbol{V}_{b\_in}|\sin(\alpha_a - \alpha_b) = -\sqrt{3}(1-d)^2$$

Thus, the elevation (θ) and azimuthal (φ) angles are obtained as

$$\theta = \text{angle}\left(\boldsymbol{U}_z + \boldsymbol{j}\sqrt{\boldsymbol{U}_x^2 + \boldsymbol{U}_y^2}\right) = \text{angle}\left\{-\sqrt{3}(1-d)^2 + j\sqrt{2}\sqrt{3}(1-d)\right\} = \pi - \arctan\left(\frac{\sqrt{2}}{1-d}\right)$$

$$\varphi = \text{angle}\left(\boldsymbol{U}_x + \boldsymbol{j}\boldsymbol{U}_y\right) = \text{angle}\left\{-\sqrt{3}(1-d) - j\sqrt{3}(1-d)\right\} = -3\pi/4$$

11) *bc*_dip_E

Following the formulation procedure as presented for *ab*_dip_E, the projected voltage magnitudes of 3-phase voltages for *bc*_dip_E are obtained as

$$|\boldsymbol{V}_{b\_in}| = |\boldsymbol{V}_{c\_in}| = 1-d\ ;\ |\boldsymbol{V}_{a\_in}| = 1$$

X, Y and Z component of normal vector *U* to the polarized plane is obtained as

$$\boldsymbol{U}_Y = -\sqrt{3}(1-d) = \boldsymbol{U}_Z;\ \ \boldsymbol{U}_X = -\sqrt{3}(1-d)^2$$

$$\theta = \text{angle}\left(\boldsymbol{U}_z + \boldsymbol{j}\sqrt{\boldsymbol{U}_x^2 + \boldsymbol{U}_y^2}\right) = \pi - \arctan\left(1 + (1-d)^2\right)$$

$$\varphi = \text{angle}\left(\boldsymbol{U}_x + \boldsymbol{j}\boldsymbol{U}_y\right) = \text{angle}\left\{-\sqrt{3}(1-d)^2 - j\sqrt{3}(1-d)\right\} = -\pi + \arctan\left(\frac{1}{1-d}\right)$$

12) *ca*_dip_E

Following the formulation procedure as presented for *ab*_dip_E, the projected voltage magnitudes of 3-phase voltages for *ca*_dip_E are obtained as

$$|\boldsymbol{V}_{a\_in}| = |\boldsymbol{V}_{c\_in}| = 1-d \; ; \; |\boldsymbol{V}_{b\_in}| = 1$$

X, Y and Z component of normal vector *U* to the polarized plane is obtained as

$$\boldsymbol{U}_X = -\sqrt{3}(1-d) = \boldsymbol{U}_Z; \;\; \boldsymbol{U}_Y = -\sqrt{3}(1-d)^2$$

$$\theta = \text{angle}\left(\boldsymbol{U}_z + \boldsymbol{j}\sqrt{\boldsymbol{U}_x^2 + \boldsymbol{U}_y^2}\right) = \pi - \arctan\left(1 + (1-d)^2\right)$$

$$\varphi = \text{angle}\left(\boldsymbol{U}_x + \boldsymbol{j}\boldsymbol{U}_y\right) = \text{angle}\left\{-\sqrt{3}(1-d) - j\sqrt{3}(1-d)^2\right\} = -\pi + \arctan(1-d)$$

13) *bc*_dip_C

3-phase voltage phasors

$$\boldsymbol{V}_a = 1, \;\; \boldsymbol{V}_b = -0.5 - \text{j}\frac{\sqrt{3}}{2}(1-d), \; \boldsymbol{V}_c = -0.5 + \text{j}\frac{\sqrt{3}}{2}(1-d)$$

$$|\boldsymbol{V}_{a\_in}| = 1;$$

$$|\boldsymbol{V}_{b\_in}| = |\boldsymbol{V}_b|\cos\left(\pi/3 - \tan^{-1}\left(\sqrt{3}(1-d)\right)\right) = \left(\frac{\sqrt{1+3(1-d)^2}}{2}\right)\left(\frac{4-3d}{2\sqrt{1+3(1-d)^2}}\right) = 1-0.75d;$$

$$|\boldsymbol{V}_{c\_in}| = |\boldsymbol{V}_c|\cos\left(\pi/3 - \tan^{-1}\left(\sqrt{3}(1-d)\right)\right) = \left(\frac{\sqrt{1+3(1-d)^2}}{2}\right)\left(\frac{4-3d}{2\sqrt{1+3(1-d)^2}}\right) = 1-0.75d;$$

X, Y and Z component of normal vector *U* to the polarized plane:

$$\boldsymbol{U}_X = -2|\boldsymbol{V}_{b\_in}||\boldsymbol{V}_{c\_in}|\sin(\alpha_b - \alpha_c) = -\sqrt{3}(1-0.75d)^2$$

$$\boldsymbol{U}_Y = -2|\boldsymbol{V}_{c\_in}||\boldsymbol{V}_{a\_in}|\sin(\alpha_c - \alpha_a) = -\sqrt{3}(1-0.75d)$$

$$\boldsymbol{U}_Z = -2|\boldsymbol{V}_{a\_in}||\boldsymbol{V}_{b\_in}|\sin(\alpha_a - \alpha_b) = -\sqrt{3}(1-0.75d)$$

$$\theta = \text{angle}\left(\boldsymbol{U}_z + \boldsymbol{j}\sqrt{\boldsymbol{U}_x^2 + \boldsymbol{U}_y^2}\right) = \pi - \arctan\left(\frac{\sqrt{32-24d+9d^2}}{4}\right)$$

$$\varphi = \text{angle}\left(\boldsymbol{U}_x + \boldsymbol{j}\boldsymbol{U}_y\right) = \text{angle}\left\{-\sqrt{3}(1-0.75d)^2 - j\sqrt{3}(1-0.75d)\right\} = -\pi + \arctan\left(\frac{4}{4-3d}\right)$$

14) *ca*_dip_C

Following the formulation procedure as presented for *bc*_dip_C, the projected voltage magnitudes of 3-phase voltages for *ca*_dip_C are obtained as

$$|\boldsymbol{V}_{a\_in}| = |\boldsymbol{V}_{c\_in}| = 1-0.75d \; ; \; |\boldsymbol{V}_{b\_in}| = 1$$

X, Y and Z component of normal vector *U* to the polarized plane is obtained as

$$\boldsymbol{U}_X = -\sqrt{3}(1-0.75d) = \boldsymbol{U}_Z; \;\; \boldsymbol{U}_Y = -\sqrt{3}(1-0.75d)^2$$

$$\theta = \text{angle}\left(\boldsymbol{U}_z + \boldsymbol{j}\sqrt{\boldsymbol{U}_x^2 + \boldsymbol{U}_y^2}\right) = \pi - \arctan\left(\frac{\sqrt{32-24d+9d^2}}{4}\right)$$

$$\varphi = \text{angle}\left(\boldsymbol{U}_x + \boldsymbol{j}\boldsymbol{U}_y\right) = \text{angle}\left\{-\sqrt{3}(1-0.75d) - j\sqrt{3}(1-0.75d)^2\right\} = -\pi + \arctan\left(\frac{4-3d}{4}\right)$$

15) *ab*_dip_C

Following the formulation procedure as presented for *bc*_dip_C, the projected voltage magnitudes of 3-phase voltages for *ab*_dip_C are obtained as

$$\left|\boldsymbol{V}_{a\_in}\right| = \left|\boldsymbol{V}_{b\_in}\right| = 1 - 0.75d \; ; \left|\boldsymbol{V}_{c\_in}\right| = 1$$

X, Y and Z component of normal vector *U* to the polarized plane is obtained as

$$\boldsymbol{U}_X = -\sqrt{3}(1-0.75d) = \boldsymbol{U}_Y; \;\; \boldsymbol{U}_Z = -\sqrt{3}(1-0.75d)^2$$

$$\theta = \text{angle}\left(\boldsymbol{U}_z + \boldsymbol{j}\sqrt{\boldsymbol{U}_x^2 + \boldsymbol{U}_y^2}\right) = \pi - \arctan\left(\frac{4\sqrt{2}}{4-3d}\right)$$

$$\varphi = \text{angle}\left(\boldsymbol{U}_x + \boldsymbol{j}\boldsymbol{U}_y\right) = \text{angle}\left\{-\sqrt{3}(1-0.75d) - j\sqrt{3}(1-0.75d)\right\} = -3\pi/4$$

16) *bc*_dip_G

3-phase voltage phasors

$$\boldsymbol{V}_a = 1 - \frac{d}{3}, \;\; \boldsymbol{V}_b = -\frac{1}{3} - \frac{1}{6}(1-d) - j\frac{\sqrt{3}}{2}(1-d), \; \boldsymbol{V}_c = -\frac{1}{3} - \frac{1}{6}(1-d) + j\frac{\sqrt{3}}{2}(1-d)$$

$$\left|\boldsymbol{V}_{a\_in}\right| = 1 - \frac{d}{3};$$

$$\left|\boldsymbol{V}_{b\_in}\right| = \left|\boldsymbol{V}_b\right|\cos\left(\pi/3 - \tan^{-1}\left(\frac{3\sqrt{3}(1-d)}{3-d}\right)\right) = \left(\frac{\sqrt{7d^2-15d+9}}{3}\right)\left(\frac{6-5d}{2\sqrt{7d^2-15d+9}}\right) = 1 - \frac{5}{6}d;$$

$$\left|\boldsymbol{V}_{c\_in}\right| = \left|\boldsymbol{V}_c\right|\cos\left(\pi/3 - \tan^{-1}\left(\frac{3\sqrt{3}(1-d)}{3-d}\right)\right) = \left(\frac{\sqrt{7d^2-15d+9}}{3}\right)\left(\frac{6-5d}{2\sqrt{7d^2-15d+9}}\right) = 1 - \frac{5}{6}d;$$

X, Y and Z component of normal vector *U* to the polarized plane:

$$\boldsymbol{U}_X = -2\left|\boldsymbol{V}_{b\_in}\right|\left|\boldsymbol{V}_{c\_in}\right|\sin(\alpha_b - \alpha_c) = -\sqrt{3}\left(1 - \frac{5d}{6}\right)^2$$

$$\boldsymbol{U}_Y = -2\left|\boldsymbol{V}_{c\_in}\right|\left|\boldsymbol{V}_{a\_in}\right|\sin(\alpha_c - \alpha_a) = -\sqrt{3}\left(1 - \frac{5d}{6}\right)\left(1 - \frac{d}{3}\right)$$

$$\boldsymbol{U}_Z = -2\left|\boldsymbol{V}_{a\_in}\right|\left|\boldsymbol{V}_{b\_in}\right|\sin(\alpha_a - \alpha_b) = -\sqrt{3}\left(1 - \frac{5d}{6}\right)\left(1 - \frac{d}{3}\right)$$

$$\theta = \text{angle}\left(\boldsymbol{U}_z + \boldsymbol{j}\sqrt{\boldsymbol{U}_x^2 + \boldsymbol{U}_y^2}\right) = \pi - \arctan\left(\frac{\sqrt{72-84d+29d^2}}{6-2d}\right)$$

$$\varphi = \text{angle}\left(\boldsymbol{U}_x + \boldsymbol{j}\boldsymbol{U}_y\right) = \text{angle}\left\{-\sqrt{3}\left(1 - \frac{5}{6}d\right)^2 - j\sqrt{3}\left(1 - \frac{5}{6}d\right)\left(1 - \frac{d}{3}\right)\right\} = -\pi + \arctan\left(\frac{6-2d}{6-5d}\right)$$

17) *ca*_dip_G

Following the formulation procedure as presented for *bc*_dip_G, the projected voltage magnitudes of 3-phase voltages for *ca*_dip_G are obtained as

$$\left|\boldsymbol{V}_{a\_in}\right| = \left|\boldsymbol{V}_{c\_in}\right| = 1 - \frac{5}{6}d \; ; \; \left|\boldsymbol{V}_{b\_in}\right| = 1 - \frac{d}{3}$$

X, Y and Z component of normal vector *U* to the polarized plane is obtained as

$$\boldsymbol{U}_X = -\sqrt{3}\left(1 - \frac{5d}{6}\right)\left(1 - \frac{d}{3}\right) = \boldsymbol{U}_Z; \;\; \boldsymbol{U}_Y = -\sqrt{3}\left(1 - \frac{5d}{6}\right)^2$$

$$\theta = \text{angle}\left(\boldsymbol{U}_z + \boldsymbol{j}\sqrt{\boldsymbol{U}_x^2 + \boldsymbol{U}_y^2}\right) = \pi - \arctan\left(\frac{\sqrt{72 - 84d + 29d^2}}{6 - 2d}\right)$$

$$\varphi = \text{angle}\left(\boldsymbol{U}_x + \boldsymbol{j}\boldsymbol{U}_y\right) = \text{angle}\left\{-\sqrt{3}\left(1 - \frac{5}{6}d\right)\left(1 - \frac{d}{3}\right) - j\sqrt{3}\left(1 - \frac{5}{6}d\right)^2\right\} = -\pi + \arctan\left(\frac{6 - 5d}{6 - 2d}\right)$$

18) *ab*_dip_G

Following the formulation procedure as presented for *bc*_dip_G, the projected voltage magnitudes of 3-phase voltages for *ab*_dip_G are obtained as

$$\left|\boldsymbol{V}_{a\_in}\right| = \left|\boldsymbol{V}_{b\_in}\right| = 1 - \frac{5}{6}d \; ; \; \left|\boldsymbol{V}_{c\_in}\right| = 1 - \frac{d}{3}$$

X, Y and Z component of normal vector *U* to the polarized plane is obtained as

$$\boldsymbol{U}_X = -\sqrt{3}\left(1 - \frac{5d}{6}\right)\left(1 - \frac{d}{3}\right) = \boldsymbol{U}_Y; \;\; \boldsymbol{U}_Z = -\sqrt{3}\left(1 - \frac{5d}{6}\right)^2$$

$$\theta = \text{angle}\left(\boldsymbol{U}_z + \boldsymbol{j}\sqrt{\boldsymbol{U}_x^2 + \boldsymbol{U}_y^2}\right) = \pi - \arctan\left(\frac{2\sqrt{2}(3 - d)}{6 - 5d}\right)$$

$$\varphi = \text{angle}\left(\boldsymbol{U}_x + \boldsymbol{j}\boldsymbol{U}_y\right) = \text{angle}\left\{-\sqrt{3}\left(1 - \frac{5}{6}d\right)\left(1 - \frac{d}{3}\right) - j\sqrt{3}\left(1 - \frac{5}{6}d\right)\left(1 - \frac{d}{3}\right)\right\} = -3\pi / 4$$

APPENDIX D

Formulation of Decision Boundaries for Classification of Dips

D.1 Decision boundaries for classification of six classes (*a*-φ, *b*-φ, *c*-φ, *ab*-φ, *bc*-φ, and *ca*-φ) of dips

As shown in Fig. (7.6), the decision boundaries used for classification of 6 classes (*a*-φ, *b*-φ, *c*-φ, *ab*-φ, *bc*-φ, and *ca*-φ) of dips are

$$D_{c-ca}(\varphi) = 0.5|\psi|_{c}(\varphi) + 0.5|\psi|_{ca}(\varphi) \tag{D.1.1}$$

$$D_{c-bc}(\varphi) = 0.5|\psi|_{c}(\varphi) + 0.5|\psi|_{bc}(\varphi) \tag{D.1.2}$$

$$D_{a-ab}(\varphi) = 0.5|\psi|_{a}(\varphi) + 0.5|\psi|_{ab}(\varphi) \tag{D.1.3}$$

$$D_{b-bc}(\varphi) = 0.5|\psi|_{b}(\varphi) + 0.5|\psi|_{bc}(\varphi) \tag{D.1.4}$$

$$D_{a-ca}(\varphi) = 0.5|\psi|_{a}(\varphi) + 0.5|\psi|_{ca}(\varphi) \tag{D.1.5}$$

$$D_{b-ab}(\varphi) = 0.5|\psi|_{b}(\varphi) + 0.5|\psi|_{ab}(\varphi) \tag{D.1.6}$$

Besides, from expression (7.7), it is evident that $|\psi|$ is a function of S_θ and S_φ; therefore, to obtain the expressions (D.1.1)-(D.1.6), firstly, S_θ and S_φ are expressed as a function of φ for *a*-φ, *b*-φ, *c*-φ, *ab*-φ, *bc*-φ, and *ca*-φ dips. Then, putting the expressions of S_θ and S_φ in (7.7) for respective classes of dips, the decision boundaries (D.1.1)-(D.1.6) are achieved. It is to be noted that from (D.1.1)-(D.1.6), $|\psi|_{a}(\varphi)$ corresponds to PE parameter $|\psi|$ for *a*-φ class of dip, and this notation-technique is followed for other expressions as well.

1) *a*-φ class of dip

$$|\boldsymbol{V}_{a\_in}| = 1-d;\ |\boldsymbol{V}_{b\_in}| = |\boldsymbol{V}_{c\_in}| = 1;$$

$$\theta = \pi - \tan^{-1}\left(\frac{\sqrt{1+(1-d)^2}}{1-d}\right);\ \varphi = -\pi + \tan^{-1}(1-d);\ \Rightarrow \sin\theta = \frac{1}{\sqrt{1+\sin^2\varphi}} \quad \text{and} \quad \cos\theta = \frac{\sin\varphi}{\sqrt{1+\sin^2\varphi}}$$

Now, S_θ and $S_\varphi$are obtained as

$$\boldsymbol{S}_\theta = |\boldsymbol{V}_{a\_in}|\boldsymbol{e}^{j\alpha_a}\cos\theta\cos\varphi + |\boldsymbol{V}_{b\_in}|\boldsymbol{e}^{j\alpha_b}\cos\theta\sin\varphi - |\boldsymbol{V}_{c\_in}|\boldsymbol{e}^{j\alpha_c}\sin\theta = \frac{\sqrt{1+\sin^2\varphi}\left(1-j\sqrt{3}\right)}{2}$$

$$\boldsymbol{S}_{\varphi}=-\left|\boldsymbol{V}_{a\_in}\right|\boldsymbol{e}^{j\alpha_a}\sin\varphi+\left|\boldsymbol{V}_{b\_in}\right|\boldsymbol{e}^{j\alpha_b}\cos\varphi=-\frac{1+\sin^2\varphi+j\sqrt{3}\cos^2\varphi}{2\cos\varphi}$$

2) *b*-φ class of dip

$$\left|\boldsymbol{V}_{b\_in}\right|=1-d;\ \left|\boldsymbol{V}_{a\_in}\right|=\left|\boldsymbol{V}_{c\_in}\right|=1;$$

$$\theta=\pi-\tan^{-1}\left(\frac{\sqrt{1+(1-d)^2}}{1-d}\right);\ \varphi=-\pi+\tan^{-1}\left(\frac{1}{1-d}\right);\Rightarrow\sin\theta=\frac{1}{\sqrt{1+\cos^2\varphi}}\quad\text{and}\ \cos\theta=\frac{\cos\varphi}{\sqrt{1+\cos^2\varphi}}$$

Now,

$$\boldsymbol{S}_{\theta}=\left|\boldsymbol{V}_{a\_in}\right|\boldsymbol{e}^{j\alpha_a}\cos\theta\cos\varphi+\left|\boldsymbol{V}_{b\_in}\right|\boldsymbol{e}^{j\alpha_b}\cos\theta\sin\varphi-\left|\boldsymbol{V}_{c\_in}\right|\boldsymbol{e}^{j\alpha_c}\sin\theta=\frac{\sqrt{1+\cos^2\varphi}\left(1-j\sqrt{3}\right)}{2}$$

$$\boldsymbol{S}_{\varphi}=-\left|\boldsymbol{V}_{a\_in}\right|\boldsymbol{e}^{j\alpha_a}\sin\varphi+\left|\boldsymbol{V}_{b\_in}\right|\boldsymbol{e}^{j\alpha_b}\cos\varphi=-\frac{1+\sin^2\varphi+j\sqrt{3}\cos^2\varphi}{2\sin\varphi}$$

3) *bc*-φ class of dip

$$\left|\boldsymbol{V}_{b\_in}\right|=\left|\boldsymbol{V}_{c\_in}\right|=1-d;\ \left|\boldsymbol{V}_{a\_in}\right|=1;$$

$$\theta=\pi-\tan^{-1}\left(\sqrt{1+(1-d)^2}\right);\ \varphi=-\pi+\tan^{-1}\left(\frac{1}{1-d}\right);\Rightarrow\sin\theta=\frac{1}{\sqrt{1+\sin^2\varphi}}\quad\text{and}\ \cos\theta=\frac{\sin\varphi}{\sqrt{1+\sin^2\varphi}}$$

Now,

$$\boldsymbol{S}_{\theta}=\left|\boldsymbol{V}_{a\_in}\right|\boldsymbol{e}^{j\alpha_a}\cos\theta\cos\varphi+\left|\boldsymbol{V}_{b\_in}\right|\boldsymbol{e}^{j\alpha_b}\cos\theta\sin\varphi-\left|\boldsymbol{V}_{c\_in}\right|\boldsymbol{e}^{j\alpha_c}\sin\theta=\frac{\cos\varphi\sqrt{1+\sin^2\varphi}\left(1-j\sqrt{3}\right)}{2\sin\varphi}$$

$$\boldsymbol{S}_{\varphi}=-\left|\boldsymbol{V}_{a\_in}\right|\boldsymbol{e}^{j\alpha_a}\sin\varphi+\left|\boldsymbol{V}_{b\_in}\right|\boldsymbol{e}^{j\alpha_b}\cos\varphi=-\frac{1+\sin^2\varphi+j\sqrt{3}\cos^2\varphi}{2\sin\varphi}$$

4) *ca*-φ class of dip

$$\left|\boldsymbol{V}_{a\_in}\right|=\left|\boldsymbol{V}_{c\_in}\right|=1-d;\ \left|\boldsymbol{V}_{b\_in}\right|=1;$$

$$\theta=\pi-\tan^{-1}\left(\sqrt{1+(1-d)^2}\right);\ \varphi=-\pi+\tan^{-1}(1-d);\Rightarrow\sin\theta=\frac{1}{\sqrt{1+\cos^2\varphi}}\quad\text{and}\ \cos\theta=\frac{\cos\varphi}{\sqrt{1+\cos^2\varphi}}$$

Now,

$$\boldsymbol{S}_{\theta}=\left|\boldsymbol{V}_{a\_in}\right|\boldsymbol{e}^{j\alpha_a}\cos\theta\cos\varphi+\left|\boldsymbol{V}_{b\_in}\right|\boldsymbol{e}^{j\alpha_b}\cos\theta\sin\varphi-\left|\boldsymbol{V}_{c\_in}\right|\boldsymbol{e}^{j\alpha_c}\sin\theta=\frac{\sin\varphi\sqrt{1+\cos^2\varphi}\left(1-j\sqrt{3}\right)}{2\cos\varphi}$$

$$\boldsymbol{S}_{\varphi}=-\left|\boldsymbol{V}_{a\_in}\right|\boldsymbol{e}^{j\alpha_a}\sin\varphi+\left|\boldsymbol{V}_{b\_in}\right|\boldsymbol{e}^{j\alpha_b}\cos\varphi=-\frac{1+\sin^2\varphi+j\sqrt{3}\cos^2\varphi}{2\cos\varphi}$$

5) *c*-φ class of dip

$$\left|\boldsymbol{V}_{c\_in}\right| = 1-d;\ \left|\boldsymbol{V}_{a\_in}\right| = \left|\boldsymbol{V}_{b\_in}\right| = 1;$$

$$\theta = \pi - \tan^{-1}\left((1-d)\sqrt{2}\right);\ \ \varphi = -3\pi/4;\ \Rightarrow \sin\varphi = \cos\varphi = -\frac{1}{\sqrt{2}}$$

$$\boldsymbol{S}_{\varphi} = -\left|\boldsymbol{V}_{a\_in}\right|\boldsymbol{e}^{j\alpha_a}\sin\varphi + \left|\boldsymbol{V}_{b\_in}\right|\boldsymbol{e}^{j\alpha_b}\cos\varphi = \frac{3+j\sqrt{3}}{2\sqrt{2}}$$

$$\boldsymbol{S}_{\theta} = \left|\boldsymbol{V}_{a\_in}\right|\boldsymbol{e}^{j\alpha_a}\cos\theta\cos\varphi + \left|\boldsymbol{V}_{b\_in}\right|\boldsymbol{e}^{j\alpha_b}\cos\theta\sin\varphi - \left|\boldsymbol{V}_{c\_in}\right|\boldsymbol{e}^{j\alpha_c}\sin\theta = \frac{-1+j\sqrt{3}}{2\sqrt{2}\cos\theta}$$

Hence, $\delta = arg(\boldsymbol{S}_{\varphi}) - arg(\boldsymbol{S}_{\theta}) = -\pi/2$; Now,

$$|\psi|_c(\varphi) = \left|\frac{1}{2}\arctan\frac{2|\boldsymbol{S}_{\theta}||\boldsymbol{S}_{\varphi}|\cos(\delta)}{|\boldsymbol{S}_{\theta}|^2 - |\boldsymbol{S}_{\varphi}|^2}\right| = \frac{\pi}{2}$$

6) *ab*-φ class of dip

$$\left|\boldsymbol{V}_{a\_in}\right| = \left|\boldsymbol{V}_{b\_in}\right| = 1-d;\ \left|\boldsymbol{V}_{c\_in}\right| = 1;$$

$$\theta = \pi - \tan^{-1}\left(\frac{\sqrt{2}}{1-d}\right);\ \ \varphi = -3\pi/4;\ \Rightarrow \sin\varphi = \cos\varphi = -\frac{1}{\sqrt{2}}$$

$$\boldsymbol{S}_{\varphi} = -\left|\boldsymbol{V}_{a\_in}\right|\boldsymbol{e}^{j\alpha_a}\sin\varphi + \left|\boldsymbol{V}_{b\_in}\right|\boldsymbol{e}^{j\alpha_b}\cos\varphi = \frac{-\cos\theta\left(3+j\sqrt{3}\right)}{2\sin\theta}$$

$$\boldsymbol{S}_{\theta} = \left|\boldsymbol{V}_{a\_in}\right|\boldsymbol{e}^{j\alpha_a}\cos\theta\cos\varphi + \left|\boldsymbol{V}_{b\_in}\right|\boldsymbol{e}^{j\alpha_b}\cos\theta\sin\varphi - \left|\boldsymbol{V}_{c\_in}\right|\boldsymbol{e}^{j\alpha_c}\sin\theta = \frac{1-j\sqrt{3}}{2\sin\theta}$$

$\delta = arg(\boldsymbol{S}_{\varphi}) - arg(\boldsymbol{S}_{\theta}) = -\pi/2$; Now,

$$|\psi|_{ab}(\varphi) = \left|\frac{1}{2}\arctan\frac{2|\boldsymbol{S}_{\theta}||\boldsymbol{S}_{\varphi}|\cos(\delta)}{|\boldsymbol{S}_{\theta}|^2 - |\boldsymbol{S}_{\varphi}|^2}\right| = 0$$

D.2 Decision boundaries for classification of different types (B, D, F, E, C, and G) of dips

As shown in Fig. (7.7), the decision boundaries used for classification of 3 types (B, D, and F) of dips are

$$D_{aB-\boldsymbol{aD}}(\theta)=0.5A_{x,aB}(\theta)+0.5A_{x,aD}(\theta) \tag{D.2.1}$$

$$D_{aD-\boldsymbol{aF}}(\theta)=0.5A_{x,aD}(\theta)+0.5A_{x,aF}(\theta) \tag{D.2.2}$$

$$D_{cB-\boldsymbol{cD}}(\theta)=0.5A_{x,cB}(\theta)+0.5A_{x,cD}(\theta) \tag{D.2.3}$$

$$D_{cD-\boldsymbol{cF}}(\theta)=0.5A_{x,cD}(\theta)+0.5A_{x,cF}(\theta) \tag{D.2.4}$$

Besides, from expression (7.9), it is evident that A_x is a function of S_θ and S_φ; therefore, to obtain the expressions (D.2.1)-(D.2.4), firstly, S_θ and S_φ are expressed as a function of θ for B, D, F types corresponding to *a*-φ, *b*-φ, and *c*-φ classes of dips. Then, putting the expressions of S_θ and S_φ in (7.9) for respective types of dips, the decision boundaries (D.2.1)-(D.2.4) are achieved. It is to be noted that from (D.2.1)-(D.2.4), $A_{x,aB}$ corresponds to PE parameter $A_{x,}$ for*a*_dip_B, i.e. *a*-φ class dip and type B; this notation-technique is followed for other expressions as well.

1) *a*_dip_B

$$\left|\boldsymbol{V}_{\boldsymbol{a\_in}}\right|=1-d;\ \left|\boldsymbol{V}_{\boldsymbol{b\_in}}\right|=\left|\boldsymbol{V}_{\boldsymbol{c\_in}}\right|=1\ ;\ \theta=\pi-\tan^{-1}\left(\frac{\sqrt{1+(1-d)^2}}{1-d}\right);\varphi=-\pi+\tan^{-1}(1-d)$$

By eliminating (1-*d*) from the expressions of θ and φ we get,

$\sin\varphi=\cot\theta$, $\cos\varphi=-\sqrt{1-\cot^2\theta}$

$$\boldsymbol{S}_\theta=\left|\boldsymbol{V}_{\boldsymbol{a\_in}}\right|\boldsymbol{e}^{j\alpha_a}\cos\theta\cos\varphi+\left|\boldsymbol{V}_{\boldsymbol{b\_in}}\right|\boldsymbol{e}^{j\alpha_b}\cos\theta\sin\varphi-\left|\boldsymbol{V}_{\boldsymbol{c\_in}}\right|\boldsymbol{e}^{j\alpha_c}\sin\theta$$

$$\Rightarrow\boldsymbol{S}_\theta=(1-\boldsymbol{d})\boldsymbol{e}^{j0}\cos\theta\left(-\sqrt{1-\cot^2\theta}\right)+\boldsymbol{e}^{j4\pi/3}\cos\theta\cot\theta-\boldsymbol{e}^{j2\pi/3}\sin\theta$$

$$\Rightarrow\boldsymbol{S}_\theta=\tan(\pi+\varphi)\cos\theta\left(-\sqrt{1-\cot^2\theta}\right)+\left(\frac{-1-j\sqrt{3}}{2}\right)\cos\theta\cot\theta-\left(\frac{-1+j\sqrt{3}}{2}\right)\sin\theta$$

$$\Rightarrow\boldsymbol{S}_\theta=\frac{\cot\theta}{\sqrt{1-\cot^2\theta}}\cos\theta\left(\sqrt{1-\cot^2\theta}\right)+\left(\frac{-1-j\sqrt{3}}{2}\right)\cos\theta\cot\theta-\left(\frac{-1+j\sqrt{3}}{2}\right)\sin\theta=\frac{1-j\sqrt{3}}{2\sin\theta}$$

$$\boldsymbol{S}_\varphi=-\left|\boldsymbol{V}_{\boldsymbol{a\_in}}\right|\boldsymbol{e}^{j\alpha_a}\sin\varphi+\left|\boldsymbol{V}_{\boldsymbol{b\_in}}\right|\boldsymbol{e}^{j\alpha_b}\cos\varphi=\frac{1+j\sqrt{3}(1-2\cos^2\theta)}{2\sin\theta\sqrt{1-2\cos^2\theta}}$$

2) *a*_dip_D

$$\left|\boldsymbol{V}_{\boldsymbol{a\_in}}\right|=1-d;\ \left|\boldsymbol{V}_{\boldsymbol{b\_in}}\right|=1-0.25d;\ \left|\boldsymbol{V}_{\boldsymbol{c\_in}}\right|=1-0.25d;$$

$$\varphi = -\pi + \tan^{-1}\left(\frac{4-4d}{4-d}\right);\ \theta = \pi - \tan^{-1}\left(\frac{\sqrt{(1-d)^2+(1-0.25d)^2}}{1-d}\right) = \pi - \tan^{-1}\left(\sqrt{1+\left(\frac{4-\boldsymbol{d}}{4-4\boldsymbol{d}}\right)^2}\right)$$

By eliminating d from the expressions of θ and φ we get,

$\sin\varphi = \cot\theta,\ \cos\varphi = -\sqrt{1-\cot^2\theta}$

$$\boldsymbol{S}_\theta = |\boldsymbol{V}_{a\_in}|\boldsymbol{e}^{j\alpha_a}\cos\theta\cos\varphi + |\boldsymbol{V}_{b\_in}|\boldsymbol{e}^{j\alpha_b}\cos\theta\sin\varphi - |\boldsymbol{V}_{c\_in}|\boldsymbol{e}^{j\alpha_c}\sin\theta$$

$$\Rightarrow \boldsymbol{S}_\theta = (1-d)\boldsymbol{e}^{j0}\cos\theta\left(-\sqrt{1-\cot^2\theta}\right) + (1-0.25d)\boldsymbol{e}^{j4\pi/3}\cos\theta\cot\theta - (1-0.25d)\boldsymbol{e}^{j2\pi/3}\sin\theta$$

$$\Rightarrow \boldsymbol{S}_\theta = \frac{1.5\left(1-j\sqrt{3}\right)\sqrt{1-2\cos^2\theta}}{\sin\theta\left(4\sqrt{1-2\cos^2\theta}+\cos\theta\right)}$$

$$\boldsymbol{S}_\varphi = -|\boldsymbol{V}_{a\_in}|\boldsymbol{e}^{j\alpha_a}\sin\varphi + |\boldsymbol{V}_{b\_in}|\boldsymbol{e}^{j\alpha_b}\cos\varphi = \frac{1.5\left(1+j\sqrt{3}\right)\left(1-2\cos^2\theta\right)}{\sin\theta\left(4\sqrt{1-2\cos^2\theta}+\cos\theta\right)}$$

3) *a*_dip_F

$$|\boldsymbol{V}_{a\_in}| = 1-d;\ |\boldsymbol{V}_{b\_in}| = 1-0.5d;\ |\boldsymbol{V}_{c\_in}| = 1-0.5d;$$

$$\varphi = -\pi + \tan^{-1}\left(\frac{2-2d}{2-d}\right);\ \theta = \pi - \tan^{-1}\left(\frac{\sqrt{(2-2d)^2+(1-0.25d)^2}}{2-2d}\right) = \pi - \tan^{-1}\left(\sqrt{1+\left(\frac{2-d}{2-2d}\right)^2}\right)$$

By eliminating d from the expressions of θ and φ we get,

$\sin\varphi = \cot\theta,\ \cos\varphi = -\sqrt{1-\cot^2\theta}$

Again, $|\boldsymbol{V}_{a\_in}| = 1-d = \frac{\sin\varphi}{2\cos\varphi - \sin\varphi};\ |\boldsymbol{V}_{b\_in}| = |\boldsymbol{V}_{c\_in}| = 1-0.5d = \frac{\cos\varphi}{2\cos\varphi - \sin\varphi};$

$$\boldsymbol{S}_\theta = |\boldsymbol{V}_{a\_in}|\boldsymbol{e}^{j\alpha_a}\cos\theta\cos\varphi + |\boldsymbol{V}_{b\_in}|\boldsymbol{e}^{j\alpha_b}\cos\theta\sin\varphi - |\boldsymbol{V}_{c\_in}|\boldsymbol{e}^{j\alpha_c}\sin\theta$$

$$\Rightarrow \boldsymbol{S}_\theta = (1-d)\boldsymbol{e}^{j0}\cos\theta\left(-\sqrt{1-\cot^2\theta}\right) + (1-0.5d)\boldsymbol{e}^{j4\pi/3}\cos\theta\cot\theta - (1-0.5d)\boldsymbol{e}^{j2\pi/3}\sin\theta$$

$$\Rightarrow \boldsymbol{S}_\theta = \frac{1.5\left(1-j\sqrt{3}\right)\sqrt{1-2\cos^2\theta}}{\sin\theta\left(2\sqrt{1-2\cos^2\theta}+\cos\theta\right)}$$

$$\boldsymbol{S}_\varphi = -|\boldsymbol{V}_{a\_in}|\boldsymbol{e}^{j\alpha_a}\sin\varphi + |\boldsymbol{V}_{b\_in}|\boldsymbol{e}^{j\alpha_b}\cos\varphi = \frac{1.5\left(1+j\sqrt{3}\right)\left(1-2\cos^2\theta\right)}{\sin\theta\left(2\sqrt{1-2\cos^2\theta}+\cos\theta\right)}$$

4) *c*_dip_B

$$|\boldsymbol{V}_{c\_in}| = 1-d;\ |\boldsymbol{V}_{a\_in}| = |\boldsymbol{V}_{b\_in}| = 1;\ \theta = \pi - \tan^{-1}\left(\sqrt{2}-\sqrt{2}d\right);\ \varphi = -3\pi/4;$$

$$\sin\varphi = \cos\varphi = -\frac{1}{\sqrt{2}};\ |\boldsymbol{V}_{c\_in}| = 1-d = -\frac{\sin\theta}{\sqrt{2}\cos\theta};$$

$$\boldsymbol{S}_\theta = |\boldsymbol{V}_{a\_in}|\boldsymbol{e}^{j\alpha_a}\cos\theta\cos\varphi + |\boldsymbol{V}_{b\_in}|\boldsymbol{e}^{j\alpha_b}\cos\theta\sin\varphi - |\boldsymbol{V}_{c\_in}|\boldsymbol{e}^{j\alpha_c}\sin\theta$$

$$\Rightarrow \boldsymbol{S}_\theta = \boldsymbol{e}^{j0}\cos\theta\left(-1/\sqrt{2}\right)+\boldsymbol{e}^{j4\pi/3}\cos\theta\left(-1/\sqrt{2}\right)-\left(\frac{-\sin\theta}{\sqrt{2}\cos\theta}\right)\boldsymbol{e}^{j2\pi/3}\sin\theta$$

$$\Rightarrow \boldsymbol{S}_\theta = \frac{-1+j\sqrt{3}}{2\sqrt{2}\cos\theta}$$

$$\boldsymbol{S}_\varphi = -\left|\boldsymbol{V}_{a\_in}\right|\boldsymbol{e}^{j\alpha_a}\sin\varphi+\left|\boldsymbol{V}_{b\_in}\right|\boldsymbol{e}^{j\alpha_b}\cos\varphi = 0.5\times\sqrt{1.5}\times\left(\sqrt{3}+j\right)$$

5) *c*_dip_D

$$\left|\boldsymbol{V}_{c\_in}\right| = 1-d;\ \left|\boldsymbol{V}_{a\_in}\right| = \left|\boldsymbol{V}_{b\_in}\right| = 1-0.25d;\ \theta = \pi-\tan^{-1}\left(\frac{4\sqrt{2}(1-d)}{4-d}\right);\ \varphi = -3\pi/4;$$

$$\sin\varphi = \cos\varphi = -\frac{1}{\sqrt{2}};\ \left|\boldsymbol{V}_{c\_in}\right| = 1-d = -\frac{3\sin\theta}{4\sqrt{2}\cos\theta+\sin\theta};$$

$$\left|\boldsymbol{V}_{a\_in}\right| = \left|\boldsymbol{V}_{b\_in}\right| = 1-0.25d = \frac{3\sqrt{2}\cos\theta}{4\sqrt{2}\cos\theta+\sin\theta};$$

$$\boldsymbol{S}_\theta = \left|\boldsymbol{V}_{a\_in}\right|\boldsymbol{e}^{j\alpha_a}\cos\theta\cos\varphi+\left|\boldsymbol{V}_{b\_in}\right|\boldsymbol{e}^{j\alpha_b}\cos\theta\sin\varphi-\left|\boldsymbol{V}_{c\_in}\right|\boldsymbol{e}^{j\alpha_c}\sin\theta$$

$$\Rightarrow \boldsymbol{S}_\theta = \frac{3\sqrt{2}\cos\theta}{4\sqrt{2}\cos\theta+\sin\theta}\boldsymbol{e}^{j0}\cos\theta\left(-1/\sqrt{2}\right)+\boldsymbol{e}^{j4\pi/3}\cos\theta\left(-1/\sqrt{2}\right)$$

$$-\left(-\frac{3\sin\theta}{4\sqrt{2}\cos\theta+\sin\theta}\right)\boldsymbol{e}^{j2\pi/3}\sin\theta$$

$$\Rightarrow \boldsymbol{S}_\theta = \frac{-1.5\left(1-j\sqrt{3}\right)}{4\sqrt{2}\cos\theta+\sin\theta}$$

$$\boldsymbol{S}_\varphi = -\left|\boldsymbol{V}_{a\_in}\right|\boldsymbol{e}^{j\alpha_a}\sin\varphi+\left|\boldsymbol{V}_{b\_in}\right|\boldsymbol{e}^{j\alpha_b}\cos\varphi = \frac{1.5\cos\theta\left(3+j\sqrt{3}\right)}{4\sqrt{2}\cos\theta+\sin\theta}$$

6) *c*_dip_F

$$\left|\boldsymbol{V}_{c\_in}\right| = 1-d;\ \left|\boldsymbol{V}_{a\_in}\right| = \left|\boldsymbol{V}_{b\_in}\right| = 1-0.5d;\ \theta = \pi-\tan^{-1}\left(\frac{2\sqrt{2}(1-d)}{2-d}\right);\ \varphi = -3\pi/4;$$

$$\sin\varphi = \cos\varphi = -\frac{1}{\sqrt{2}};\ \left|\boldsymbol{V}_{c\_in}\right| = 1-d = -\frac{\sin\theta}{2\sqrt{2}\cos\theta+\sin\theta};$$

$$\left|\boldsymbol{V}_{a\_in}\right| = \left|\boldsymbol{V}_{b\_in}\right| = 1-0.5d = \frac{\sqrt{2}\cos\theta}{2\sqrt{2}\cos\theta+\sin\theta};$$

$$\boldsymbol{S}_\theta = \left|\boldsymbol{V}_{a\_in}\right|\boldsymbol{e}^{j\alpha_a}\cos\theta\cos\varphi+\left|\boldsymbol{V}_{b\_in}\right|\boldsymbol{e}^{j\alpha_b}\cos\theta\sin\varphi-\left|\boldsymbol{V}_{c\_in}\right|\boldsymbol{e}^{j\alpha_c}\sin\theta = \frac{-0.5\left(1-j\sqrt{3}\right)}{2\sqrt{2}\cos\theta+\sin\theta}$$

$$\boldsymbol{S}_\varphi = -\left|\boldsymbol{V}_{a\_in}\right|\boldsymbol{e}^{j\alpha_a}\sin\varphi+\left|\boldsymbol{V}_{b\_in}\right|\boldsymbol{e}^{j\alpha_b}\cos\varphi = \frac{0.5\cos\theta\left(3+j\sqrt{3}\right)}{2\sqrt{2}\cos\theta+\sin\theta}$$

As shown in Fig. (7.8), the decision boundaries used for classification of E, C, and G types of *ab*-φ dips are

$$D_{abE-\mathbf{abG}}(\theta) = 0.5A_{x,abE}(\theta) + 0.5A_{x,abG}(\theta) \quad \text{(D.2.5)}$$

$$D_{abE-\mathbf{abC}}(\theta) = 0.5A^{out}_{y,abE}(\theta) + 0.5A^{out}_{y,abC}(\theta) \quad \text{(D.2.6)}$$

Firstly, S_θ and S_φ are expressed as a function of θ for E, and G types corresponding to *ab*-φ class of dip. Then, putting the expressions of S_θ and S_φ in (7.9) for respective types of dips, the decision boundary (D.2.5) is achieved. Similarly, for decision boundary (D.2.6), E and C types of *ab*-φ dip is considered; then, S_θ and S_φ corresponding to $A^{out}_{y,abE}(\theta), A^{out}_{y,abC}(\theta)$ are derived and put in (7.8).

1) *ab*_dip_E

The variables S_θ and $S_{\varphi,}$ corresponding to $A_{x,abE}(\theta)$, are developed below:

$$|\boldsymbol{V}_{a\_in}| = |\boldsymbol{V}_{b\_in}| = 1-d \;;\; |\boldsymbol{V}_{c\_in}| = 1 \;; \theta = \pi - \tan^{-1}\left(\frac{\sqrt{2}}{1-d}\right); \varphi = -3\pi/4;$$

$$\sin\varphi = \cos\varphi = -\frac{1}{\sqrt{2}}; |\boldsymbol{V}_{a\_in}| = |\boldsymbol{V}_{b\_in}| = 1-d = -\frac{\sqrt{2}\cos\theta}{\sin\theta};$$

$$\boldsymbol{S}_\theta = |\boldsymbol{V}_{a\_in}|\boldsymbol{e}^{j\alpha_a}\cos\theta\cos\varphi + |\boldsymbol{V}_{b\_in}|\boldsymbol{e}^{j\alpha_b}\cos\theta\sin\varphi - |\boldsymbol{V}_{c\_in}|\boldsymbol{e}^{j\alpha_c}\sin\theta = \frac{\left(1-j\sqrt{3}\right)}{2\sin\theta}$$

$$\boldsymbol{S}_\varphi = -|\boldsymbol{V}_{a\_in}|\boldsymbol{e}^{j\alpha_a}\sin\varphi + |\boldsymbol{V}_{b\_in}|\boldsymbol{e}^{j\alpha_b}\cos\varphi = -\frac{\cos\theta\left(3+j\sqrt{3}\right)}{2\sin\theta}$$

For the variables S_θ and $S_{\varphi,}$ corresponding to $A^{out}_{y,abE}(\theta)$, out of phase components of 3-phase voltage phasors, i.e., $\boldsymbol{V}_{a\_out}, \boldsymbol{V}_{b\_out}$ and $\boldsymbol{V}_{c\_out}$, are considered. From the phasor diagram shown in Fig. C.1 (k), it is evident that $\boldsymbol{V}_{a\_out} = \boldsymbol{V}_{b\_out} = \boldsymbol{V}_{c\_out} = 0$. Therefore, $A^{out}_{y,abE}(\theta)$ is obtained as $A^{out}_{y,abE}(\theta) = 0$.

2) *ab*_dip_C

The variables S_θ and $S_{\varphi,}$ corresponding to $A^{out}_{y,abC}(\theta)$, are developed below:

Out of phase components of 3-phase voltage phasors are considered. Thus,

$$|\boldsymbol{V}_{c\_out}| = 0;$$

$$|\boldsymbol{V}_{a\_out}| = |\boldsymbol{V}_{b\_out}| = |\boldsymbol{V}_a|\sin\left\{\frac{\pi}{3} - \tan^{-1}\left(\sqrt{3}-\sqrt{3}d\right)\right\} = 0.5\sqrt{1+3(1-d)^2}\,\frac{\sqrt{3}d}{2\sqrt{1+3(1-d)^2}} = \frac{\sqrt{3}d}{4};$$

$$\boldsymbol{U}_X = \boldsymbol{U}_Y = 0; \boldsymbol{U}_Z = -2\left|\boldsymbol{V}_{a\_out}\right|\left|\boldsymbol{V}_{b\_out}\right|\sin(\alpha_a - \alpha_b) = -\frac{3\sqrt{3}d}{16}$$

$$\theta = \text{angle}\left(\boldsymbol{U}_z + \boldsymbol{j}\sqrt{\boldsymbol{U}_x^2 + \boldsymbol{U}_y^2}\right) = \pi;\ \varphi = \text{angle}\left(\boldsymbol{U}_x + \boldsymbol{j}\boldsymbol{U}_y\right) = 0;$$

$$\boldsymbol{S}_\theta = \left|\boldsymbol{V}_{a\_out}\right|\boldsymbol{e}^{j\alpha_a}\cos\theta\cos\varphi + \left|\boldsymbol{V}_{b\_out}\right|\boldsymbol{e}^{j\alpha_b}\cos\theta\sin\varphi - \left|\boldsymbol{V}_{c\_out}\right|\boldsymbol{e}^{j\alpha_c}\sin\theta = -\frac{\sqrt{3}d}{4}$$

$$\Rightarrow \boldsymbol{S}_\theta = -\frac{\sin\theta + \sqrt{2}\cos\theta}{\sqrt{3}\sin\theta}$$

$$\boldsymbol{S}_\varphi = -\left|\boldsymbol{V}_{a\_out}\right|\boldsymbol{e}^{j\alpha_a}\sin\varphi + \left|\boldsymbol{V}_{b\_out}\right|\boldsymbol{e}^{j\alpha_b}\cos\varphi = -\frac{0.5\left(\sin\theta + \sqrt{2}\cos\theta\right)\left(1 + j\sqrt{3}\right)}{\sqrt{3}\sin\theta}$$

3) *ab*_dip_G

The variables S_θ and S_φ, corresponding to $A_{x,abG}(\theta)$, are developed below:

$$\left|\boldsymbol{V}_{a\_in}\right| = \left|\boldsymbol{V}_{b\_in}\right| = 1 - \frac{5}{6}d\ ;\ \left|\boldsymbol{V}_{c\_in}\right| = 1 - \frac{d}{3}; \theta = \pi - \tan^{-1}\left(\frac{2\sqrt{2}(3-d)}{6-5d}\right); \varphi = -3\pi/4;$$

$$\sin\varphi = \cos\varphi = -\frac{1}{\sqrt{2}}; \left|\boldsymbol{V}_{a\_in}\right| = \left|\boldsymbol{V}_{b\_in}\right| = 1 - \frac{5}{6}d = -\frac{3\sqrt{2}\cos\theta}{2\sqrt{2}\cos\theta + 5\sin\theta};$$

$$\left|\boldsymbol{V}_{c\_in}\right| = 1 - \frac{1}{3}d = \frac{3\sin\theta}{2\sqrt{2}\cos\theta + 5\sin\theta}$$

$$\boldsymbol{S}_\theta = \left|\boldsymbol{V}_{a\_in}\right|\boldsymbol{e}^{j\alpha_a}\cos\theta\cos\varphi + \left|\boldsymbol{V}_{b\_in}\right|\boldsymbol{e}^{j\alpha_b}\cos\theta\sin\varphi - \left|\boldsymbol{V}_{c\_in}\right|\boldsymbol{e}^{j\alpha_c}\sin\theta = \frac{1.5\left(1 - j\sqrt{3}\right)}{2\sqrt{2}\cos\theta + 5\sin\theta}$$

$$\boldsymbol{S}_\varphi = -\left|\boldsymbol{V}_{a\_in}\right|\boldsymbol{e}^{j\alpha_a}\sin\varphi + \left|\boldsymbol{V}_{b\_in}\right|\boldsymbol{e}^{j\alpha_b}\cos\varphi = -\frac{1.5\cos\theta\left(3 + j\sqrt{3}\right)}{2\sqrt{2}\cos\theta + 5\sin\theta}$$

The decision boundaries corresponding to E, C and G types of *bc*-φ and *ca*-φ dips are

$$D_{bcE-\boldsymbol{bcG}}(\theta) = 0.5A_{x,bcE}(\theta) + 0.5A_{x,bcG}(\theta) \quad \text{(D.2.7)}$$

$$D_{bcE-\boldsymbol{bcC}}(\theta) = 0.5A^{out}_{y,bcE}(\theta) + 0.5A^{out}_{y,bcC}(\theta) \quad \text{(D.2.8)}$$

$$D_{caE-\boldsymbol{caG}}(\theta) = 0.5A_{x,caE}(\theta) + 0.5A_{x,caG}(\theta) \quad \text{(D.2.9)}$$

$$D_{caE-\boldsymbol{caC}}(\theta) = 0.5A^{out}_{y,caE}(\theta) + 0.5A^{out}_{y,caC}(\theta) \quad \text{(D.2.10)}$$

Following the similar technique as used for the formulation of decision boundaries corresponding to *ab*-φ dip, the decision boundaries corresponding to E, C and G types of *bc*-φ and *ca*-φ dips can be easily obtained. The developed expressions are presented in Section 7.3 and Table 7.7.

APPENDIX E

Formulation of Decision Boundaries for Classification of Swells

Two types (H and I type) of swells comprise 6 groups of swells. The phasor diagram representing these 6 groups of swells are illustrated in Fig. E.1, where three phase voltages before and during the occurrence of swell is represented by dotted and solid arrow line, respectively.

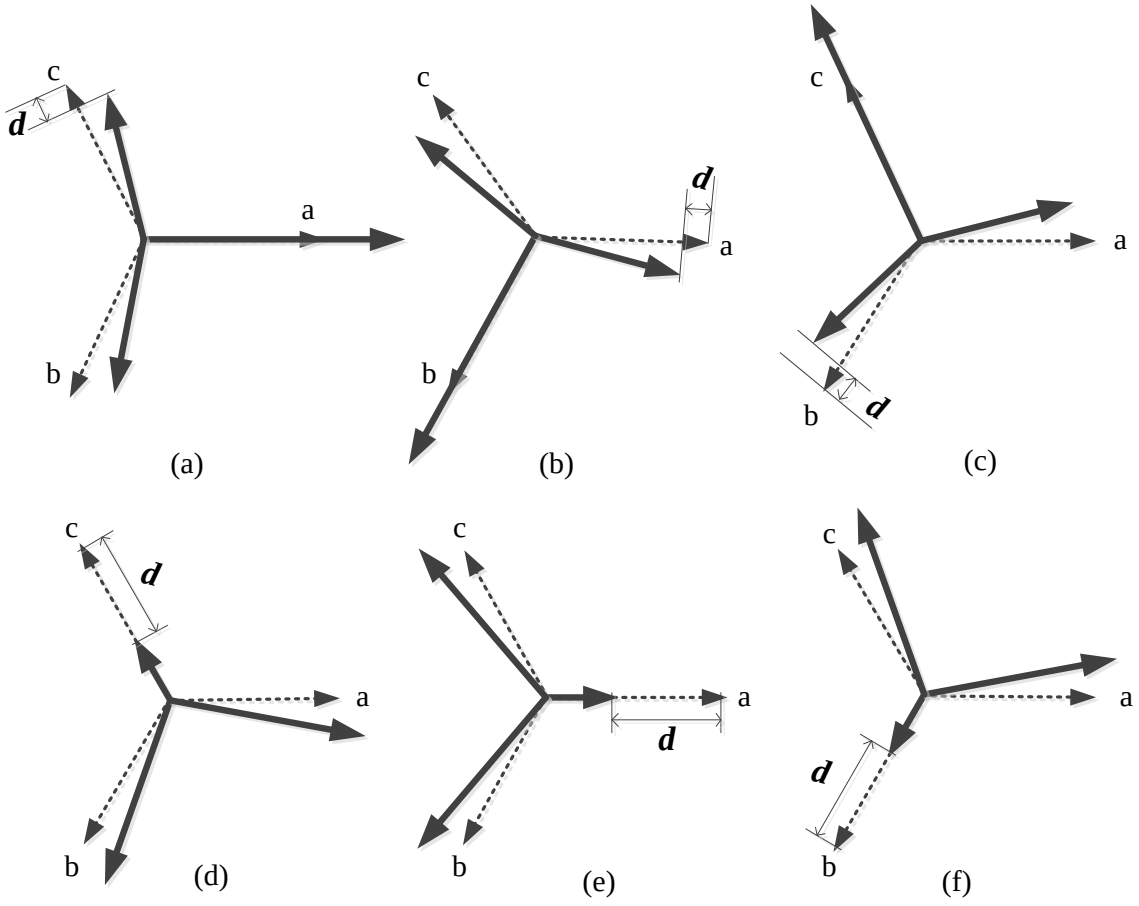

Fig. E.1. Phasor diagram representing 6 groups of swells: (a) *a*-φ, (b) *b*-φ, (c) *c*-φ, (d) *ab*-φ, (e) *bc*-φ, and (f) *ca*-φ.

As shown in Fig. (7.9), the decision boundaries used for classification of 6 groups of swells, which include I-type (*a*-φ, *b*-φ, and *c*-φ swell) and H-type (*ab*-φ, *bc*-φ, and *ca*-φ swell), can be presented as

$$D_{AB-B}(\varphi)=0.5|\psi|_{AB}(\varphi)+0.5|\psi|_{B}(\varphi) \tag{E.1}$$

$$D_{AB-A}(\varphi)=0.5|\psi|_{AB}(\varphi)+0.5|\psi|_{A}(\varphi) \tag{E.2}$$

$$D_{BC-C}(\varphi)=0.5|\psi|_{BC}(\varphi)+0.5|\psi|_{C}(\varphi) \tag{E.3}$$

$$D_{CA-A}(\varphi)=0.5|\psi|_{CA}(\varphi)+0.5|\psi|_{A}(\varphi) \tag{E.4}$$

$$D_{B-BC}(\varphi)=0.5|\psi|_{B}(\varphi)+0.5|\psi|_{BC}(\varphi) \tag{E.5}$$

$$D_{C-CA}(\varphi)=0.5|\psi|_{C}(\varphi)+0.5|\psi|_{CA}(\varphi) \tag{E.6}$$

Besides, from expression (7.7), it is evident that $|\psi|$ is a function of S_θ and S_φ; therefore, to obtain the expressions (E.1)-(E.6), firstly, S_θ and S_φ are expressed as a function of φ for *a*-φ, *b*-φ, *c*-φ, *ab*-φ, *bc*-φ, and *ca*-φ swells. Then, putting the expressions of S_θ and S_φ in (7.7) for respective classes of swells, the decision boundaries (E.1)-(E.6) are achieved. It is to be noted that from (E.1)-(E.6), $|\psi|_A(\varphi)$ corresponds to PE parameter $|\psi|$ for *a*-φ swell, and this notation-technique is followed for other expressions as well.

1) *a*-φ swell

$|\boldsymbol{V}_{b\_in}|=|\boldsymbol{V}_{c\_in}|=1-d;\ |\boldsymbol{V}_{a\_in}|=1+2d;$

$$\theta=\pi-\tan^{-1}\left(\sqrt{1+\left(\frac{1-d}{1+2d}\right)^2}\right);\ \varphi=-\pi+\tan^{-1}\left(\frac{1+2d1}{1-d}\right);$$

Now eliminating d from the expressions of θ and φ we get,

$$\sin\theta=\frac{1}{\sqrt{1+\sin^2\varphi}}\quad\text{and}\quad\cos\theta=\frac{\sin\varphi}{\sqrt{1+\sin^2\varphi}};$$

$$\boldsymbol{S}_\theta=|\boldsymbol{V}_{a\_in}|\boldsymbol{e}^{j\alpha_a}\cos\theta\cos\varphi+|\boldsymbol{V}_{b\_in}|\boldsymbol{e}^{j\alpha_b}\cos\theta\sin\varphi-|\boldsymbol{V}_{c\_in}|\boldsymbol{e}^{j\alpha_c}\sin\theta=\frac{1.5\cos\varphi\sqrt{1+\sin^2\varphi}\left(1-j\sqrt{3}\right)}{2\cos\varphi+\sin\varphi}$$

$$\boldsymbol{S}_\varphi=-|\boldsymbol{V}_{a\_in}|\boldsymbol{e}^{j\alpha_a}\sin\varphi+|\boldsymbol{V}_{b\_in}|\boldsymbol{e}^{j\alpha_b}\cos\varphi=-\frac{1.5\left(1+\sin^2\varphi+j\sqrt{3}\cos^2\varphi\right)}{2\cos\varphi+\sin\varphi}$$

2) *b*-φ swell

$|\boldsymbol{V}_{a\_in}|=|\boldsymbol{V}_{c\_in}|=1-d;\ |\boldsymbol{V}_{b\_in}|=1+2d;$

$$\theta=\pi-\tan^{-1}\left(\sqrt{1+\left(\frac{1-d}{1+2d}\right)^2}\right);\ \varphi=-\pi+\tan^{-1}\left(\frac{1-d1}{1+2d}\right);$$

Now eliminating d from the expressions of θ and φ we get,

$$\sin\theta = \frac{1}{\sqrt{1+\cos^2\varphi}} \quad \text{and} \quad \cos\theta = \frac{\cos\varphi}{\sqrt{1+\cos^2\varphi}}$$

$$\boldsymbol{S}_\theta = \left|\boldsymbol{V}_{a\_in}\right| e^{j\alpha_a} \cos\theta\cos\varphi + \left|\boldsymbol{V}_{b\_in}\right| e^{j\alpha_b} \cos\theta\sin\varphi - \left|\boldsymbol{V}_{c\_in}\right| e^{j\alpha_c} \sin\theta = \frac{1.5\sin\varphi\sqrt{1+\cos^2\varphi}\left(1-j\sqrt{3}\right)}{\cos\varphi+2\sin\varphi}$$

$$\boldsymbol{S}_\varphi = -\left|\boldsymbol{V}_{a\_in}\right| e^{j\alpha_a} \sin\varphi + \left|\boldsymbol{V}_{b\_in}\right| e^{j\alpha_b} \cos\varphi = -\frac{1.5\left\{1+\sin^2\varphi+j\sqrt{3}\cos^2\varphi\right\}}{\cos\varphi+2\sin\varphi}$$

3) *bc*-φ swell

$$\left|\boldsymbol{V}_{a\_in}\right| = 1-d;\ \left|\boldsymbol{V}_{b\_in}\right| = \left|\boldsymbol{V}_{c\_in}\right| = 1;$$

$$\theta = \pi - \tan^{-1}\left(\frac{\sqrt{1+(1-d)^2}}{1-d}\right);\ \varphi = -\pi + \tan^{-1}(1-d);\ \Rightarrow \sin\theta = \frac{1}{\sqrt{1+\sin^2\varphi}} \quad \text{and} \quad \cos\theta = \frac{\sin\varphi}{\sqrt{1+\sin^2\varphi}}$$

Now, S_θ and $S_\varphi$are obtained as

$$\boldsymbol{S}_\theta = \left|\boldsymbol{V}_{a\_in}\right| e^{j\alpha_a} \cos\theta\cos\varphi + \left|\boldsymbol{V}_{b\_in}\right| e^{j\alpha_b} \cos\theta\sin\varphi - \left|\boldsymbol{V}_{c\_in}\right| e^{j\alpha_c} \sin\theta = \frac{\sqrt{1+\sin^2\varphi}\left(1-j\sqrt{3}\right)}{2}$$

$$\boldsymbol{S}_\varphi = -\left|\boldsymbol{V}_{a\_in}\right| e^{j\alpha_a} \sin\varphi + \left|\boldsymbol{V}_{b\_in}\right| e^{j\alpha_b} \cos\varphi = -\frac{1+\sin^2\varphi+j\sqrt{3}\cos^2\varphi}{2\cos\varphi}$$

4) *ca*-φ swell

$$\left|\boldsymbol{V}_{b\_in}\right| = 1-d;\ \left|\boldsymbol{V}_{a\_in}\right| = \left|\boldsymbol{V}_{c\_in}\right| = 1;$$

$$\theta = \pi - \tan^{-1}\left(\frac{\sqrt{1+(1-d)^2}}{1-d}\right);\ \varphi = -\pi + \tan^{-1}\left(\frac{1}{1-d}\right);\ \Rightarrow \sin\theta = \frac{1}{\sqrt{1+\cos^2\varphi}} \quad \text{and} \quad \cos\theta = \frac{\cos\varphi}{\sqrt{1+\cos^2\varphi}}$$

Now,

$$\boldsymbol{S}_\theta = \left|\boldsymbol{V}_{a\_in}\right| e^{j\alpha_a} \cos\theta\cos\varphi + \left|\boldsymbol{V}_{b\_in}\right| e^{j\alpha_b} \cos\theta\sin\varphi - \left|\boldsymbol{V}_{c\_in}\right| e^{j\alpha_c} \sin\theta = \frac{\sqrt{1+\cos^2\varphi}\left(1-j\sqrt{3}\right)}{2}$$

$$\boldsymbol{S}_\varphi = -\left|\boldsymbol{V}_{a\_in}\right| e^{j\alpha_a} \sin\varphi + \left|\boldsymbol{V}_{b\_in}\right| e^{j\alpha_b} \cos\varphi = -\frac{1+\sin^2\varphi+j\sqrt{3}\cos^2\varphi}{2\sin\varphi}$$

5) *c*-φ swell

$$\left|\boldsymbol{V}_{a\_in}\right| = \left|\boldsymbol{V}_{b\_in}\right| = 1-d;\ \left|\boldsymbol{V}_{c\_in}\right| = 1+2d;$$

$$\theta = \pi - \tan^{-1}\left(\frac{\sqrt{2}(1+2d)}{1-d}\right);\ \varphi = -3\pi/4;\ \Rightarrow \sin\varphi = \cos\varphi = -\frac{1}{\sqrt{2}}$$

$$\boldsymbol{S}_\varphi = -\left|\boldsymbol{V}_{a\_in}\right| e^{j\alpha_a} \sin\varphi + \left|\boldsymbol{V}_{b\_in}\right| e^{j\alpha_b} \cos\varphi = \frac{1.5\cos\theta\left(3+j\sqrt{3}\right)}{2\sqrt{2}\cos\theta-\sin\theta}$$

$$\boldsymbol{S}_\theta = \left|\boldsymbol{V}_{a\_in}\right| e^{j\alpha_a} \cos\theta\cos\varphi + \left|\boldsymbol{V}_{b\_in}\right| e^{j\alpha_b} \cos\theta\sin\varphi - \left|\boldsymbol{V}_{c\_in}\right| e^{j\alpha_c} \sin\theta = \frac{-1.5\left(1-j\sqrt{3}\right)}{2\sqrt{2}\cos\theta - \sin\theta}$$

$\delta = arg(\boldsymbol{S}_\varphi) - arg(\boldsymbol{S}_\theta) = -\pi/2$; Now,

$$|\psi|_C(\varphi) = \left|\frac{1}{2}\arctan\frac{2|\boldsymbol{S}_\theta||\boldsymbol{S}_\varphi|\cos(\delta)}{|\boldsymbol{S}_\theta|^2 - |\boldsymbol{S}_\varphi|^2}\right| = 0$$

6) *ab*-φ swell

$\left|\boldsymbol{V}_{c\_in}\right| = 1-d;\ \left|\boldsymbol{V}_{a\_in}\right| = \left|\boldsymbol{V}_{b\_in}\right| = 1;$

$\theta = \pi - \tan^{-1}\left((1-d)\sqrt{2}\right);\ \ \varphi = -3\pi/4;\ \Rightarrow \sin\varphi = \cos\varphi = -\frac{1}{\sqrt{2}}$

$$\boldsymbol{S}_\varphi = -\left|\boldsymbol{V}_{a\_in}\right| e^{j\alpha_a} \sin\varphi + \left|\boldsymbol{V}_{b\_in}\right| e^{j\alpha_b} \cos\varphi = \frac{3+j\sqrt{3}}{2\sqrt{2}}$$

$$\boldsymbol{S}_\theta = \left|\boldsymbol{V}_{a\_in}\right| e^{j\alpha_a} \cos\theta\cos\varphi + \left|\boldsymbol{V}_{b\_in}\right| e^{j\alpha_b} \cos\theta\sin\varphi - \left|\boldsymbol{V}_{c\_in}\right| e^{j\alpha_c} \sin\theta = \frac{-1+j\sqrt{3}}{2\sqrt{2}\cos\theta}$$

Hence, $\delta = arg(\boldsymbol{S}_\varphi) - arg(\boldsymbol{S}_\theta) = -\pi/2$; Now,

$$|\psi|_{AB}(\varphi) = \left|\frac{1}{2}\arctan\frac{2|\boldsymbol{S}_\theta||\boldsymbol{S}_\varphi|\cos(\delta)}{|\boldsymbol{S}_\theta|^2 - |\boldsymbol{S}_\varphi|^2}\right| = \frac{\pi}{2}$$